WADD TECHNICAL REPORT 60-220

A STUDY OF THE CHARACTERISTICS OF MODERN ENGINE NOISE AND THE RESPONSE CHARACTERISTICS OF STRUCTURES

R. J. COX
H. J. PARRY
J. CLOUGH

LOCKHEED AIRCRAFT CORPORATION
BURBANK, CALIFORNIA

DECEMBER 1961

AERONAUTICAL SYSTEMS DIVISION

NOTICES

When Government drawings, specifications, or other data are used for any purpose other than in connection with a definitely related Government procurement operation, the United States Government thereby incurs no responsibility nor any obligation whatsoever; and the fact that the Government may have formulated, furnished, or in any way supplied the said drawings, specifications, or other data, is not to be regarded by implication or otherwise as in any manner licensing the holder or any other person or corporation, or conveying any rights or permission to manufacture, use, or sell any patented invention that may in any way be related thereto.

Qualified requesters may obtain copies of this report from the Armed Services Technical Information Agency, (ASTIA), Arlington Hall Station, Arlington 12, Virginia.

This report has been released to the Office of Technical Services, U. S. Department of Commerce, Washington 25, D. C., for sale to the general public.

Copies of ASD Technical Reports and Technical Notes should not be returned to the Aeronautical Systems Division unless return is required by security considerations, contractual obligations, or notice on a specific document.

WADD TECHNICAL REPORT 60-220

A STUDY OF THE CHARACTERISTICS OF MODERN ENGINE NOISE AND THE RESPONSE CHARACTERISTICS OF STRUCTURES

R. J. COX
H. J. PARRY
J. CLOUGH

LOCKHEED AIRCRAFT CORPORATION
BURBANK, CALIFORNIA

DECEMBER 1961

CONTRACT No. AF 33(616)-5546
PROJECT No. 1370
TASK No. 14004

FLIGHT DYNAMICS LABORATORY
AERONAUTICAL SYSTEMS DIVISION
AIR FORCE SYSTEMS COMMAND
UNITED STATES AIR FORCE
WRIGHT-PATTERSON AIR FORCE BASE, OHIO

300 - March 1962 - 22-921

FOREWORD

This report was prepared by the Lockheed Aircraft Corporation in Burbank, California, under United States Air Force Contract Number AF 33(616)-5546. The project was initiated by the Aeronautical Systems Division Flight Dynamics Laboratory under Project Number 1370, "Dynamic Problems in Flight Vehicles," Task Number 14004, "Method of Vibration Predictions, Control and Measurements" for "A Study of the Characteristics of Modern Engine Noise and the Response Characteristics of Structures." Mr. R. J. Cox of the Lockheed Aircraft Corporation was the engineer in charge of the work covered under Contract AF 33(616)-5546. Mr. R. F. Wilkus of the Flight Dynamics Laboratory was project engineer. Research was started in March 1958 and completed in January 1960.

The authors wish to acknowledge the major contributions of Mr. Elias Moness in the field of structural response.

ABSTRACT

This is a final report on a study of jet engine noise and the response of structure to that noise.

The near sound field characteristics of a jet engine operating on the ground at both military and afterburner thrust were measured. Sound pressure levels were obtained in the near field and within the jet wake. Pressure levels and cross-correlation coefficients were obtained at two locations in the noise field for the free field, a rigid boundary and a flexible boundary.

Several panels, representative of typical airframe structure, were subjected to this jet engine noise environment. Structural response in terms of strain and accelerations was measured and analyzed. These panels were also subjected to discrete frequency excitation to determine basic response parameters.

An analytical method for the prediction of response of complex structures in an actual jet noise environment was developed. Predicted and measured responses were compared.

PUBLICATION REVIEW

This report has been reviewed and is approved.

FOR THE COMMANDER:

William C. Nielsen

WILLIAM C. NIELSEN
Colonel, USAF
Chief, Flight Dynamics Laboratory

TABLE OF CONTENTS

Section		Page
I	Introduction and Objectives	1
II	Noise Study	3
	A. Scope	3
	B. General Description of the Acoustic Noise Tests	3
	1. The Test Site	3
	2. Description of the YJ-79 Engine	4
	3. Description of the Noise Tests	5
	a. Free Field Survey	5
	b. Bounded Field Survey	8
	4. Field Test Instrumentation	8
	C. Data Processing	12
	1. Correlation Computer System	12
	2. Analysis of Error for the Correlation Computer	15
	3. Narrow Band Analyzer	16
	4. Probability Distribution Analyzer	18
	D. Results	18
	1. Free Field Survey Results	19
	a. Sound Pressure Level Contours	19
	b. Narrow Band Sound Pressure Spectra	28
	c. Probability Distribution of Amplitudes	41
	2. Bounded Field Survey Results	45

TABLE OF CONTENTS

Section		Page
	a. Space-Phase Correlation	45
	b. Sound Pressure Spectra	64
	c. Probability Distribution of Pressure Amplitude	74
	3. Miscellaneous Results	74
E.	Accuracy of the Data	85
	1. Microphones (Altec Lansing)	85
	2. Microphones (Photocon Research Products)	85
	3. Amplifying-Recording-Playback System	85
	4. Data Plotting	86
F.	Discussion of Results	86
	1. The Free Field Survey	86
	a. Sound Pressure Level Contours	86
	b. Free Field Spectra	87
	2. Probability Distribution of Amplitude	88
	3. Bounded Field Survey	89
	a. Space-Phase Correlation of Sound Pressure	89
	b. Sound Pressure Spectra	90
	4. Miscellany	91
G.	Conclusions	91
III	Theoretical Panel Response	93
A.	Introduction	93

TABLE OF CONTENTS

Section		Page
	B. Theoretical Panel Modes and Comparison with Laboratory Resonance Tests	93
	1. 6- x 20-inch Panel	93
	2. Flat Panel A	94
	C. Panel Dumping from Laboratory Resonance Tests	98
	1. 6- x 20-inch Panel	98
	2. Flat Panel A	98
	D. Theoretical Panel Response in Jet Noise Field	99
	1. Outline of Theory	99
	2. Response Calculations for 6- x 20-inch Panel	101
	3. Response Calculation for Flat Panel A	102
	E. Correlation of Accelerations and Bending Strains	105
	F. Discussion	106
	1. Panel Natural Modes	106
	a. 6- x 20-inch Panel	106
	b. Flat Panel A	107
	2. Panel Response in Jet Noise Field	107
	a. Mode Frequency Shift	107
	b. Comparison of Predicted and Test Acceleration Response	108
IV	Response Measurements	110
	A. Introduction and Objectives	110

TABLE OF CONTENTS

Section		Page
	1. Introduction	110
	2. Objectives	110
	B. Test Specimens and Equipment	111
	1. Description of Test Panels	111
	2. Jigs and Fixtures	116
	a. Field Tests	116
	b. Laboratory Tests	120
	C. Test Procedures and Results	121
	1. Laboratory Test Procedures and Results	121
	a. Static Pressure Test (6- x 20-inch Panel)	121
	b. Static Pressure Test (Panel A)	121
	c. Dynamic Test (6- x 20-inch Panel)	125
	d. Dynamic Test (Panel A)	125
	e. Dynamic Test (Panel E)	130
	2. Jet Noise Field Test Procedures and Results	132
	a. General Test Procedure	132
	b. Procedures and Results	133
	(1) 6- x 20-inch Test Panel	133
	(2) Panel A	140
V	Fatigue	148
	A. Introduction and Objectives	148

TABLE OF CONTENTS

Section		Page
	B. Procedure	148
	C. Results	148
	D. Conclusions	150
VI	Summary	150
	A. Summary of Conclusions	150
	B. Recommendations	151
	References	153

LIST OF ILLUSTRATIONS

Figure		Page
II-1	Test Site Configuration	2
II-2	Test Site - Buildings and Engine	4
II-3	YJ-79 Engine and Control Console	4
II-4	Temperature and Sound Pressure Measurement Limits and Test Panel Locations	6
II-5a - II-5c	Microphone Stations for Free Field Survey	6-7
II-6	Microphone Coordinate System for Boundary Tests	9
II-7	Multi-Channel Microphone System for Measurement of Turbo-jet Engine Exhaust Noise Field	10
II-8	Test Instrumentation inside the Instrument Shelter	10
II-9	Typical Microphone Arrangement During the Free Field Survey	11
II-10	Typical Microphone Arrangement During Cross-Correlation Measurements	11
II-11	Jet Wake Probe	11
II-12	Correlation Computer System	13
II-13	Data Reduction System	14
II-14	Electronic Analog Correlation Computer and Magnetic Tape Reproducer	14
II-15	Correlation Computer Error	17
II-16	Narrow Band Spectrum Level Analysis System	17
II-17	Power Spectral Density Analysis System	17
II-18	Narrow Band Analyzer System	18
II-19	Probability Distribution Analyzer System	19

LIST OF ILLUSTRATIONS

Figure		Page
II-20a - II-21h	Near Field Contours of Sound Pressure Spectrum Levels ...	20-27
II-22a - II-25g	Narrow Band (10 cps) Analysis of Sound Pressure Levels - Free Field Survey	28-37
II-26a - II-27c	Narrow Band (10 cps) Analysis of Sound Pressure Levels - Jet Wake Survey	38-41
II-28a - II-29c	Probability Distribution of Pressure Amplitudes - Free Field Survey	42-44
II-30a - II-31c	Probability Distribution of Pressure Amplitudes - Jet Wake Survey	44-45
II-32a - II-35	Longitudinal Sound Pressure Correlation	46-58
II-36a - II-36d	Initial Zero Crossing of Correlation Curves	59-60
II-37a - II-38d	Comparison of Longitudinal Correlation Coefficients	61-63
II-39a - II-41d	Narrow Band (10 cps) Analysis of Sound Pressure Levels (Free Field, Flat Panel A, Rigid Panel)	66-71
II-42a - II-42d	Comparison of Sound Pressure Spectra	72-73
II-43a - II-45d	Probability Distribution of Pressure Amplitudes (Free Field, Flat Panel A, Rigid Panel)	75-77
II-46a - II-46b	Narrow Band (10 cps) Analysis of Sound Pressure Levels (Microphone Shadow)	78
II-46c	Comparison of Sound Pressure Spectra (Microphone Shadow)	79
II-47	Ratio of Excess Mean-Square Pressure Measured with a Flush Mounted Microphone	79
II-48a - II-48d	Narrow Band (10 cps) Analysis of Sound Pressure Levels - Normal Volume Test	80-81

LIST OF ILLUSTRATIONS

Figure		Page
II-48e - II-48h	Narrow Band (10 cps) Analysis of Sound Pressure Levels - Minimum Volume Test	82-83
II-49a - II-49b	Comparison of Sound Pressure Spectra - 2 Volume Test	84
III-1	6- x 20-inch Panel Natural Frequency - Comparison of Theoretical and Test Results	94
III-2	6- x 20-inch Panel Mode Shapes - Comparison of Theoretical and Lab Test Results	94
III-3	Coordinates for Panel A Theoretical Mode Shape Determination	95
III-4	Panel A Mode Determination	96
III-5a - III-5c	Panel A Natural Frequencies and Mode Shapes - Comparison of Theoretical and Lab Test Results	97
III-6a - III-8	Comparison of Predicted and Measured Acceleration Spectrum in Jet Noise Field (at Panel Center):	103-104
	6- x 20-inch Panel	103-104
	Panel A	104
III-9	Relation between Acceleration and Bending Stress at Center of Panel - in Fundamental Mode - 6- x 20-inch Panel	106
IV-1	Panel A	112
IV-2	Panel B	113
IV-3	Panel D	114
IV-4	Panel E	115
IV-5	6" x 20" Test Panel	116
IV-6	Flat Panel Support Jig	117
IV-7	Support Jig, Curved Panel	118
IV-8	Acoustical Chamber	119
IV-9	Engine Stand Setup	120

LIST OF ILLUSTRATIONS

Figure			Page
IV-10	Test Setup for Dynamic Response and Mode Survey under Discrete Frequencies - Panel A		120
IV-11	Static Pressure Test - 6- x 20-inch x .032 Panel		121
IV-12	Velocity Contour Survey under Discrete Frequencies - Panel A		122
IV-13	Static Deflection - Panel A		122
IV-14 - IV-17	Static Bending Strain - Panel A		123-124
IV-18	Strain Distribution - Panel A - Static		125
IV-19	Dynamic Response - 6- x 20-inch x .032 Alum Test Panel		126
IV-20	Frequency Response - 6- x 20-inch Panel		126
IV-21	Characteristics of Discrete Frequency Excitation and Response of Panel A		127
IV-22a - IV-22b	Discrete Frequency Mode Shapes - Panel A		128
IV-23	Discrete Frequency Response at Center of Panel A		129
IV-24	Frequency Response of Panel E		131
IV-25a - IV-25b	Discrete Frequency Mode Shapes for Panel E		131
IV-26	Panel E Response - Discrete Frequency Excitation - Sta. F-20		132
IV-27 - IV-55	Power Spectral Density Analysis of:		133-147
IV-27	Pressure	6- x 20-inch Test Panel - Afterburner	133
IV-28-30	Acceleration	6- x 20-inch Test Panel - Afterburner	133-134
IV-31-33	Bending Strain	6- x 20-inch Test Panel - Afterburner	135-136
IV-34	Pressure	6- x 20-inch Test Panel - Military	136
IV-35-37	Acceleration	6- x 20-inch Test Panel - Military	137-138
IV-38-40	Bending Strain	6- x 20-inch Test Panel - Military	138-139

LIST OF ILLUSTRATIONS

Figure			Page
IV-41	Pressure	Flat Panel A - Afterburner	140
IV-42-44	Acceleration	Flat Panel A - Afterburner	141-142
IV-45-47	Bending Strain	Flat Panel A - Afterburner	142-143
IV-48-49	Pressure	Flat Panel A - Military	144
IV-50-52	Acceleration	Flat Panel A - Military	145-146
IV-53-55	Bending Strain	Flat Panel A - Military	146-147
V-1	Fatigue Failures in Panel A		149
V-2	Doubler Installation - Typical for Type A and Type E Panels		149

LIST OF TABLES

Table		Page
II-1	Average Engine-Operating Conditions	5
II-2	Location of Panel Boundary Sites	8
II-3	Average Microphone Characteristics	8
II-4	Microphone Coordinates Used for the Panel Boundary Site Test Recordings for Correlation	9
II-5	Microphone Coordinates Used for the Panel Response Tests	9
II-6	Filter Band Widths	15
II-7	Analysis of Probability Distribution of Sound Pressure Amplitudes Assuming a Rayleigh Distribution	42
II-8a	Spatial Average of Sound Spectrum Pressure Levels in Decibels (re: 0.0002 dynes/cm^2) for Three Sound Field Boundaries and Two Engine Conditions, Upstream Site	64
II-8b	Comparison of Sound Spectrum Pressure Levels in Decibels (re: 0.0002 dynes/cm^2) for Various Field Boundary Conditions - Upstream Site	64
II-9a	Spatial Average of Sound Spectrum Pressure Levels in Decibels (re: 0.0002 dynes/cm^2) for Three Sound Field Boundaries and Two Engine Conditions - Downstream Site	65
II-9b	Comparison of Sound Spectrum Pressure Levels in Decibels (re: 0.0002 dynes/cm^2) for Various Field Boundary Conditions - Downstream Site	65
II-10	Range of Overall Sound Pressure Levels at the Free Field Monitor Microphone	74
II-11	Jet Wake Probe Maximum Temperatures	74
III-1	Panel A Theoretical Model Determination	95
III-2	Damping Ratios - 6- x 20-inch Panel	98
III-3	Damping Ratios - Panel A	99

LIST OF TABLES

Table		Page
III-4	Panel A Data for Field Response Calculations	99
III-5	Response of 6- x 20-inch Panel	102
III-6	Response of Panel A	103
IV-1	Identification of Test Panels	111
IV-2	Discrete Frequency Strain Response - Panel A	129
IV-3	Discrete Frequency Strain Response - Panel E	130
V-1	Log of Fatigue Failures	149

LIST OF SYMBOLS

a - Panel length (in.)

a_i, a_j - Displacements in mode at points "i" and "j" (Ratio of displacements to reference displacement)

ΔA - Element of area on panel over which pressure is assumed to be constant (ft.^{2})

C_{ij} - Power spectral density of pressure correlation coefficient

$= \dfrac{\phi_{ij}}{(\phi_i \phi_j)^{1/2}}$ (non-dimensional)

E - Young's Modulus (lbs./in.^{2})

f - Frequency cps

f_o - Natural frequency of mode cps

g - Accelerations due to gravity (in./sec.^{2})

h - Panel thickness (ins.)

i, j - Suffixes denoting locations on panel

Δm - Element of mass of panel (slugs)

M_e - Generalized mass of panel = $\sum_i \Delta m_i a_i^2$ (slugs)

p - Instantaneous pressure (lbs./ft.^{2})

P - RMS pressure (lb./ft.^{2})

R, I - Suffixes denoting real and imaginary parts, respectively

γ - Dynamic magnification factor (non-dimensional)

δ - Relative damping in mode (non-dimensional)

ρ - Mass density (lbs./in.^{3})

σ - Poisson's Ratio (non-dimensional)

LIST OF SYMBOLS
(Continued)

λ - Frequency factor (non-dimensional)

ξ_o - RMS reference displacement

ω - Frequency (rad./sec.)

ω_o - Natural frequency (rad./sec.)

ϕ_i - Power spectral density of pressure at "i" $(\text{lbs./ft.}^2)^2/\text{cps}$

ϕ_F - Power spectral density of generalized force $(\text{lb.}^2/\text{cps})$

ϕ_{ij} - Cross-spectral density of pressure at points "i" and "j" $(\text{lb./ft.}^2)^2/\text{cps}$

SECTION I

INTRODUCTION AND OBJECTIVES

A significant amount of important work has been devoted to the study of structural fatigue under acoustic excitation. As outlined in the Phase I report (Reference 9) of this study, many have contributed to understanding the nature of the noise source and the response of structure to that noise. However, at the outset of this particular program the state-of-the-art had yet to provide a proven method of analysis which would predict the full character of the response of typical flight vehicle structure subjected to a realistic noise source, such as a modern turbojet engire. Once response prediction could be established, the fatigue integrity of the structure should be more firmly indicated.

The method for predicting response, suggested in the Phase I report, adopted the approach of generalized harmonic analysis. It assumed light damping and the validity of superposition of the response spectra of the individual modes. It also considered the spatial correlations of the acoustic excitation. To verify or further develop this theoretical approach, considerable test data were necessary. Data were needed to describe the excitation, the structural response to the excitation, the basic dynamic parameters of the structure and some actual sonic fatigue results for the conditions studied.

The objectives for the program, then, were:

1. to describe by test the noise field of a modern turbojet power plant
   a. free field
   b. bounded (rigid and flexible) field
   c. within jet wake;
2. to describe by test the response of structure to sonic excitation of a turbojet engine
   a. simple panel
   b. typical aircraft structure;
3. to adapt and develop theory and analytical methods for predicting the response of structure to sonic excitation from a turbojet engine;
4. to conduct fatigue tests of typical structure in the turbojet noise environment.

Early in the program it was decided that major effort would be devoted to obtaining data describing these phenomena. Theory development would receive less emphasis. Only minor effort would be applied to the fatigue testing.

This report presents the results of the entire program. As noted from the table of contents, the work toward each of the major objectives is treated in a separate section.

Manuscript released by authors August 1961 for publication as a WADD Technical Report.

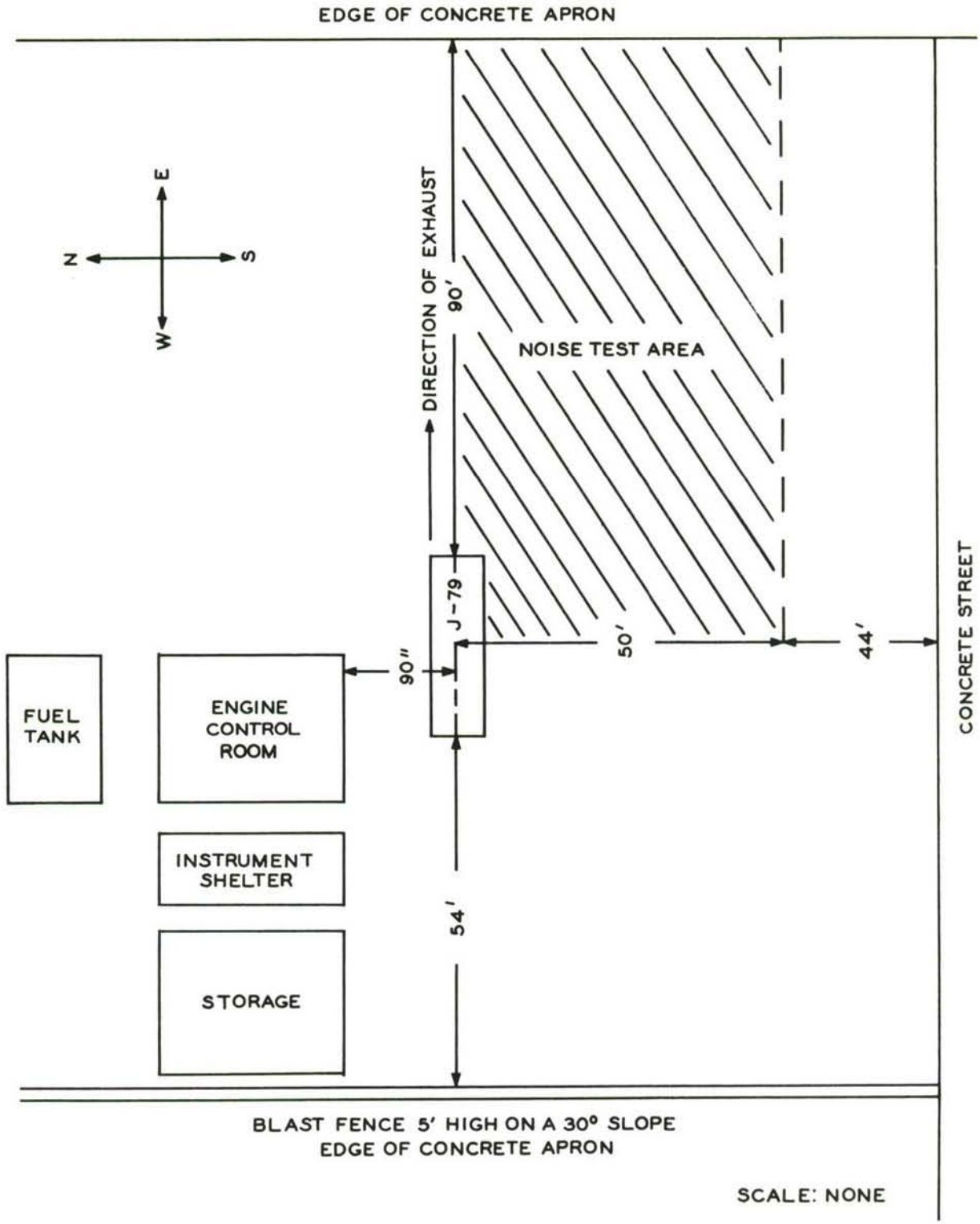

Figure II-1. Test Site Configuration

SECTION II

NOISE STUDY

A. Scope

The purpose of the noise study portion of the program was to define the acoustic noise field created by the turbojet engine. This section of the report describes the procedures and equipment used for the noise study and the results obtained. Some interpretation of these results has also been undertaken for those aspects which are not explicit in the consideration of structural response.

B. General Description of the Acoustic Noise Tests

All field tests were conducted at the Palmdale, California, municipal airport test facility. Measurements of near field sound pressures were obtained using a YJ-79 turbojet engine operated with and without afterburning. Investigation included the free field (actually quasi-free field) inside and outside the jet wake, and the sound field at rigid and flexible boundaries. In addition to determining mean-square and r.m.s. pressures, measurements were also made of the space-phase correlation coefficients for several noise field boundary conditions.

Noise data was recorded at the test site on magnetic tape using condenser microphones as the primary sensing elements. A monitor microphone was used during all tests. Subsequent processing of the recorded signals was accomplished using a specially constructed correlation computer and a narrow-band analyzer system. Summaries of pertinent results are presented in this section.

1. The Test Site

The general configuration of the test site is shown in Figure II-1. The areas directly east and south of the site are completely free of obstructions for several thousands of yards. The area north of the engine is clear of obstructions except for the instrument shelters and an aircraft run-up area at a distance of about 500 yards. West of the area beyond the blast fence is clear for about 200 yards. Since the test stand is located in the vicinity of aircraft operations of various sorts, a survey of ambient sound levels was made. For the worst conditions encountered during all tests the ambient overall SPL was never in excess of 110 decibels, re: 0.0002 dynes/cm^2. The ground surface over the entire noise test area is covered by a concrete apron.

Figure II-2 shows the physical construction of the test site buildings. For all measurements in this program the engine was completely uncovered, as shown. The instrument shelter was acoustically treated to protect personnel and equipment from the intense noise levels produced by the engine.

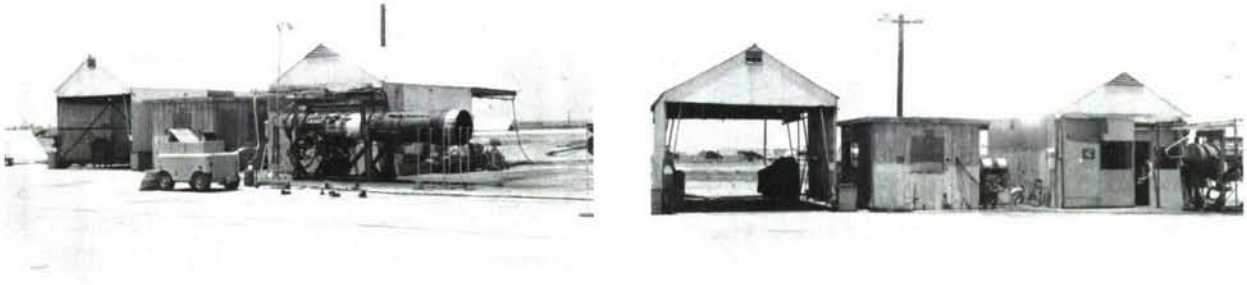

Figure II-2. Test Site - Buildings and Engine

The actual noise test area located with respect to the engine is shown in Figure II-1. This point is mentioned specifically since, for convenience of display, all other figures in this report referred to this area are shown as if being on the opposite (north) side of the jet centerline.

2. Description of the YJ-79 Engine

A close-up view of the YJ-79 engine and its control console are shown in Figure II-3. The engine is an axial flow turbojet, with afterburner, capable of thrust modulation. Basic components of the engine include a 17-stage compressor, a three-stage turbine, variable pitch inlet guide vanes, ten combustion chambers, and a variable converging-diverging exhaust nozzle.

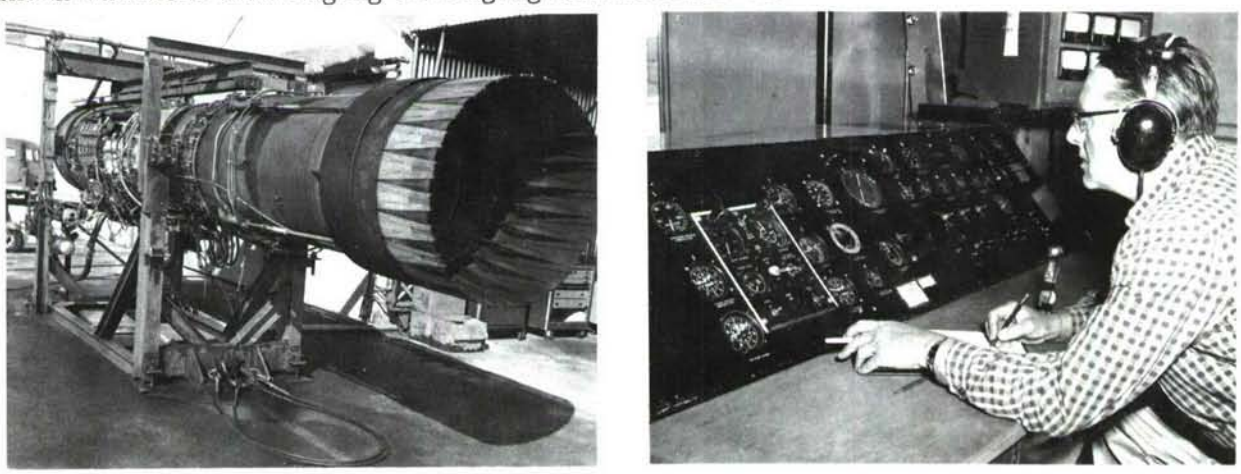

Figure II-3. YJ-79 Engine and Control Console

Since no thrust measuring instrumentation was available on the test stand, rpm and exhaust gas temperature were used as the operating criteria. Table II-1 gives rpm, exhaust gas temperature, and several other variable engine parameters for each of three engine thrust ratings: normal (rpm 100), military, and afterburner. The average values given in Table II-1 for jet velocity and nozzle pressure ratio are calculated values based on the prevailing atmospheric conditions and typical engine performance data. Jet velocity was computed from the manufacturer's performance data on thrust and airflow.

TABLE II-1

AVERAGE ENGINE-OPERATING CONDITIONS					
Engine Condition	Exhaust Gas Temperature (Degrees C)	Pressure Ratio (Calculated)	Nozzle Area $(Inches)^2$	Nozzle Dia. Inches	Velocity (ft/sec) (Calculated)
RPM 100	510	1.82	420	23.1	1595
Military	565	1.73	370	21.7	1740
Afterburner	585	1.78	576	27.1	2290

3. Description of the Noise Tests

For convenience of reporting, the noise tests have been divided into two classes: free field surveys, and bounded field surveys. In this report, the free field surveys are considered to be all data taken to define the sound field of the engine including the area inside the wake. Bounded field surveys are considered to include all data taken to produce detailed information on the sound fields immediately adjacent to a test panel boundary location.

a. Free Field Survey

The surveys were conducted for three engine power conditions: normal, military, and afterburner. Definition of the areas outside and inside the jet wake was made on the basis of temperature measurements along the boundary of the jet exhaust wake. The division between these two regions was arbitrarily defined as the locus of points along the exhaust wake boundary where the mean temperature measured 5°F above the mean ambient temperature. This temperature limit is shown in Figure II-4. It was observed during the temperature limit measurements that the exhaust wake impinged on the concrete apron approximately 25 feet downstream of the nozzle. This fact accounts for the two temperature limits shown on Figure II-4, beyond 25 feet downstream. The temperature limit was determined for the military engine power condition only.

The free field survey region extended to a maximum of 50 feet radially from the jet centerline, 70 feet downstream of the nozzle exit, and 10 feet forward of the nozzle exit. Figures II-5a, b, and c, pages 6 and 7, show the microphone stations used with the exception of three stations inside the exhaust, 80 feet downstream. The monitor microphone used during these tests was located 20 feet downstream from the nozzle exit and 20 feet from the jet centerline. Height of the microphones for the free field surveys was kept constant at 5 feet, the nominal height of the jet centerline as determined with surveying equipment.

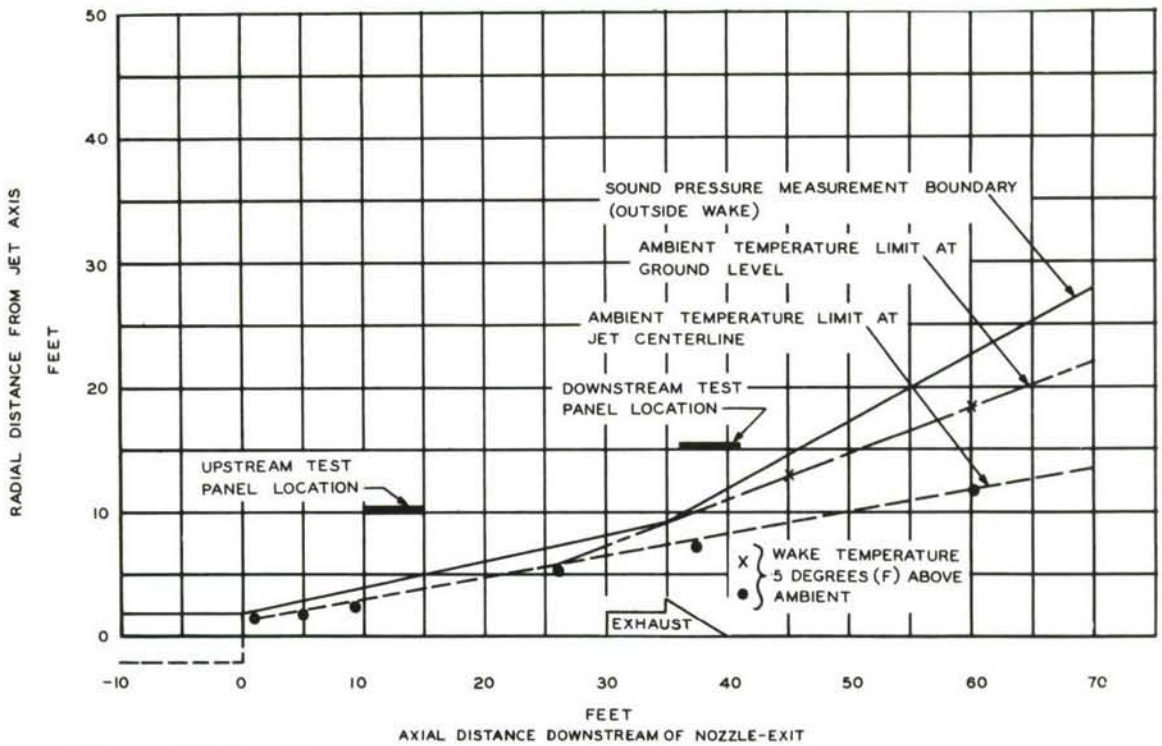

Figure II-4. Temperature and Sound Pressure Measurement Limits and Test Panel Locations

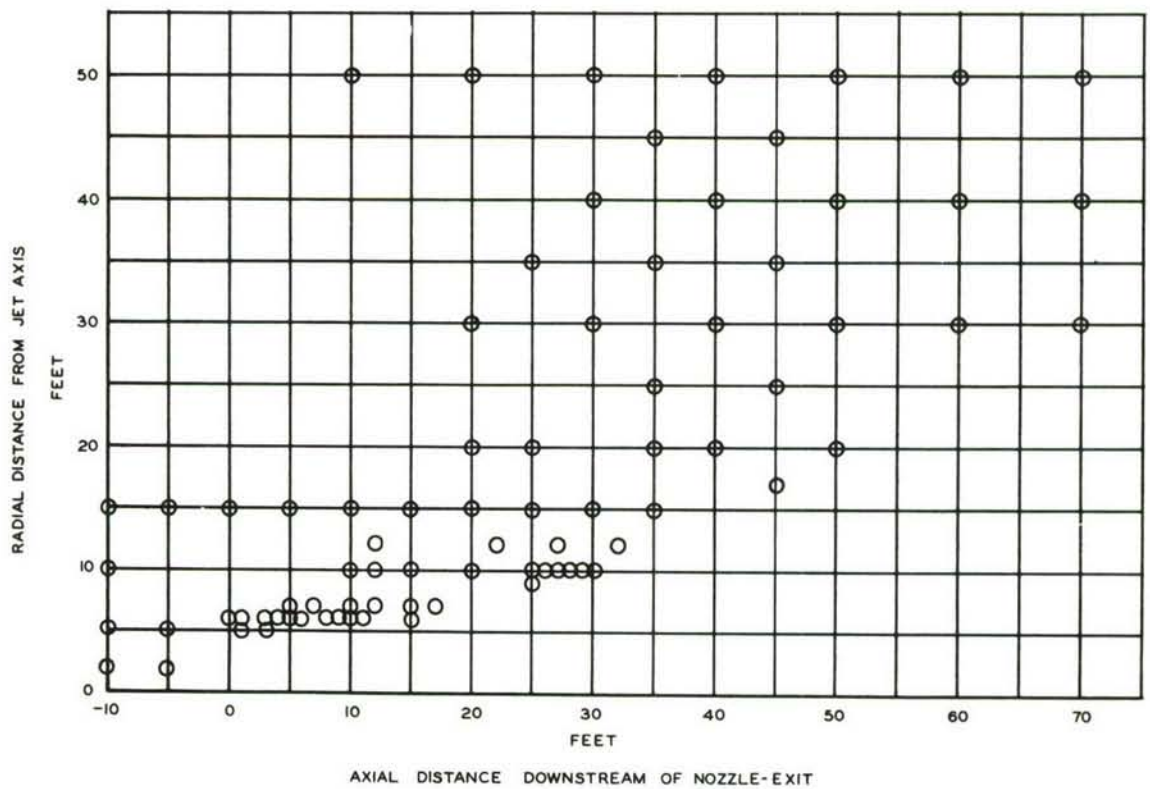

Figure II-5a. Microphone Stations for Free Field Survey - RPM 100

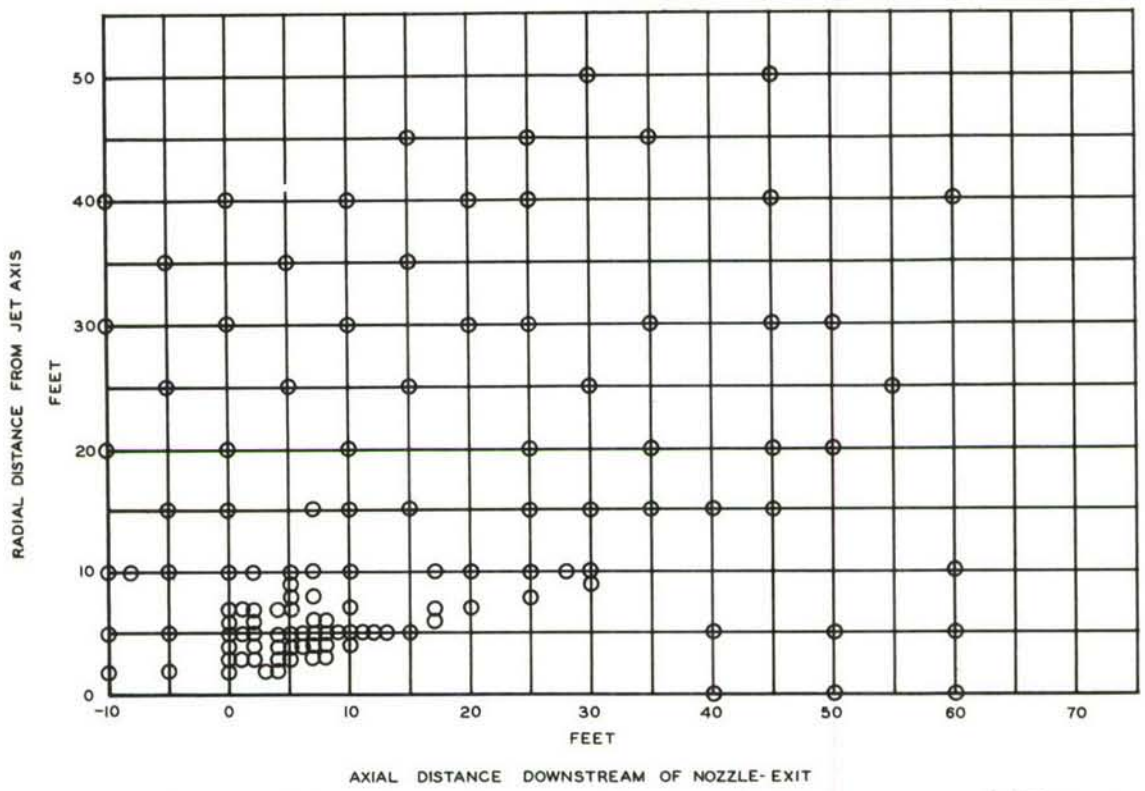

Figure II-5b. Microphone Stations for Free Field Survey - Military

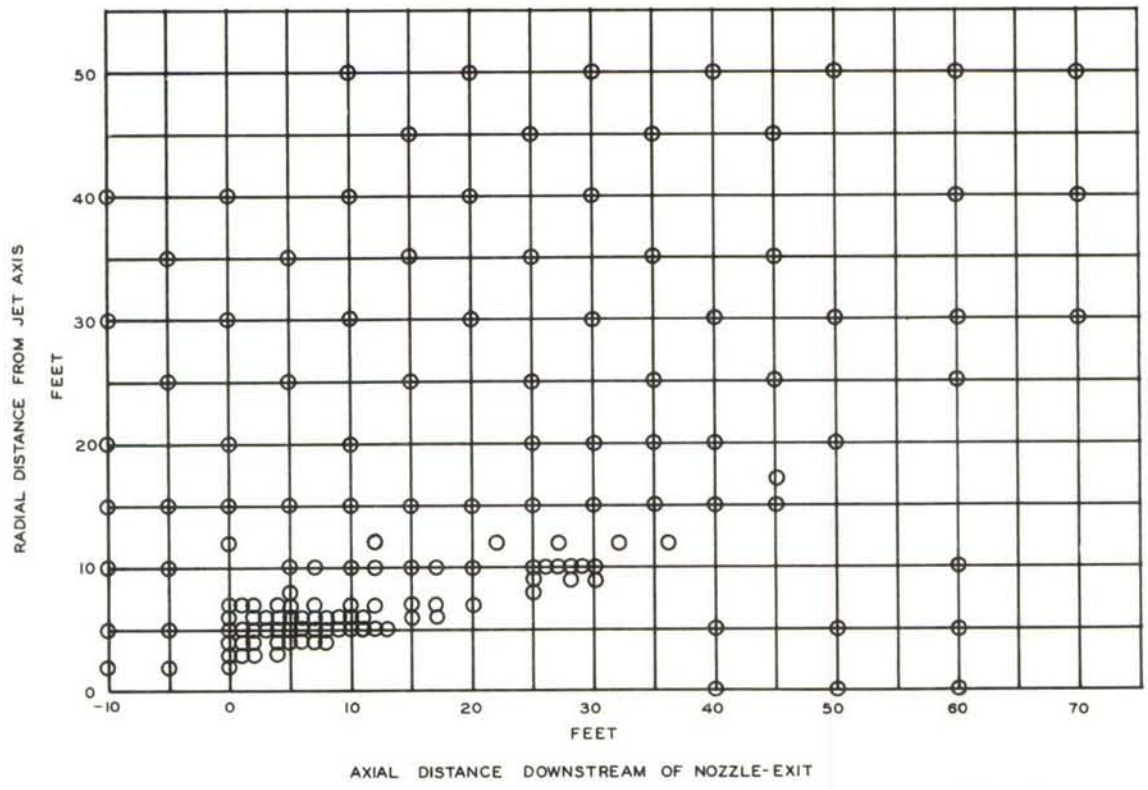

Figure II-5c. Microphone Stations for Free Field Survey - Afterburner

b. Bounded Field Survey

Bounded field survey measurements were conducted at the two locations shown in Figure II-4. These locations will be referred to as the upstream and downstream panel sites. Table II-2 gives the coordinates of these two locations in feet and the equivalent number of nozzle-exit diameters for two engine conditions: military and afterburner.

TABLE II-2

LOCATION OF PANEL BOUNDARY SITES

Site	Distance					
	From Nozzle-Exit			From Jet Centerline		
	Feet	Nozzle Diameters		Feet	Nozzle Diameters	
		Afterburner	Military		Afterburner	Military
Upstream	14.2	6.3	7.8	10	4.4	5.5
Downstream	40.1	17.8	22.2	15	6.6	8.3

TABLE II-3

AVERAGE MICROPHONE CHARACTERISTICS

Microphone Type		Sensitivity re: IV/dyne/cm^2	Sensitivity with Long Cable and Impedance Matching Transformer	Linear SPL Limit re: 0.0002 dynes/cm^2
Altec Lansing Corp.	21D	-50db	-70db	150db
	21BR-150-1	-58db	-78db	158db
	21BR-180-1	-70db	-90db	170db
	21BR-200-1	-85db	-105db	185db
	21BR-180-7	-70db	-90db	170db
	21BR-200-7	-85db	-105db	185db
	21BR-220-3	-100db	-120db	200db
Photocon Research Products	320T	-98db	---	200db
	342	-115db	---	215db

Location of cross-correlation measurements made at both panel sites are summarized in Tables II-4 and II-5. The microphone row and column coordinates used in those two figures refer to the coordinate system shown in Figure II-6.

4. Field Test Instrumentation

All acoustic measurements in the areas outside the jet wake were made with Altec Lansing Type 21 microphones equipped with wind screens and anti-microphonic pre-amplifier bases. Measurements inside the jet wake were made with water-cooled microphones manufactured by Photocon Research Products. Table II-3 lists typical microphone characteristics. Frequency compensating networks were employed for all microphones to minimize the effect of long microphone cable lengths.

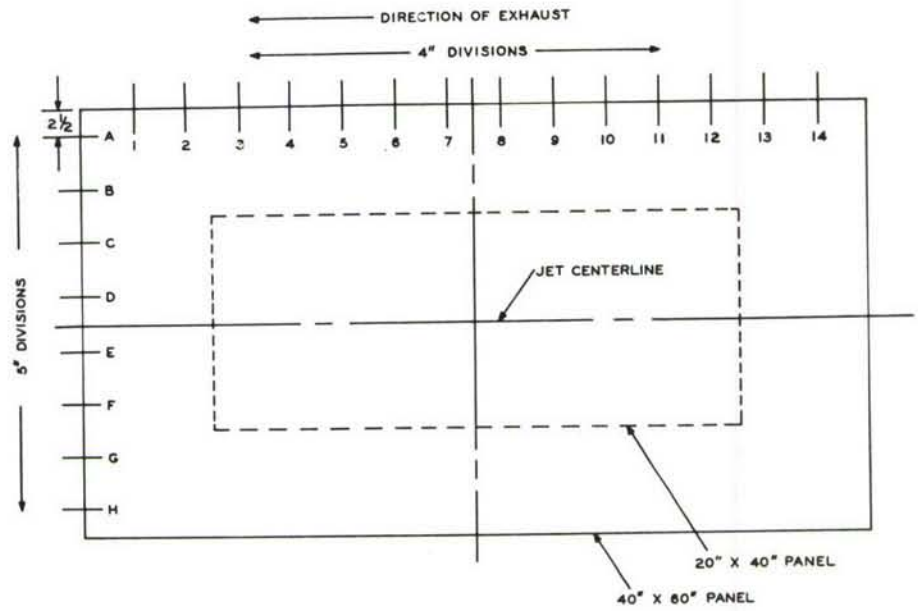

Figure II-6. Microphone Coordinate System for Boundary Tests

TABLE II-4

MICROPHONE COORDINATES USED FOR THE PANEL BOUNDARY SITE TEST RECORDINGS FOR CORRELATION

Test	Row	Columns
Rigid Panel Upstream - M Upstream - A/B Downstream - M Downstream - A/B	C, D	3, 4, 5, 6, 7, 8, 9, 10, 11, 12
Flat Panel A Upstream - M Upstream - A/B Downstream - M Downstream - A/B	C, D	3, 4, 5, 6, 7, 8, 9, 10, 11, 12
Free Field at the Panel Upstream - M Upstream - A/B Downstream - M Downstream - A/B	C, D	3, 4, 5, 6, 7, 8, 9, 10, 11, 12
Curved Panel A Downstream - RPM 100 Downstream - A/B	C, D	3, 4, 5, 6, 7, 8, 9, 10, 11, 12
Rigid Panel Downstream - M Downstream - A/B	C D E F	3, 12 3 3 3, 12

Engine Conditions

M = Military
A/B = Afterburner
RPM 100 = 100% RPM

TABLE II-5

MICROPHONE COORDINATES USED FOR THE PANEL RESPONSE TESTS

Test	Row	Columns
Flat Panel A Downstream - M Downstream - A/B	D	3, 4, 5, 7, 9, 11
Flat Panel B Downstream - RPM 100 Downstream - A/B	D	3, 4, 5, 7, 9, 11
Flat Panel D Downstream - M Downstream - A/B	D	3, 4, 5, 7, 9, 11
Flat Panel E Downstream - M Downstream - A/B	D	3, 4, 5, 7, 9, 11
Curved Panel B Downstream - M Downstream - A/B	D	3, 4, 5, 7, 9, 11
Curved Panel D Downstream - RPM 100 Downstream - A/B	D	3, 4, 5, 7, 9, 11
Two-Volume (Flat Panel A) Downstream - RPM 100 Downstream - A/B	D	4, 7, 11 (Outside and Inside)

Engine Conditions

M = Military
A/B = Afterburner
RPM 100 = 100% RPM

Signals from the microphones were recorded on an Ampex Type FR-114 magnetic tape recorder which provided 14 channels of data storage. Calibrated amplifiers and attenuators at the recorder input were used to obtain standardized recording levels with a minimum peak factor of 15 db. Recordings were monitored during the tests with a cathode ray oscilloscope and a R.M.S. vacuum tube voltmeter. Figure II-7 shows the essential features of the microphone recording system. Figure II-8 shows the physical arrangement of the various instrumentation and equipment inside the instrument shelter

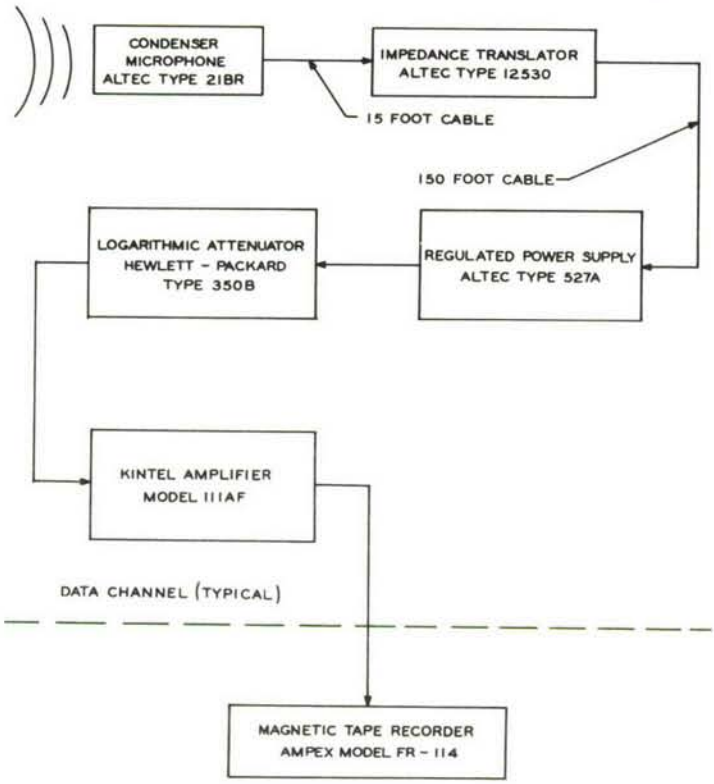

Figure II-7. Multi-Channel Microphone System for Measurement of Turbojet Engine Exhaust Noise Field

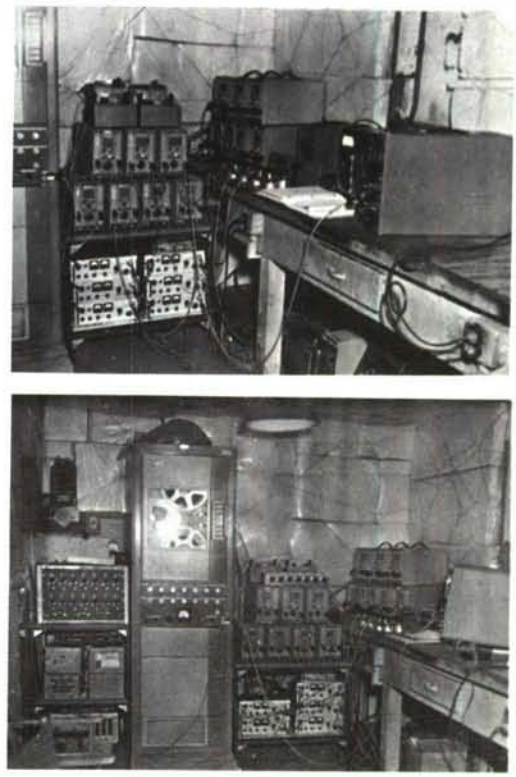

Figure II-8. Test Instrumentation Inside the Instrument Shelter

During the free field survey and cross-correlation tests, seven microphone output signals were recorded simultaneously, one channel being the monitor microphone. The particular microphones used were selected to give optimum signal-to-noise ratio and peak factor for the noise obtaining at the measurement position.

Figures II-9 and II-10 show typical microphone arrangements during the free field survey, the free field at a panel boundary, and a flat flexible panel.

The water-cooled Photocon Type microphones were mounted in two sides and the top of a stainless steel probe for sound pressure measurements in the jet wake. In addition, a thermocouple was installed in the probe for temperature monitoring. The assembled probe and details of the water tubes and wiring are shown in Figure II-11.

Figure II-9. Typical Microphone Arrangement during the Free Field Survey

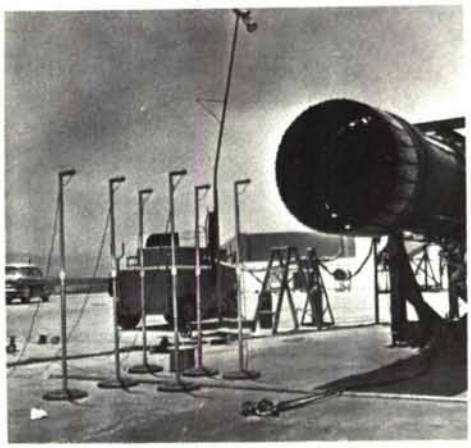

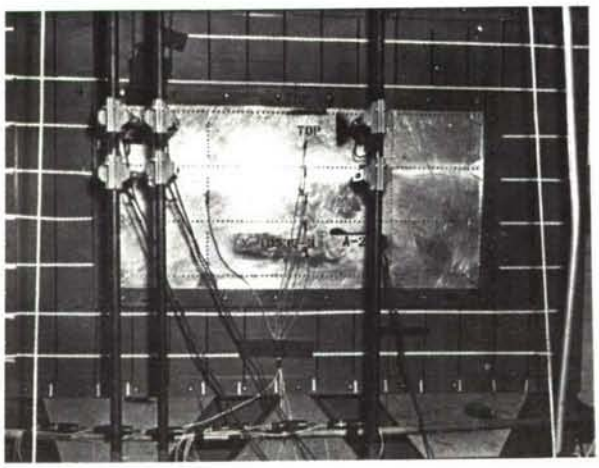

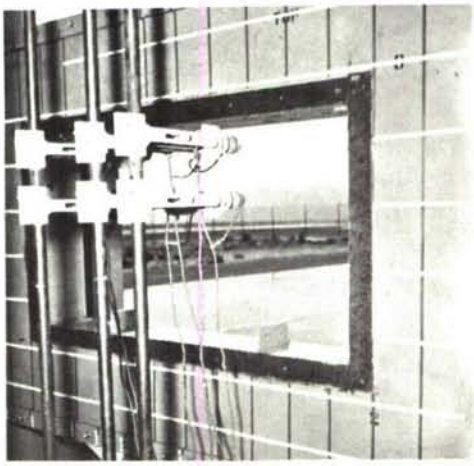

Figure II-10. Typical Microphone Arrangements during Cross-Correlation Measurements

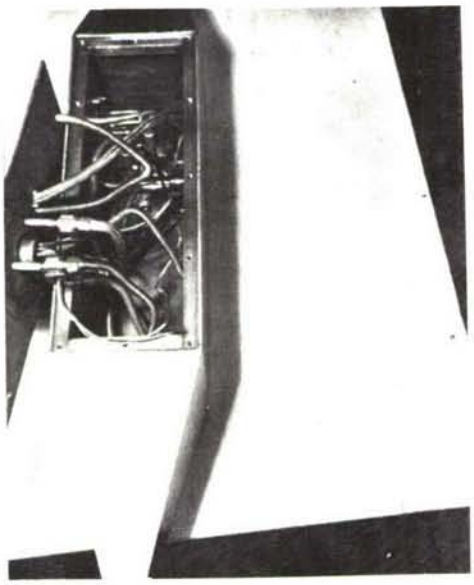

Figure II-11. Jet Wake Probe

C. Data Processing

This section describes techniques and equipment used for processing all basic acoustic data.

1. Correlation Computer System

A special electronic analog computer was constructed to determine space-phase correlation of sound pressures at the panel boundary locations.

From the definition (Reference 5) of the time cross-correlation function of two real quantities $e_1(t)$ and $e_2(t)$

$$\overline{e_1(t)\, e_2(t)} = \lim_{T \to \infty} \frac{1}{T} \int_0^T e_1(t)\, e_2(t)\, dt \tag{1}$$

It can be seen that the computation requires at least three mathematical operations: multiplication, integration, and division. (Note that in the present case where $e_1(t)$ and $e_2(t)$ are two random signals with no time shift involved, but rather a pseudo-phase shift due to spatial displacement, the time cross-correlation has been termed space-phase correlation.) Further, in order to instrument these computations with an analog computer it is necessary to approximate the limit condition with a finite integration time which results in the following modified form of the defining equation -

$$\overline{e_1(t)\, e_2(t)} \doteq \frac{1}{T} \int_0^T e_1(t)\, e_2(t)\, dt \tag{2}$$

The normalized form of this equation is, for purposes of this report, termed the space-phase correlation coefficient

$$r = \frac{\overline{e_1(t)\, e_2(t)}}{\sqrt{\overline{e_1^2(t)}} \cdot \sqrt{\overline{e_2^2(t)}}} \tag{3}$$

where $\overline{e^2(t)}$ is the time auto-correlation function with the argument set equal to zero, i.e.,

$$\overline{e^2(t)} \doteq \frac{1}{T} \int_0^T e(t+0) \cdot e(t)\, dt \tag{4}$$

which is an approximation of

$$R = \lim_{T \to \infty} \frac{1}{T} \int_0^T e(t+0) \cdot e(t)\, dt \tag{5}$$

as in the time cross-correlation case. Thus, $\overline{e^2(t)}$ is the mean-square of $e(t)$. Note that the approximate form of the equations for the mean-square and space-phase correlation require identical mathematical operations. The computer to be described solves equations (2) and (4) in the process of determining equation (3).

Computer system operation can be described most easily with reference to Figure II-12. Basic data signals were recorded on a magnetic tape record-reproduce system selected to give minimum recording error due to head spacing gap scatter. All other test information, including items such as transducer calibration factors, engine condition, transducer location, plus signal amplification and attenuation data, was recorded on preprinted data sheets.

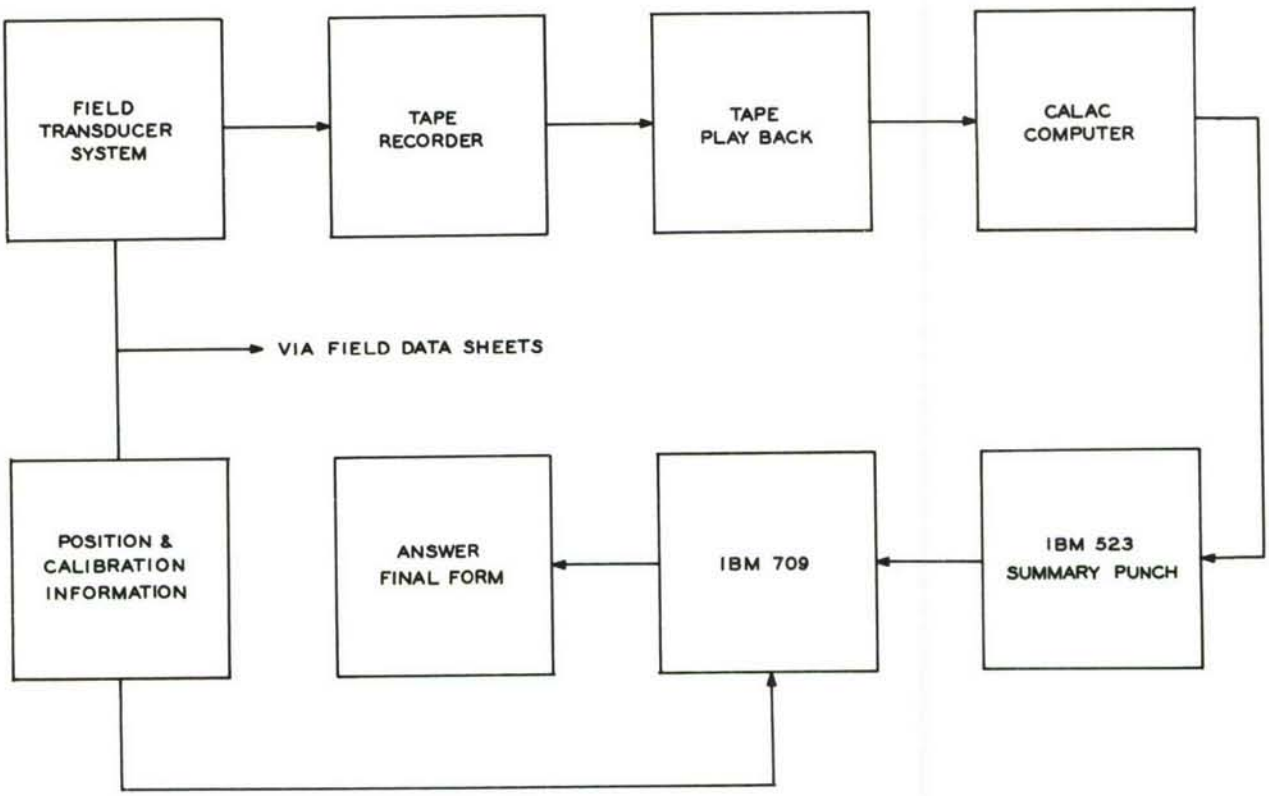

Figure II-12. Correlation Computer System

The specialized electronic analog computer accepts the recorded signals from the tape reproducer, performs the mathematical operations defined in equations (2) and (4) above and produces coded punched card outputs via the summary punch unit.

The analog computer also performs signal frequency limiting as required and establishes punched card coding identifying frequency limiting and other information including test number, tape channel numbers, internal amplification factors, and type of computation.

The resulting punched cards, along with the information from the preprinted data sheets are then processed with an IBM Type 709 digital computer which solves equation (3).

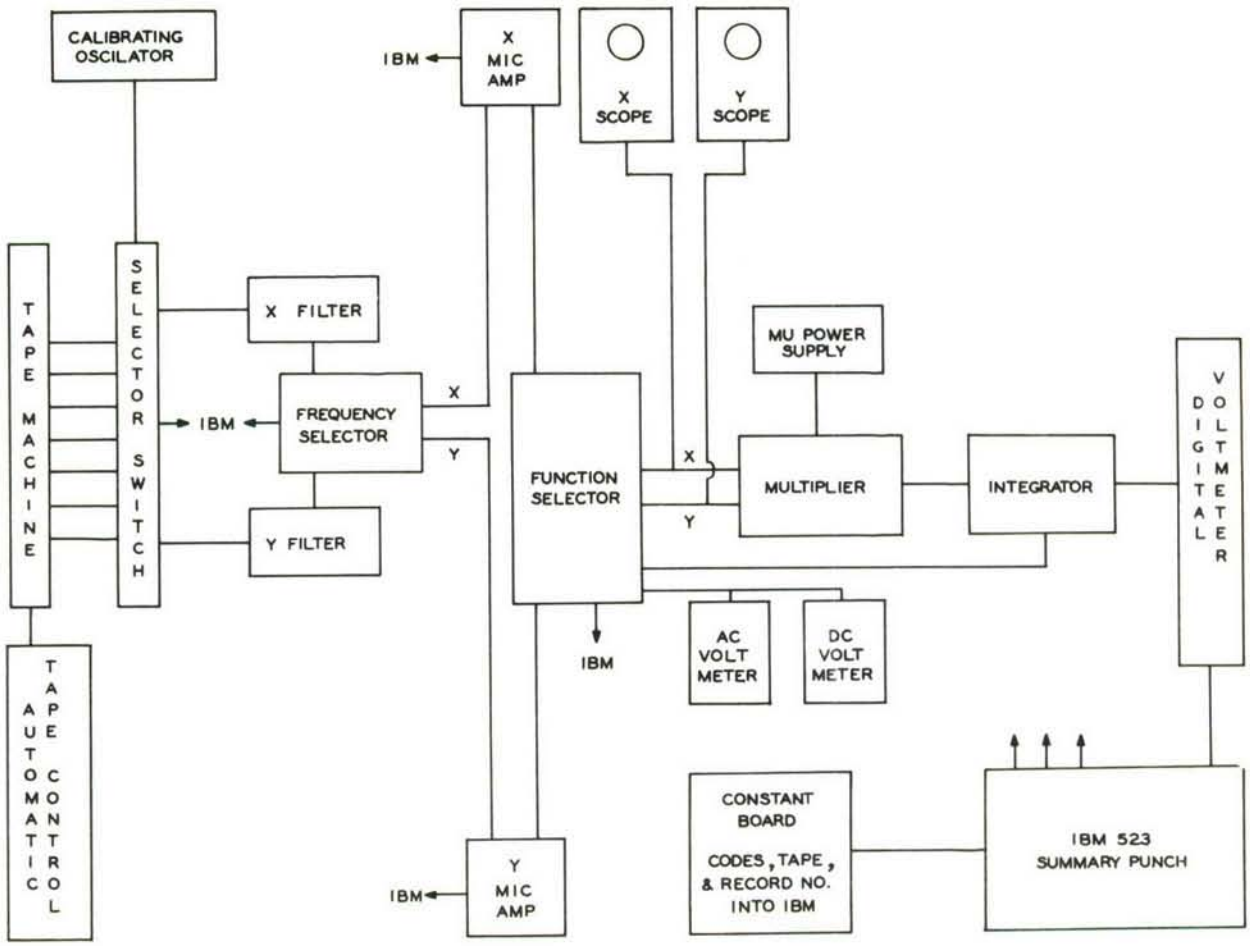

Figure II-13. Data Reduction System

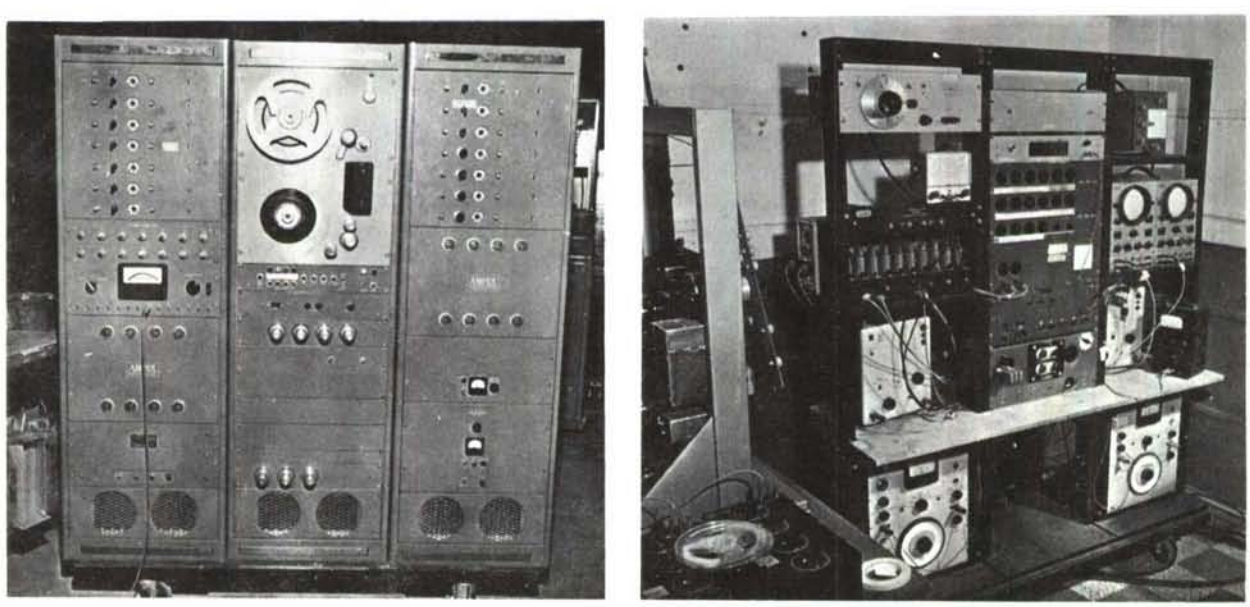

Figure II-14. Electronic Analog Correlation Computer and Magnetic Tape Reproducer

The analog computer is shown in the block diagram and photograph of Figures II-13 and II-14. The following list of equipment describes the major components of the computer:

EQUIPMENT LIST

Tape Playback Machine:	Ampex Type 375 (frequency response 0-5000 cps ± 2 db, signal to noise ratio 45 db or better)
Filters:	Bruel and Kjaer Type 2109 (1/3 Octave Band) General Radio Type 1550 (Octave Band)
Microphone Amplifiers:	Bruel and Kjaer Type 2601
Oscilloscopes:	Eico Type 425
AC Voltmeter:	Ballantine Type 310A (3% full scale accuracy)
DC Voltmeter:	RCA Type WV-98A (3% full scale accuracy)
Integrator:	Kintel Type 114A (Converted to an operational amplifier)
Digital Voltmeter:	Electro Instrument Type 3500P (0.1% accuracy)
Card Punch:	IBM Type 523 Summary Punch
Multiplier:	George A. Philbrick Researches, Inc., Model MV/DV 456

TABLE II-6

FILTER BAND WIDTHS

1/3 OCTAVE BAND FILTERS				OCTAVE BAND FILTERS	
Mid-Band Frequency (cps)	Band Width (cps)	Mid-Band Frequency (cps)	Band Width (cps)	Mid-Band Frequency (cps)	Band Width (cps)
40	9	250	57	39	55
50	11	320	73	52	38
63	15	400	93	105	75
80	18	500	115	210	150
100	23	630	149	420	300
125	29	800	179	850	600
160	37	1000	222	1700	1200
200	45			3400	2400

2. Analysis of Error for the Correlation Computer

Because of the finite integration time, 30 seconds for the data in this report, there is an error involved in computing equations (1) and (5) using (2) and (4). This error can be expressed (Reference 6, Chapter 7) as

$$\left(\frac{R}{\sigma}\right)_{OUT} = \frac{R(\tau)}{\sigma(\tau, t)}$$

which for 95% certainty is also shown to be

$$\left(\frac{R}{\sigma}\right)_{OUT} = \frac{200}{P}$$

where P = percentage error

σ = standard deviation

R = mean value of the correlation function.

For single tuned filters (also from Reference 6)

$$\sigma^2(\alpha,\theta) \leq \frac{1}{2\theta} + \frac{e^{-2\alpha}}{\theta}(2\alpha + 1)$$

where $\alpha = \pi\beta\tau$

$\theta = \pi\beta T$

τ = delay function

β = filter bandwidth

T = integration time

e = base of natural logarithms

For the special case

$$\tau = 0; \quad R = \overline{e^2(t)}$$

$$\sigma^2(0,\theta) \leq \frac{3}{2}\left(\frac{1}{\pi\beta T}\right)$$

and

$$\sigma \leq \frac{P}{200}$$

then if $W_o \sim B$ (W_o = Center frequency)

$$P \cong (200)\sqrt{\frac{3}{2}\left(\frac{1}{\pi\beta T}\right)}$$

This relation is plotted in Figure II-15 for T = 30 seconds as a function of filter bandwidth.

Several sources of error are inherent in the multiplier section of the computer due to drift, noise, and tracking at small phase angles. On the average these are estimated to contribute less than 5% error.

3. Narrow Band Analyzer

This system consists of the instruments shown in Figures II-16, II-17, and II-18. For spectrum level analysis the output of the analyzer is converted to a logarithmic scale to enable the xy recorder to plot spectrum level directly. The frequency bandwidth of the filter used is 10 cps. The region of uniform transmission (not the ± 3 db points) is defined as the bandwidth, and attenuation of this filter at ± 50 cps is 38 db. The frequency response of the system is ± 2.5 db from 2 to 25000 cps and the signal to noise ratio is 60 db. The frequency ranges are 0-250, 0-2500, and 0-25000 cps. The automatic frequency sweep drive system, which also actuates the x-axis of the recorder, requires either 11 or 22

minutes to scan any one frequency range. In the analyses presented in this report the longer sweep time was used with the 0-2500 cps range. This permitted each frequency to be in the filter for 5.34 seconds, providing a reasonable compromise between frequency resolution and statistical certainty. The x-y recorder response provides low-pass filter action which acts to smooth the curve.

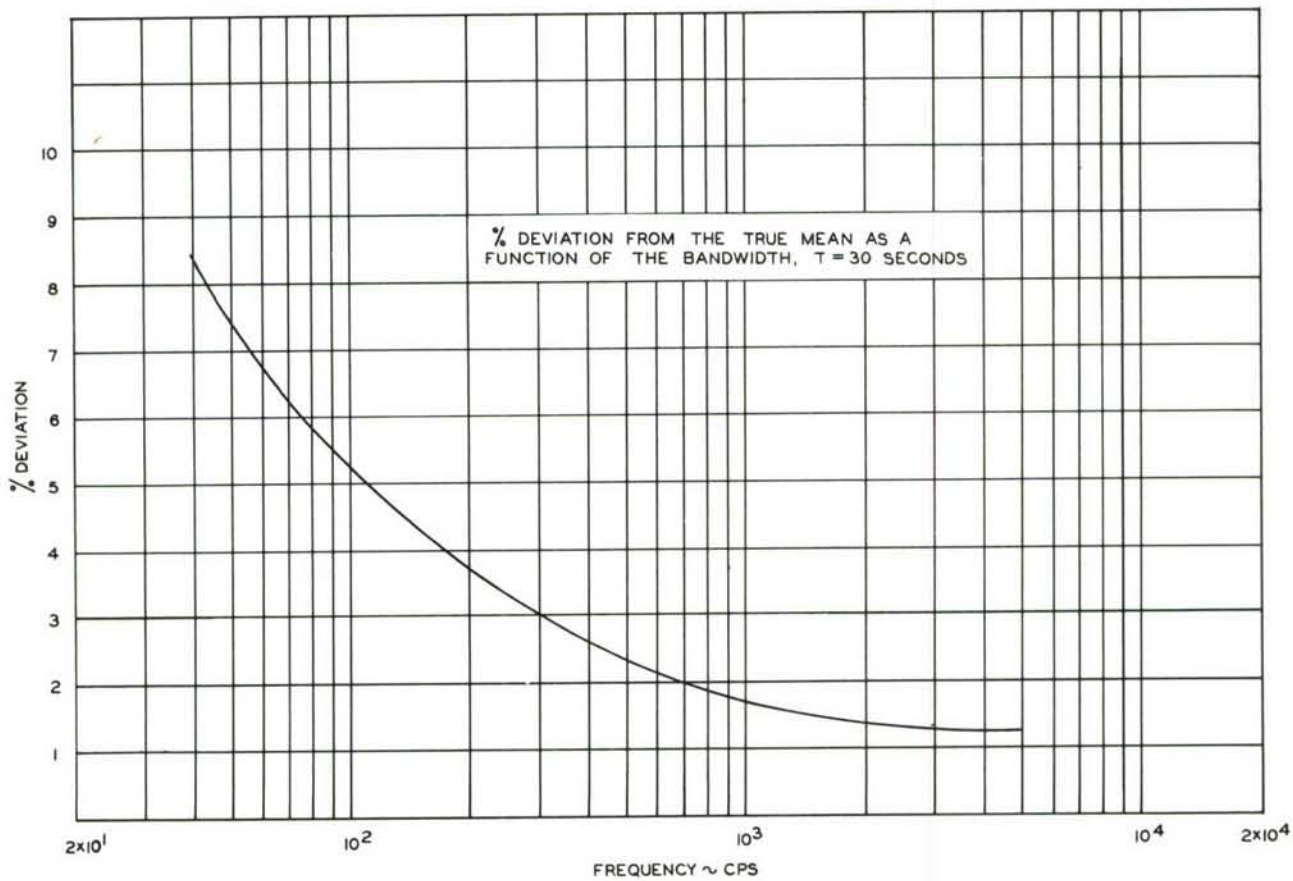

Figure II-15. Correlation Computer Error

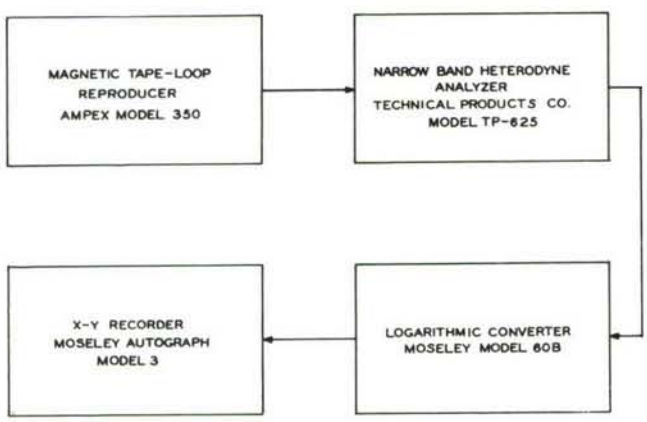

Figure II-16. Narrow Band Spectrum Level Analysis System

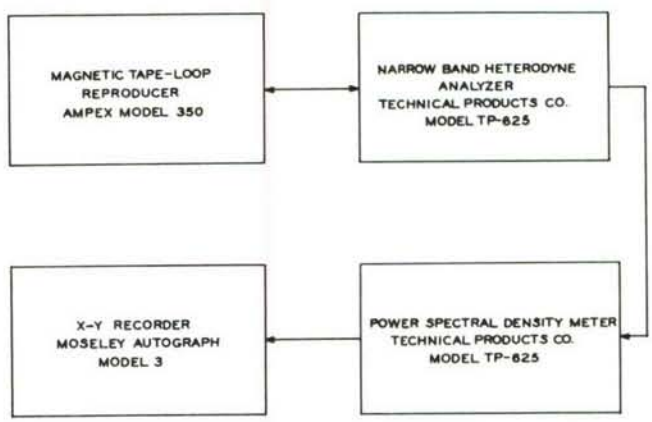

Figure II-17. Power Spectral Density Analysis System

For power spectral density (mean-square per unit bandwidth) measurements the output of the filter is fed directly into the power integrator unit and thence to the recorder. The averaging circuit of the integrator is used and the averaging time was set at six seconds. Any longer time would effectively widen the bandwidth and deteriorate the response of the system. Sound pressure, acceleration, and strain data were analyzed.

Figure II-18. Narrow Band Analyzer System

4. Probability Distribution Analyzer

The purpose of this system is to gather information about number and amplitude of signal peaks above or below the signal rms value during a given length of time; from this finformation probability distribution curves can be plotted. A block diagram is shown in Figure II-19.

The original records on one-inch tape were transcribed to the 1/4 inch magnetic tape machine (Ampex Model 350) for loop operation. The amplifier and attenuator are used to adjust the level of the signal to 0.8 volts rms, which is read on the true rms meter.

The minimum level limiter is essentially an electronic threshold or dead zone analog. The data that results from this device has as the "x" axis quantity

$$\frac{\text{Peak}}{\text{RMS}} \Big/ \sqrt{2}, \quad \text{and probability of exceeding the peak} \left[P(x)\right]$$

as the "y" coordinate. The latter is calibrated by inserting a known peak value signal into the limiter and adjusting the bias of the unit to pass peaks with amplitudes just higher than the peak of the calibrating signal. The length of an individual count is forty seconds, the output being read on an electronic counter. The frequency bands investigated were Overall, 75-150, 300-600, and 1200-2400. The total count (zero threshold) is taken for each filter band used, normalizing each of the frequency bands so that their individual curves have the same scaling.

D. Results

A description of the sound-in-air data obtained is given in this section. These results have been grouped in three divisions: free field survey results, bounded field survey results, and miscellaneous results. Free field survey results are derived from those tests wherein no test structures were involved. Bounded field results include all data taken to define the acoustic pressure excitation for test structures. Miscellaneous results include additional data taken in conjunction with the above testing.

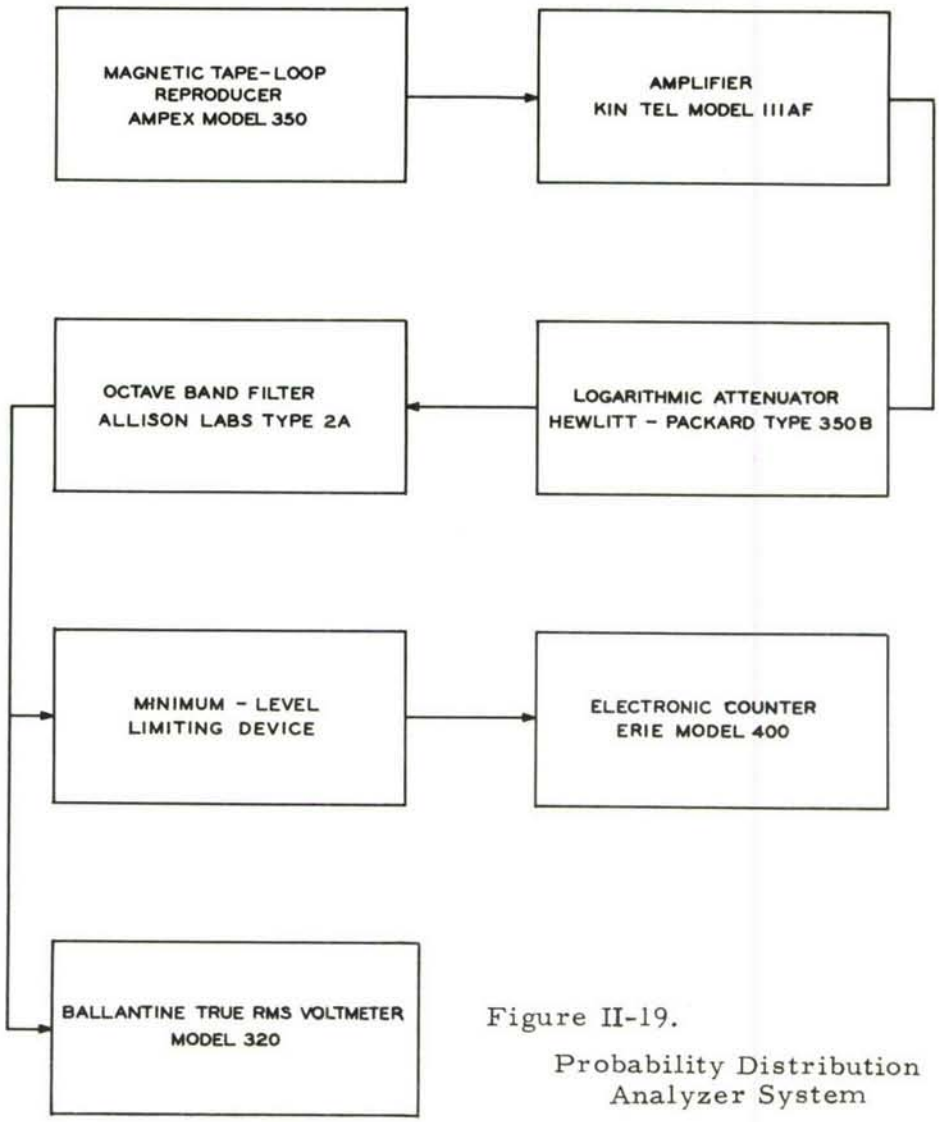

Figure II-19.

Probability Distribution
Analyzer System

1. Free Field Survey Results

a. Sound Pressure Level Contours

The constant sound pressure level contour maps of Figures II-20 and II-21, pages 20 through 27, were prepared using the sound pressure spectra data. The level (re: .0002 dynes/cm^2) in each octave band was reduced to spectrum level by the standard method (see Reference 7). The sound field for two-engine conditions, namely, military and afterburner, are represented with distances given in feet and the equivalent number of nozzle-exit diameters which are different for each engine condition.

Broken portions of the contours for some curves inside the jet exhaust indicate that the curve shapes are not known with certainty in those areas.

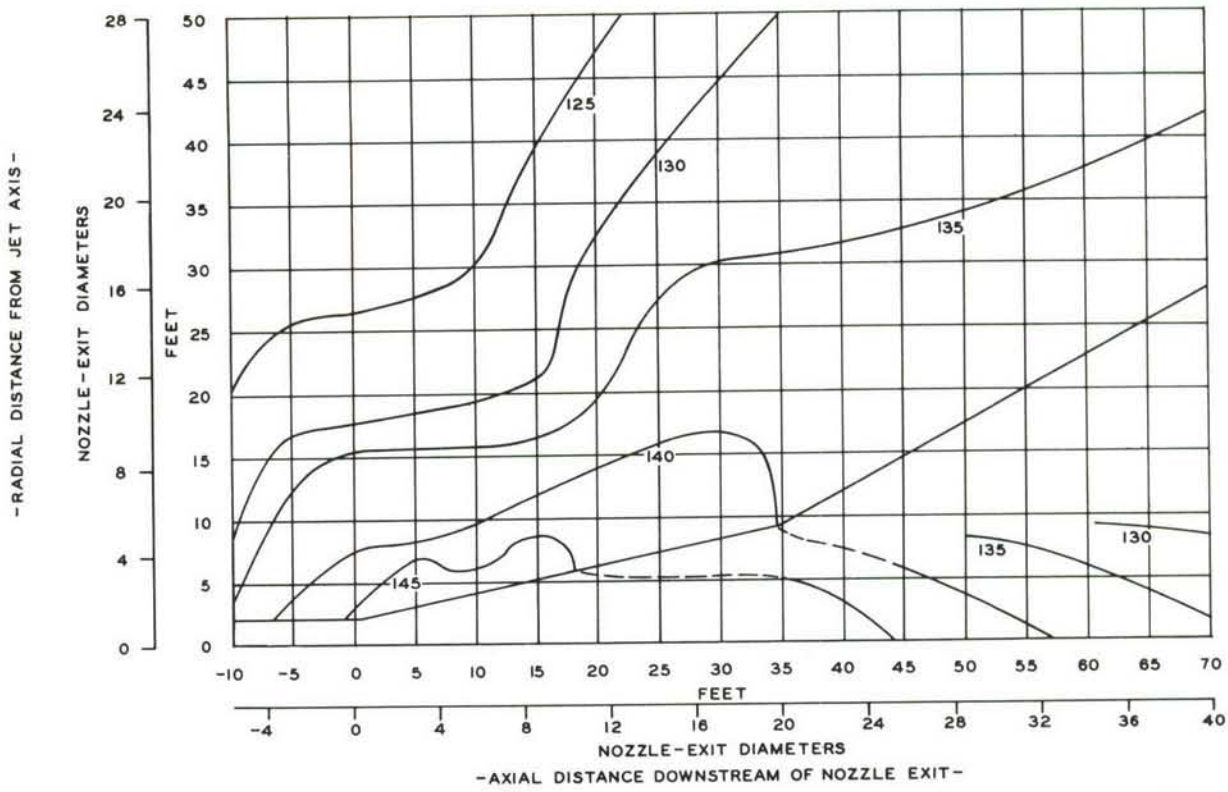

Figure II-20a. Near Field Contours of Sound Pressure Spectrum Levels
Frequency Band - Overall Military

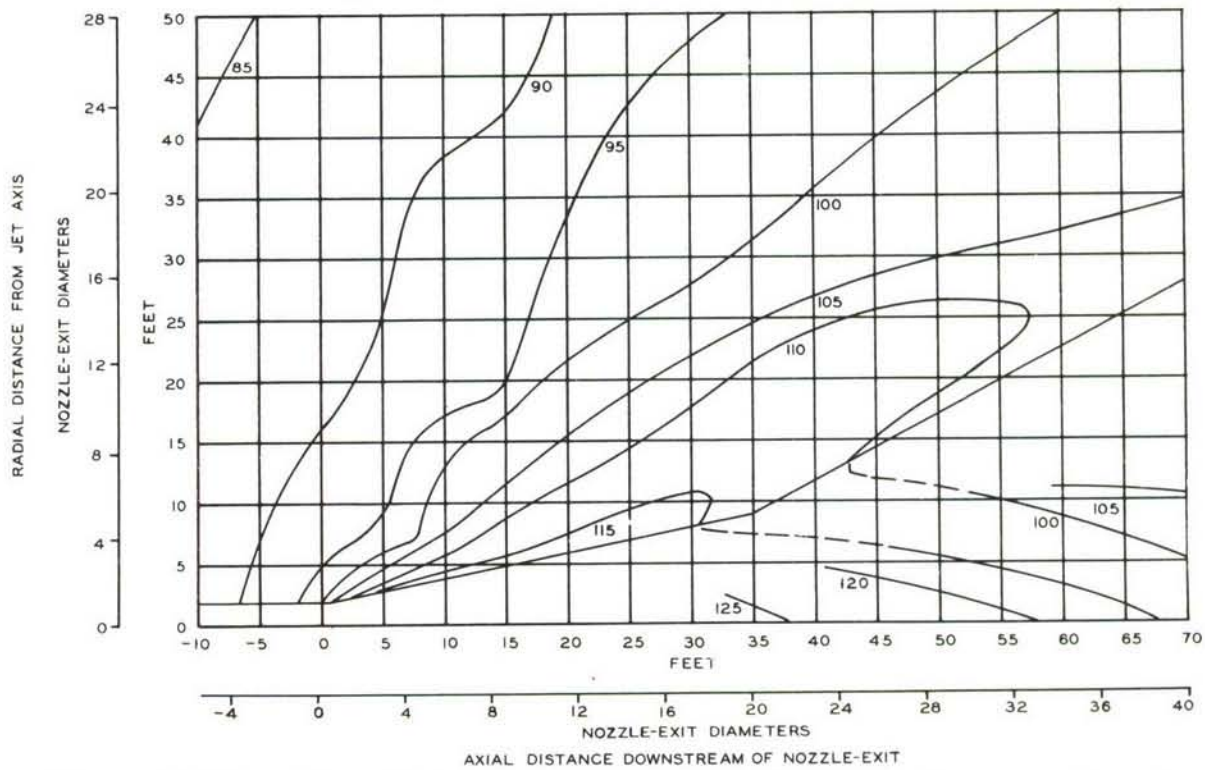

Figure II-20b. Near Field Contours of Sound Pressure Spectrum Levels
Frequency Band - 39 Military

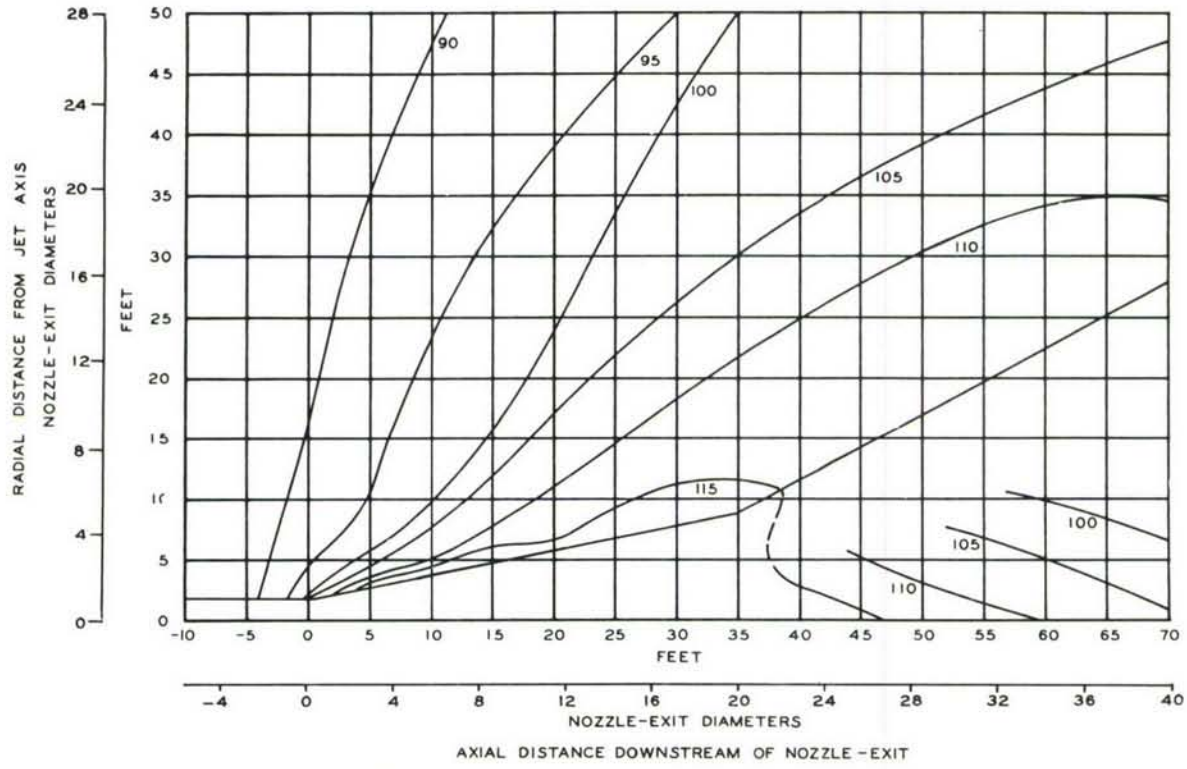

Figure II-20c. Near Field Contours of Sound Pressure Spectrum Levels
Frequency Band - 105 Military

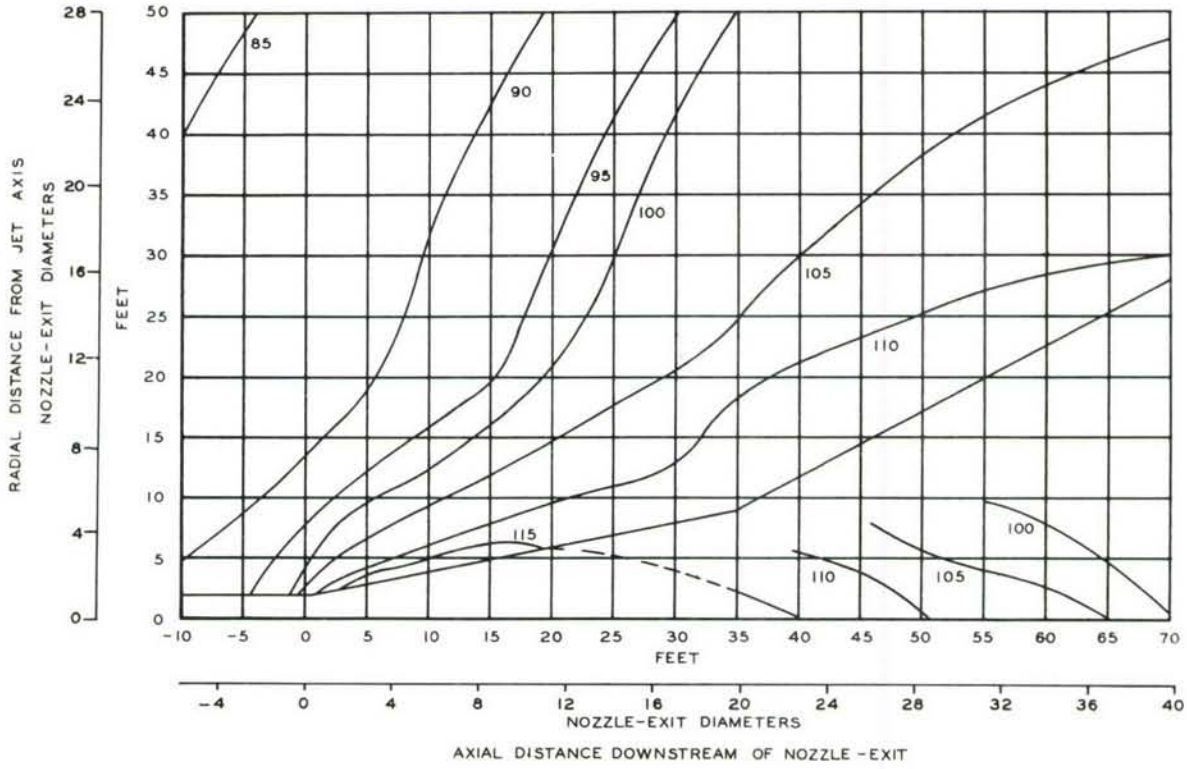

Figure II-20d. Near Field Contours of Sound Pressure Spectrum Levels
Frequency Band - 210 Military

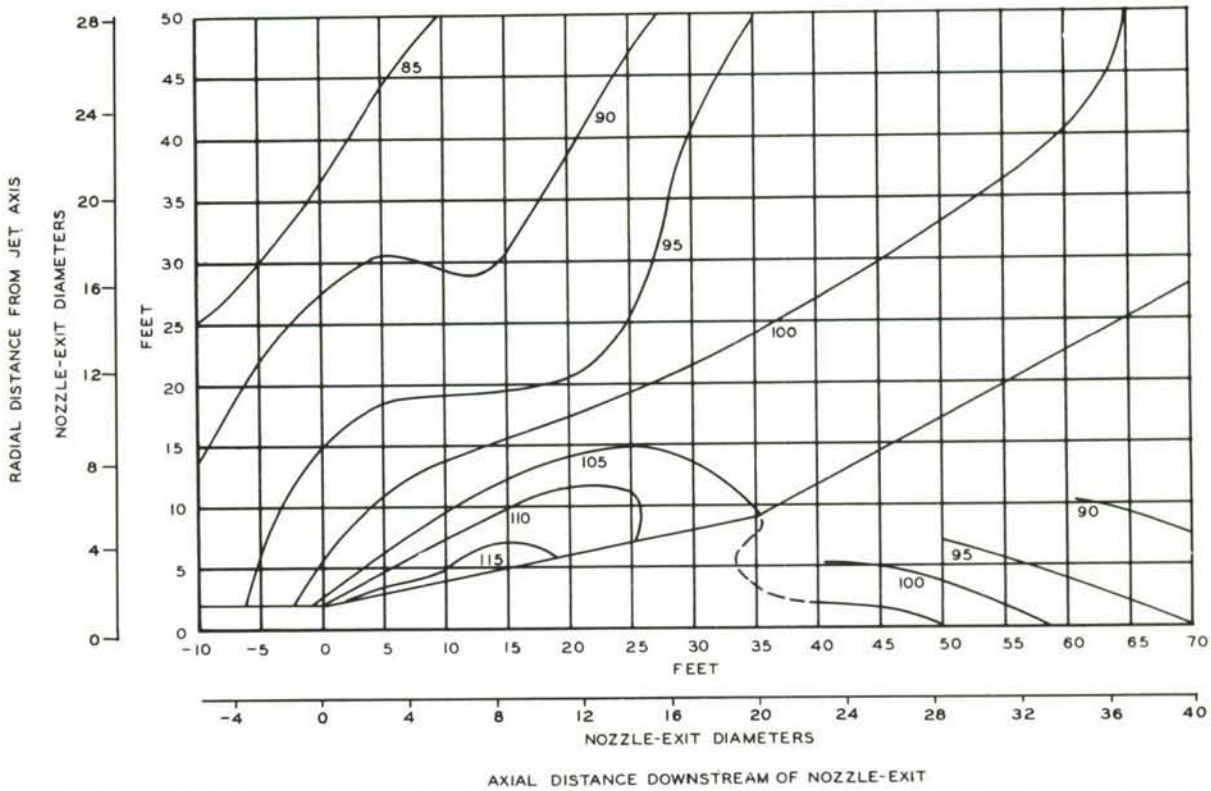

Figure II-20e. Near Field Contours of Sound Pressure Spectrum Levels
Frequency Band - 420 Military

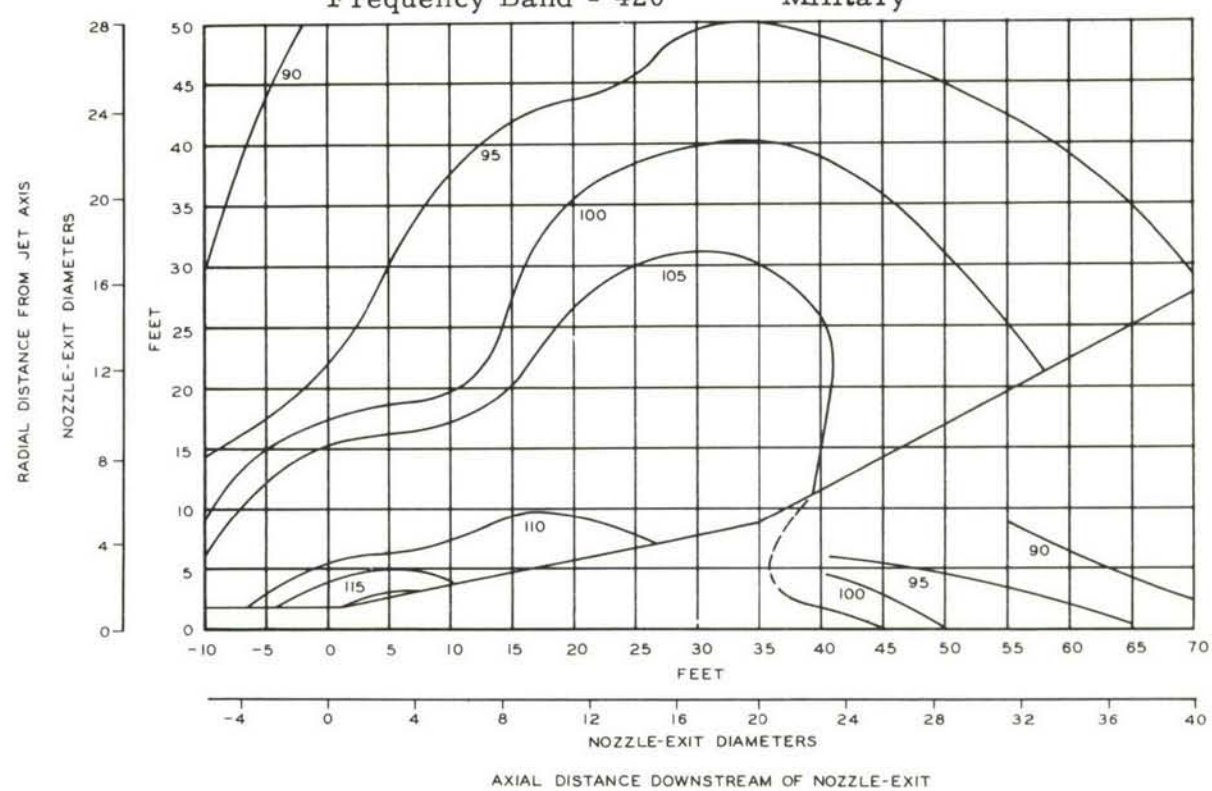

Figure II-20f. Near Field Contours of Sound Pressure Spectrum Levels
Frequency Band - 850 Military

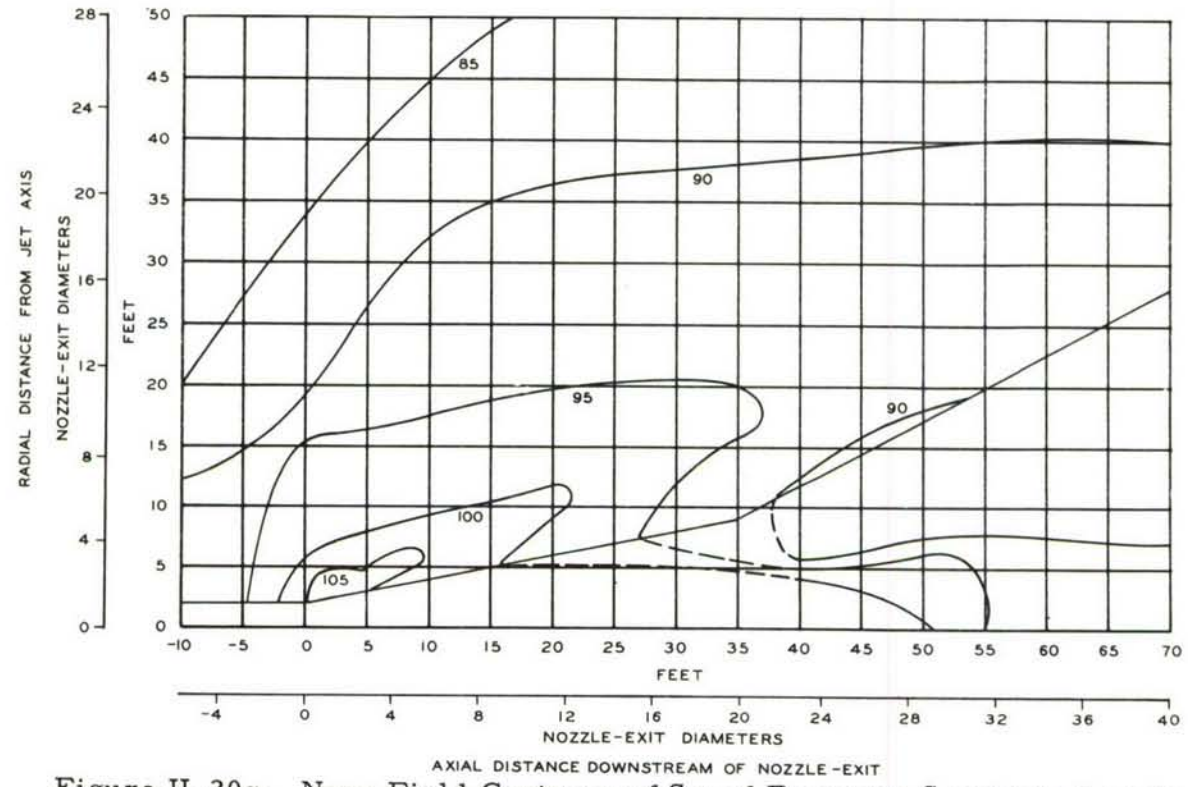

Figure II-20g. Near Field Contours of Sound Pressure Spectrum Levels
Frequency Band - 1700 Military

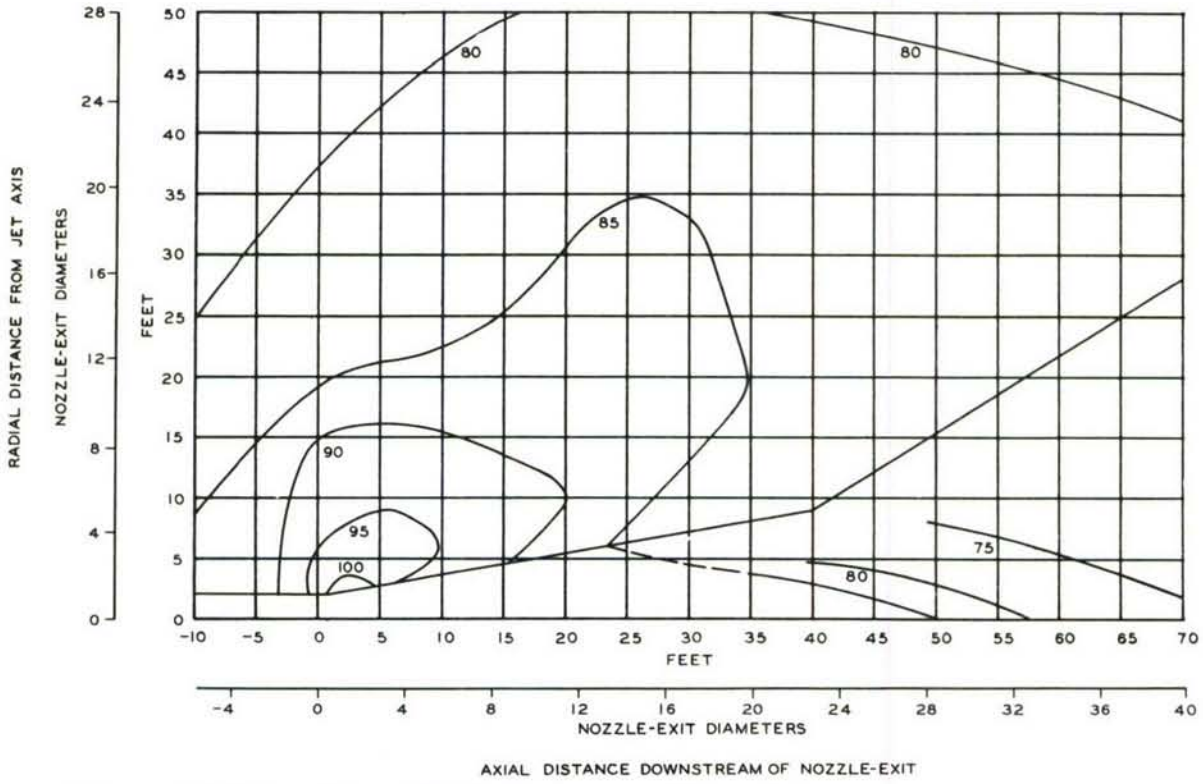

Figure II-20h. Near Field Contours of Sound Pressure Spectrum Levels
Frequency Band - 3400 Military

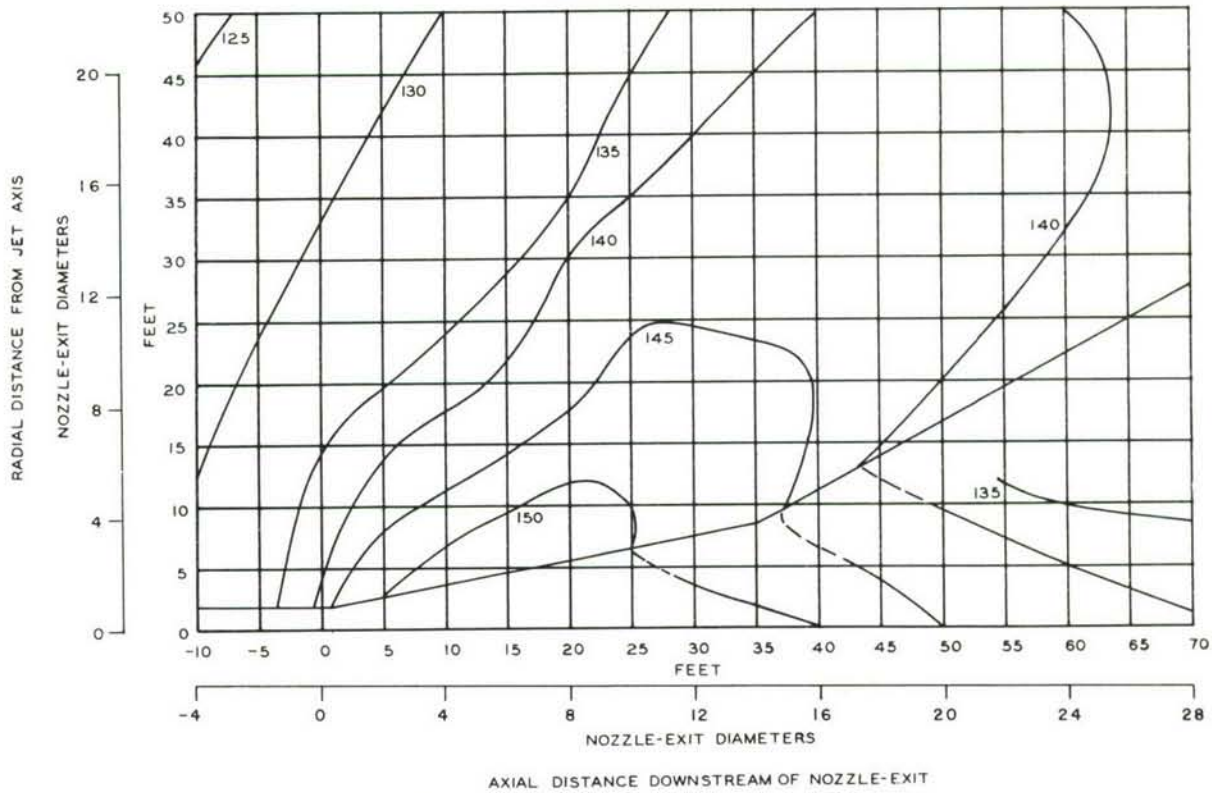

Figure II-21a. Near Field Contours of Sound Pressure Spectrum Levels
Frequency - Overall Afterburner

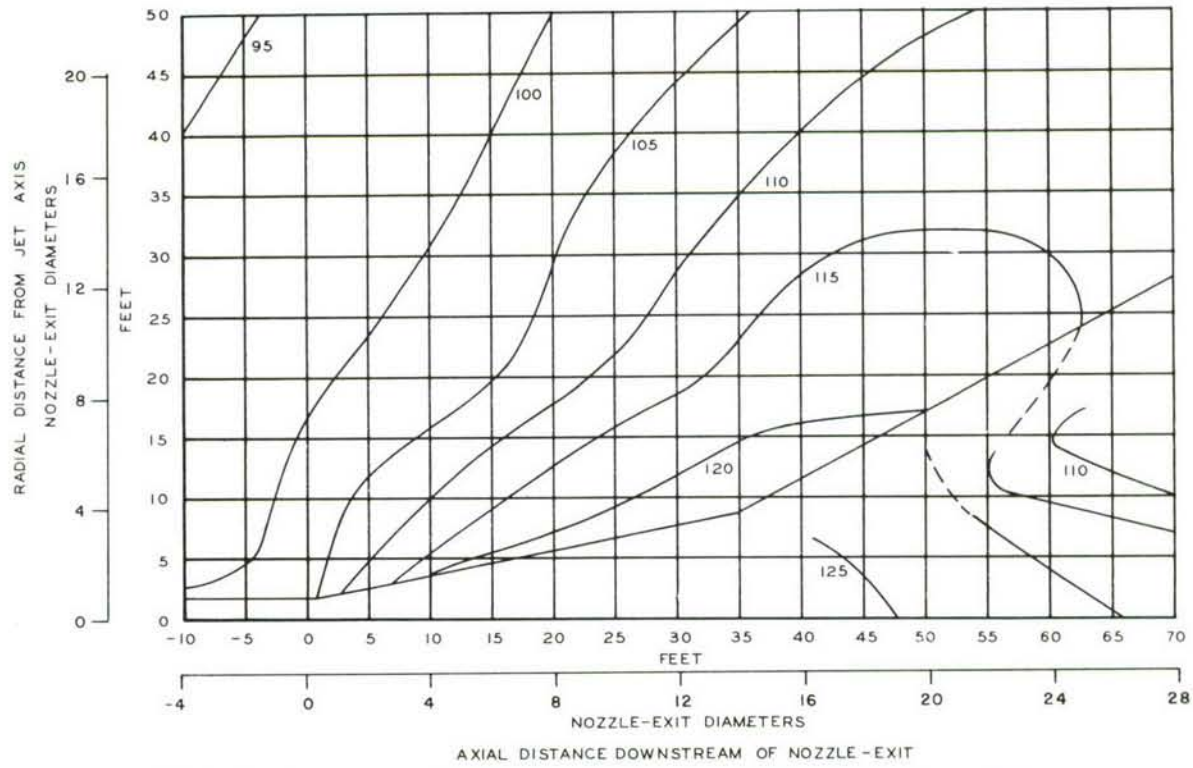

Figure II-21b. Near Field Contours of Sound Pressure Spectrum Levels
Frequency - 39 Afterburner

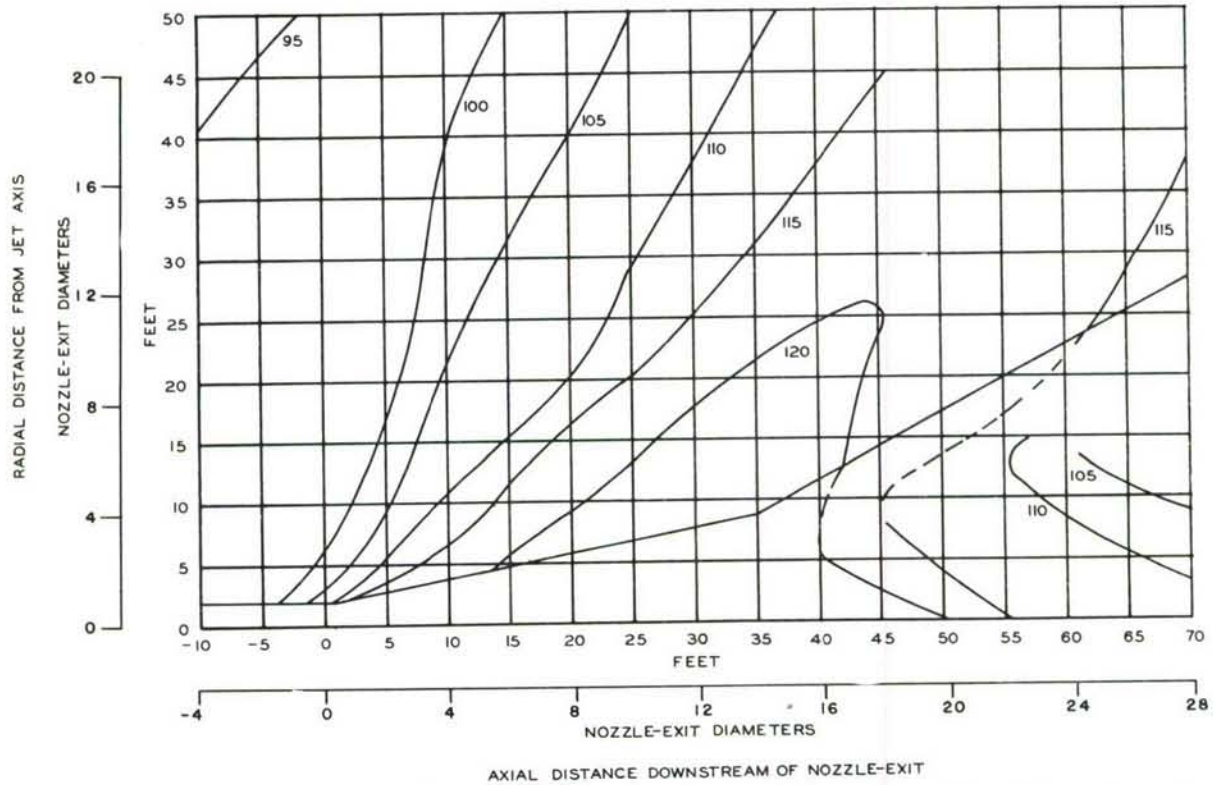

Figure II-21c. Near Field Contours of Sound Pressure Spectrum Levels
Frequency Band - 105 Afterburner

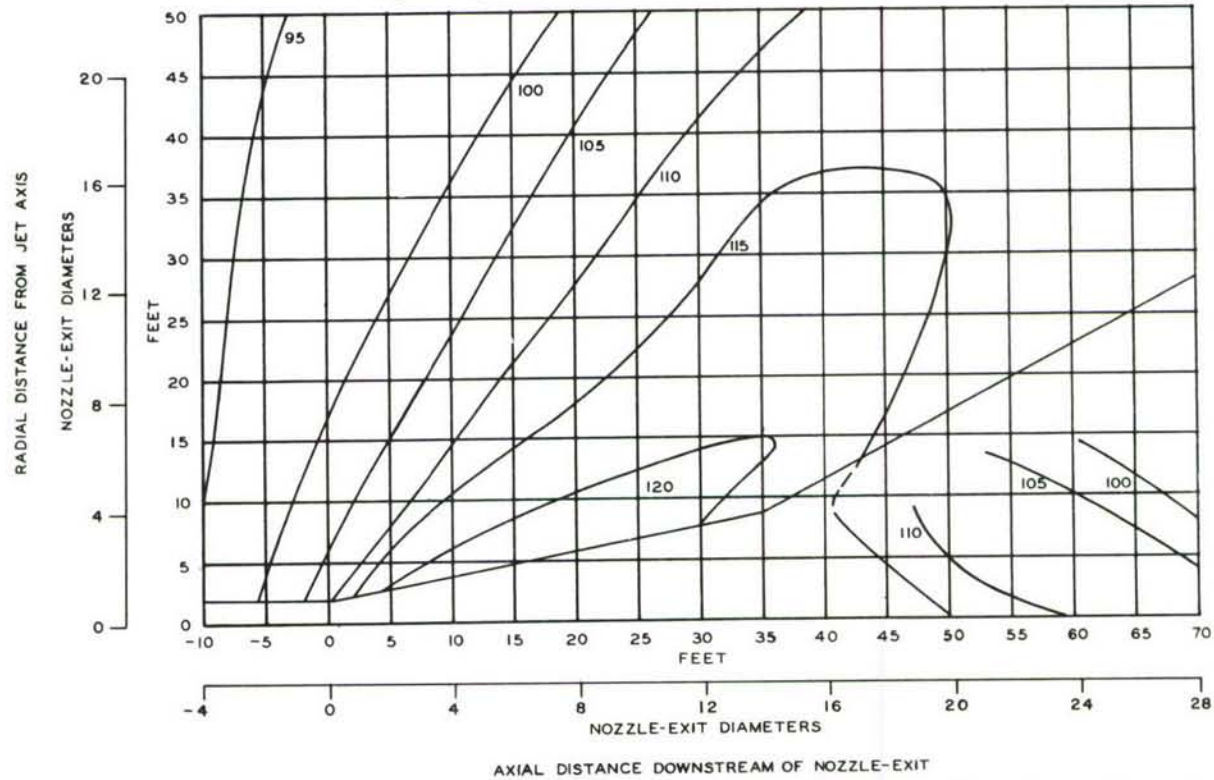

Figure II-21d. Near Field Contours of Sound Pressure Spectrum Levels
Frequency Band - 210 Afterburner

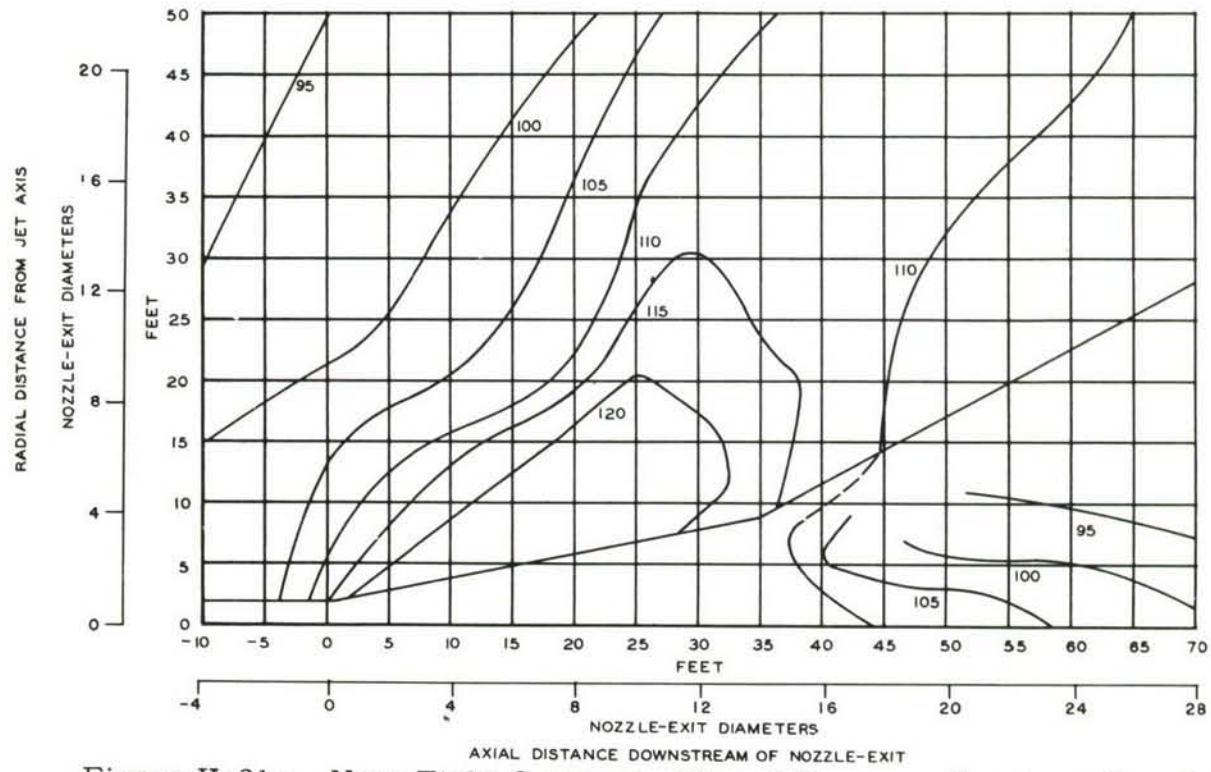

Figure II-21e. Near Field Contours of Sound Pressure Spectrum Levels
Frequency Band - 420 Afterburner

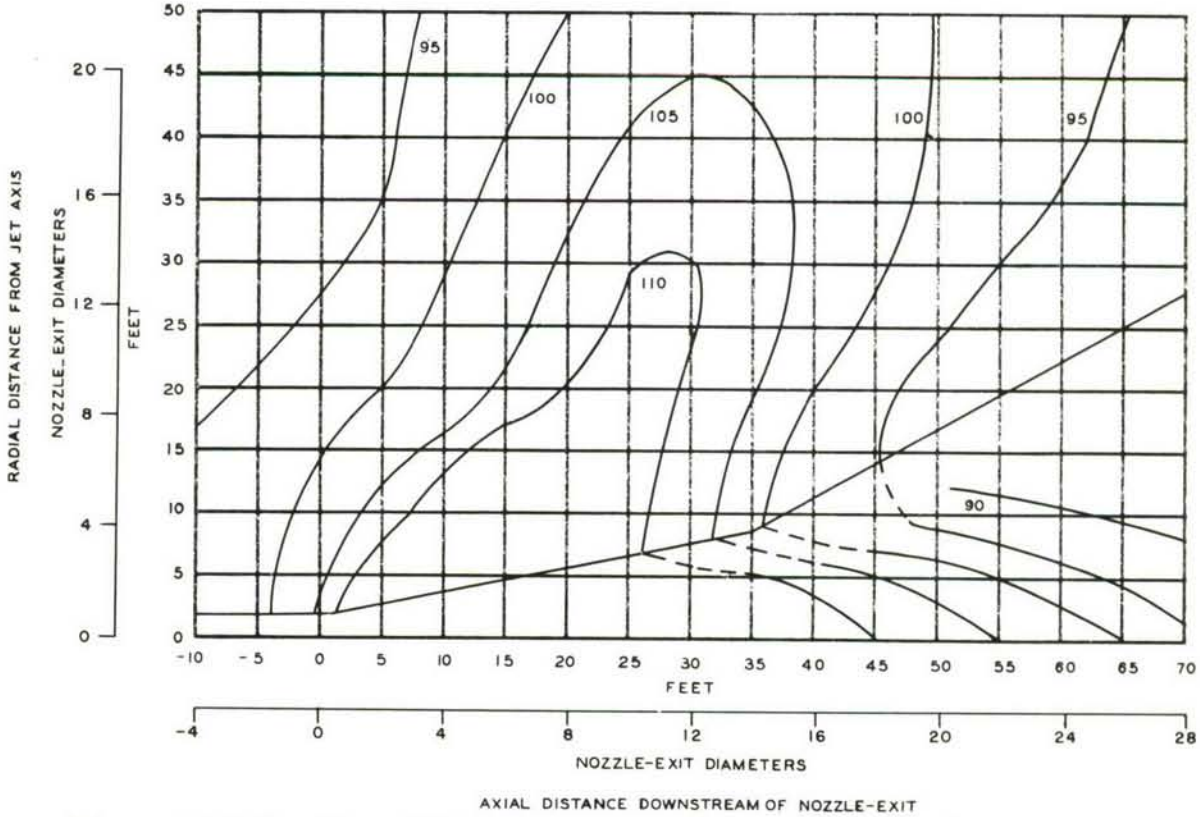

Figure II-21f. Near Field Contours of Sound Pressure Spectrum Levels
Frequency Band - 850 Afterburner

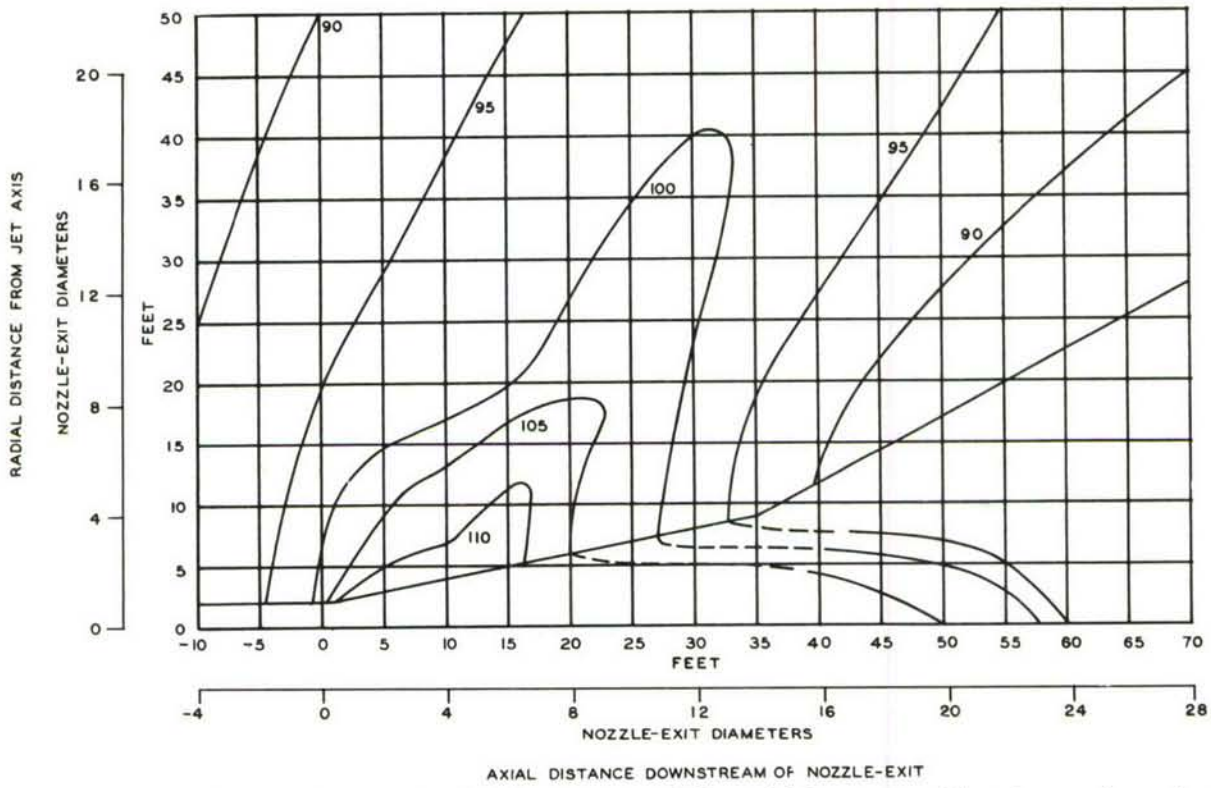

Figure II-21g. Near Field Contours of Sound Pressure Spectrum Levels
Frequency Band - 1700 Afterburner

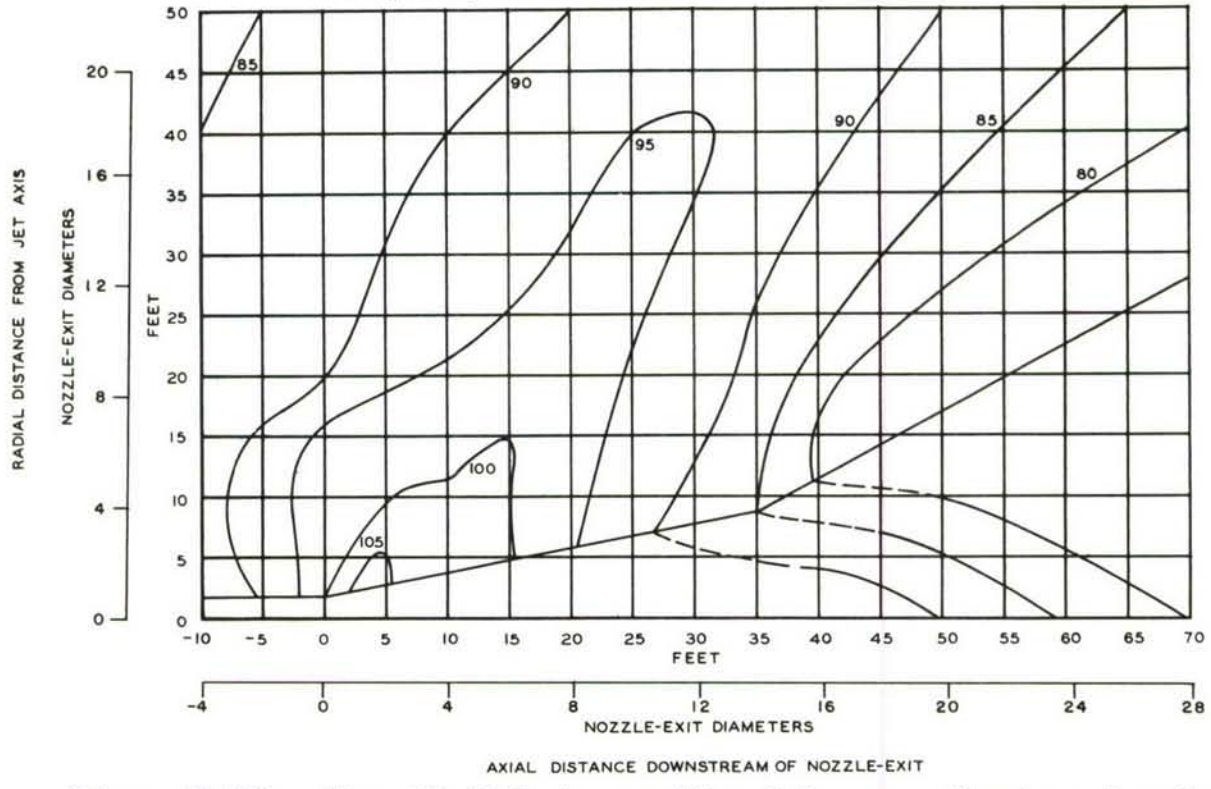

Figure II-21h. Near Field Contours of Sound Pressure Spectrum Levels
Frequency Band - 3400 Afterburner

b. Narrow Band Sound Pressure Spectra

Narrow Band (10 cps) spectra reduced to spectrum level (re: 0.0002 dynes/cm^2) for the military and afterburner engine conditions are displayed in Figures II-22 through II-27, pages 28 through 41, for a variety of positions in the near sound field. Of these, Figures II-22 through II-23 show spectra along a

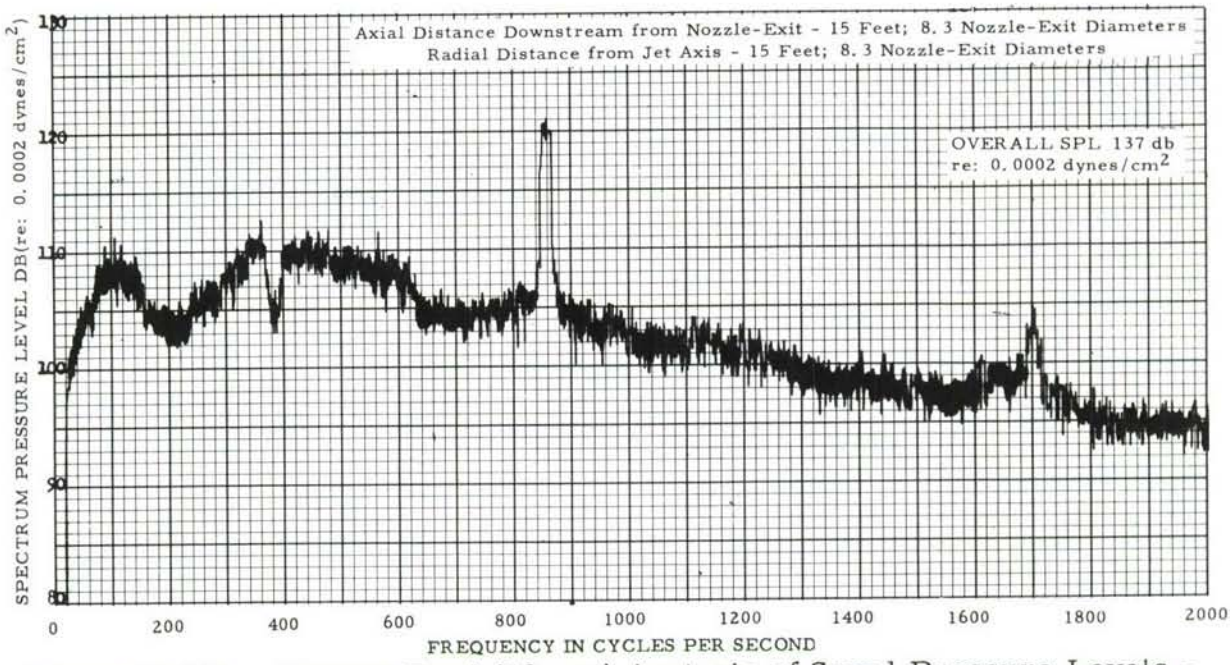

Figure II-22a. Narrow Band (10 cps) Analysis of Sound Pressure Levels - Free Field Survey - Military

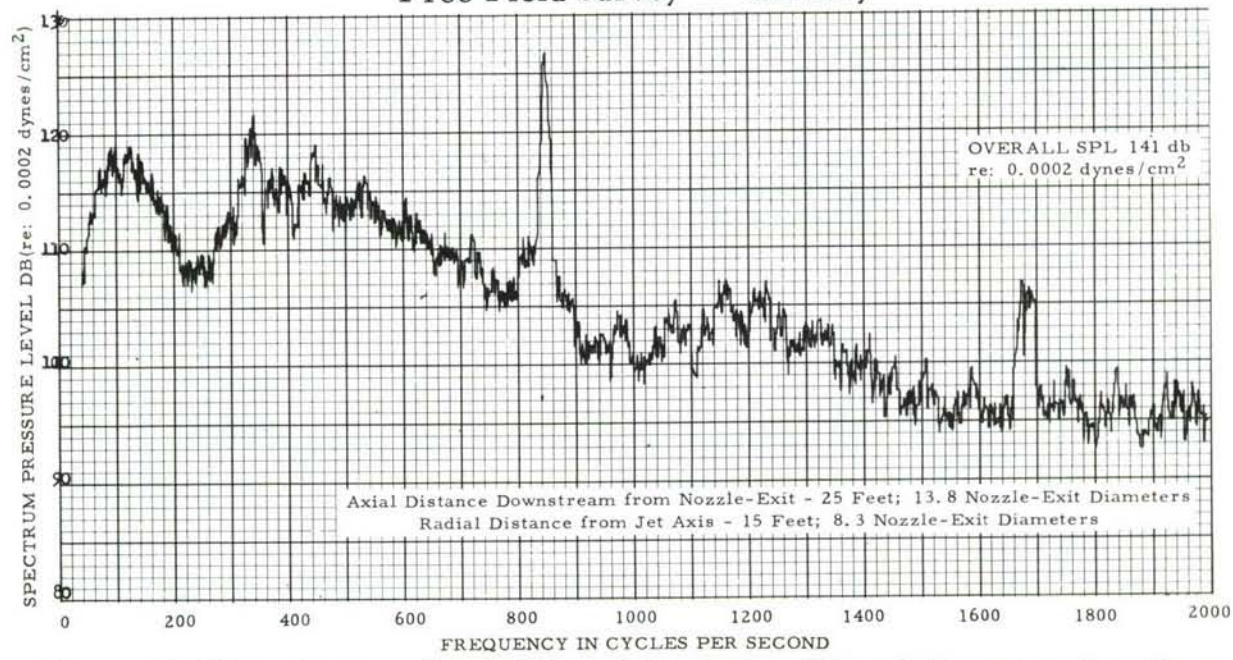

Figure II-22b. Narrow Band (10 cps) Analysis of Sound Pressure Levels - Free Field Survey - Military

line 15 feet from the jet axis and parallel to it, Figures II-24 and II-25 include positions along the jet boundary, while Figures II-26 through II-27 are spectra obtained along the jet wake centerline. Each curve is identified by record number, test and engine condition, and microphone location in feet and equivalent nozzle-exit diameters. Overall sound pressure levels are also given for each spectrum.

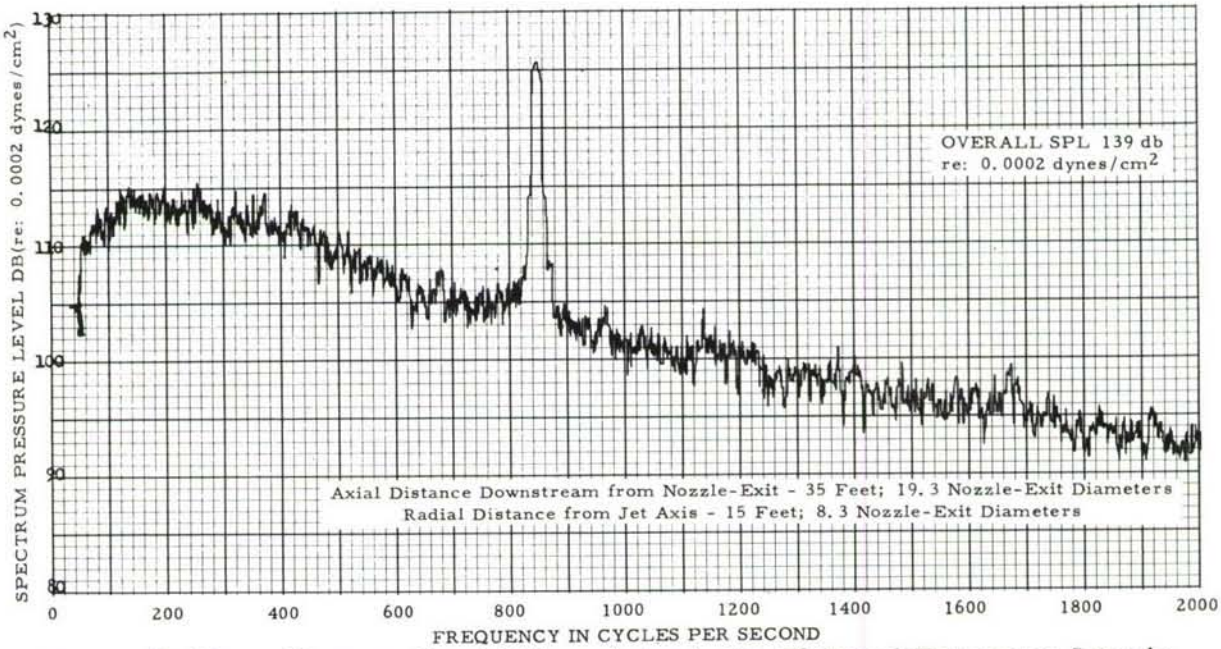

Figure II-22c. Narrow Band (10 cps) Analysis of Sound Pressure Levels - Free Field Survey - Military

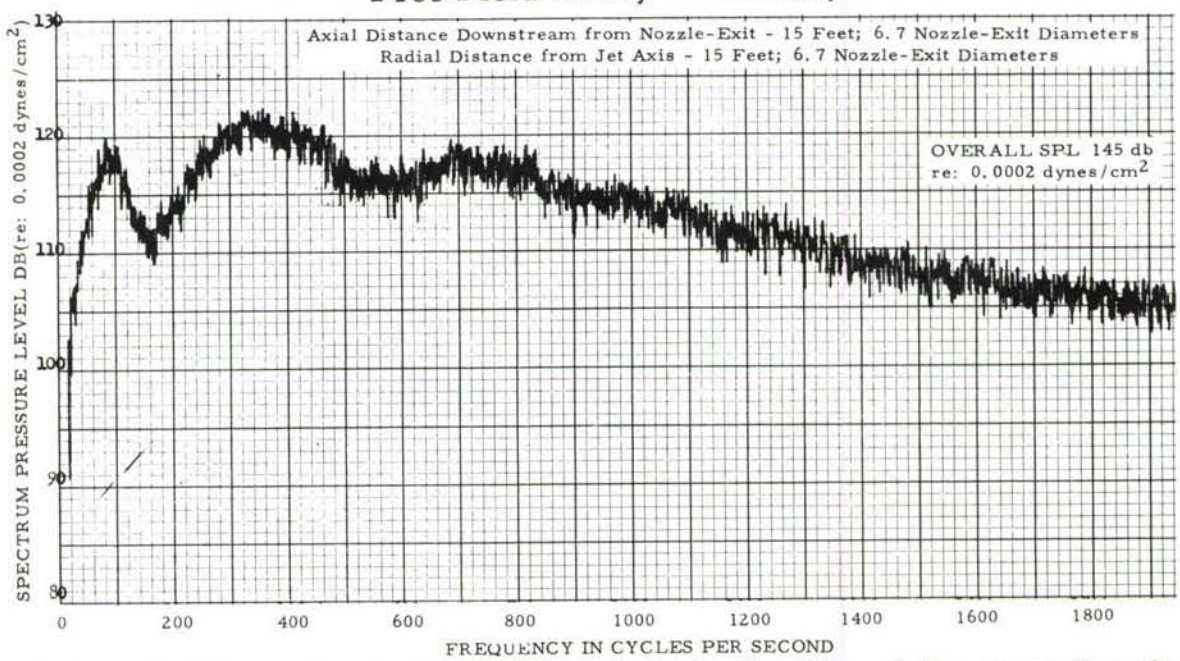

Figure II-23a. Narrow Band (10 cps) Analysis of Sound Pressure Levels - Free Field Survey - Afterburner

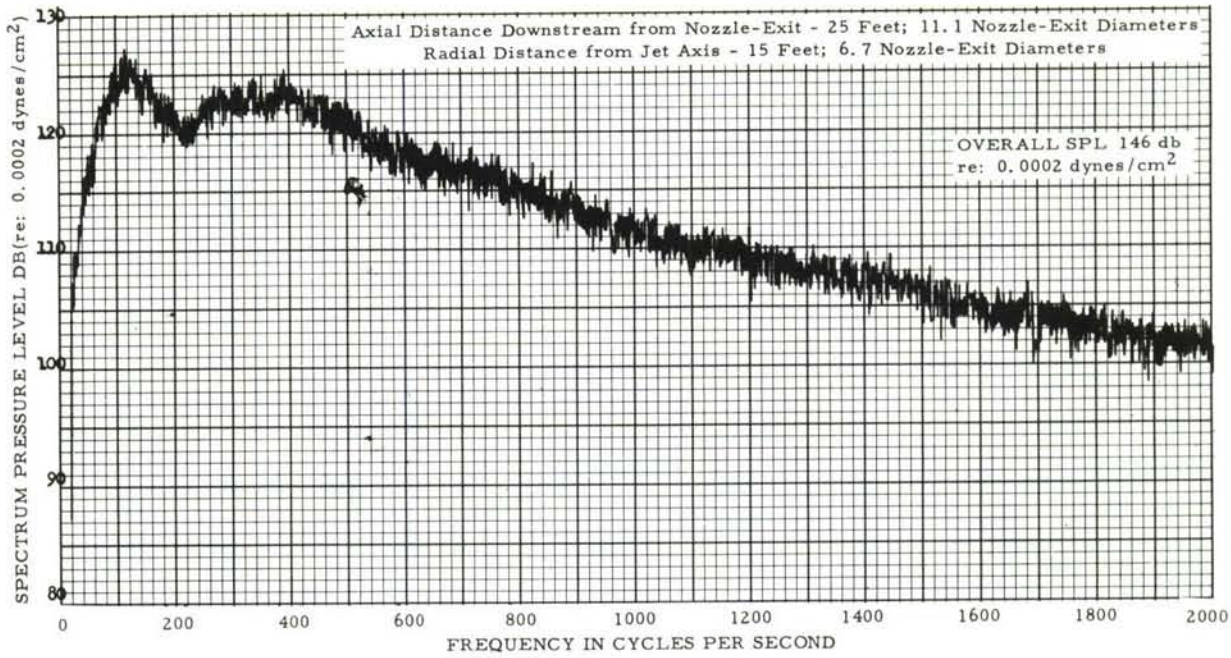

Figure II-23b. Narrow Band (10 cps) Analysis of Sound Pressure Levels - Free Field Survey - Afterburner

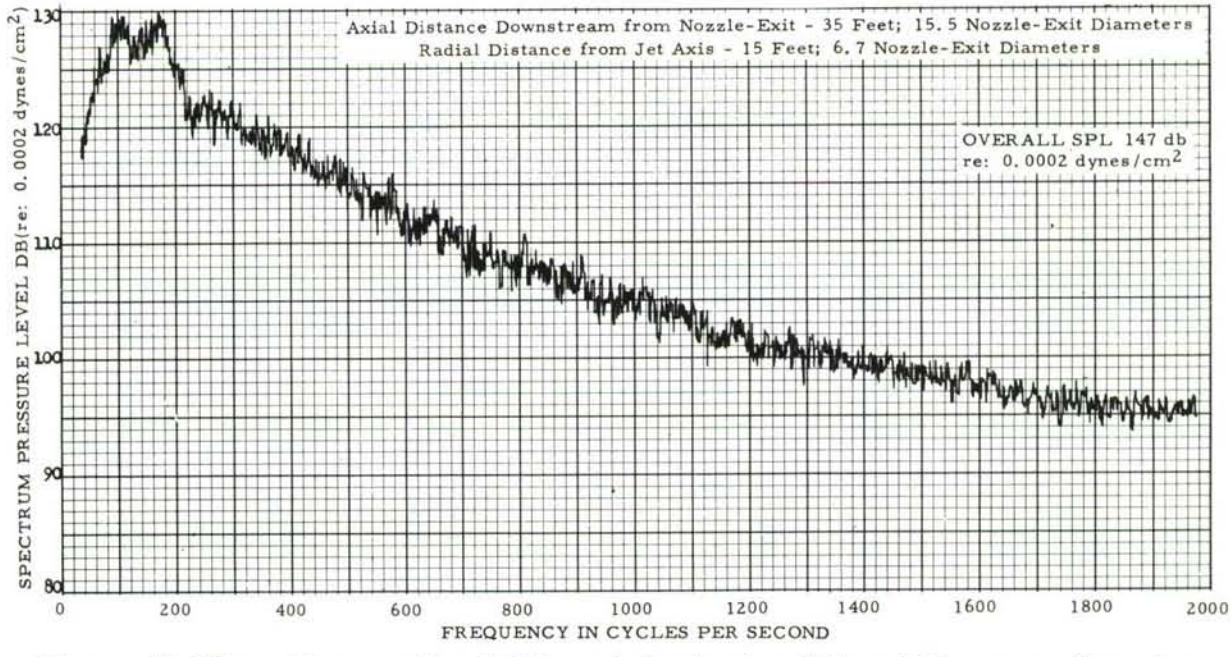

Figure II-23c. Narrow Band (10 cps) Analysis of Sound Pressure Levels - Free Field Survey - Afterburner

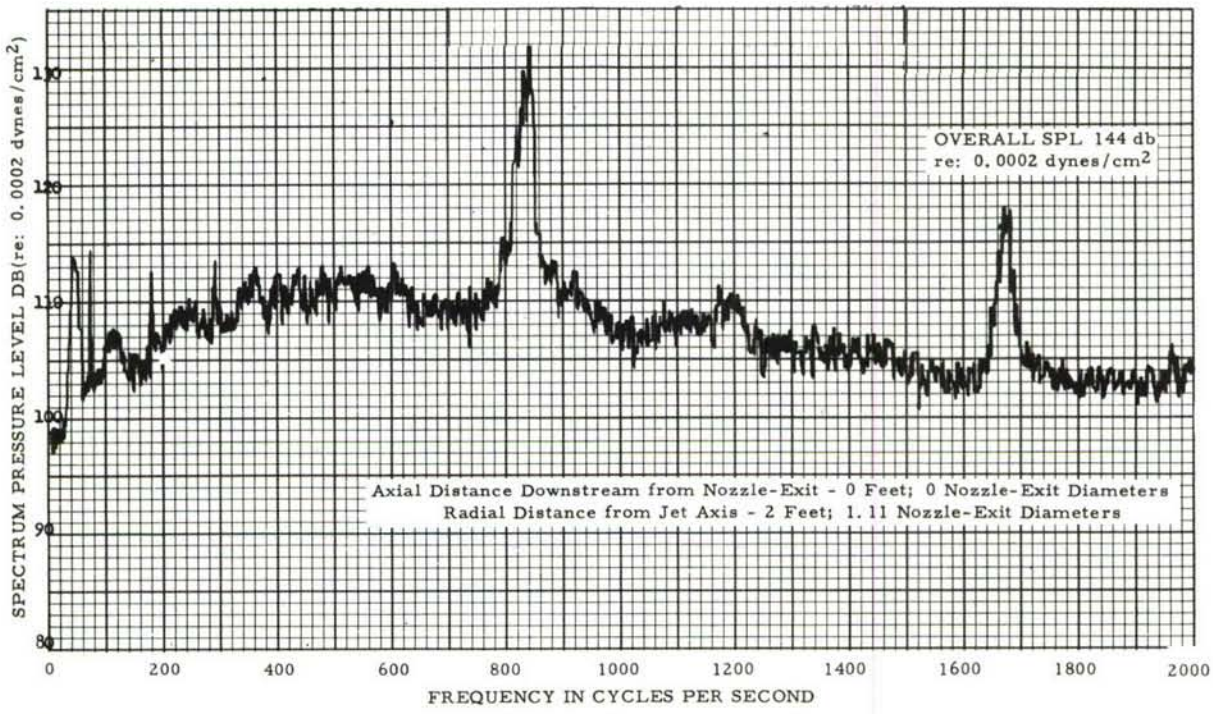

Figure II-24a. Narrow Band (10 cps) Analysis of Sound Pressure Levels - Free Field Survey - Military

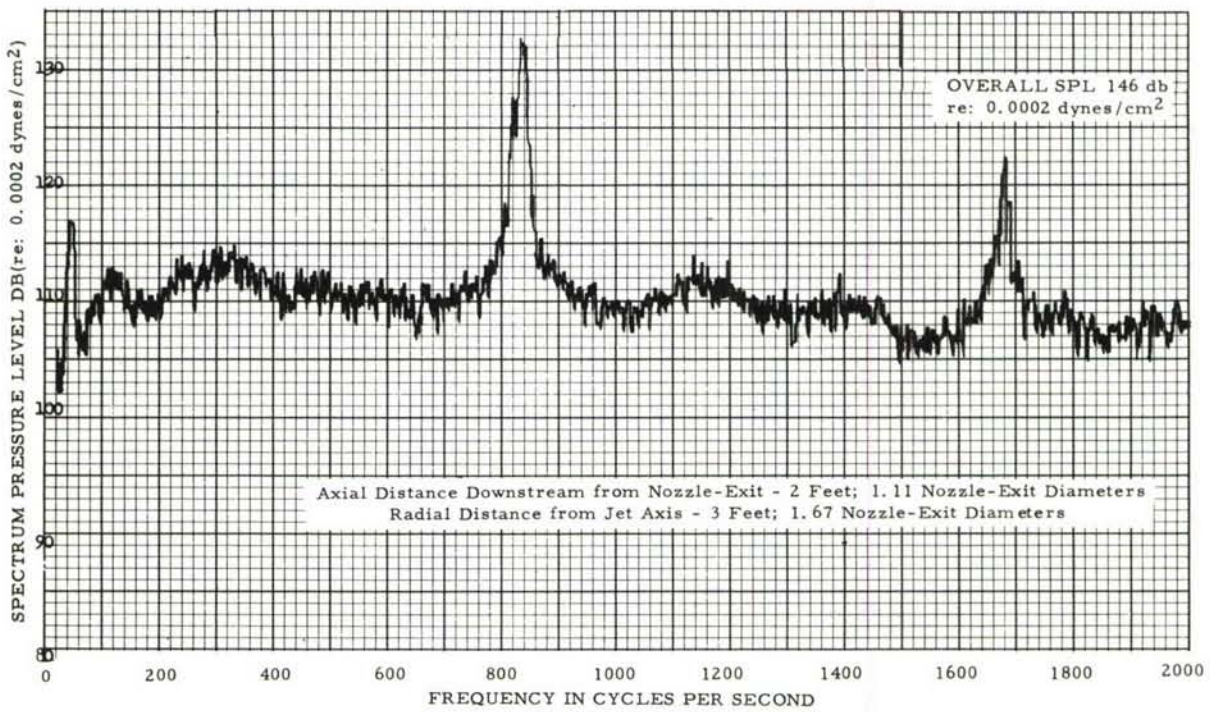

Figure II-24b. Narrow Band (10 cps) Analysis of Sound Pressure Levels - Free Field Survey - Military

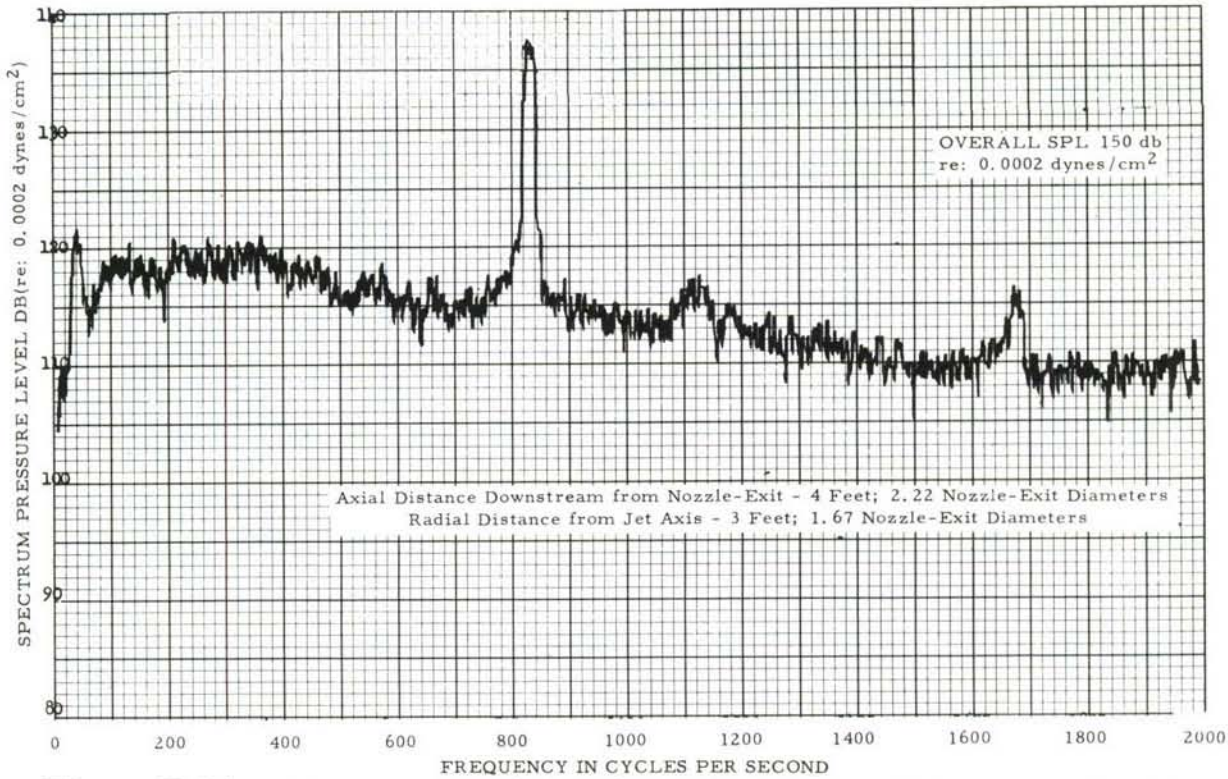

Figure II-24c. Narrow Band (10 cps) Analysis of Sound Pressure Levels - Free Field Survey - Military

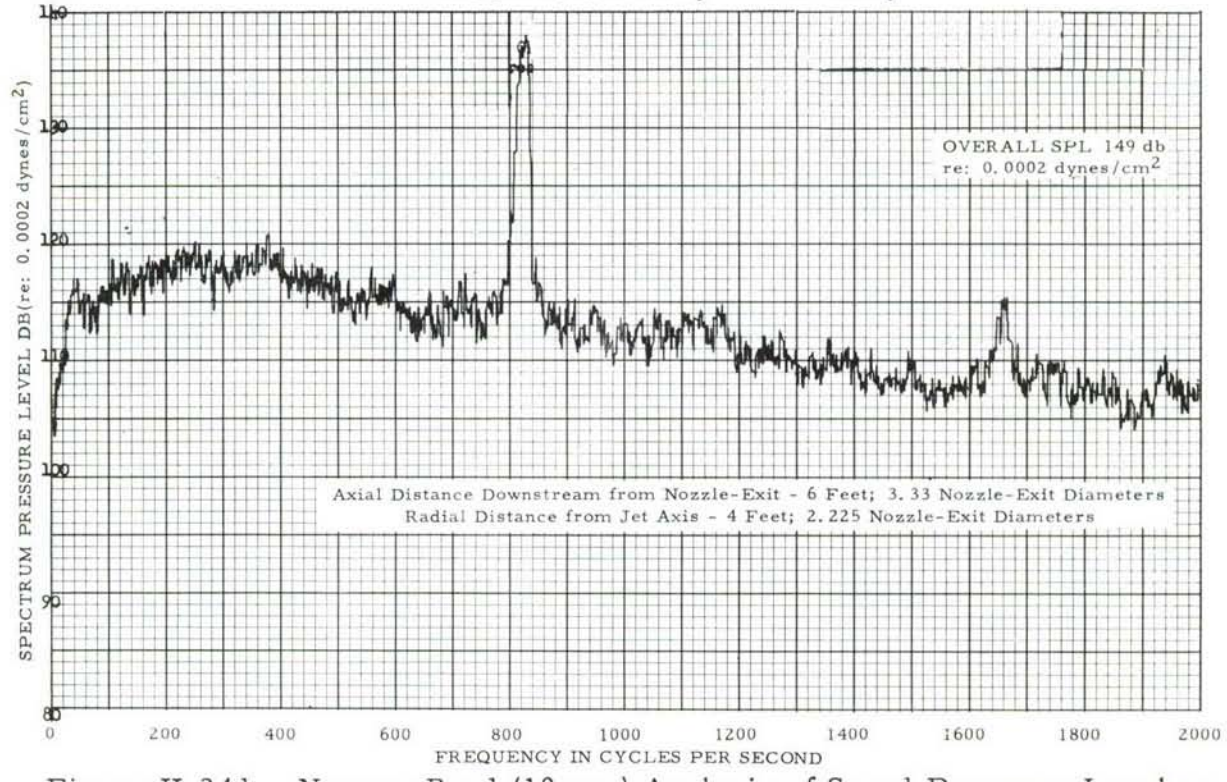

Figure II-24d. Narrow Band (10 cps) Analysis of Sound Pressure Levels - Free Field Survey - Military

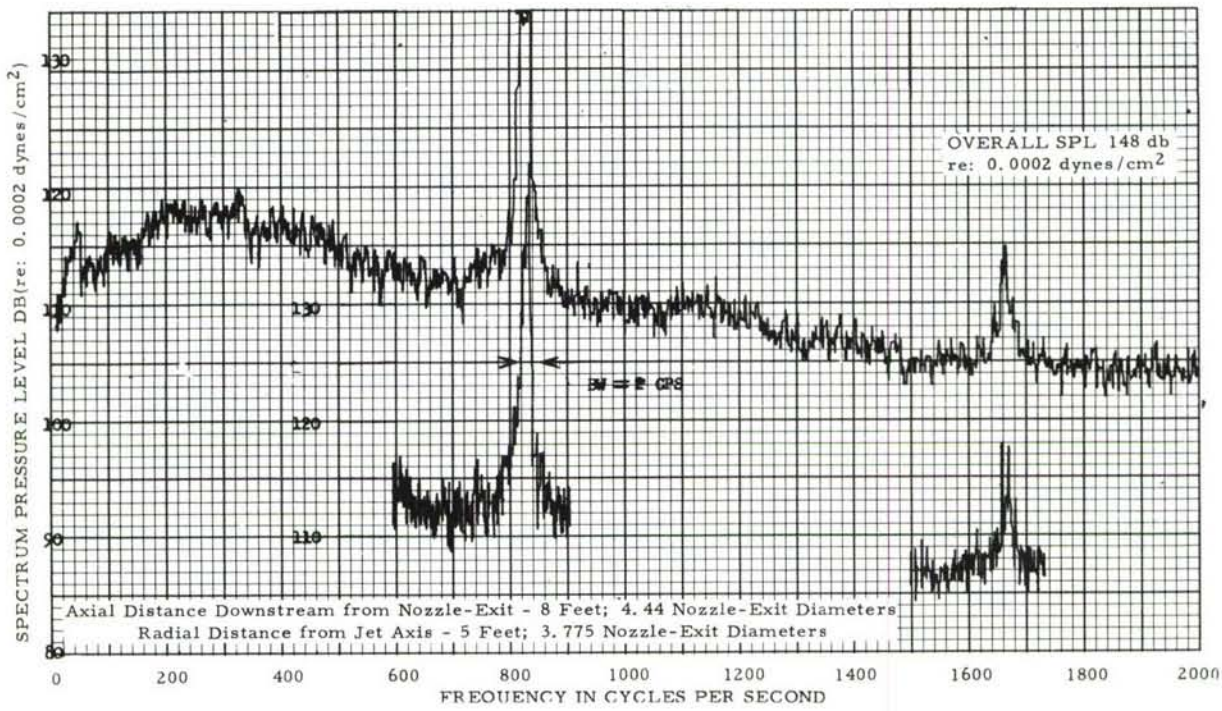

Figure II-24e. Narrow Band (10 cps) Analysis of Sound Pressure Levels - Free Field Survey - Military

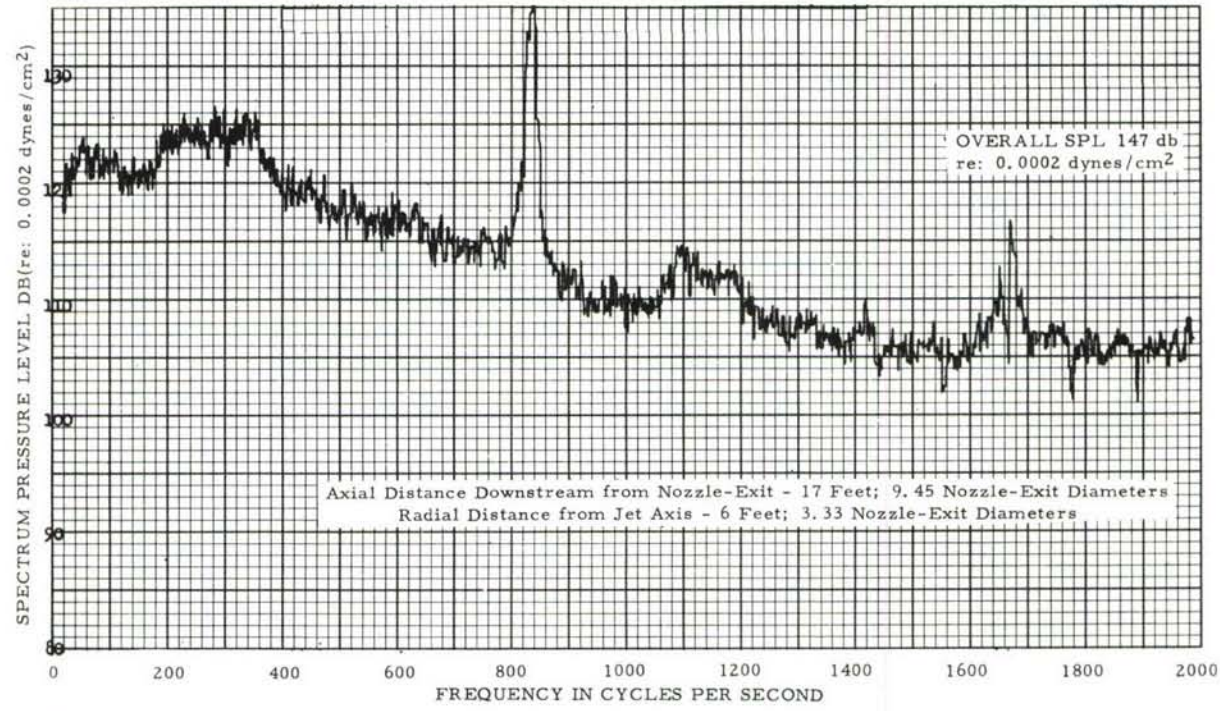

Figure II-24f. Narrow Band (10 cps) Analysis of Sound Pressure Levels - Free Field Survey - Military

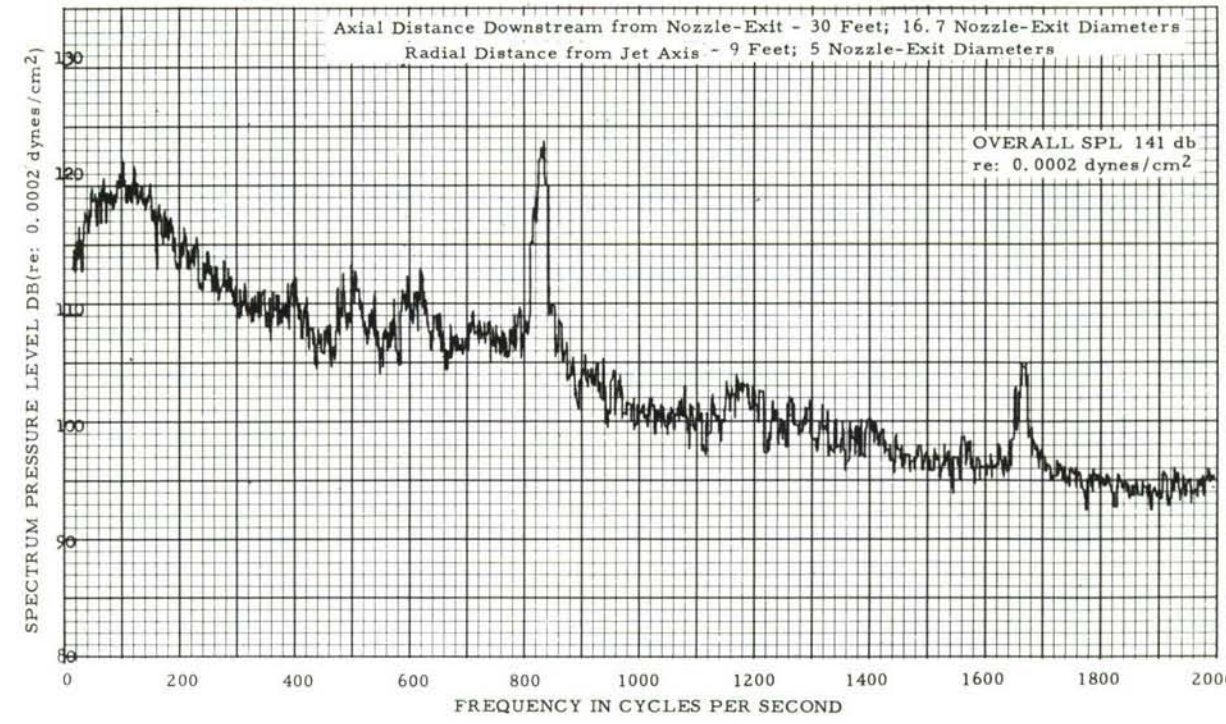

Figure II-24g. Narrow Band (10 cps) Analysis of Sound Pressure Levels - Free Field Survey - Military

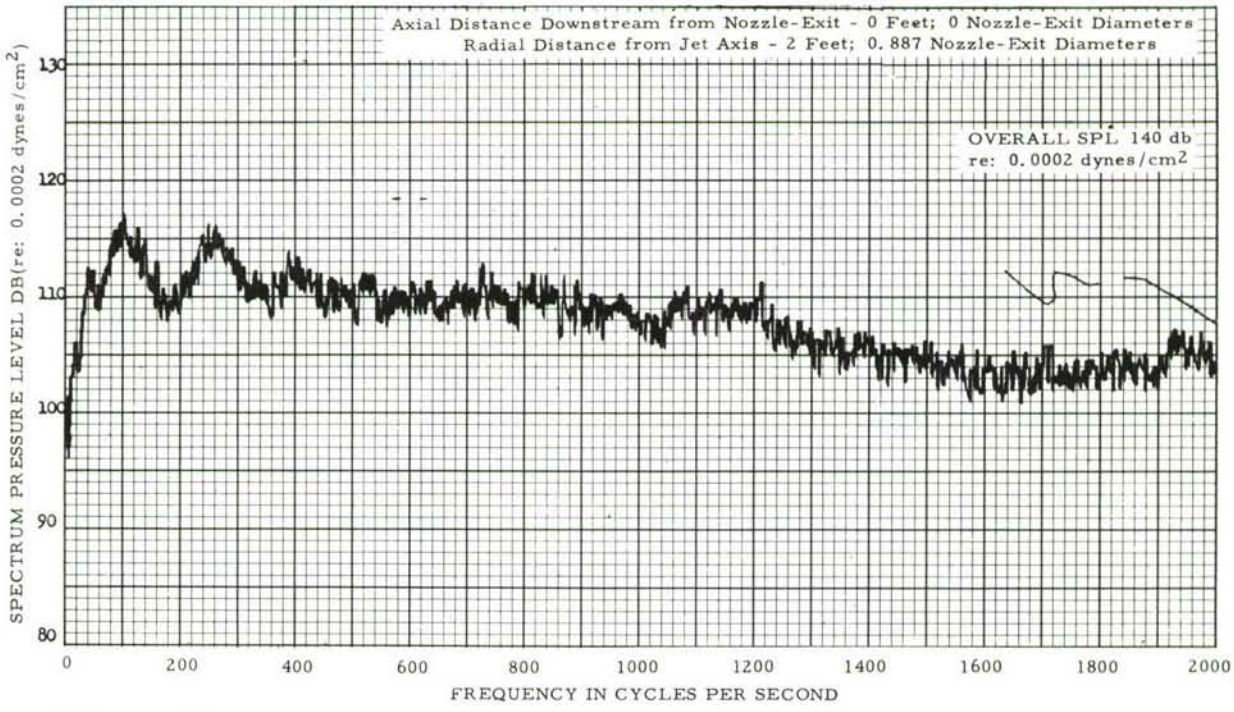

Figure 25a. Narrow Band (10 cps) Analysis of Sound Pressure Levels - Free Field Survey - Afterburner

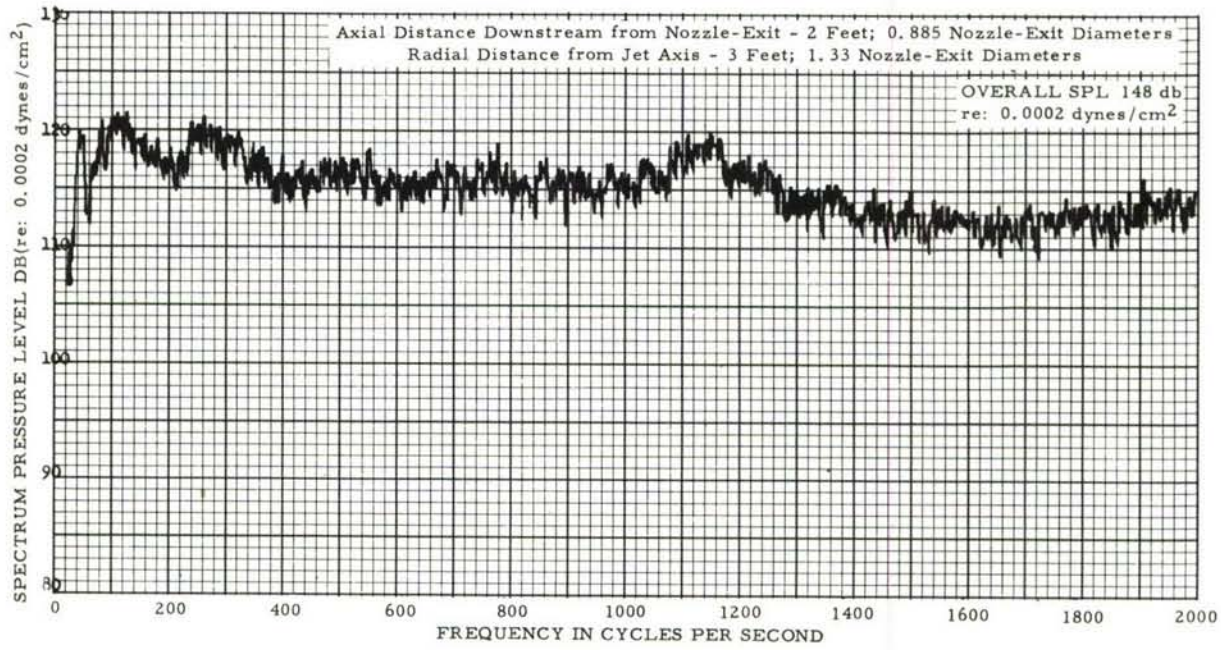

Figure II-25b. Narrow Band (10 cps) Analysis of Sound Pressure Levels - Free Field Survey - Afterburner

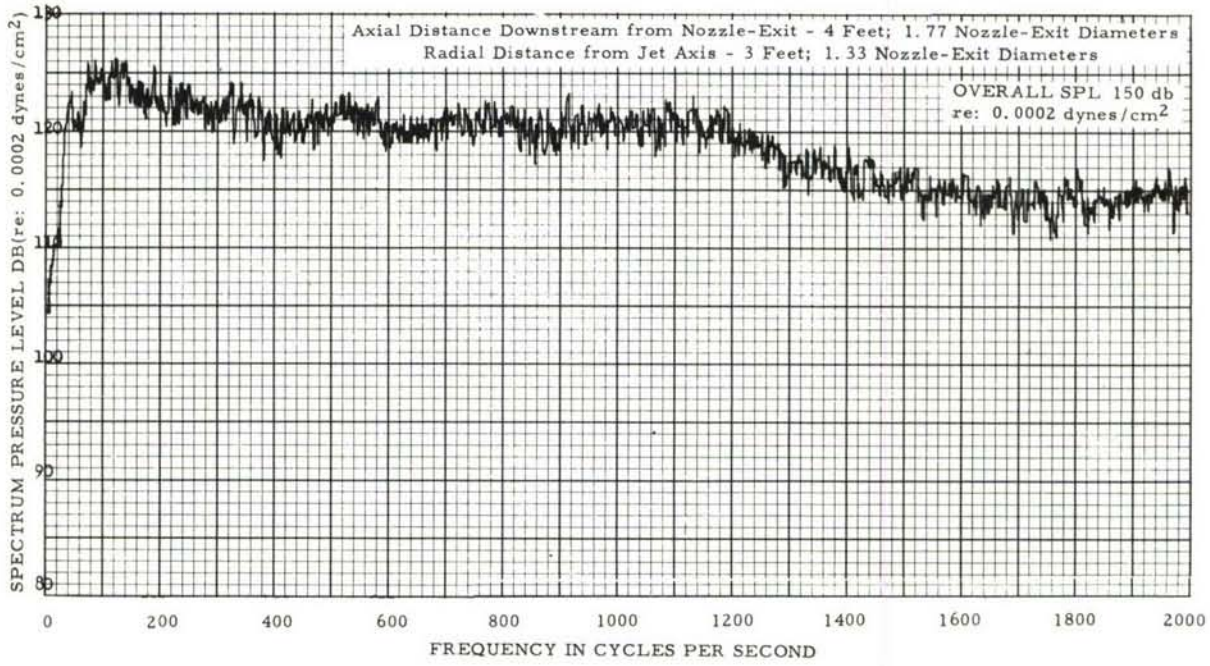

Figure II-25c. Narrow Band (10 cps) Analysis of Sound Pressure Levels - Free Field Survey - Afterburner

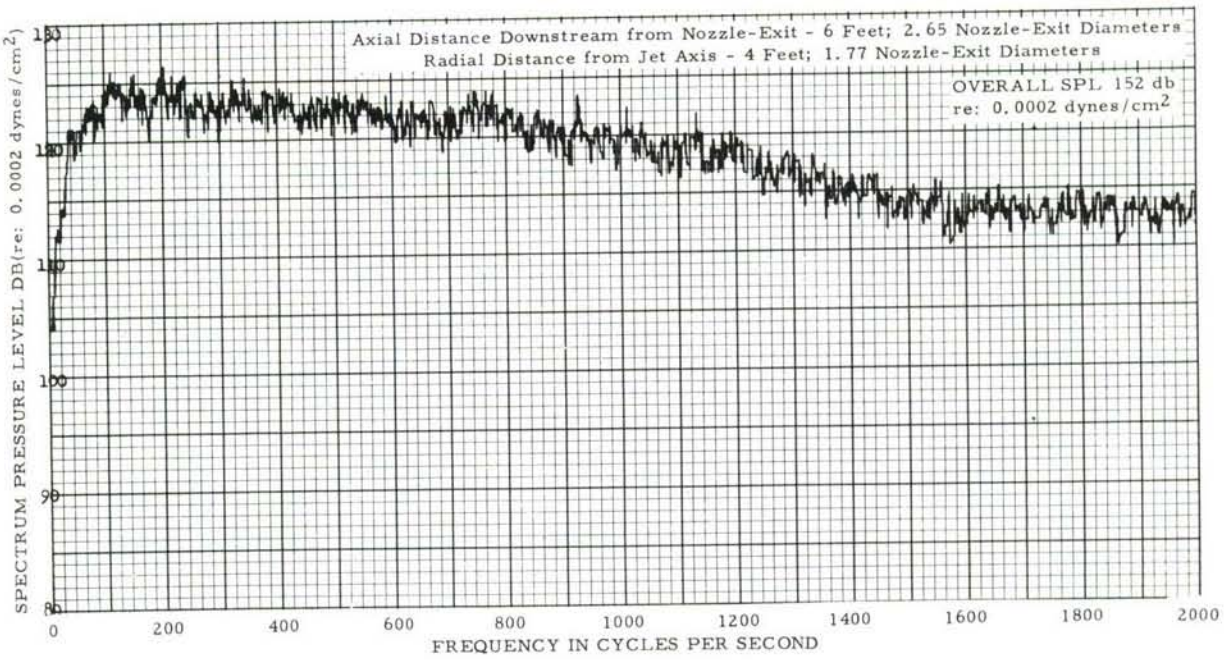

Figure II-25d. Narrow Band (10 cps) Analysis of Sound Pressure Levels - Free Field Survey - Afterburner

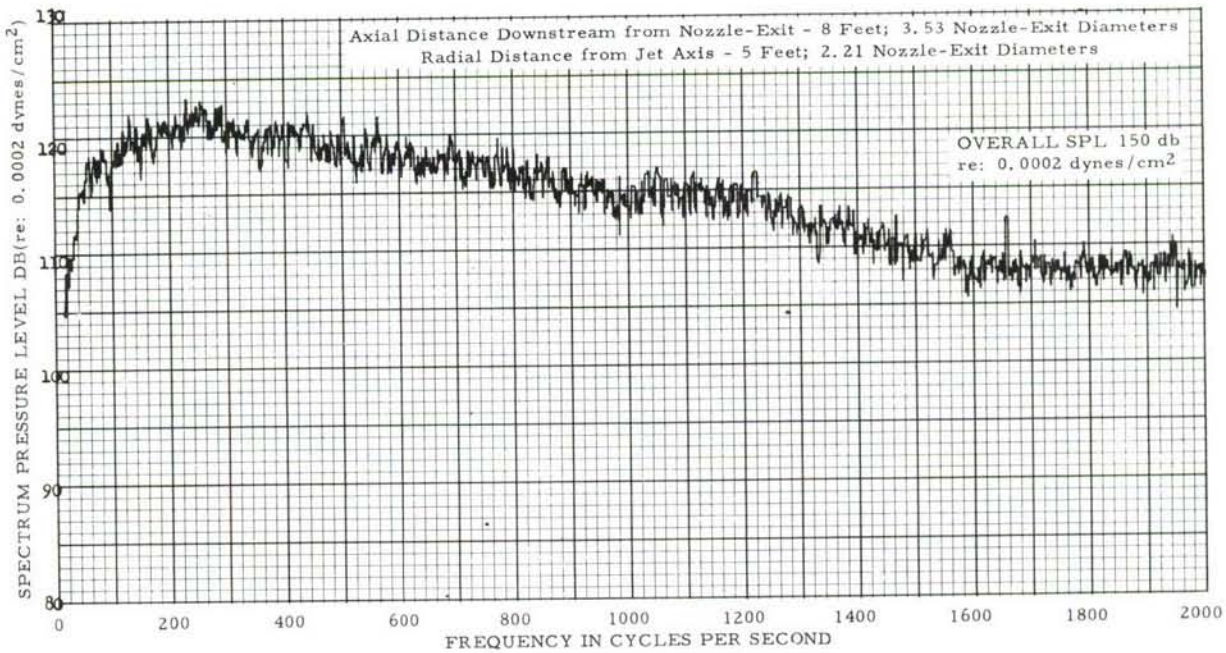

Figure II-25e. Narrow Band (10 cps) Analysis of Sound Pressure Levels - Free Field Survey - Afterburner

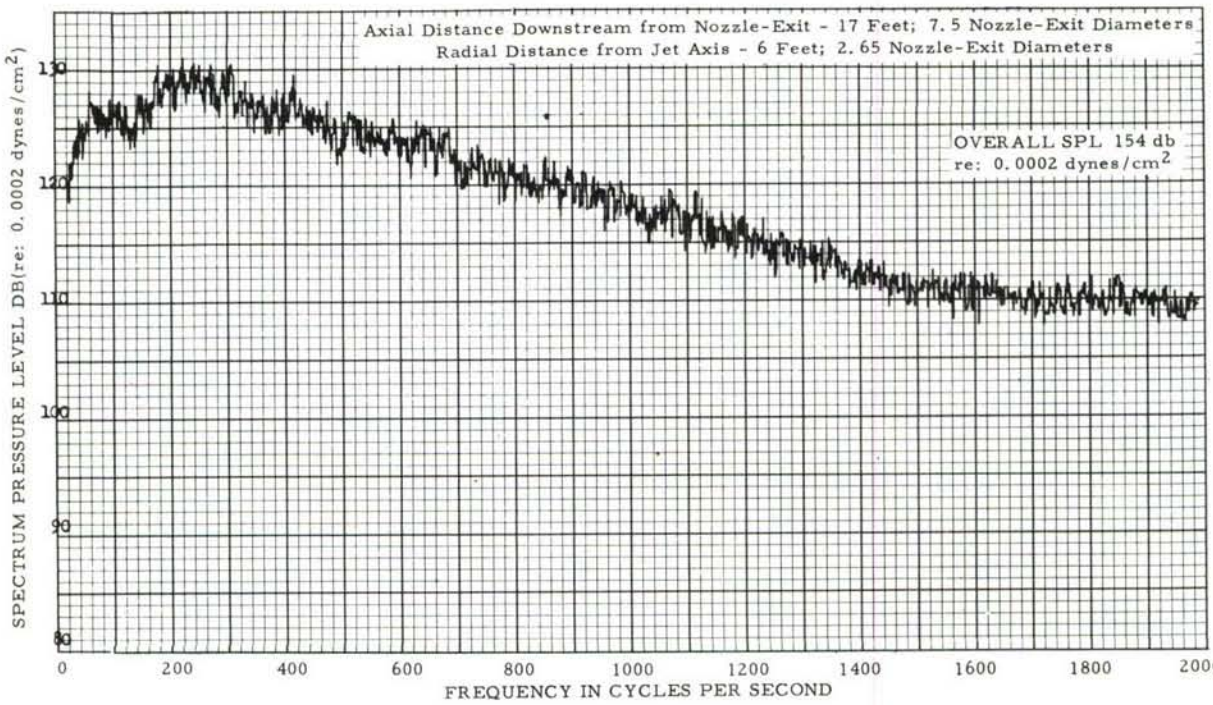

Figure II-25f. Narrow Band (10 cps) Analysis of Sound Pressure Levels - Free Field Survey - Afterburner

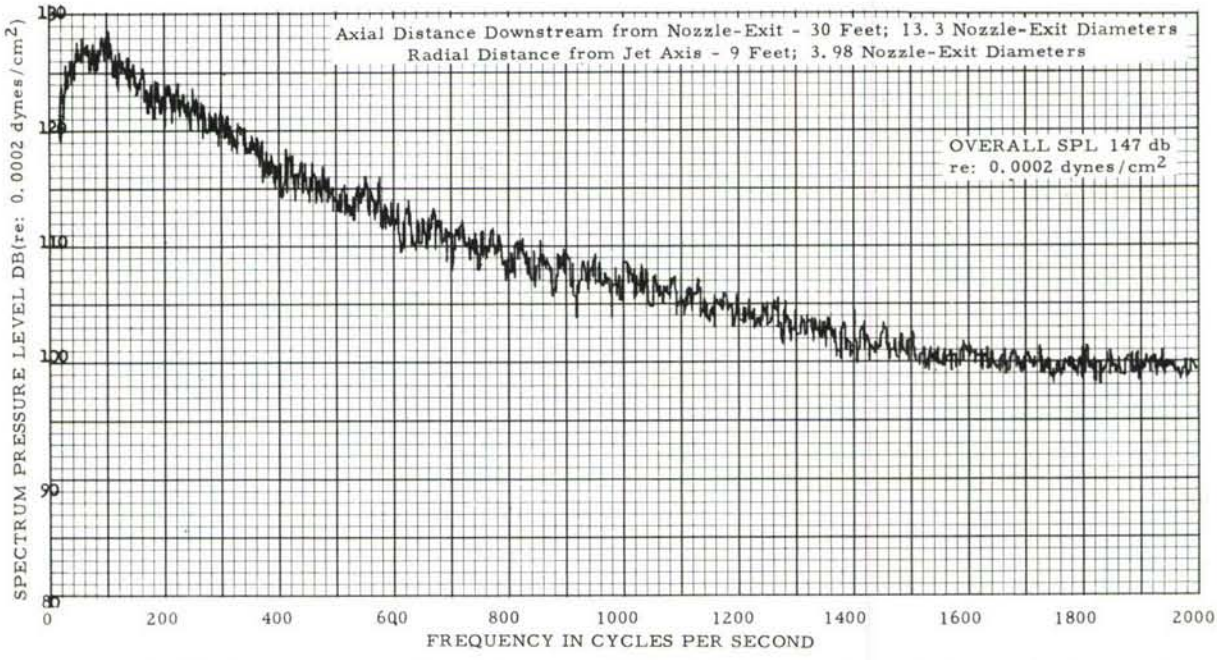

Figure II-25g. Narrow Band (10 cps) Analysis of Sound Pressure Levels - Free Field Survey - Afterburner

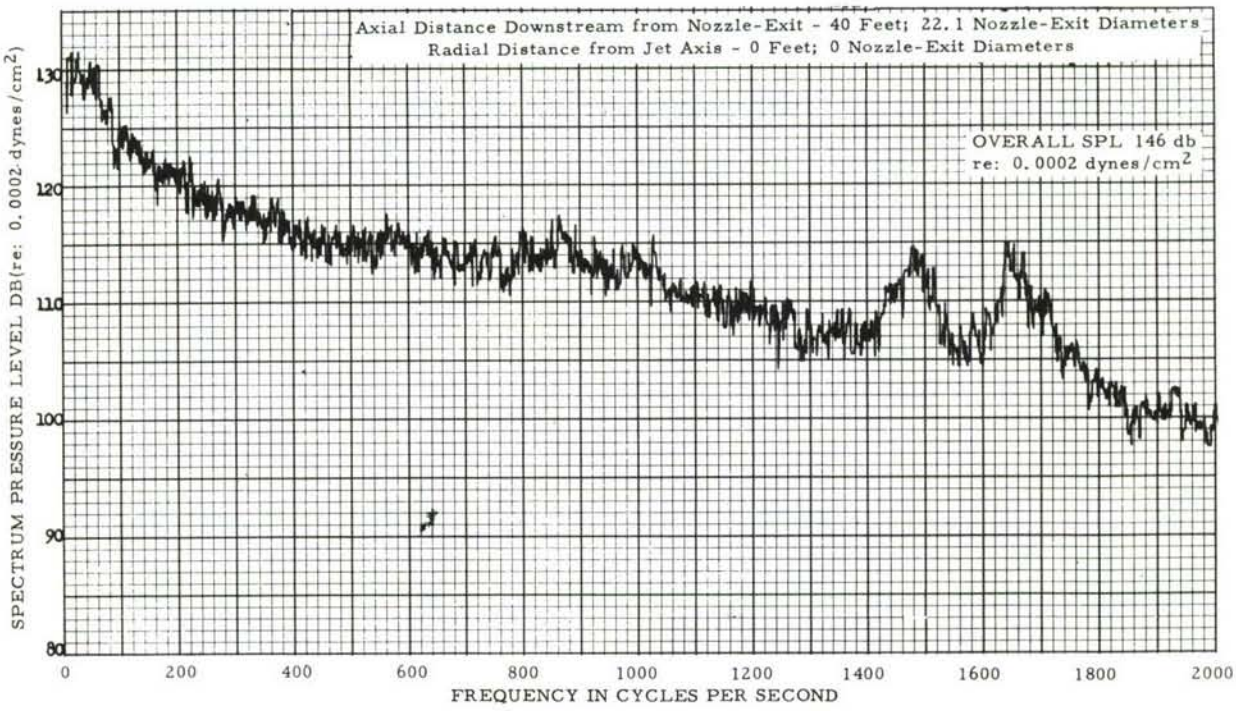

Figure II-26a. Narrow Band (10 cps) Analysis of Sound Pressure Levels - Jet Wake Survey - Military

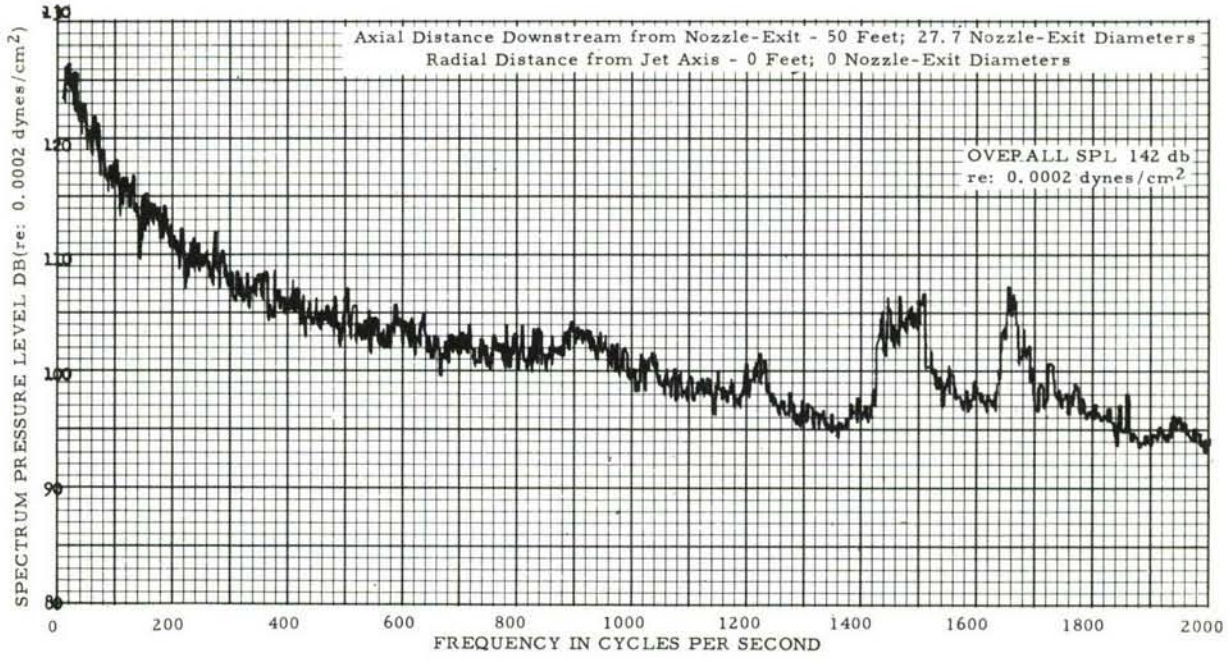

Figure II-26b. Narrow Band (10 cps) Analysis of Sound Pressure Levels - Jet Wake Survey - Military

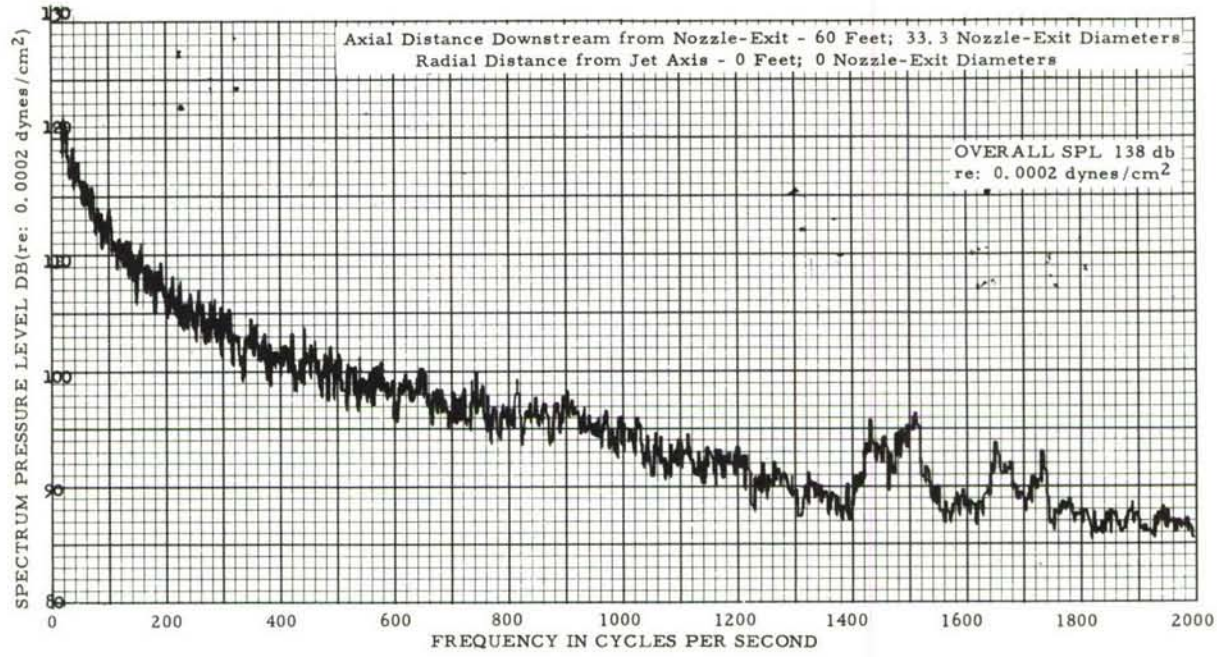

Figure II-26c. Narrow Band (10 cps) Analysis of Sound Pressure Levels - Jet Wake Survey - Military

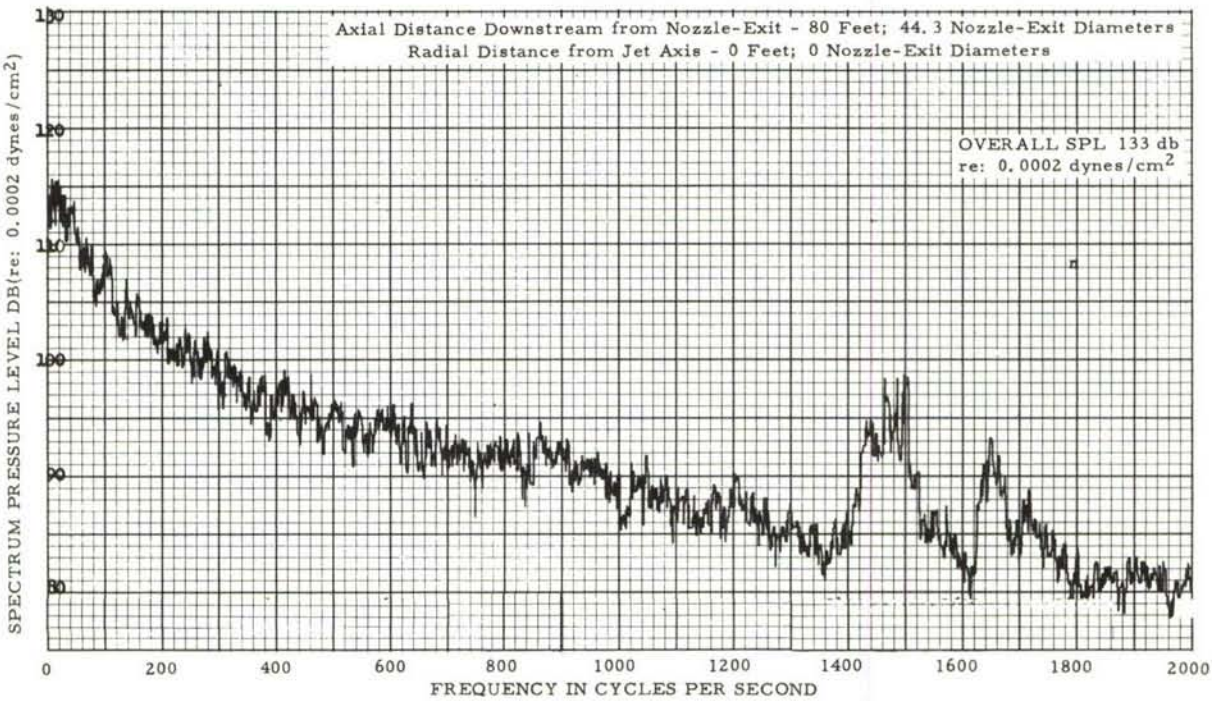

Figure II-26d. Narrow Band (10 cps) Analysis of Sound Pressure Levels - Jet Wake Survey - Military

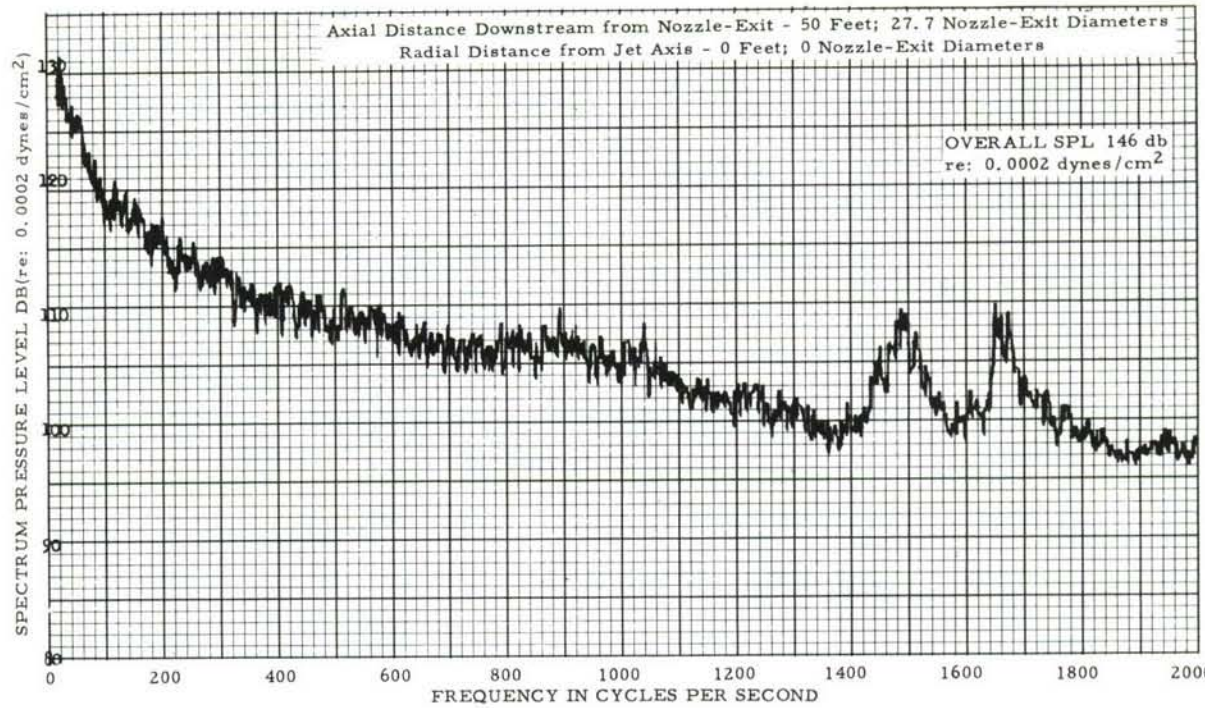

Figure II-27a. Narrow Band (10 cps) Analysis of Sound Pressure Levels - Jet Wake Survey - Military

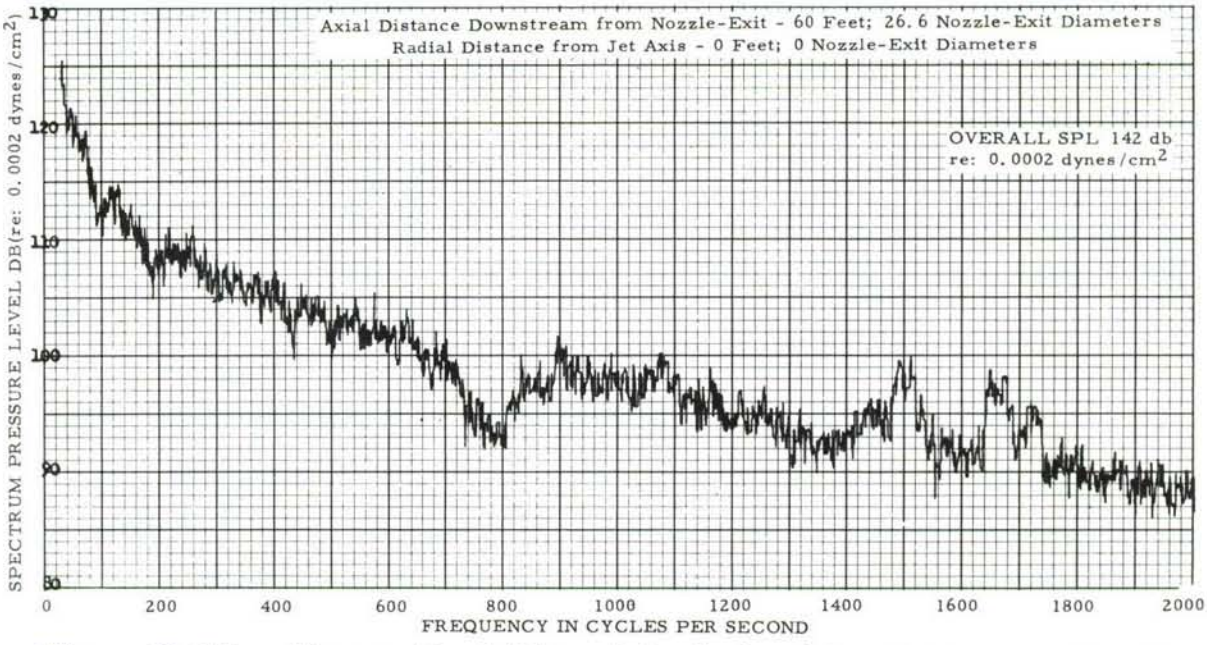

Figure II-27b. Narrow Band (10 cps) Analysis of Sound Pressure Levels - Jet Wake Survey - Afterburner

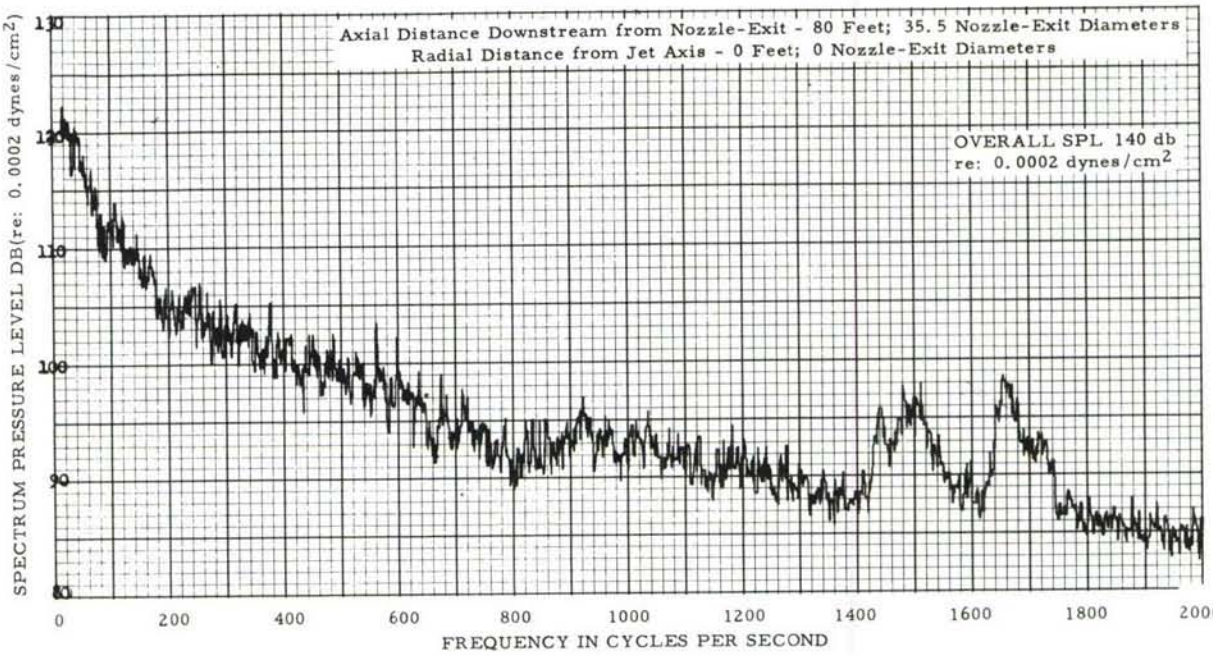

Figure II-27c. Narrow Band (10 cps) Analysis of Sound Pressure Levels - Jet Wake Survey - Afterburner

c. Probability Distribution of Amplitudes

Probability distribution of amplitude for several free field locations both inside and outside the jet for two-engine conditions, military and afterburner, are shown in Figures II-28 through II-31, pages 42 through 45. Each graph shows the probability distribution for the overall and three octave bands of sound pressures. The distributions are uniquely identified by test and engine condition, free field location, and record number. An analysis of these and other distributions, in terms of a Rayleigh distribution, is given in Table II-7.

This table shows values of $\overline{\sigma}$, $\overline{2\sigma}$, and $\overline{3\sigma}$, as well as the ratios of these quantities as determined from the appropriate distribution curve. (The average bar indicates an average value for all four curves on a distribution graph.) These quantities are the values along the distribution abscissa for ordinate values of 0.607, 0.135, and 0.012 which correspond to σ , 2σ , and 3σ , respectively, for a theoretical Rayleigh distribution. For a detailed discussion of the properties of a Rayleigh distribution see Reference 5 or 6.

TABLE II-7

ANALYSIS OF PROBABILITY DISTRIBUTION OF PRESSURE AMPLITUDES
ASSUMING A RAYLEIGH DISTRIBUTION

Data		X	Y	Record No.	$\bar{6}$	$\overline{26}$	$\overline{36}$	$\overline{26/6}$	$\overline{36/6}$	Distribution Graph No.
Free Field Survey	M	25	15	061159-1005	0.82	1.98	2.97	2.42	3.62	3
	M	35	15	1006	0.71	1.90	2.84	2.68	4.00	4
	M	15	15	1008	0.79	1.92	2.97	2.43	3.76	5
	M	0	15	1009	0.73	1.87	3.10	2.57	4.25	6
	A/B	0	15	011559-3008	0.79	1.98	2.98	2.50	3.77	7
	A/B	15	15	1012	0.87	2.03	3.10	2.33	3.55	8
	A/B	35	15	3008	0.76	1.97	2.96	2.52	3.90	10
Jet Wake	A/B	80	0	032559-1004	0.99	2.25	3.50	2.27	3.53	
	A/B	40	0	2011	1.10	2.50	3.44	2.27	3.13	
	M	50	0	2006	1.01	2.37	3.44	2.34	3.44	
	M	80	0	1003	1.05	2.34	3.50	2.23	3.33	
	A/B	60	0	1010	1.07	2.31	----	2.20	----	
Rigid Panel	M	US		032759-1009	0.85	1.84	3.26	2.16	3.83	15
	A/B	US		1010	0.62	1.40	2.26	2.26	3.64	
	M	DS		020959-1007	0.82	2.10	3.40	2.56	4.15	17
	A/B	DS		1008	0.85	2.10	3.40	2.47	4.00	18
Panel A	M	US		040159-1009	0.74	1.87	2.76	2.52	3.73	19
	A/B	US		1010	0.90	2.10	3.20	2.33	3.55	20
	M	DS		031659-1010	0.79	2.12	2.98	2.68	3.77	21
	A/B	DS		1011	0.79	1.98	3.26	2.50	4.12	22
Free Field at Panel	M	US		032559-1009	0.85	2.10	3.54	2.47	4.16	11
	A/B	US		1010	0.85	2.20	3.54	2.59	4.16	12
	M	DS		021759-1009	0.85	2.20	3.54	2.59	4.16	13
	A/B	DS		1010	0.85	2.20	3.54	2.59	4.16	14

Notes:
US - Upstream Boundary Site
DS - Downstream Boundary Site
M - Military Engine Condition
A/B - Afterburner Engine Condition
X, Y - Field Coordinates in Feet
X - Distance from Nozzle-Exit; Y - Distance from Jet Centerline

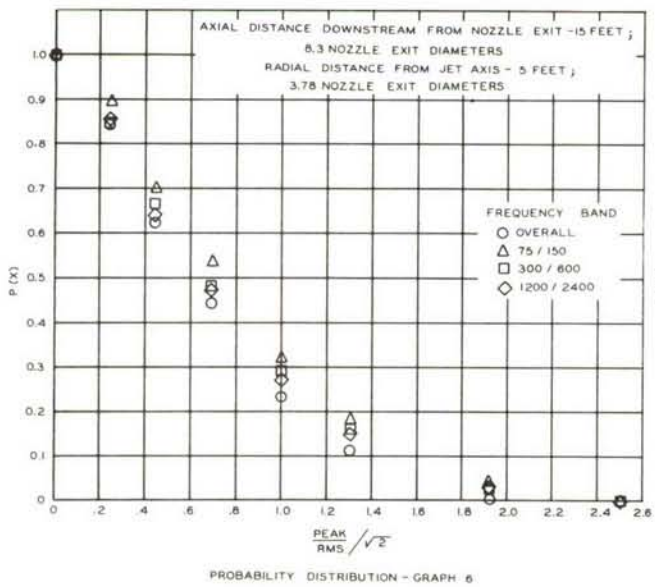

Figure II-28a. Probability Distribution of Pressure Amplitudes - Free Field Survey - Military

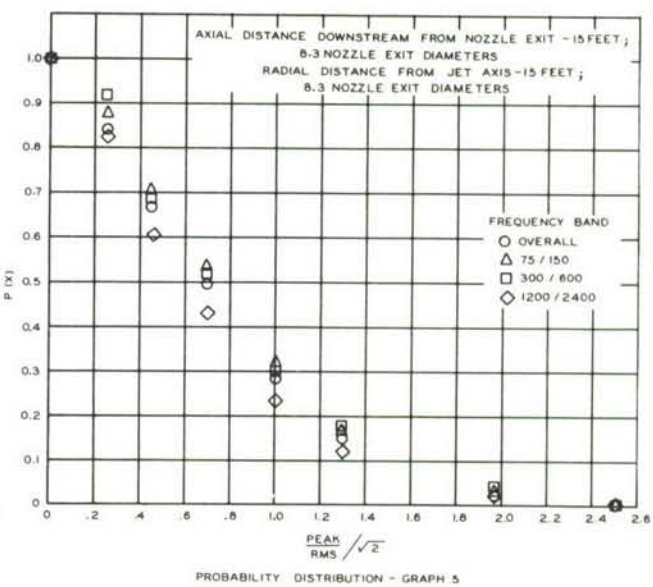

Figure II-28b. Probability Distribution of Pressure Amplitudes - Free Field Survey - Military

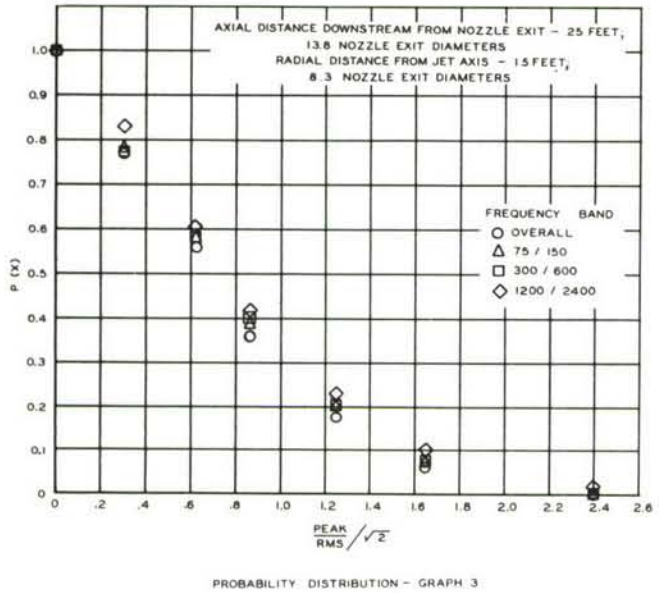

Figure II-28c. Probability Distribution of Pressure Amplitudes - Free Field Survey - Military

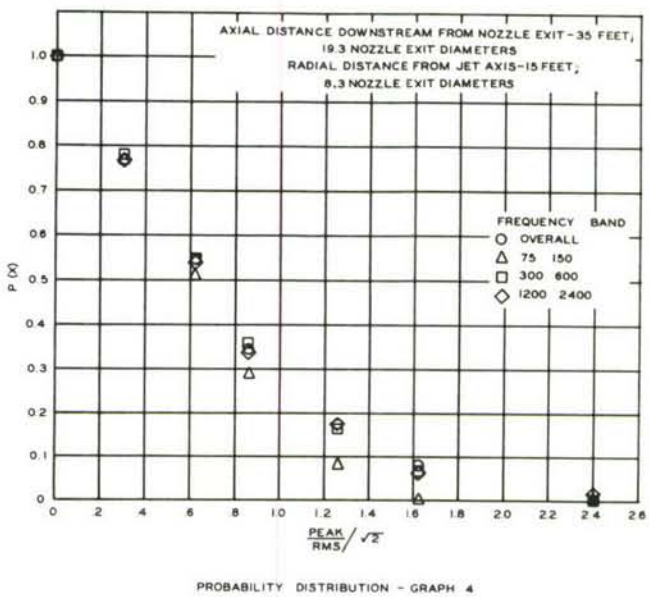

Figure II-28d. Probability Distribution of Pressure Amplitudes - Free Field Survey - Military

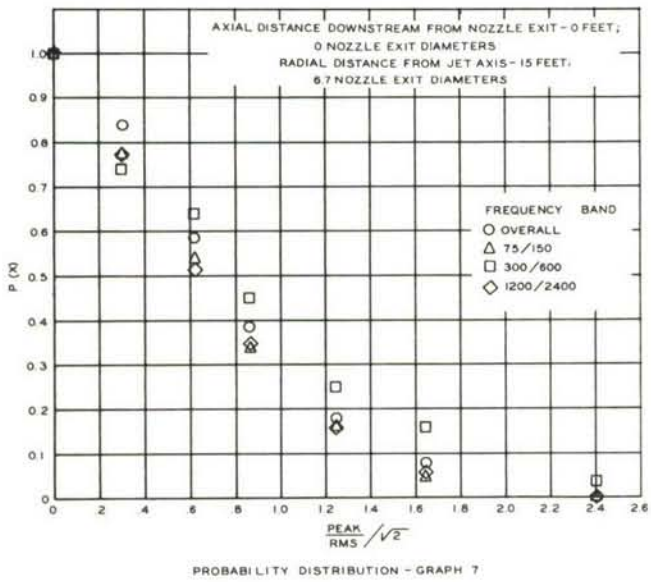

Figure II-29a. Probability Distribution of Pressure Amplitudes - Free Field Survey - Afterburner

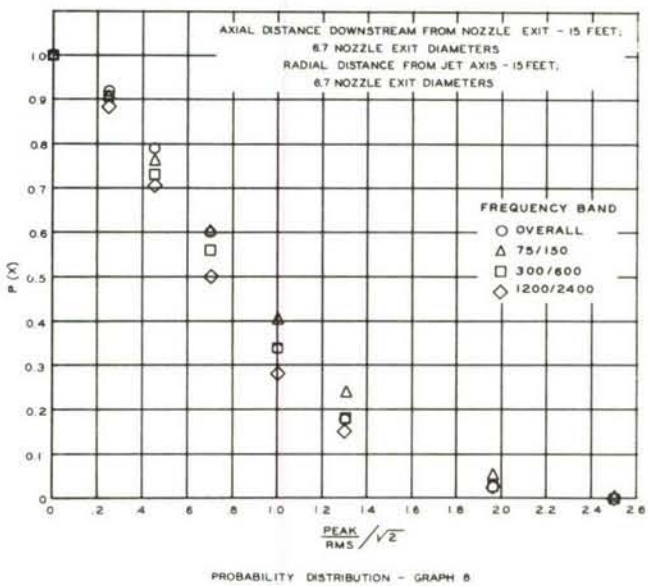

Figure II-29b. Probability Distribution of Pressure Amplitudes - Free Field Survey - Afterburner

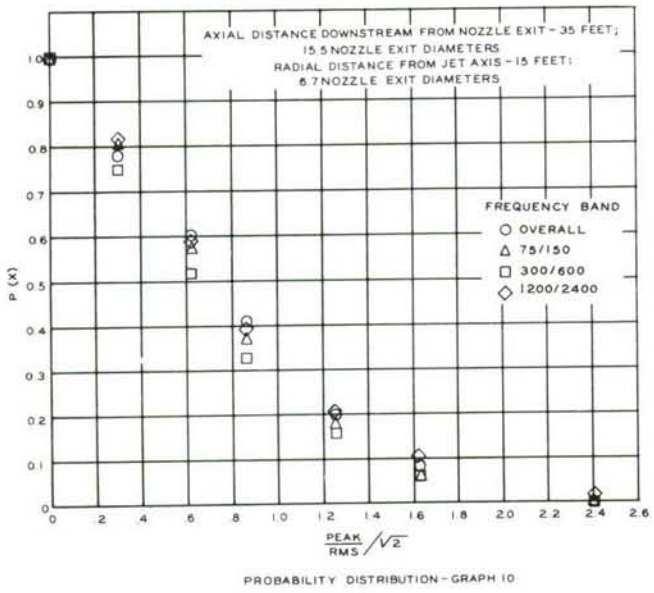

Figure II-29c. Probability Distribution of Pressure Amplitudes - Free Field Survey - Afterburner

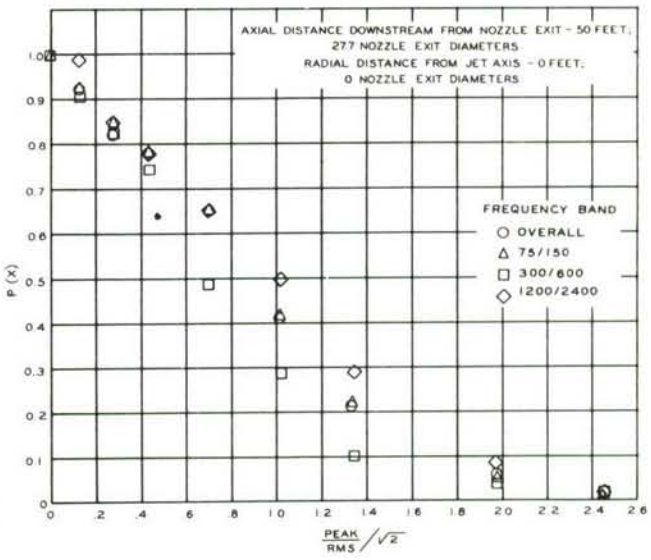

Figure II-30a. Probability Distribution of Pressure Amplitudes Jet Wake Survey - Military

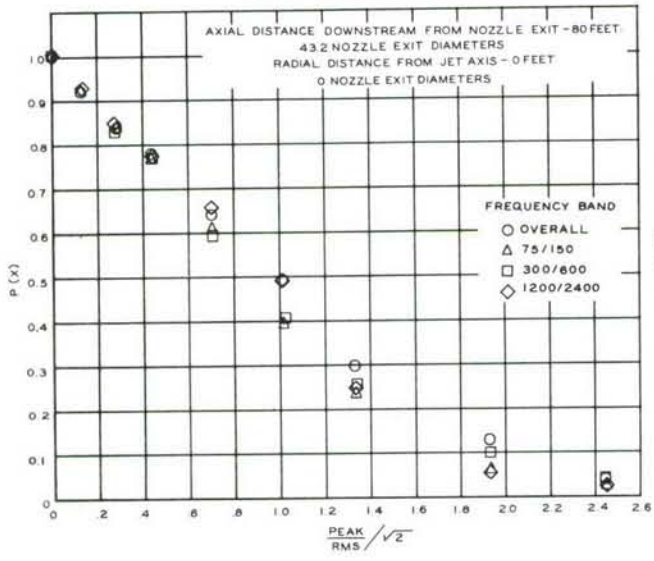

Figure II-30b. Probability Distribution of Pressure Amplitudes - Jet Wake Survey - Military

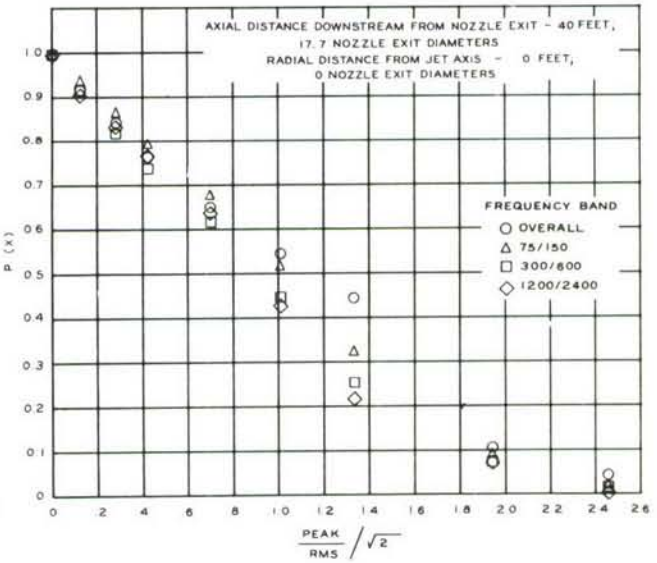

Figure II-31a. Probability Distribution of Pressure Amplitudes - Jet Wake Survey - Afterburner

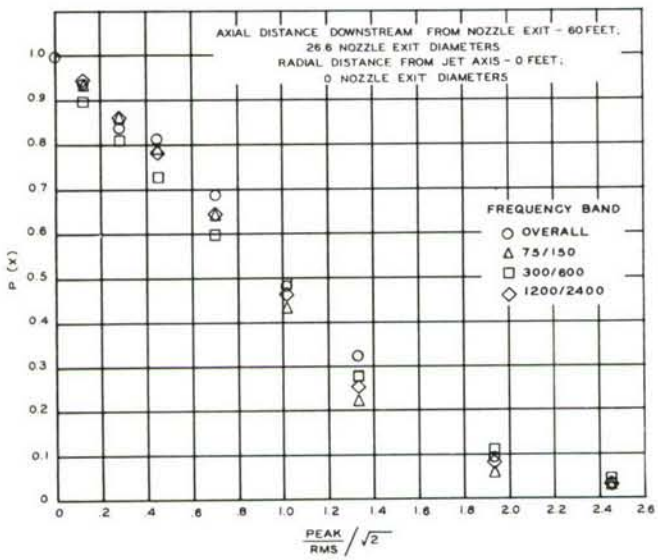

Figure II-31b. Probability Distribution of Pressure Amplitudes - Jet Wake Survey - Afterburner

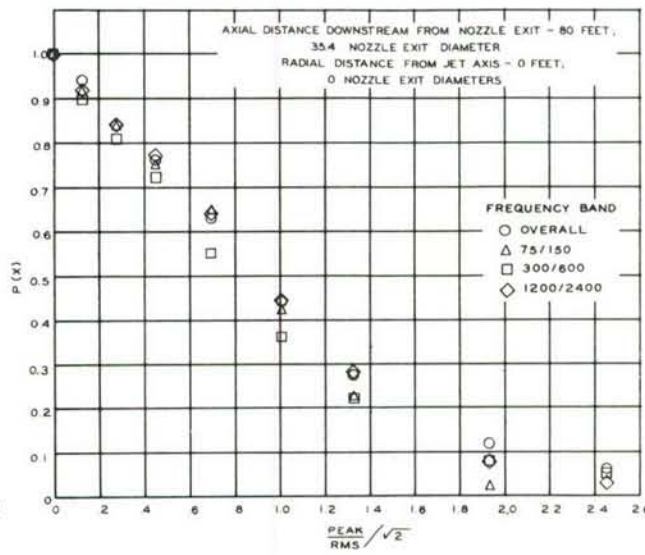

Figure II-31c. Probability Distribution of Pressure Amplitudes - Jet Wake Survey - Afterburner

2. Bounded Field Survey Results

a. Space-Phase Correlation

The tabulated space-phase correlation coefficients have been plotted as correlograms for certain of the 1/3 octave band filter center frequencies: overall, 100, 200, 320, 400, 500, 640, and 1000 cps. These are shown in Figures II-32 through II-35, pages 46 through 58: Longitudinal Sound Pressure Correlation for the Free Field, Flat Panel A, Rigid Panel, and Curved Panel A, respectively. In these figures, the correlation coefficients are plotted as both functions of distance and equivalent nozzle-exit diameters. There are eight graphs for each of the free field, flat panel A, and rigid panel boundary conditions displaying correlation for two-engine conditions: military and afterburner; two boundary sites: upstream and downstream; and two longitudinal survey lines: C and D (referred to the panel coordinate system of Figure II-6, page 9).

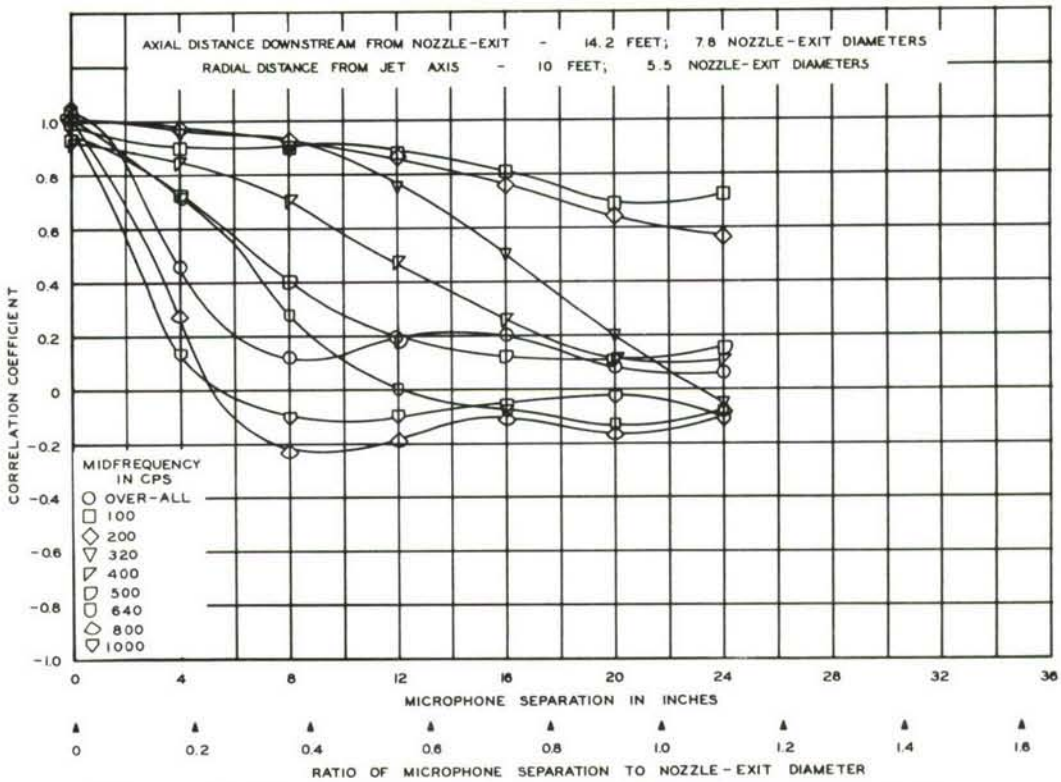

Figure II-32a. Longitudinal Sound Pressure Correlation: Free Field - Military - Survey Line C - Upstream Site

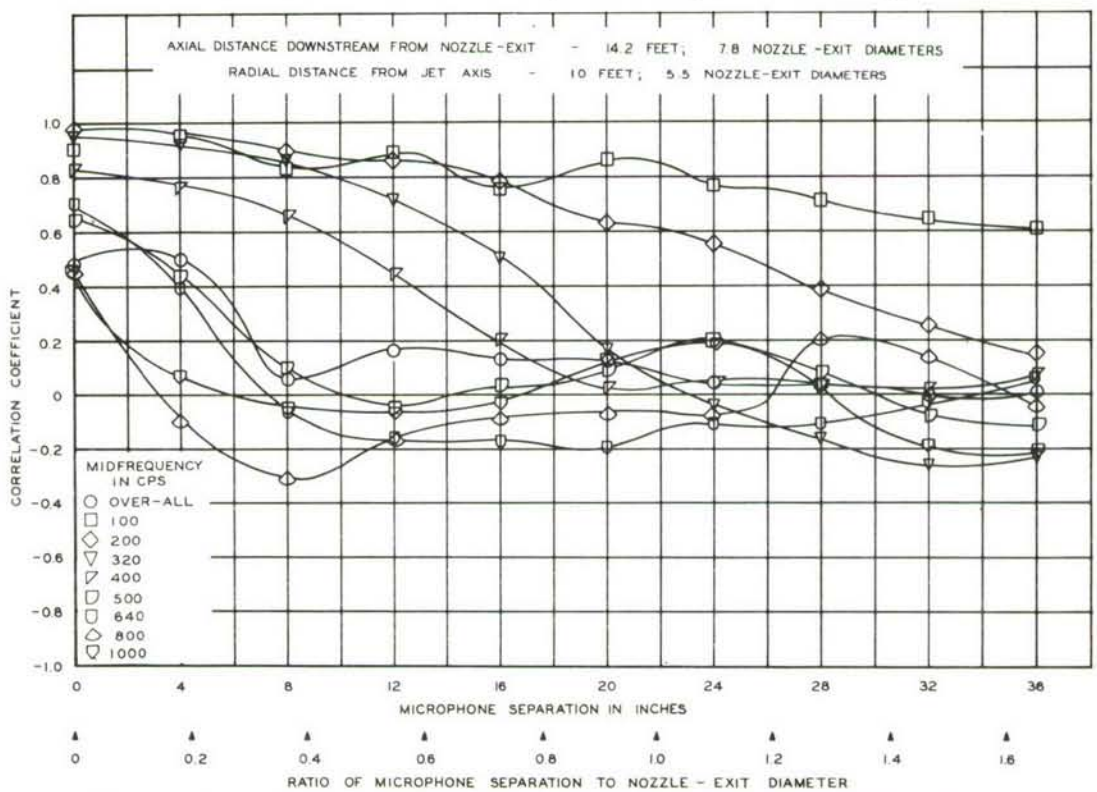

Figure II-32b. Longitudinal Sound Pressure Correlation: Free Field - Military - Survey Line D - Upstream Site

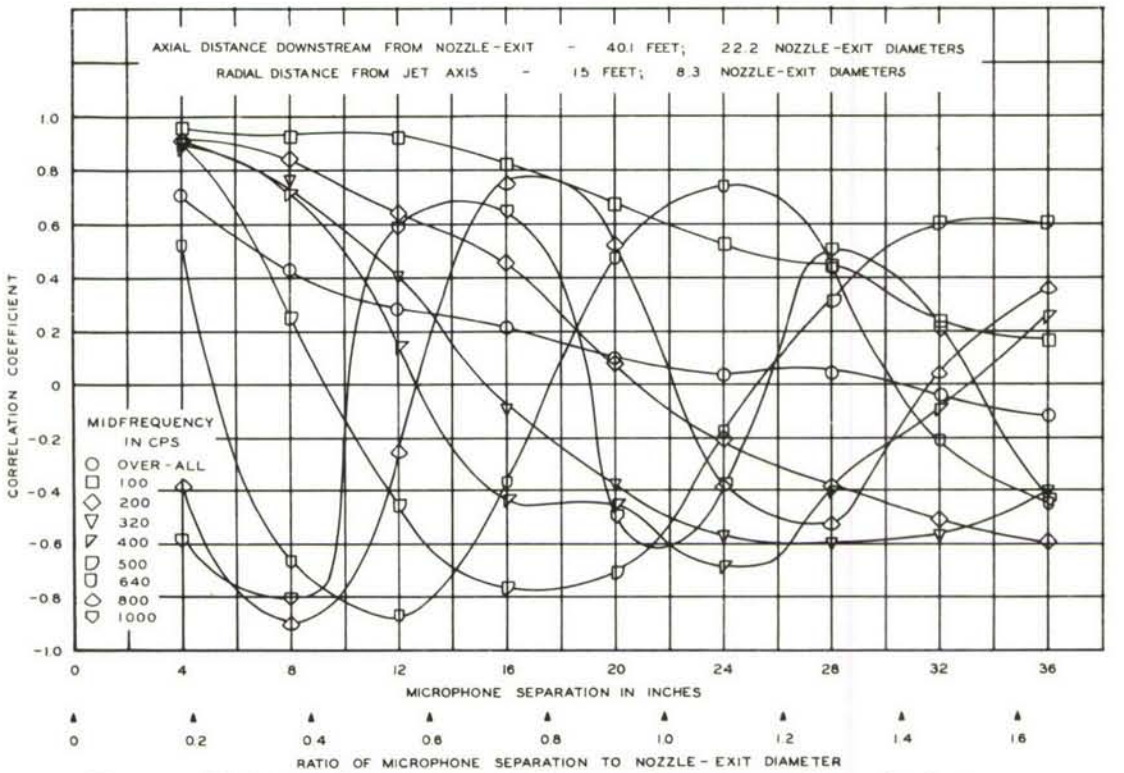

Figure II-32c. Longitudinal Sound Pressure Correlation: Free Field - Military - Survey Line C - Downstream Site

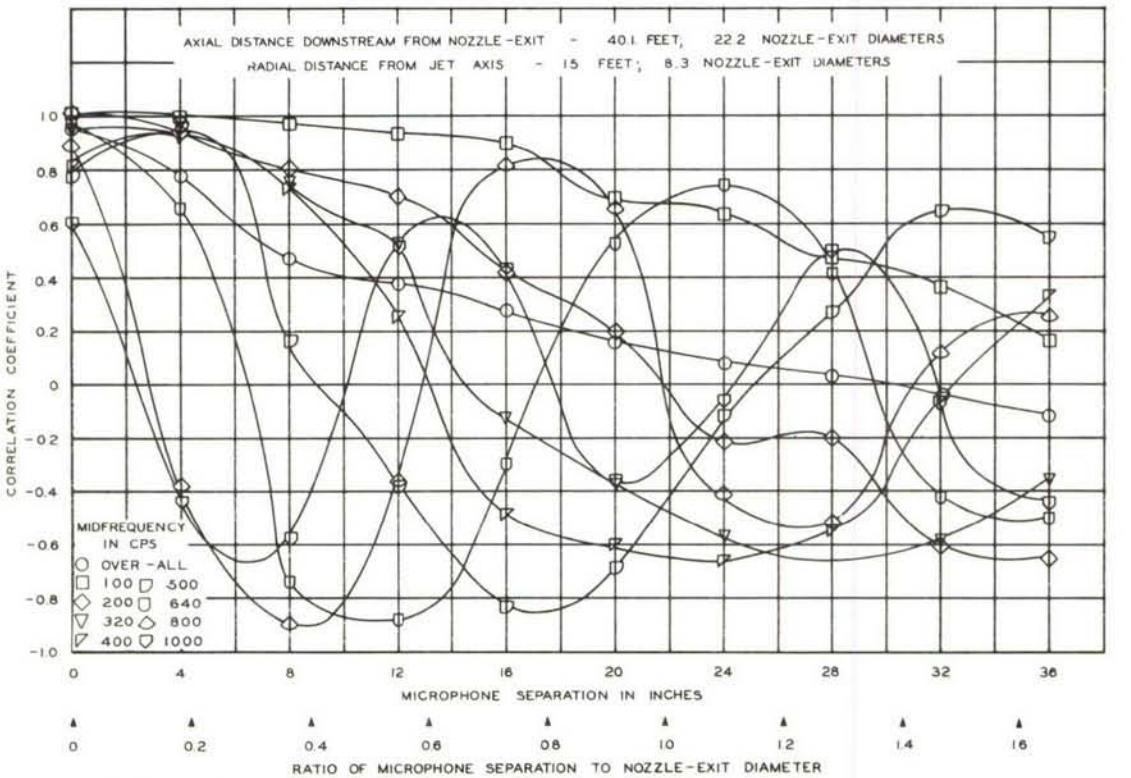

Figure II-32d. Longitudinal Sound Pressure Correlation Free Field - Military - Survey Line D - Downstream Site

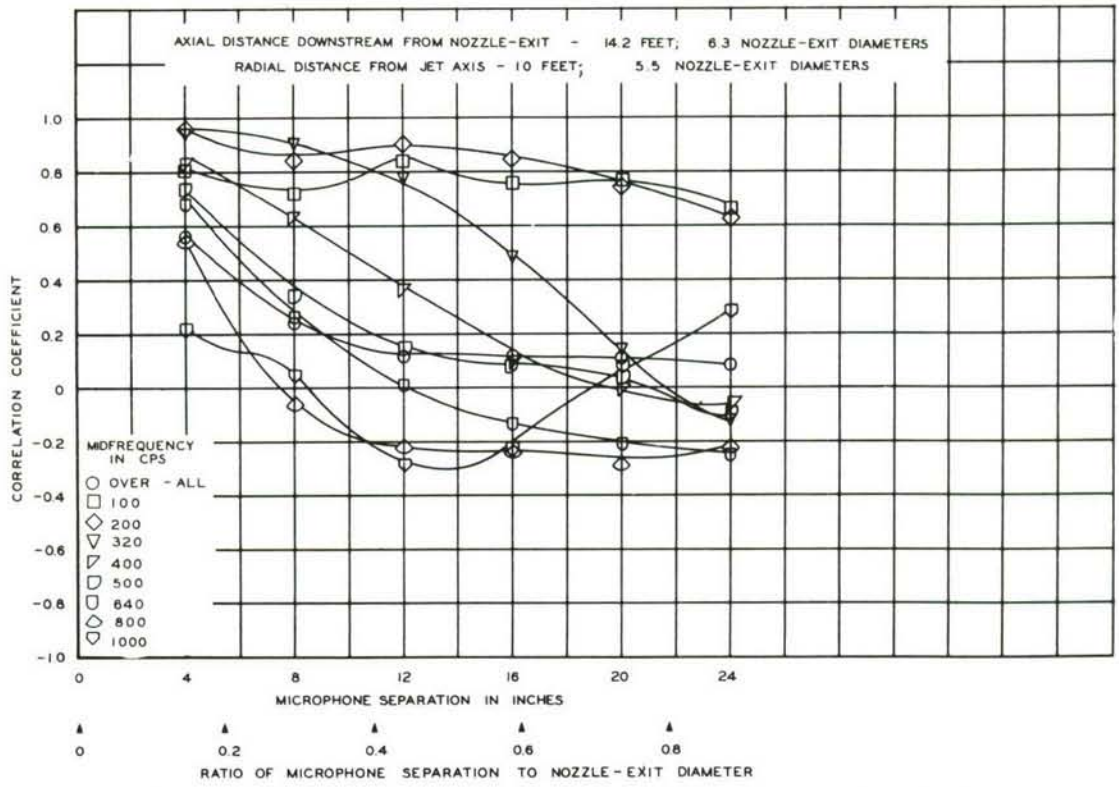

Figure II-32e. Longitudinal Sound Pressure Correlation
Free Field - Afterburner - Survey Line C - Upstream Site

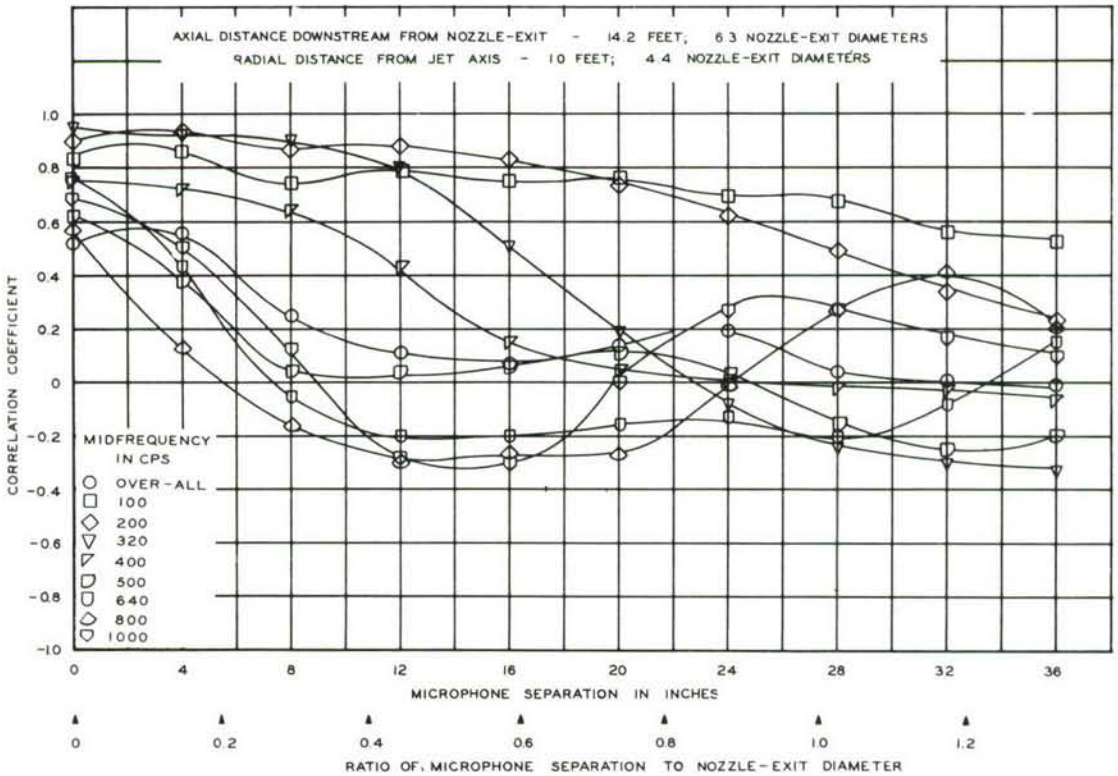

Figure II-32f. Longitudinal Sound Pressure Correlation
Free Field - Afterburner - Survey Line D - Upstream Site

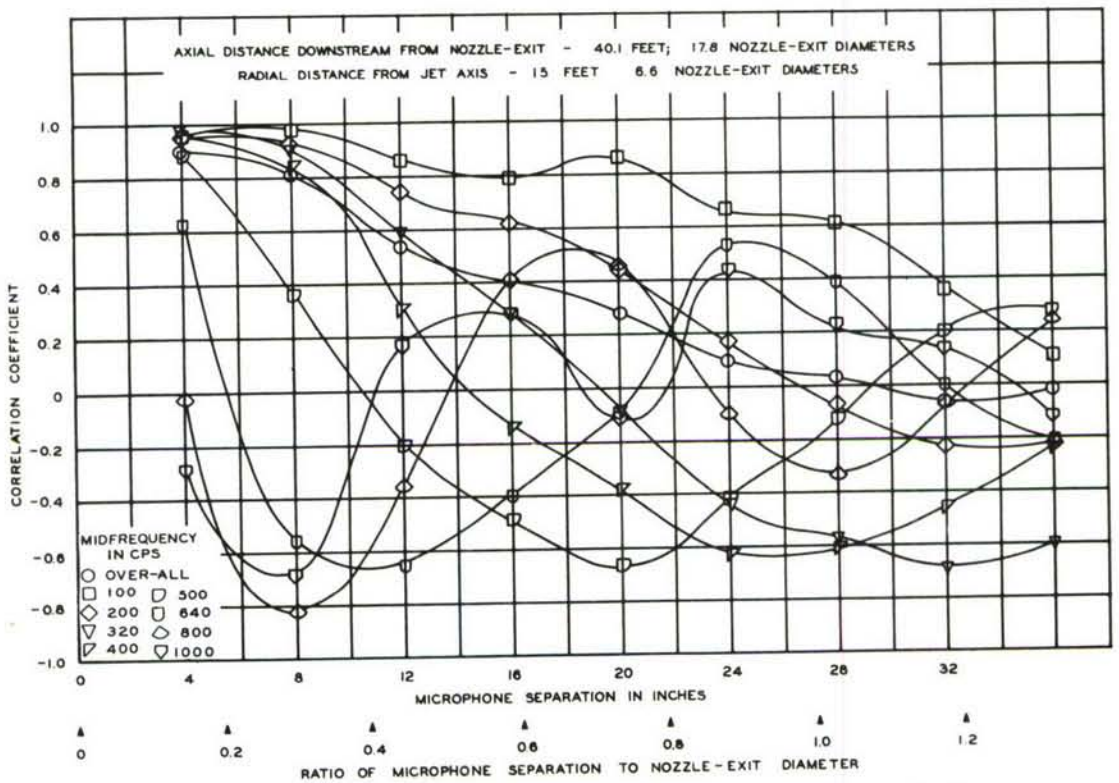

Figure II-32g. Longitudinal Sound Pressure Correlation
Free Field - Afterburner - Survey Line C - Downstream Site

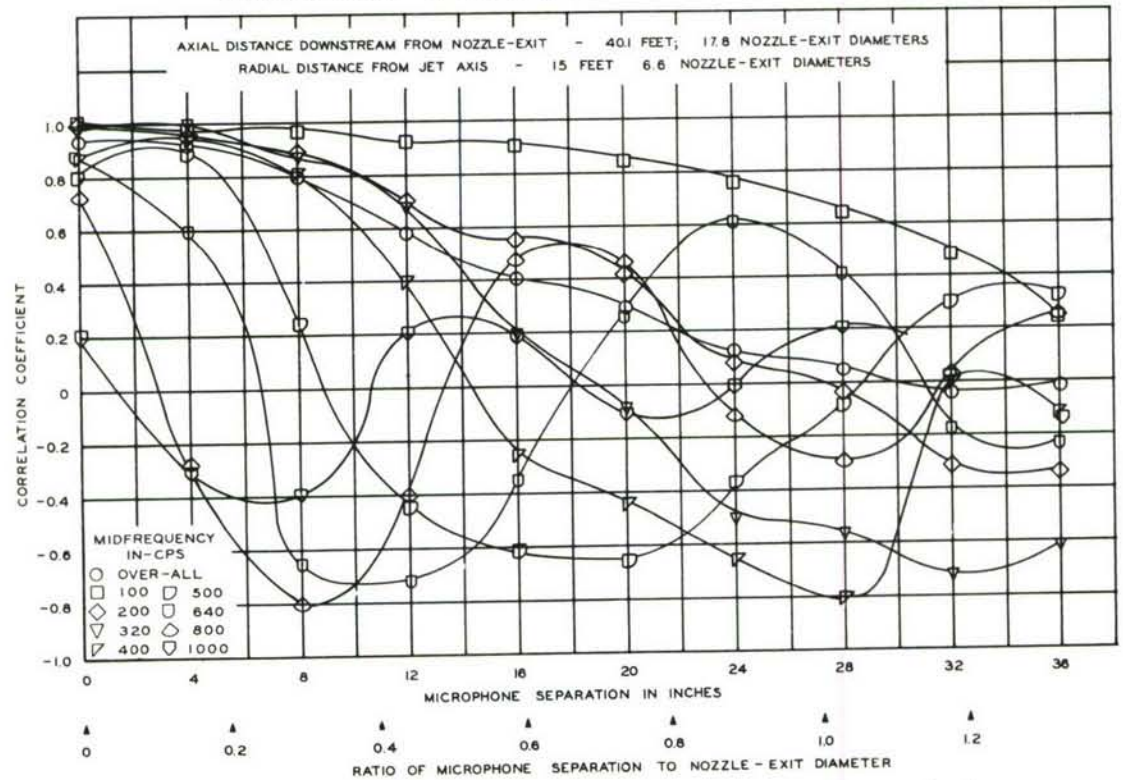

Figure II-32h. Longitudinal Sound Pressure Correlation
Free Field - Afterburner - Survey Line D - Downstream Site

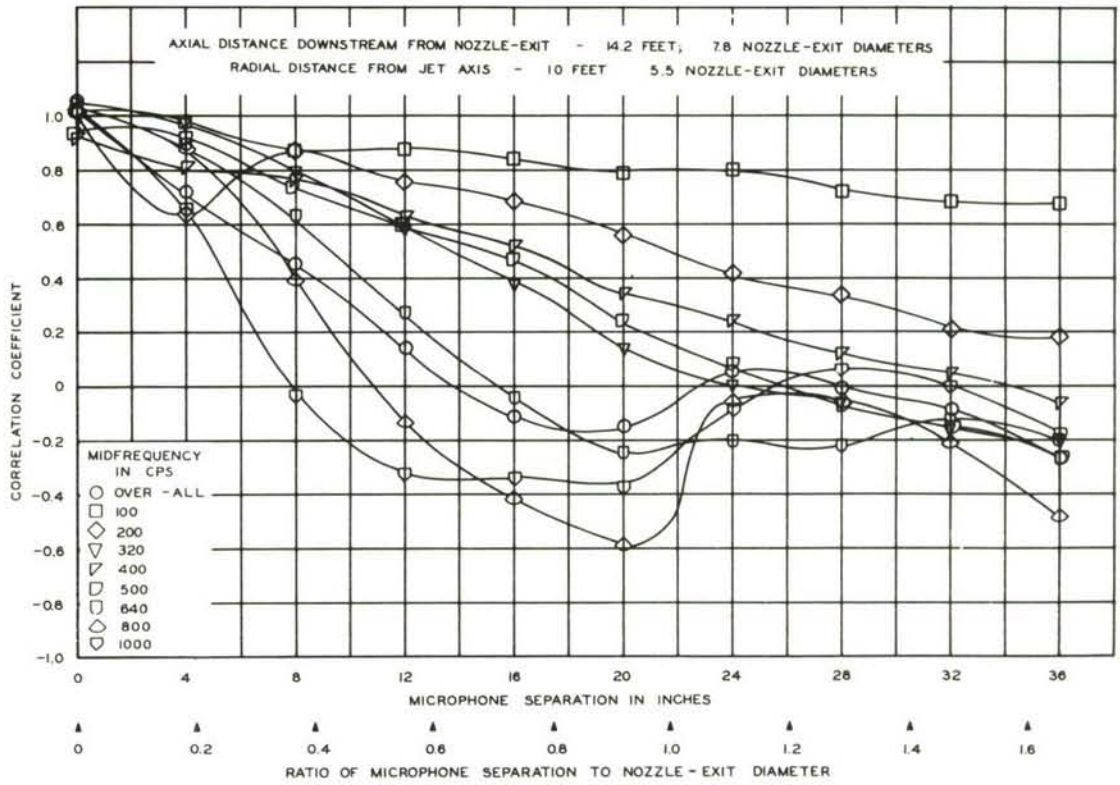

Figure II-33a. Longitudinal Sound Pressure Correlation
Flat Panel A - Military - Survey Line C - Upstream Site

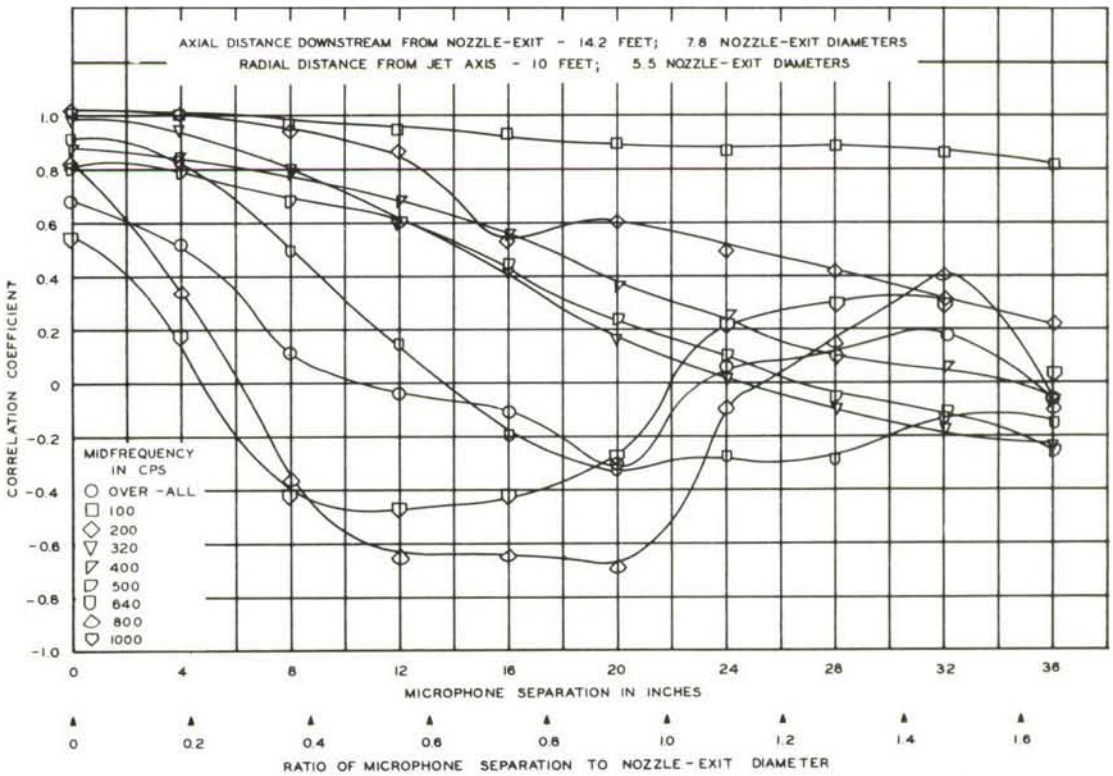

Figure II-33b. Longitudinal Sound Pressure Correlation
Flat Panel A - Military - Survey Line D - Upstream Site

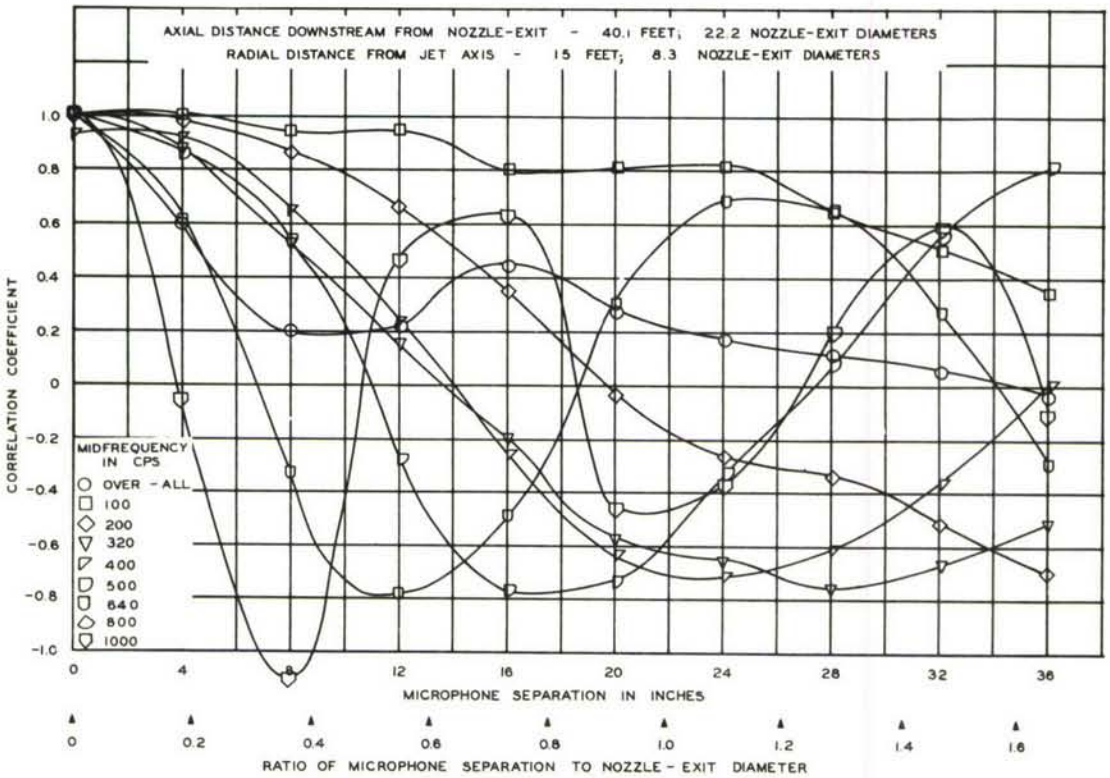

Figure II-33c. Longitudinal Sound Pressure Correlation
Flat Panel A - Afterburner - Survey Line C - Upstream Site

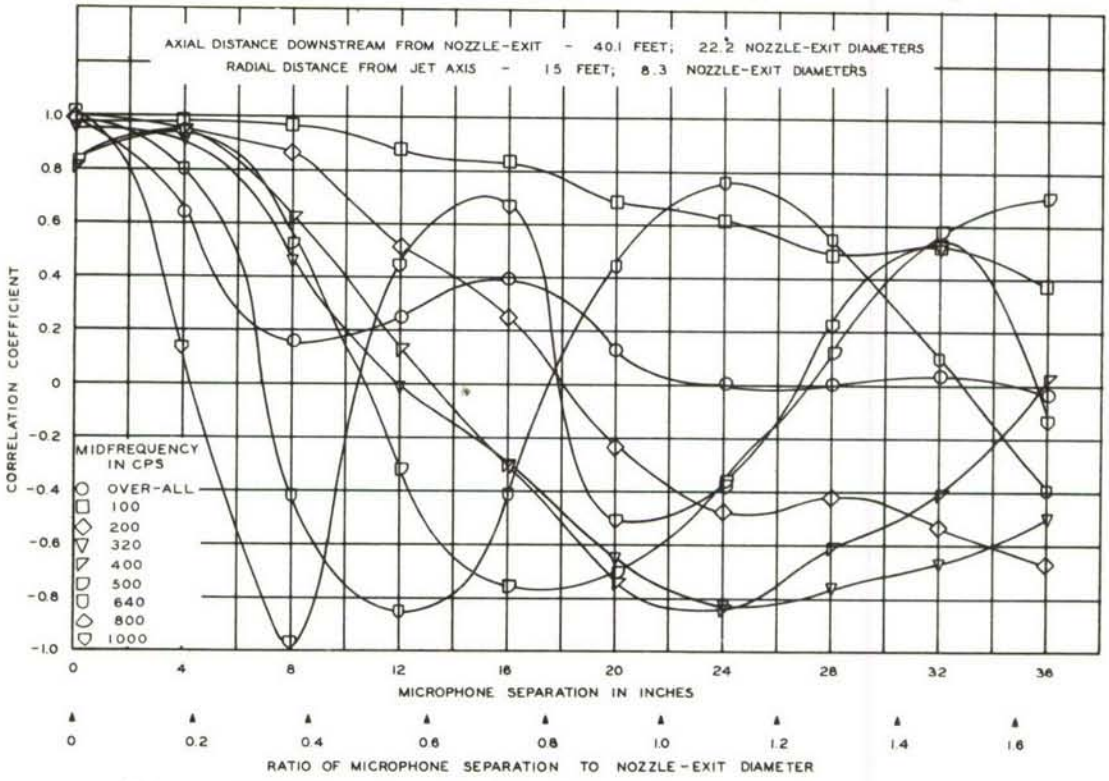

Figure II-33d. Longitudinal Sound Pressure Correlation
Flat Panel A - Afterburner - Survey Line D - Upstream Site

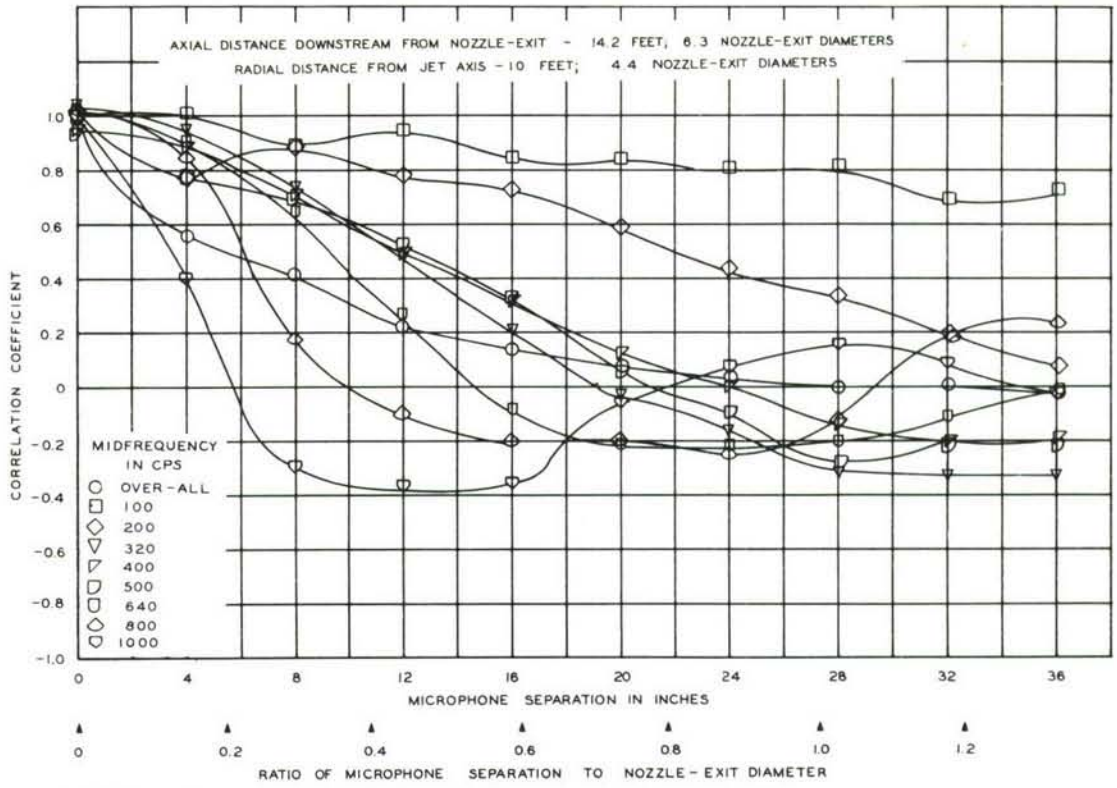

Figure II-33e. Longitudinal Sound Pressure Correlation
Flat Panel A - Afterburner - Survey Line C - Downstream Site

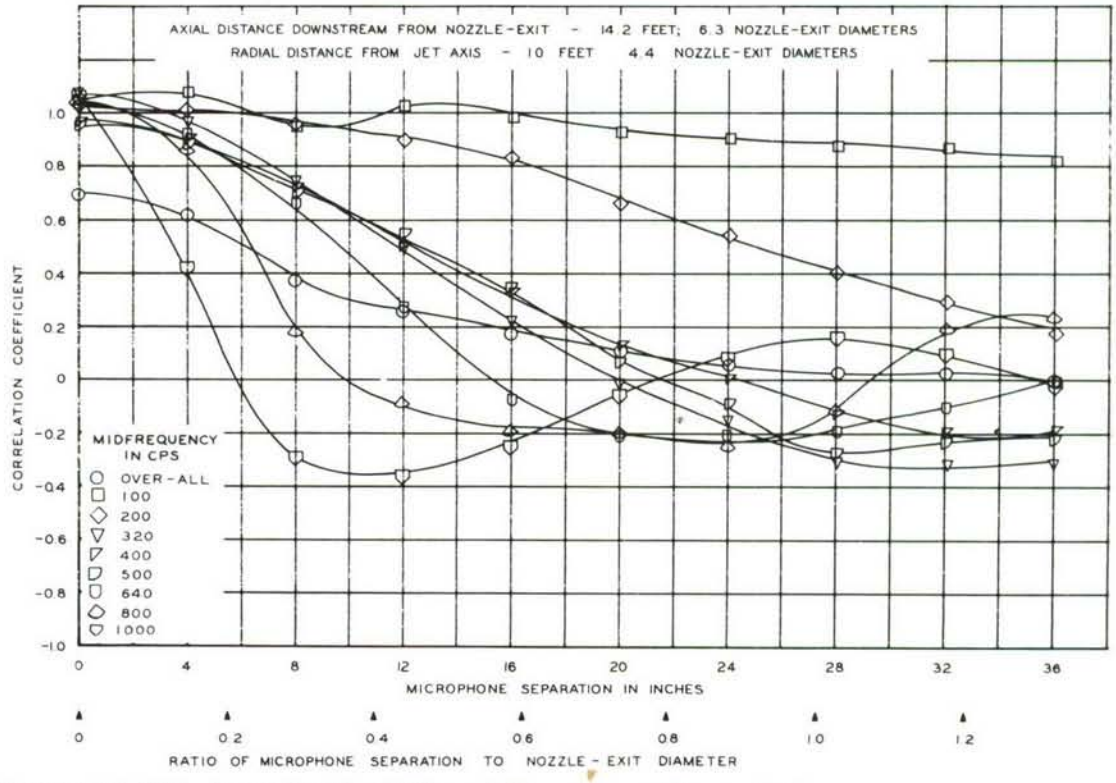

Figure II-33f. Longitudinal Sound Pressure Correlation
Flat Panel A - Military - Survey Line C - Downstream Site

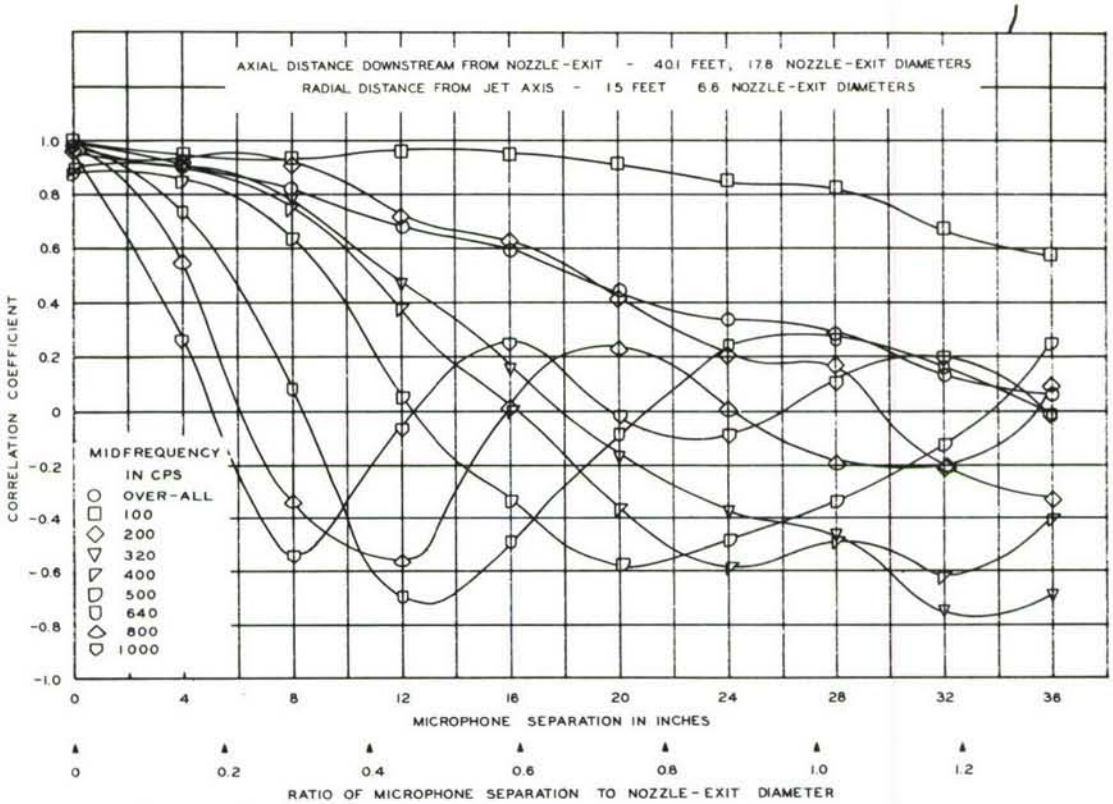

Figure II-33g. Longitudinal Sound Pressure Correlation
Flat Panel A - Military - Survey Line D - Downstream Site

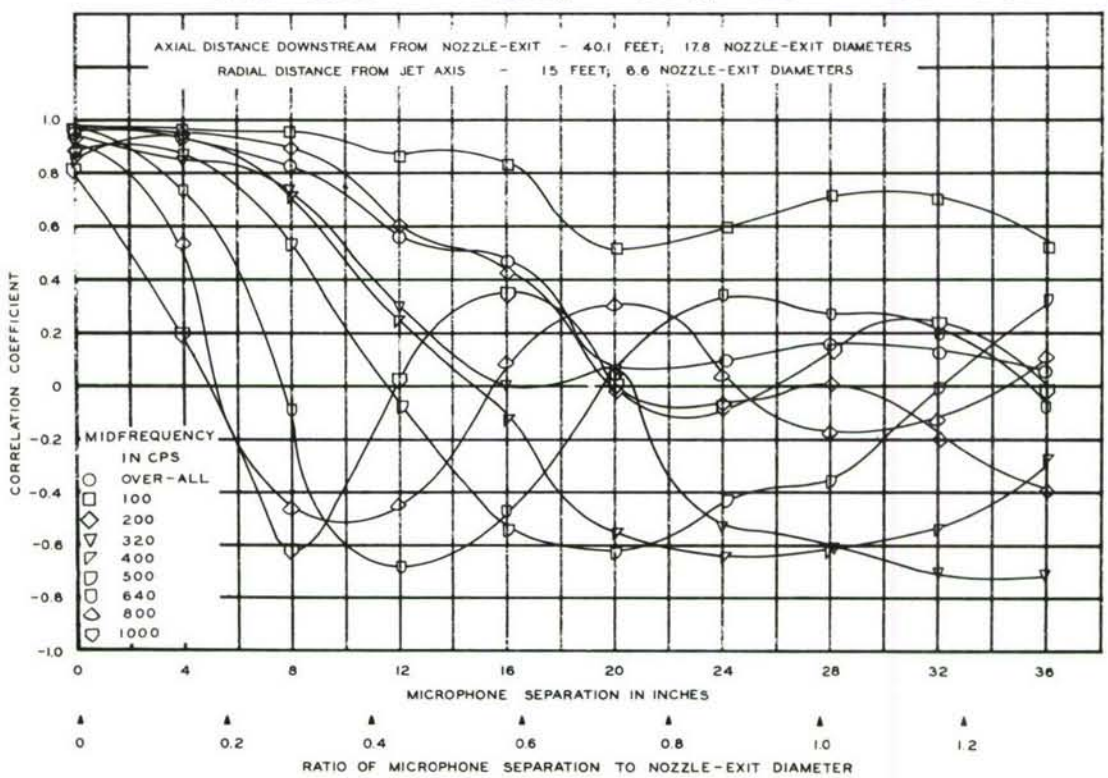

Figure II-33h. Longitudinal Sound Pressure Correlation
Flat Panel A - Afterburner - Survey Line D - Downstream Site

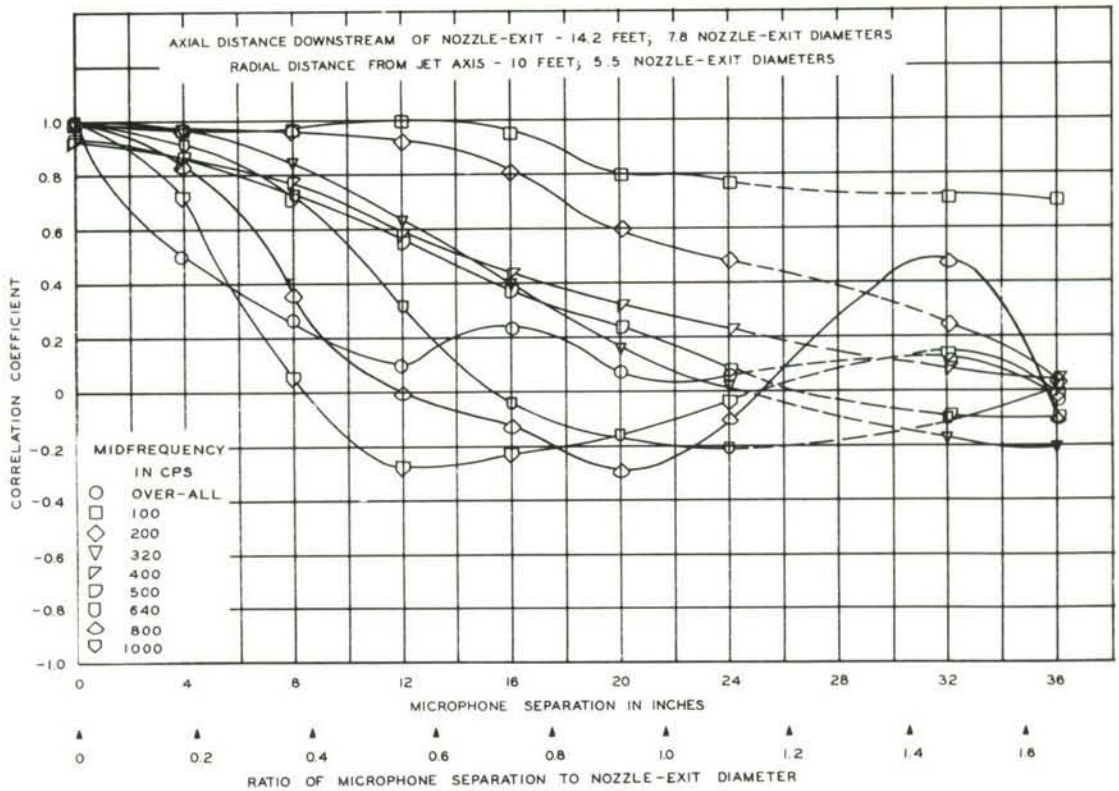

Figure II-34a. Longitudinal Sound Pressure Correlation
Rigid Panel - Military - Survey Line C - Upstream Site

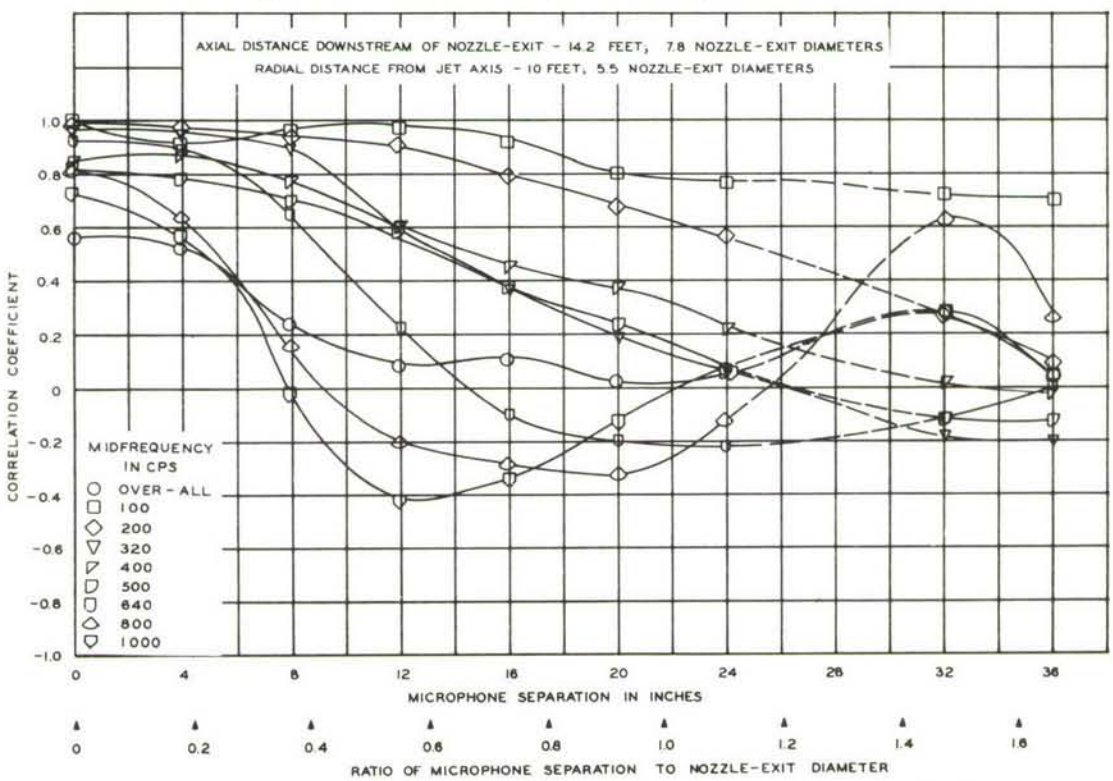

Figure II-34b. Longitudinal Sound Pressure Correlation
Rigid Panel - Military - Survey Line D - Upstream Site

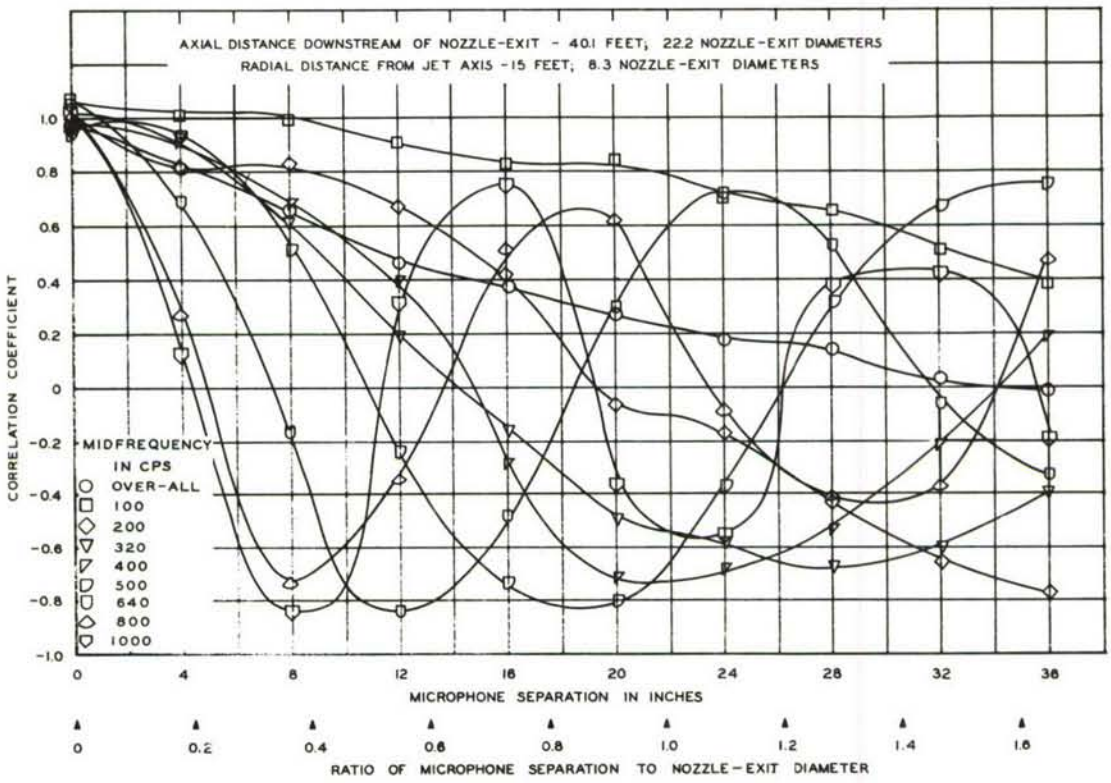

Figure II-34c. Longitudinal Sound Pressure Correlation
Rigid Panel - Military - Survey Line C - Downstream Site

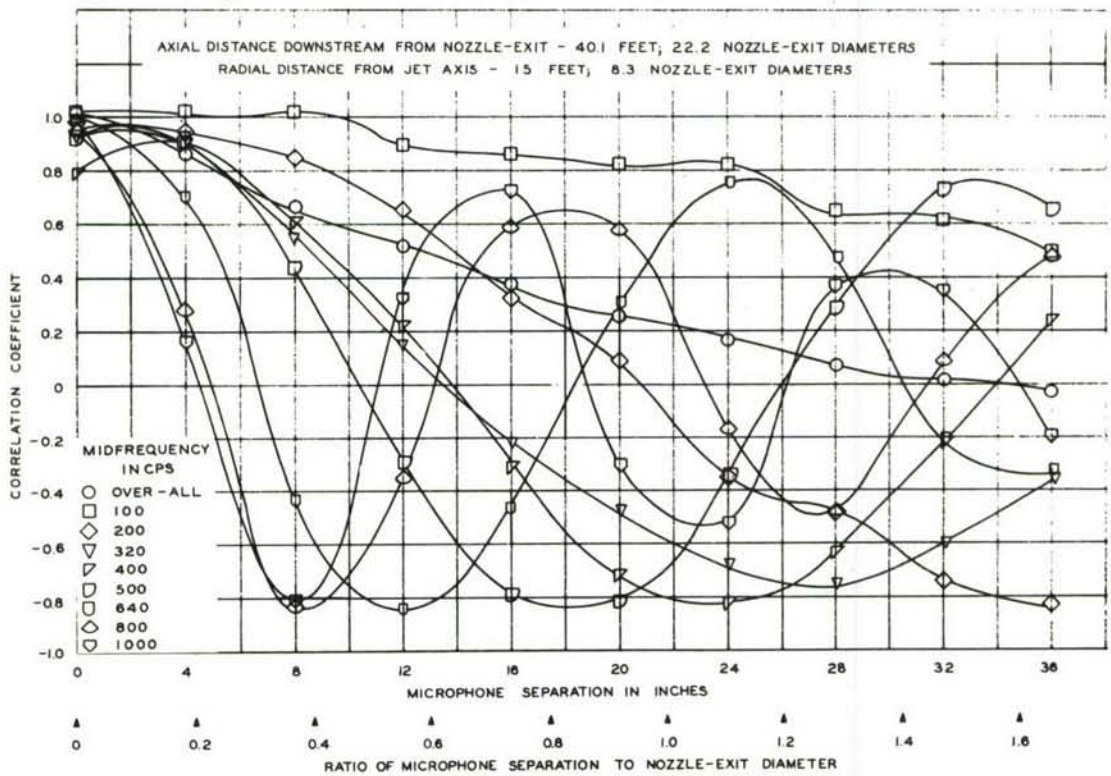

Figure II-34d. Longitudinal Sound Pressure Correlation
Rigid Panel - Military - Survey Line D - Downstream Site

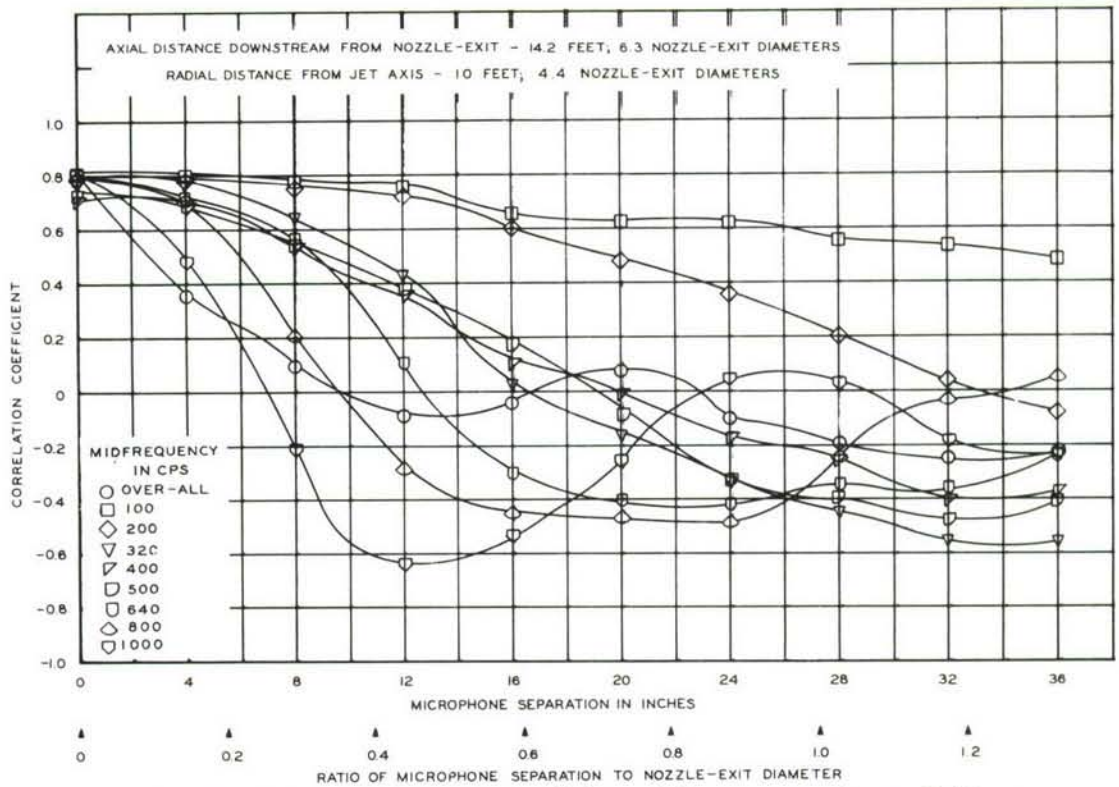

Figure II-34e. Longitudinal Sound Pressure Correlation Rigid Panel - Afterburner - Survey Line C - Upstream Site

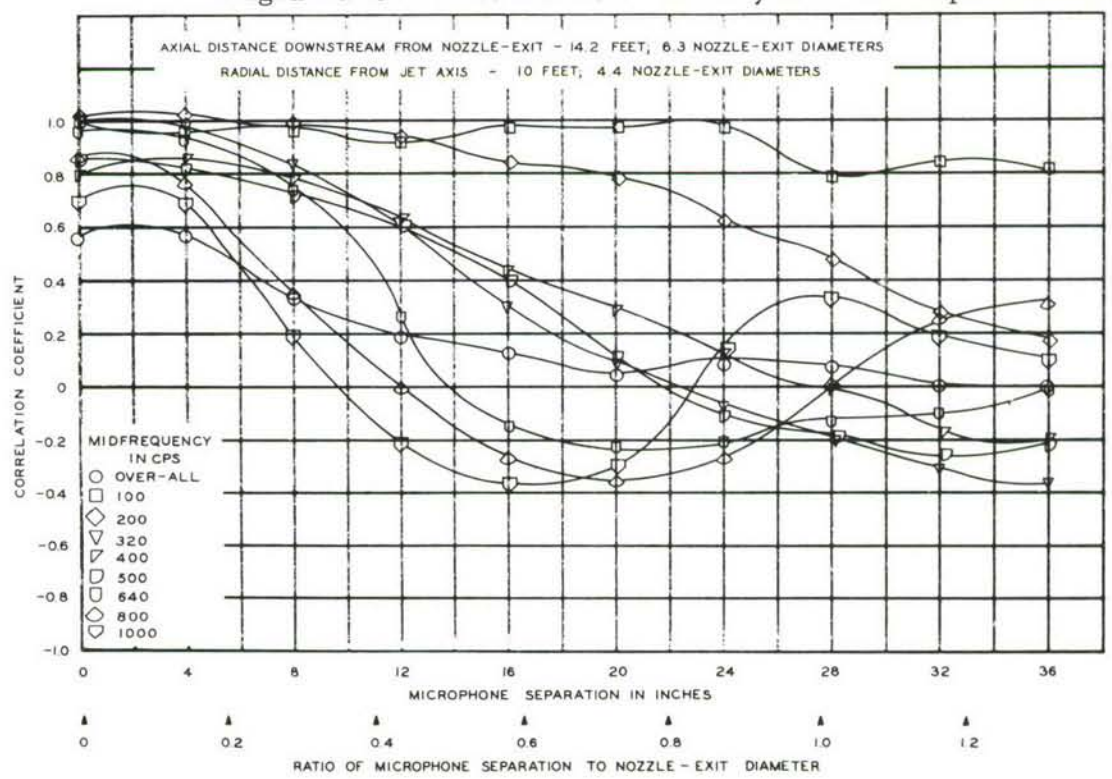

Figure II-34f. Longitudinal Sound Pressure Correlation Rigid Panel - Afterburner - Survey Line D - Upstream Site

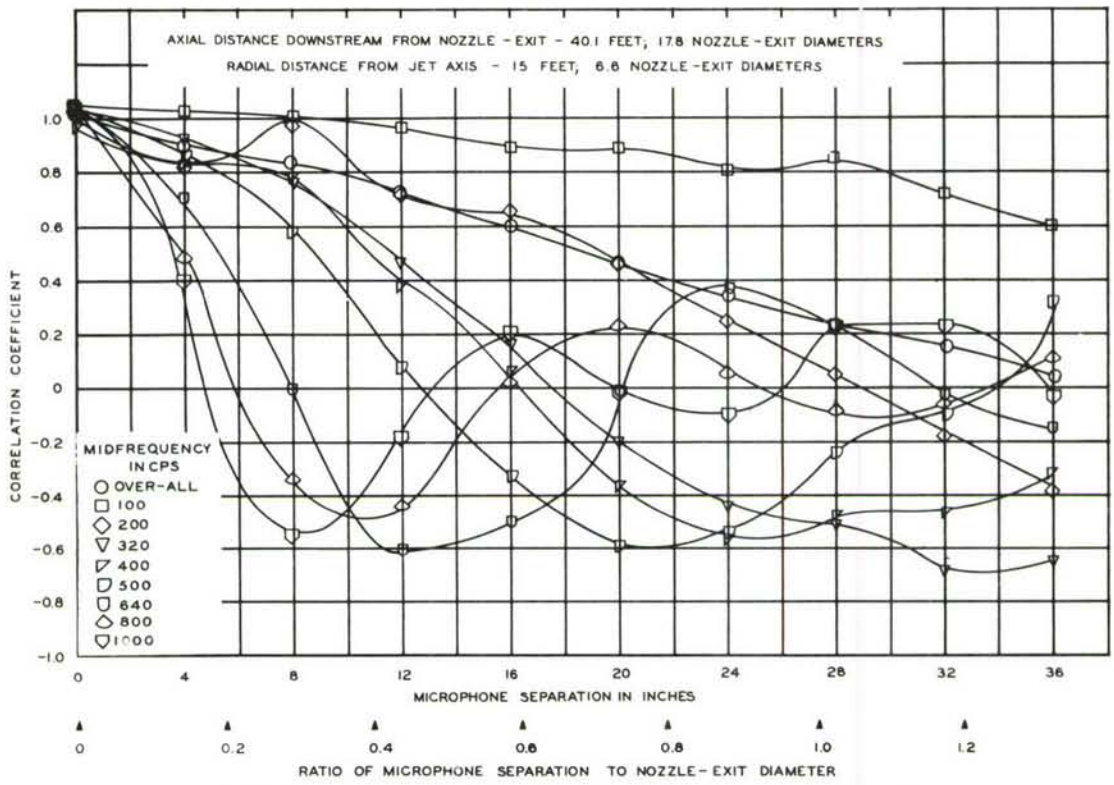

Figure II-34g. Longitudinal Sound Pressure Correlation
Rigid Panel - Afterburner - Survey Line C - Downstream Site

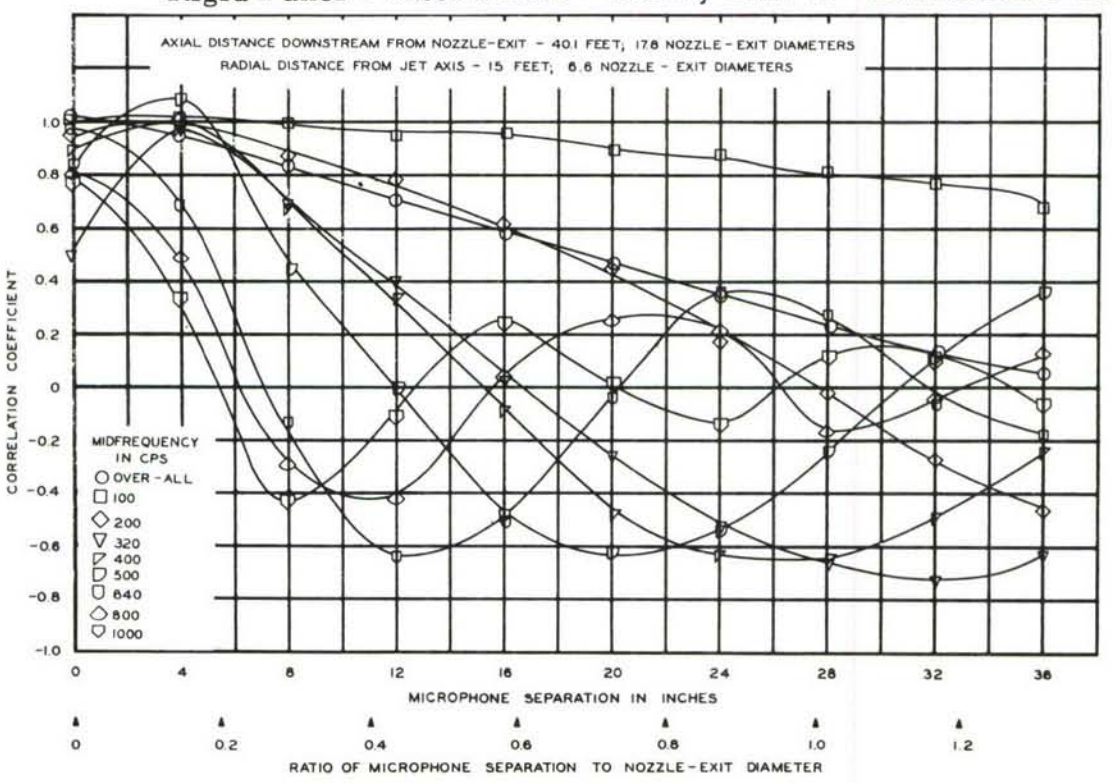

Figure II-34h. Longitudinal Sound Pressure Correlation
Rigid Panel - Afterburner - Survey Line D - Downstream Site

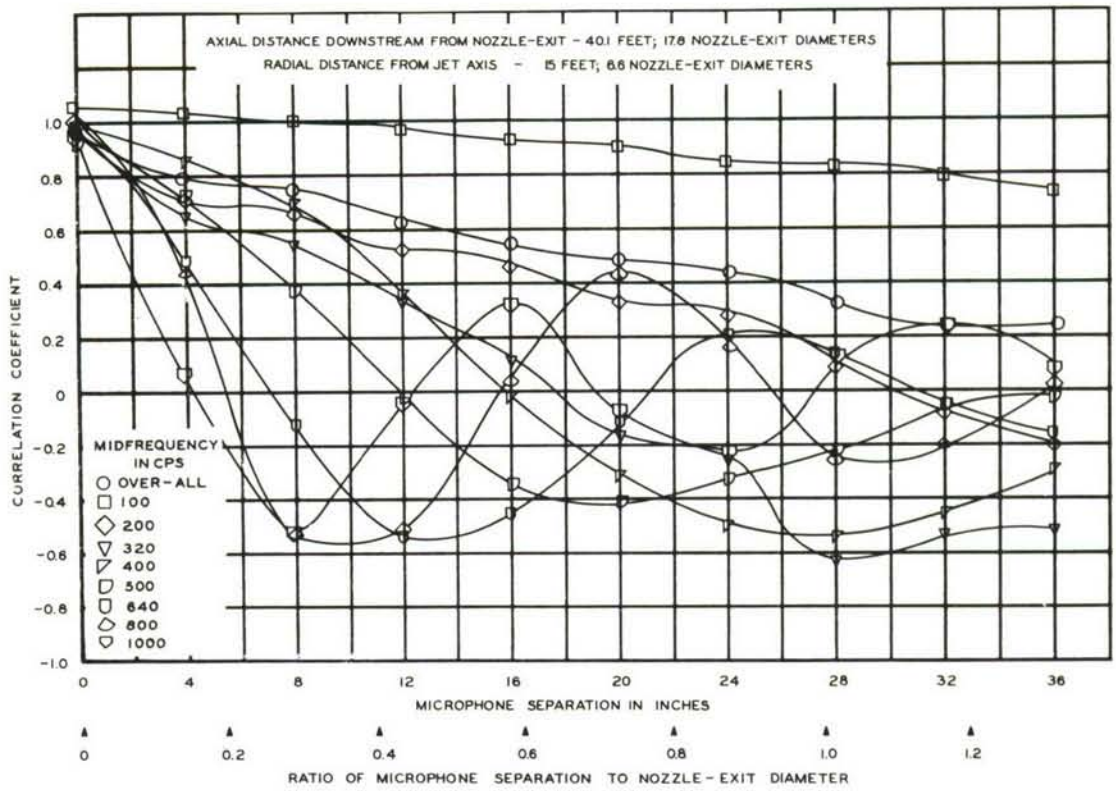

Figure II-35. Longitudinal Sound Pressure Correlation Curved Panel A - Afterburner - Survey Line C - Downstream Site

The correlation coefficients for both survey lines C and D are referred to panel boundary coordinates 3C; that is, each coefficient was computed using the signal from the microphone at position 3C. Figure II-35 shows the correlation coefficients for curved panel A along longitudinal survey line C at the downstream site for the afterburner condition only. Initial zero crossing of the correlation curves as a function of frequency is shown in Figure II-36. Comparison of correlation curves for various test conditions and selected frequencies are displayed in Figures II-37 and II-38. Figure II-37 compares correlations for three 1/3 octave filter bands with center frequencies, 100, 320 and 1000 cps by boundary condition for each site and engine condition. The first four parts of this figure compare correlations for the free field, flat panel A and the rigid panel. Part Five displays correlation for the flat and curved A type panels. Figure II-38 compares correlations for the two survey lines C and D, each for two frequencies, again by boundary and engine conditions.

In Figures II-32a and II-32e no data is available beyond 24 inches from the reference position due to malfunction of an amplifier in one data channel. Figures II-32c, e, and g lack correlation values for the reference position by virtue of a computer programming error, but this value may be assumed unity since this value would obtain for the reference microphone correlated with itself.

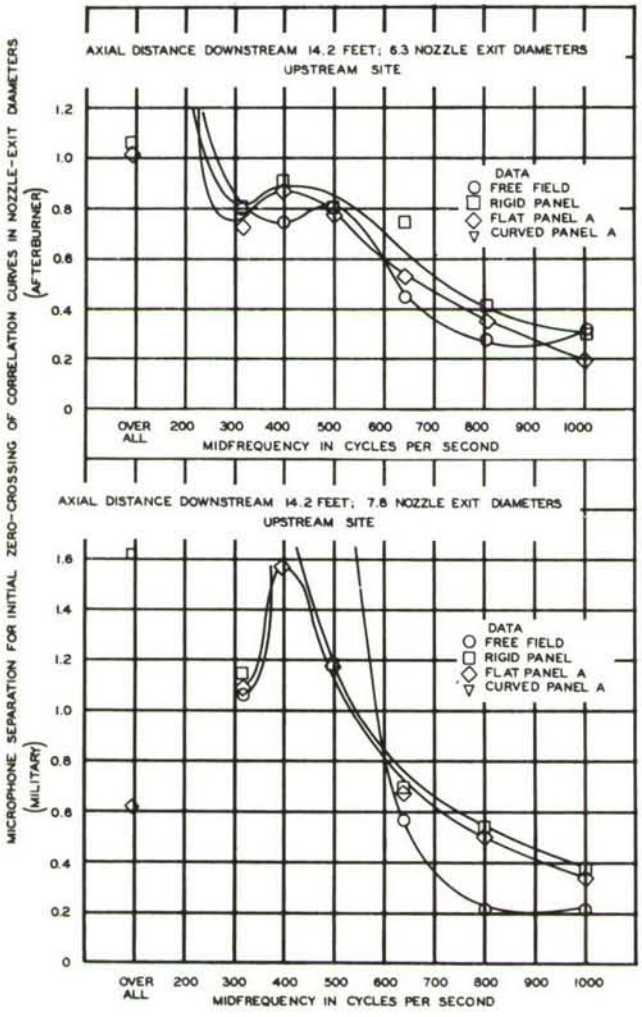

Figure II-36a. Initial Zero Crossing of Correlation Curves Survey Line C

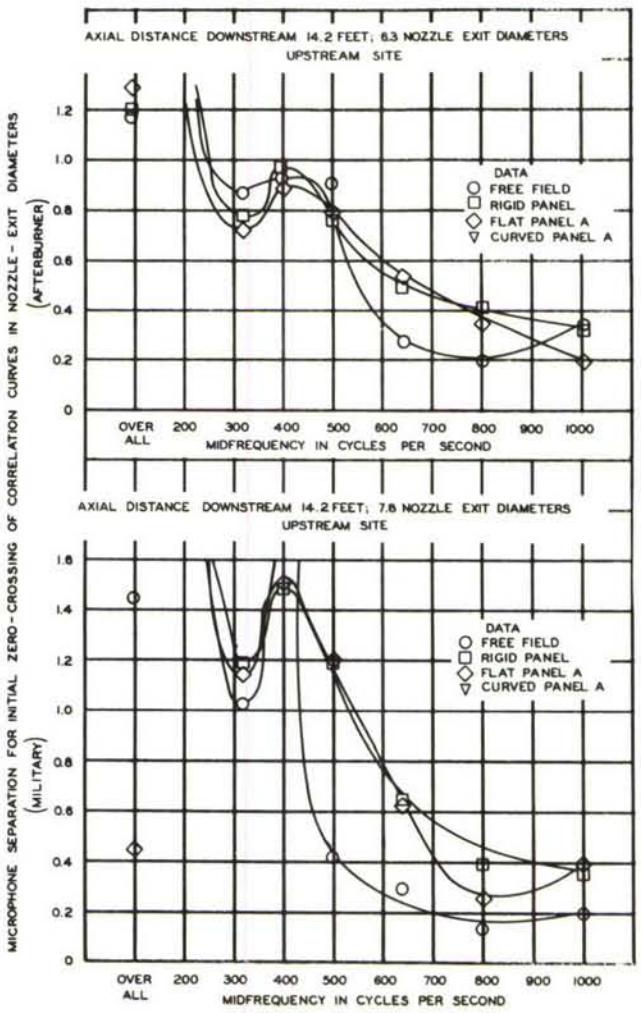

Figure II-36b. Initial Zero Crossing of Correlation Curves Survey Line D

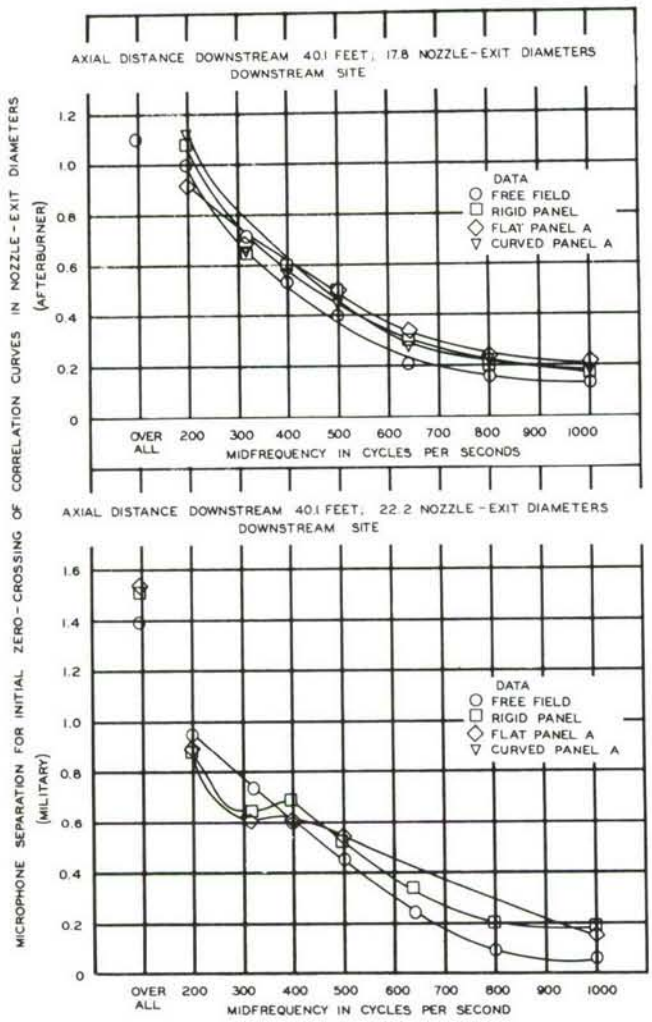

Figure II-36c. Initial Zero Crossing of Correlation Curves Survey Line C

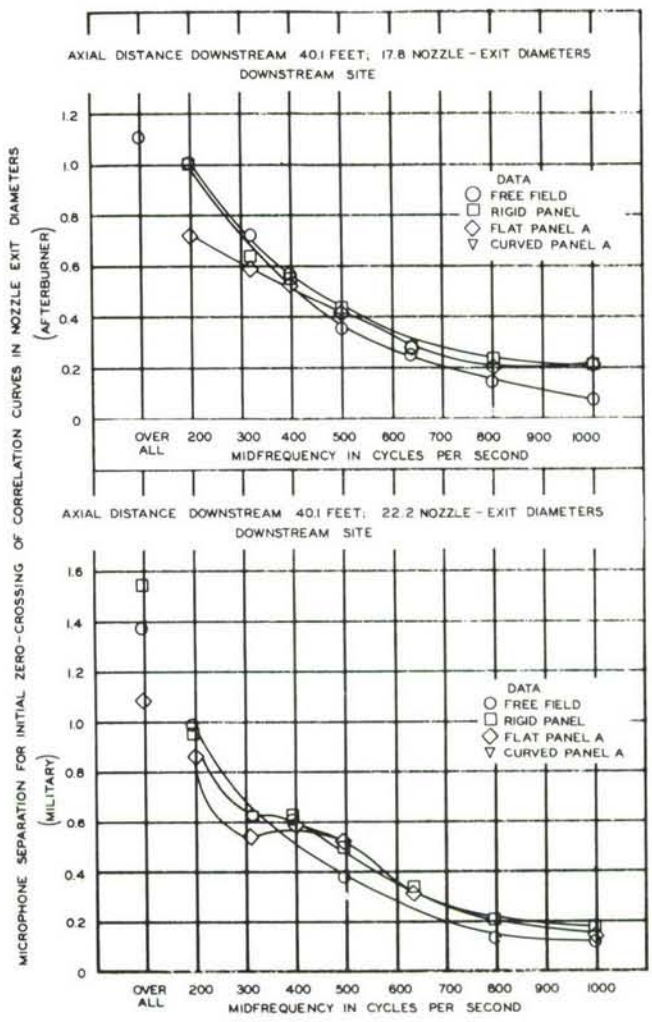

Figure II-36d. Initial Zero Crossing of Correlation Curves Survey Line D

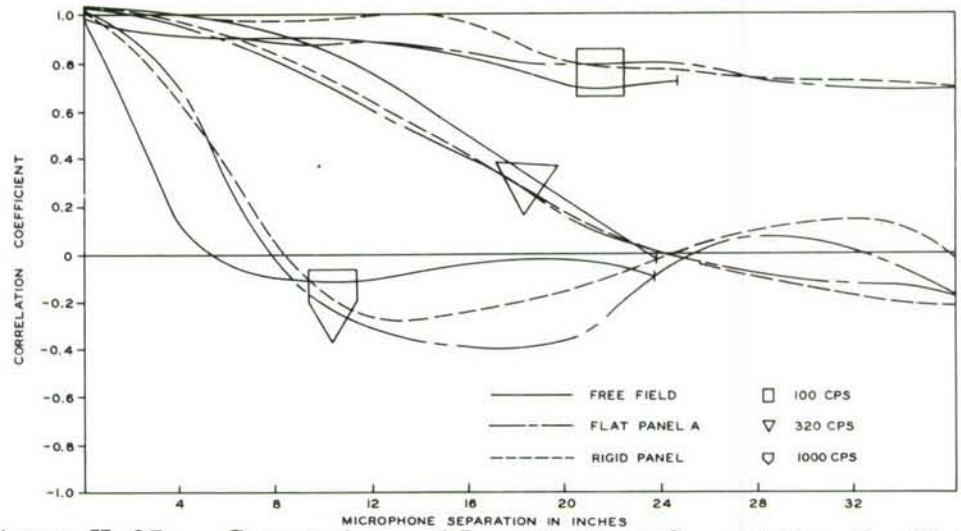

Figure II-37a. Comparison of Longitudinal Correlation Coefficients Survey Line C - Military - Upstream Site

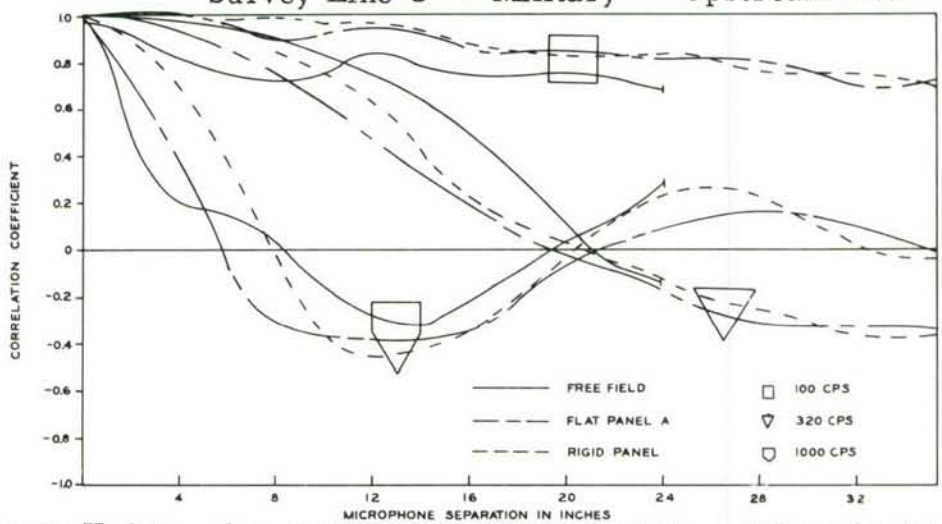

Figure II-37b. Comparison of Longitudinal Correlation Coefficients Survey Line C - Afterburner - Upstream Site

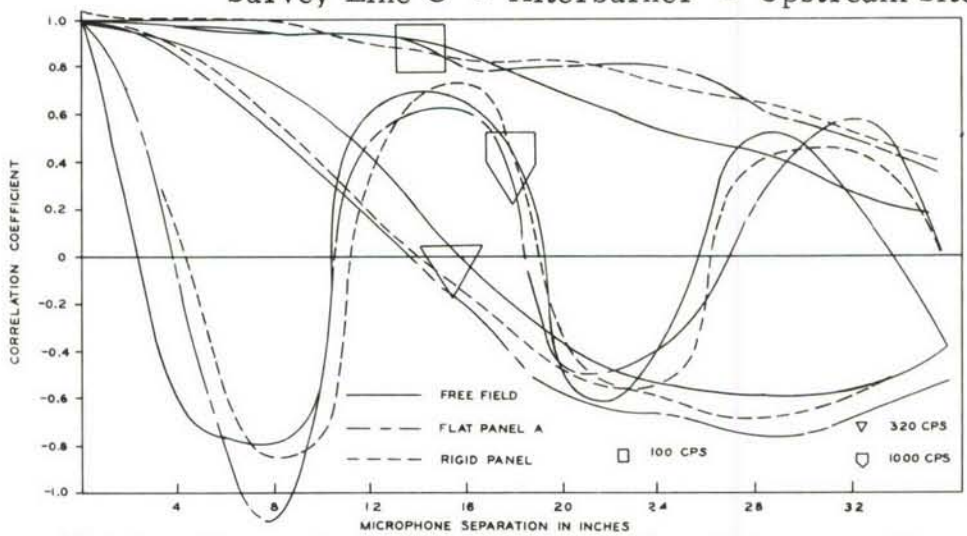

Figure II-37c. Comparison of Longitudinal Sound Pressure Correlations Survey Line C - Military - Downstream Site

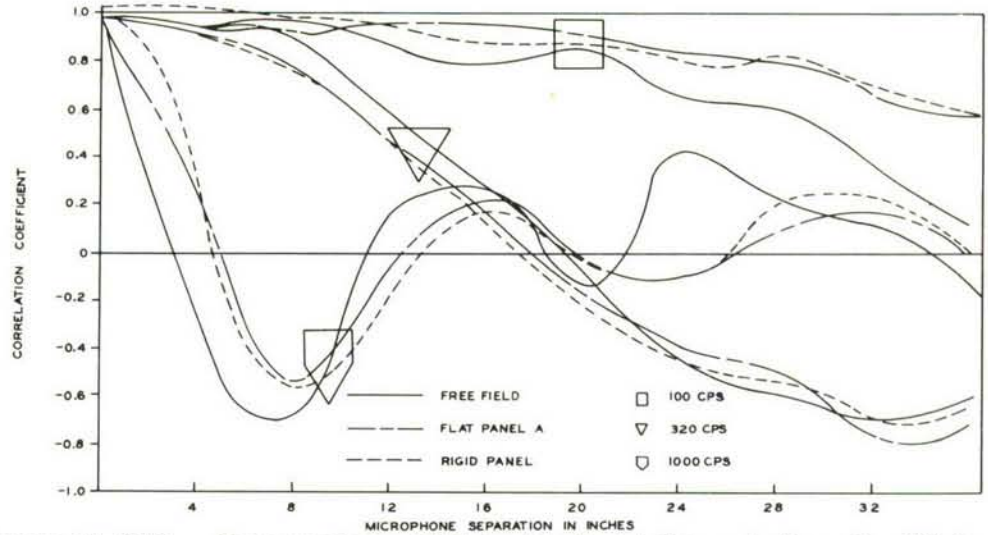

Figure II-37d. Comparison of Longitudinal Correlation Coefficients Survey Line C - Afterburner - Downstream Site

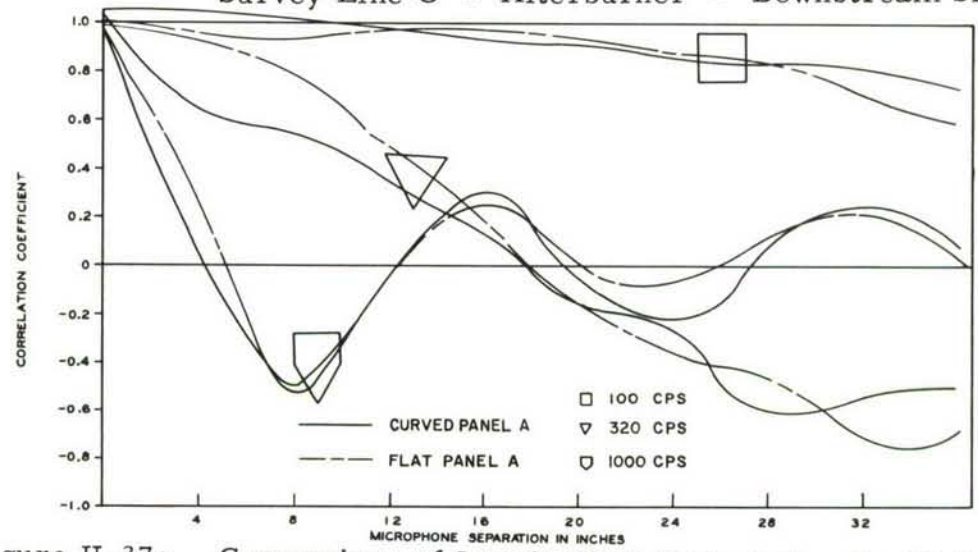

Figure II-37e. Comparison of Longitudinal Correlation Coefficients Survey Line C - Afterburner - Downstream Site

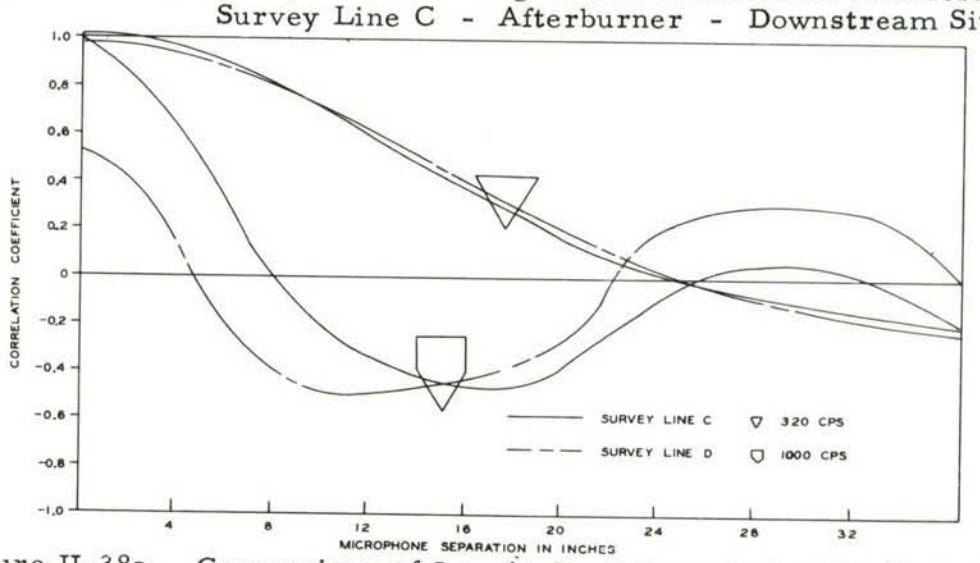

Figure II-38a. Comparison of Longitudinal Correlation Coefficients Flat Panel A - Military - Upstream Site

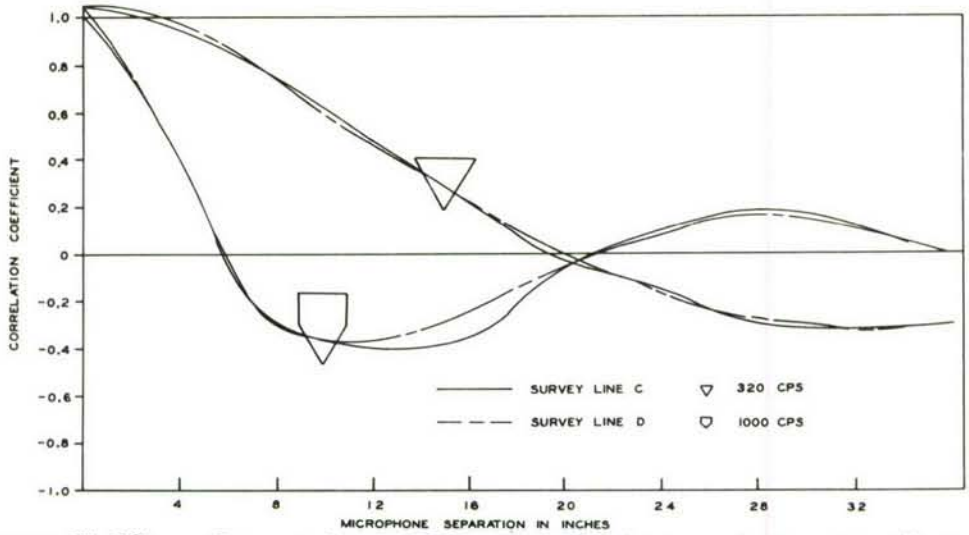

Figure II-38b. Comparison of Longitudinal Correlation Coefficients Flat Panel A - Afterburner - Upstream Site

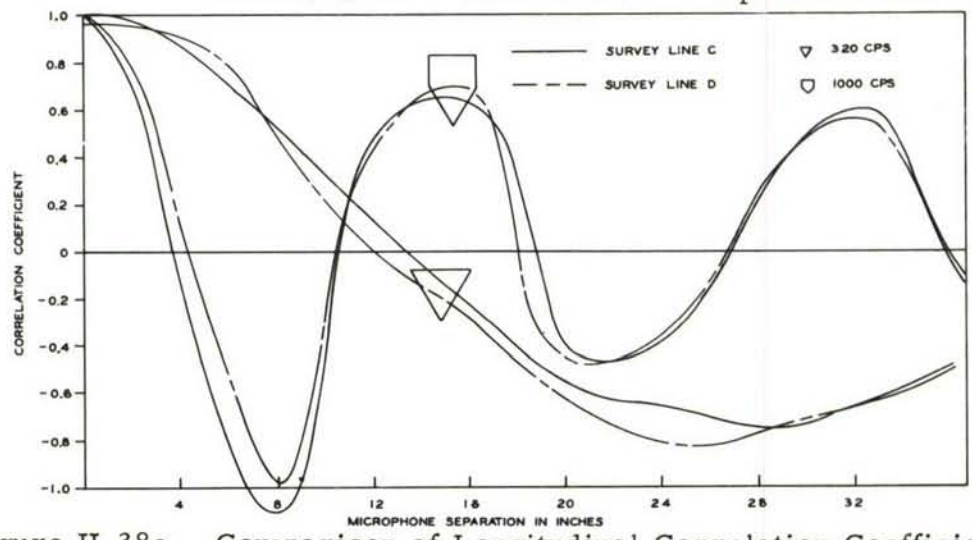

Figure II-38c. Comparison of Longitudinal Correlation Coefficients Flat Panel A - Military - Downstream Site

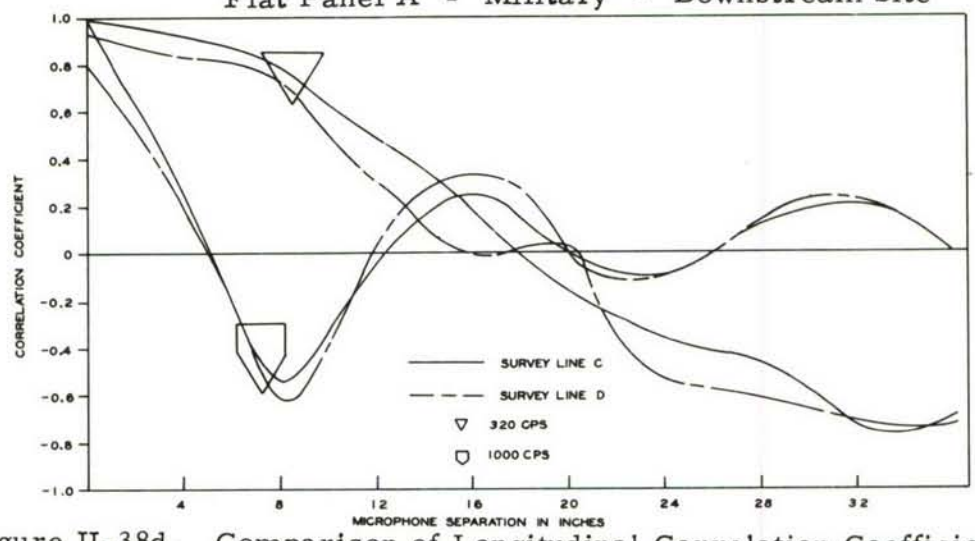

Figure II-38d. Comparison of Longitudinal Correlation Coefficients Flat Panel A - Afterburner - Downstream Site

b. Sound Pressure Spectra

Narrow band (10 cps) sound pressure spectra for three boundary conditions, i.e., free field at the panel site, flat panel A and rigid panel, are shown in Figures II-39, II-40 and II-41, pages 66 through 71, respectively. The ordinate of these curves gives spectrum level in decibels (i.e., corrected to 1 cps bandwidth re: 0.0002 dynes/cm^2). Four curves are given for each figure, two for each boundary site: upstream and downstream; two for engine conditions: military and

TABLE II-8a

SPATIAL AVERAGE OF SOUND SPECTRUM PRESSURE LEVELS IN DECIBELS (re: 0.0002 dynes/cm^2) FOR THREE SOUND FIELD BOUNDARIES AND TWO ENGINE CONDITIONS
UPSTREAM SITE
Axial Distance Downstream from Nozzle-Exit - 14.2 Feet
Radical Distance from Jet Axis - 10 Feet

1/3 Octave-Band Center Frequency	Free Field		Flat Panel A		Rigid Panel	
	Military	Afterburner	Military	Afterburner	Military	Afterburner
Overall	138	146	141	147	141	148
40	96	105	99	107	98	106
50	98	106	101	109	100	108
64	97	106	100	105	100	109
80	106	106	102	112	102	116
100	110	104	104	114	104	113
125	98	107	105	113	104	112
160	100	109	106	114	105	114
200	101	115	109	118	110	118
250	108	118	110	118	112	114
320	108	117	110	117	110	118
400	104	112	107	114	108	114
500	101	111	106	114	107	114
640	101	110	106	113	107	115
800	104	112	113	113	105	116
1000	103	112	102	108	106	113

TABLE II-8b

COMPARISON OF SOUND SPECTRUM PRESSURE LEVELS IN DECIBELS (re: 0.0002 dynes/cm^2) FOR VARIOUS FIELD BOUNDARY CONDITIONS
UPSTREAM SITE
Axial Distance Downstream from Nozzle-Exit - 14.2 Feet
Radical Distance from Jet Axis - 10 Feet

1/3 Octave-Band Center Frequency	Free Field/Flat Panel A		Free Field/Rigid Panel	
	Military	Afterburner	Military	Afterburner
Overall	3	1	3	2
40	3	2	2	1
50	3	3	2	2
64	3	1	3	3
80	4	6	4	10
100	6	10	6	9
125	7	6	6	5
160	6	5	5	5
200	8	3	9	3
250	2	0	4	4
320	2	0	2	1
400	3	2	4	2
500	5	3	6	3
640	5	3	6	5
800	9	1	1	4
1000	1	4	3	1
Average of 1/3 Octave Bands	4.4	3.1	4.1	3.8

afterburner. To facilitate comparisons, these spectra have been redrawn in Figure II-42, pages 72 and 73, in groups of panel conditions by test site and engine condition. Spatial averages and comparisons of sound spectrum pressure levels, neglecting correlation for three boundary conditions and two engine conditions are tabulated in Table II-8 for the upstream boundary and in Table II-9 for the downstream boundary. The tables of comparison show the average sound level increase in decibels produced by the rigid panel and flat panel A above the sound level for the free field at the panel condition.

TABLE II-9a

SPATIAL AVERAGE OF SOUND SPECTRUM PRESSURE LEVELS IN DECIBELS (re: 0.0002 dynes/cm^2) FOR THREE SOUND FIELD BOUNDARIES AND TWO ENGINE CONDITIONS
DOWNSTREAM SITE
Axial Distance Downstream from Nozzle-Exit - 40.1 Feet
Radical Distance from Jet Axis - 15 Feet

1/3 Octave-Band Center Frequency	Free Field		Flat Panel A		Rigid Panel	
	Military	Afterburner	Military	Afterburner	Military	Afterburner
Overall	140	146	145	152	145	151
40	108	117	109	119	110	119
50	112	120	113	122	113	122
64	112	121	114	123	114	123
80	115	122	117	126	117	123
100	116	121	121	129	121	128
125	114	120	121	129	122	129
160	114	121	121	128	121	128
200	114	122	119	128	117	126
250	111	120	115	124	115	123
320	110	120	112	123	112	122
400	108	115	110	119	111	118
500	108	111	110	116	111	115
640	106	106	109	113	110	112
800	105	104	112	111	110	110
1000	99	100	106	107	105	106

TABLE II-9b

COMPARISON OF SOUND SPECTRUM PRESSURE LEVELS IN DECIBELS (re: 0.0002 dynes/cm^2) FOR VARIOUS FIELD BOUNDARY CONDITIONS
DOWNSTREAM SITE
Axial Distance Downstream from Nozzle-Exit - 40.1 Feet
Radical Distance from Jet Axis - 15 Feet

1/3 Octave-Band Center Frequency	Free Field/Flat Panel A		Free Field/Rigid Panel	
	Military	Afterburner	Military	Afterburner
Overall	5	6	5	5
40	1	2	2	2
50	1	2	1	2
64	2	2	2	2
80	2	4	2	1
100	5	8	5	7
125	7	9	8	9
160	7	7	7	7
200	5	6	3	4
250	4	4	4	3
320	2	3	2	2
400	2	4	3	3
500	2	5	3	4
640	3	7	4	6
800	7	7	5	6
1000	7	7	6	6
Average of 1/3 Octave Bands	3.9	5.2	3.9	4.3

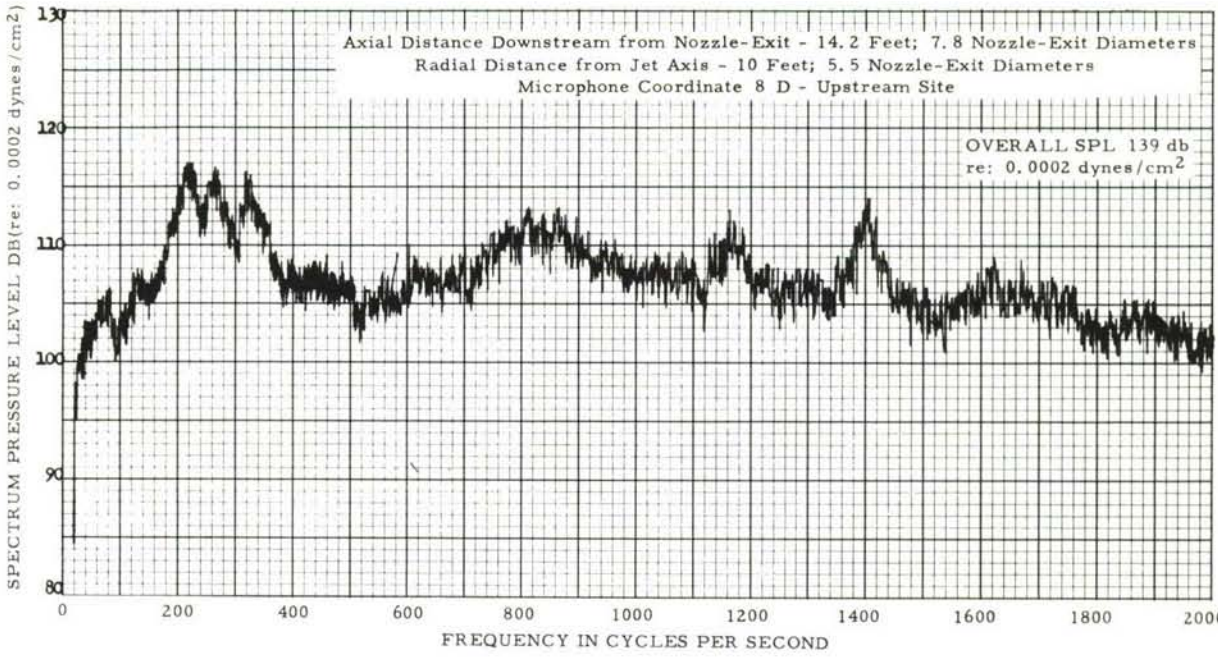

Figure II-39a. Narrow Band (10 cps) Analysis of Sound Pressure Levels Free Field - Military

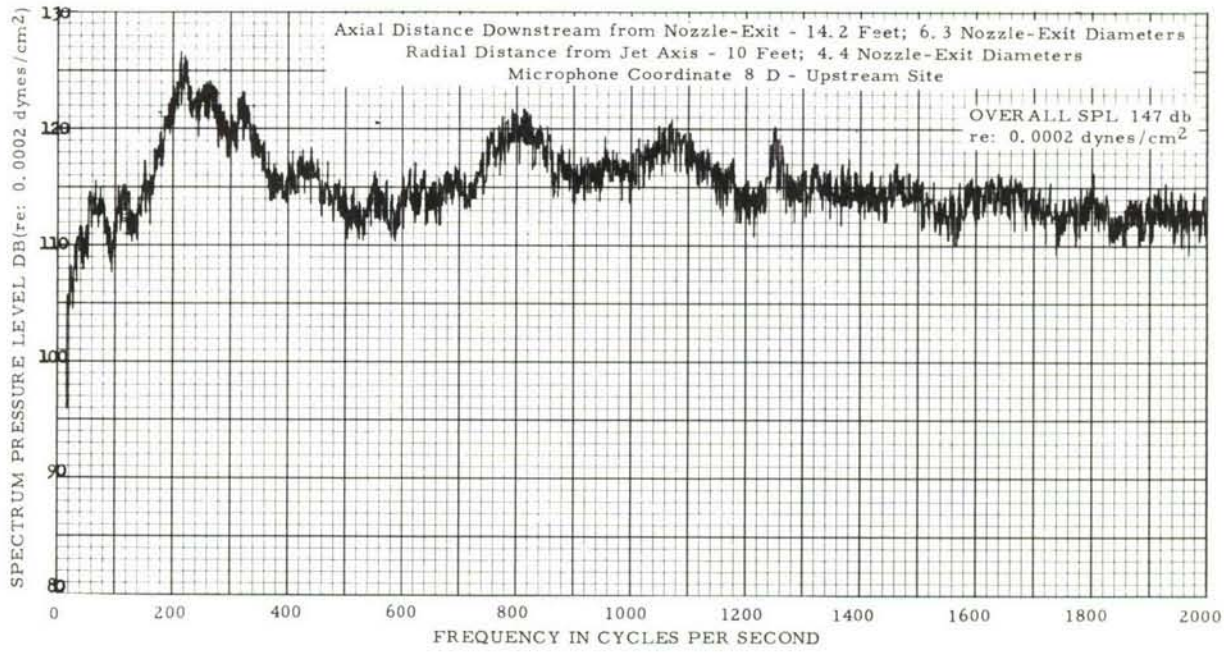

Figure II-39b. Narrow Band (10 cps) Analysis of Sound Pressure Levels Free Field - Afterburner

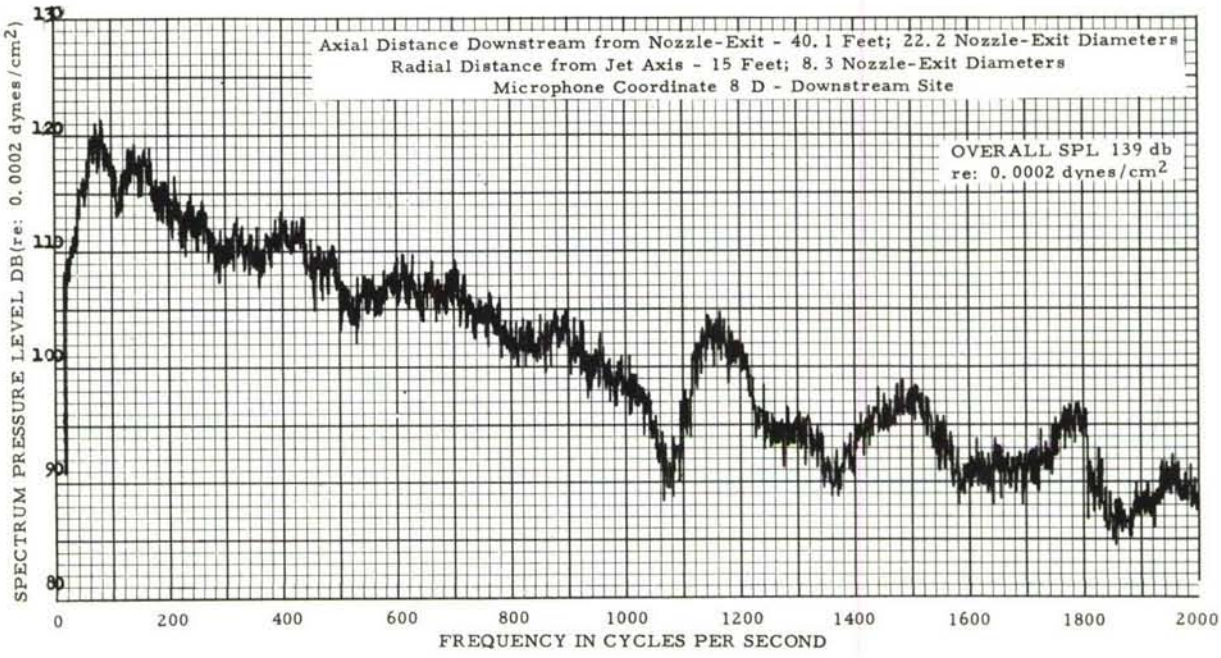

Figure II-39c. Narrow Band (10 cps) Analysis of Sound Pressure Levels
Free Field - Military

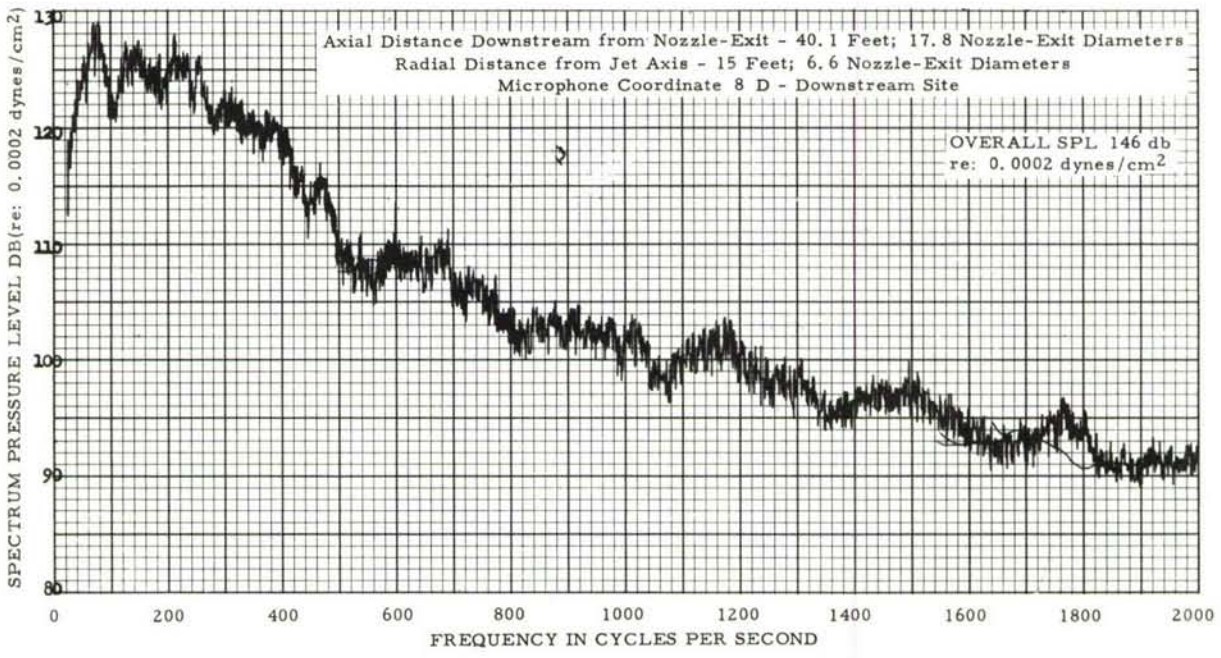

Figure II-39d. Narrow Band (10 cps) Analysis of Sound Pressure Levels
Free Field - Afterburner

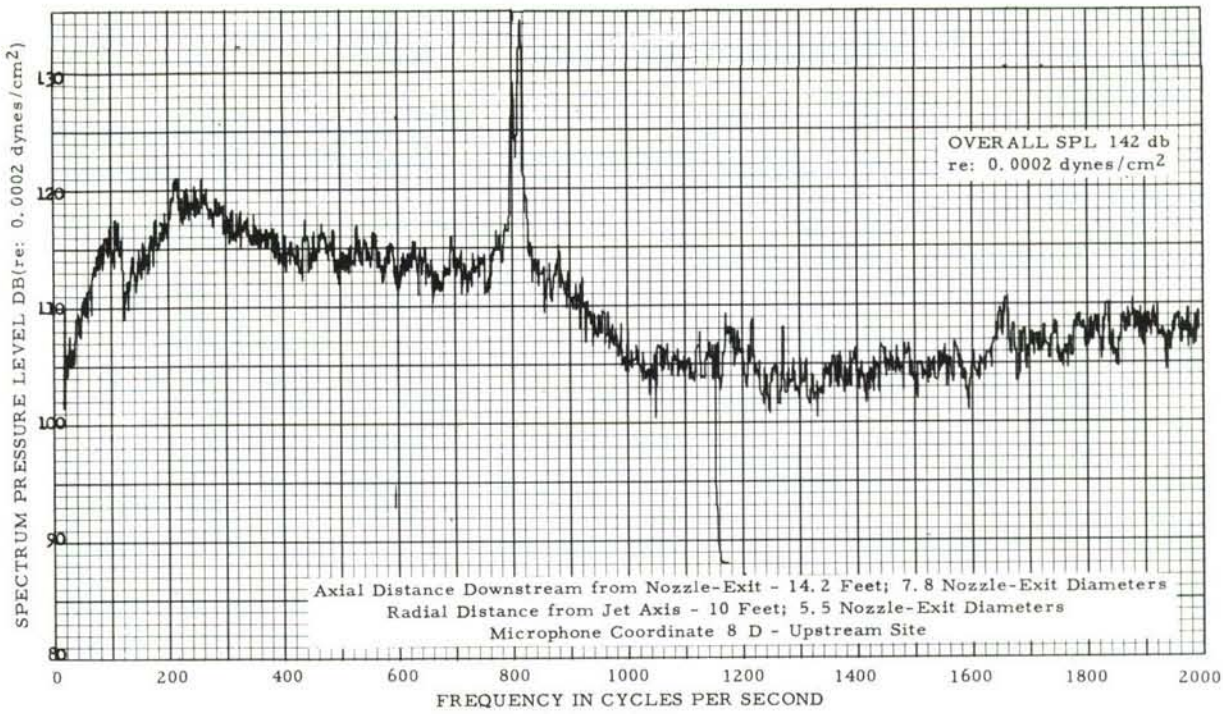

Figure II-40a. Narrow Band (10 cps) Analysis of Sound Pressure Levels
Flat Panel A - Military

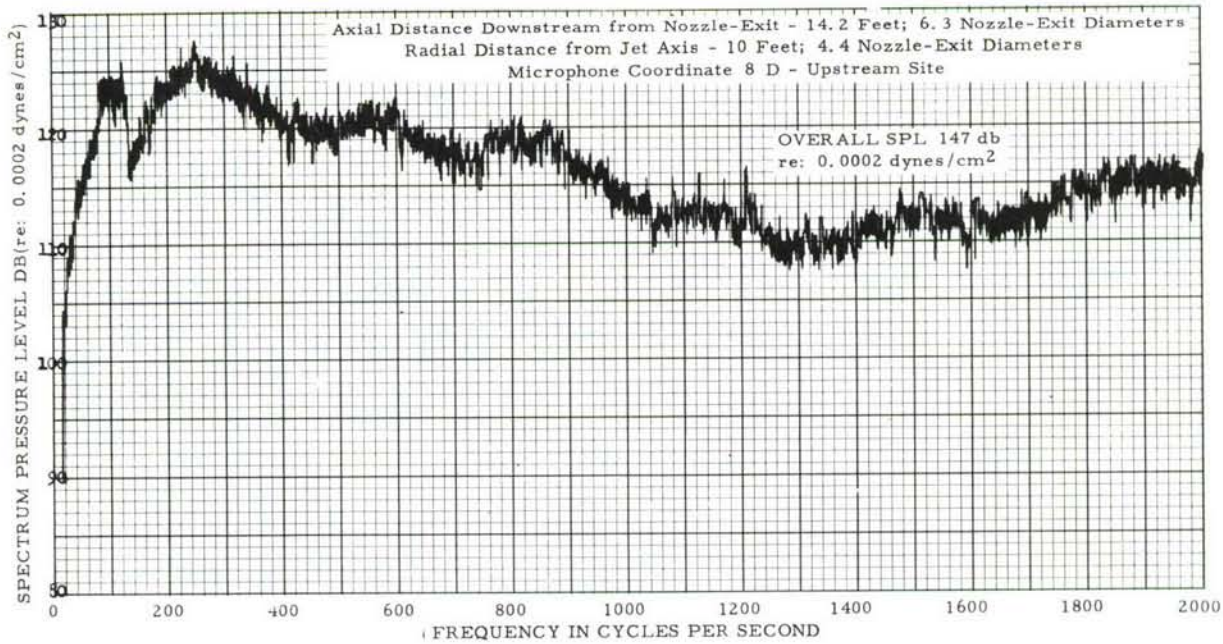

Figure II-40b. Narrow Band (10 cps) Analysis of Sound Pressure Levels
Flat Panel A - Afterburner

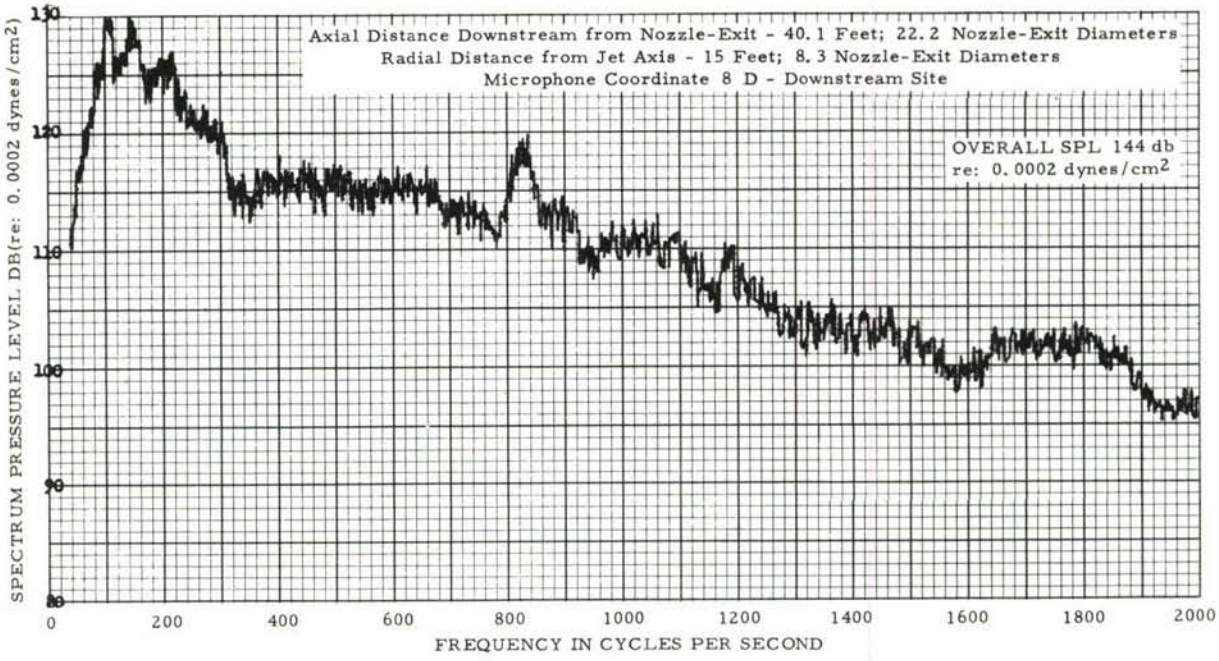

Figure II-40c. Narrow Band (10 cps) Analysis of Sound Pressure Levels
Flat Panel A - Military

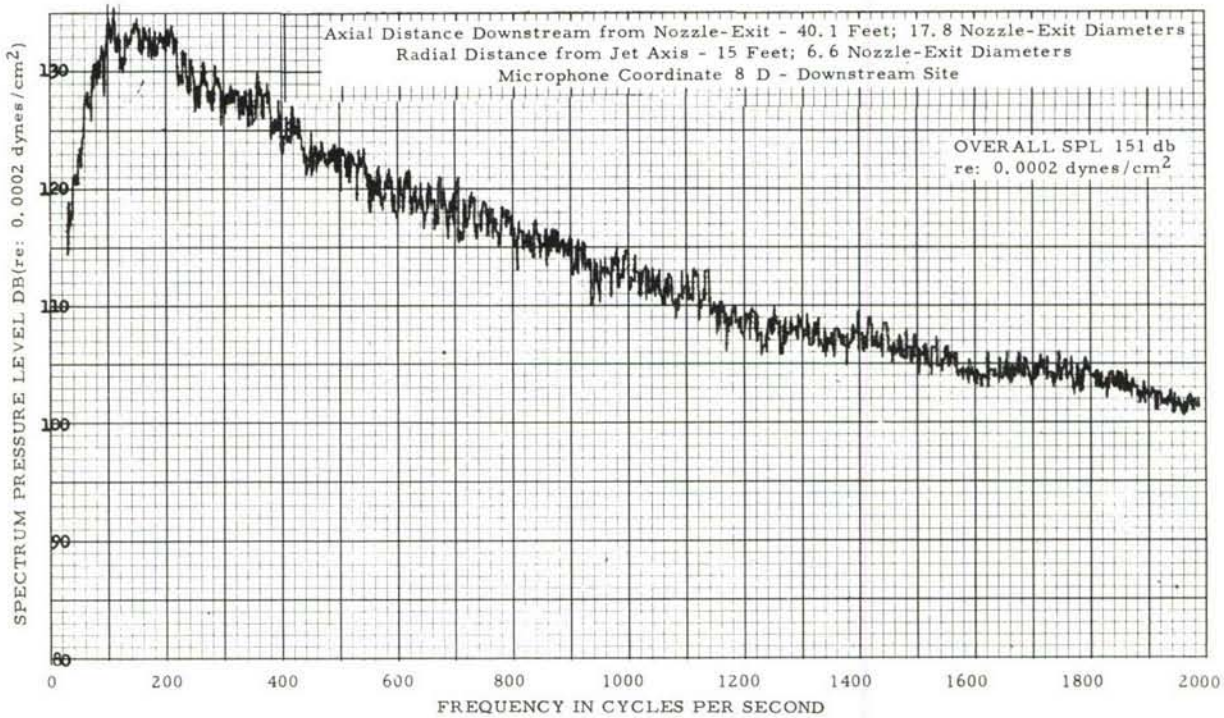

Figure II-40d. Narrow Band (10 cps) Analysis of Sound Pressure Levels
Flat Panel A - Afterburner

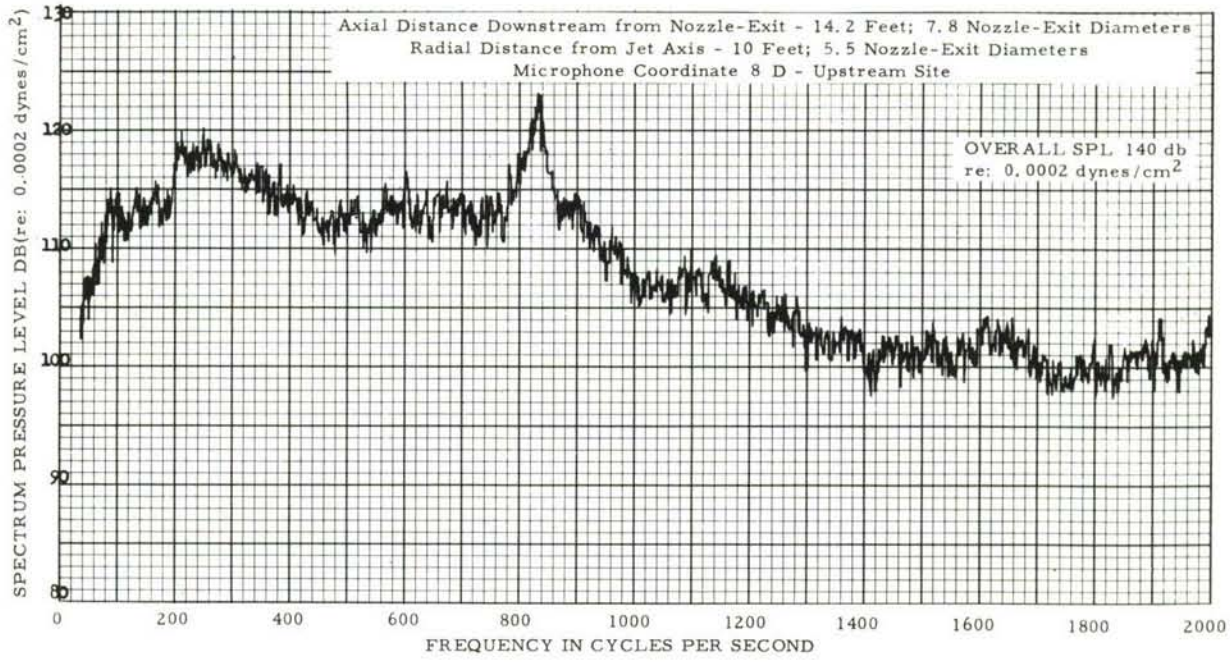

Figure II-41a. Narrow Band (10 cps) Analysis of Sound Pressure Levels Rigid Panel - Military

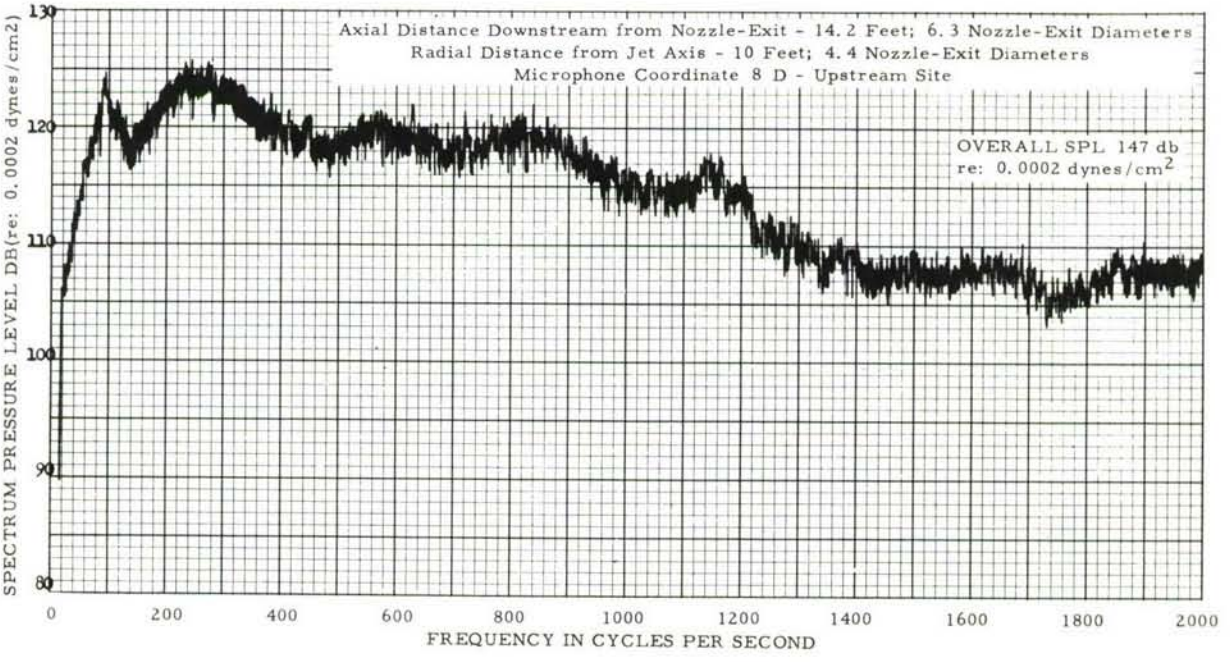

Figure II-41b. Narrow Band (10 cps) Analysis of Sound Pressure Levels Rigid Panel - Afterburner

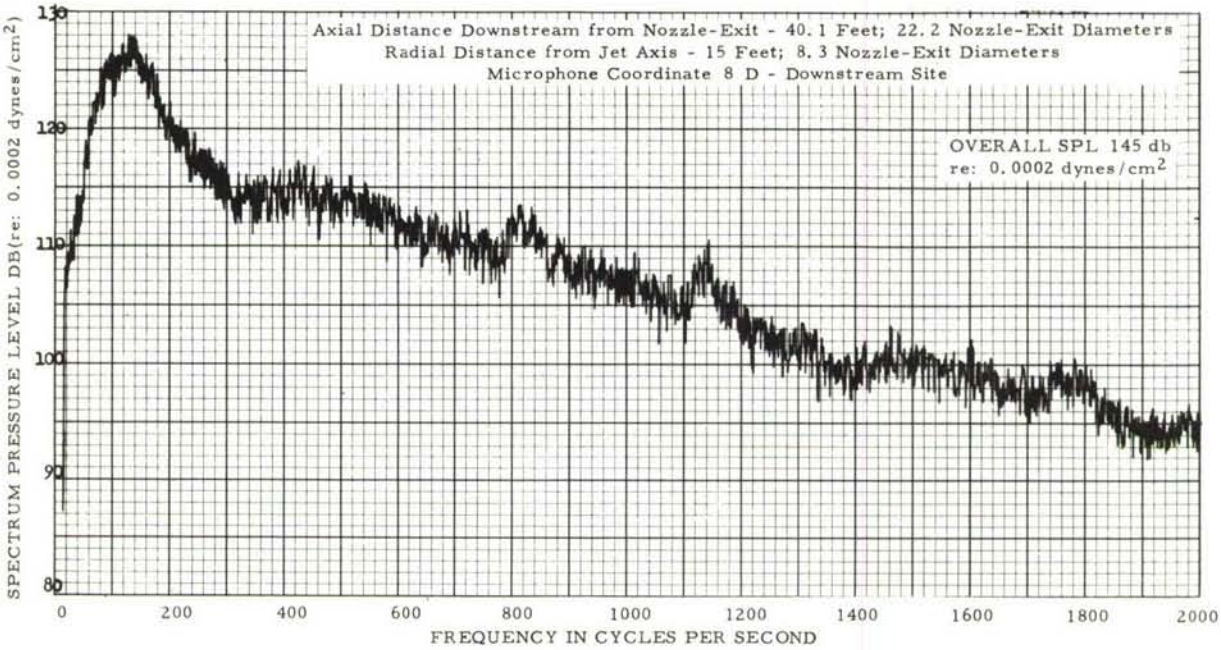

Figure II-41c. Narrow Band (10 cps) Analysis of Sound Pressure Levels
Rigid Panel - Military

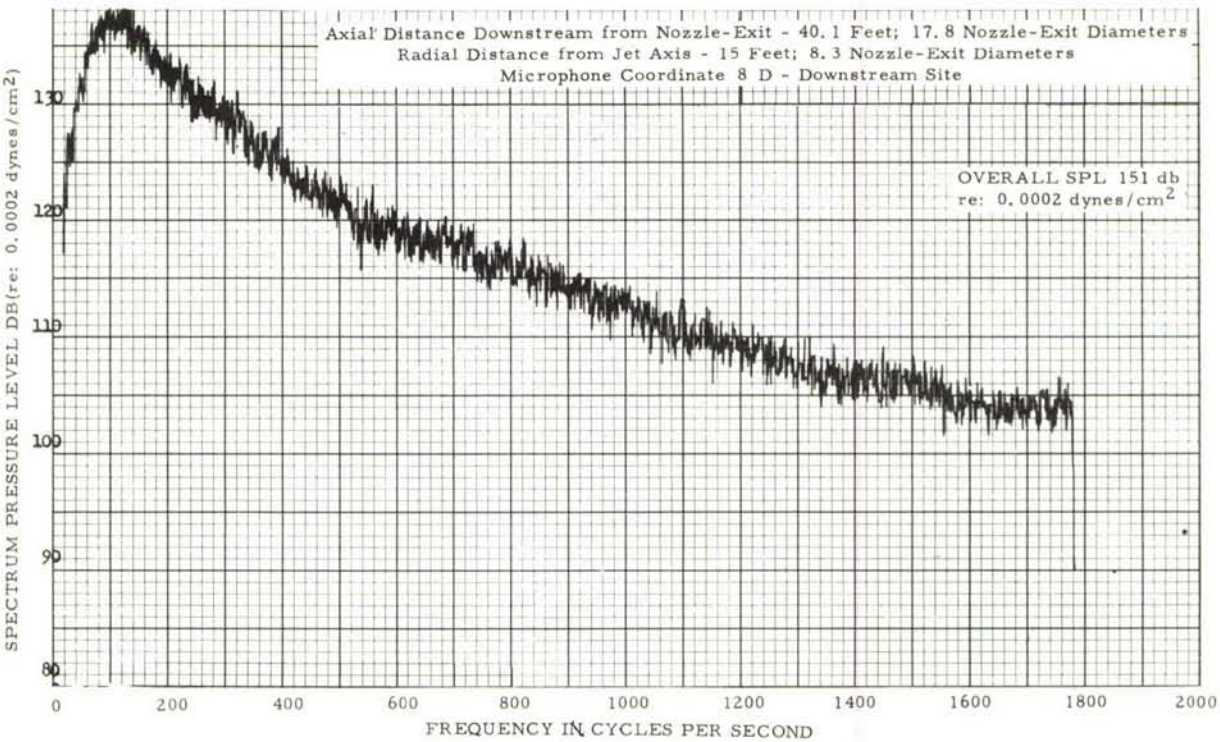

Figure II-41d. Narrow Band (10 cps) Analysis of Sound Pressure Levels
Rigid Panel - Afterburner

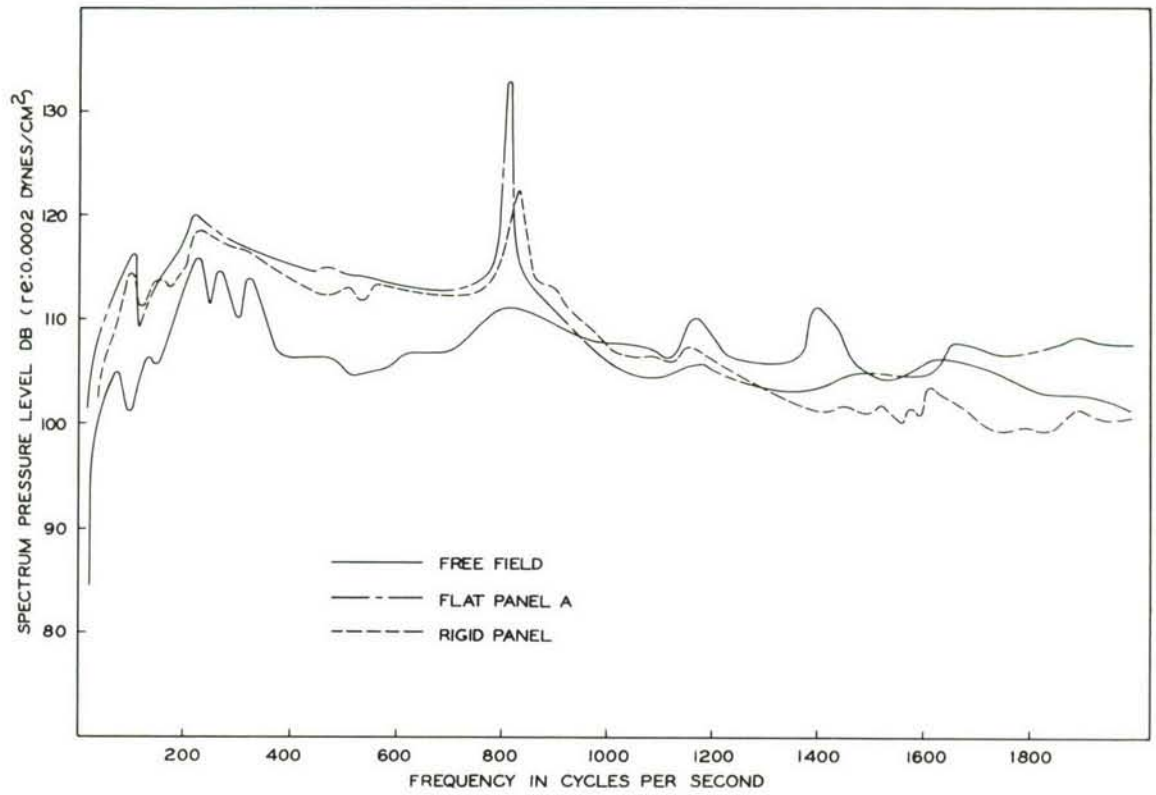

Figure II-42a. Comparison of Sound Pressure Spectra
Upstream Site - Military

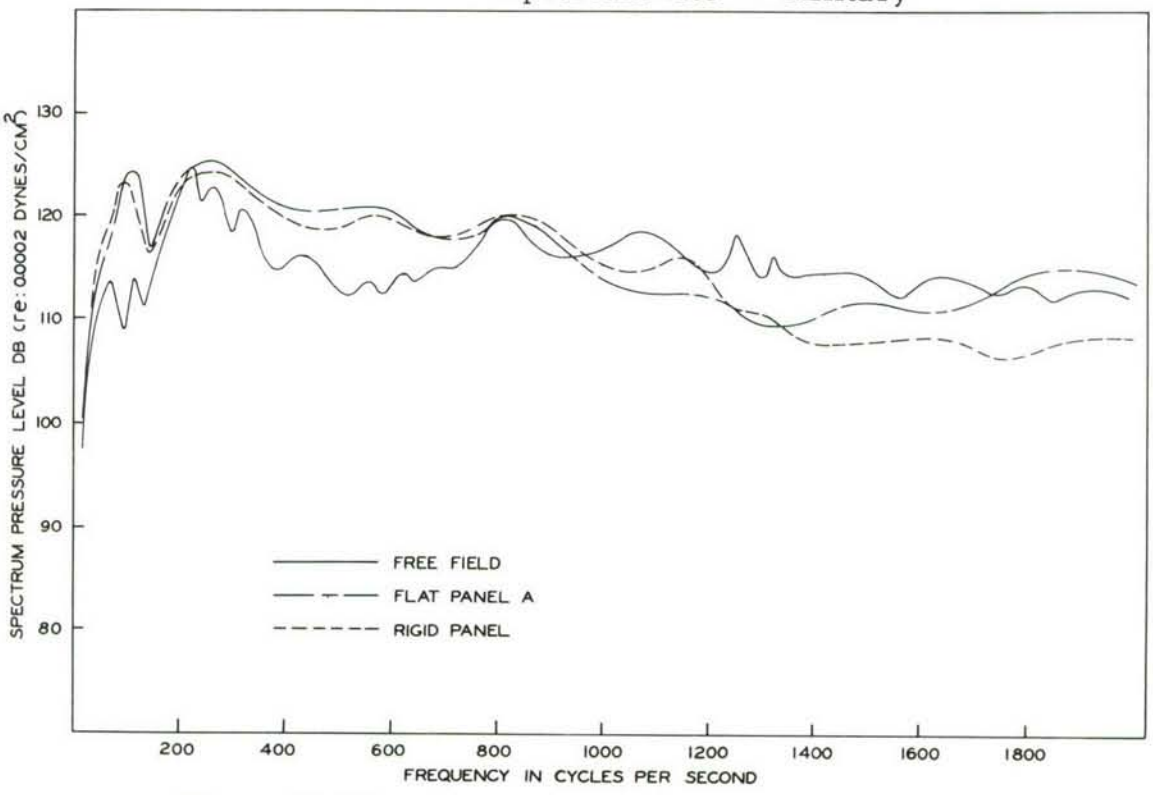

Figure II-42b. Comparison of Sound Pressure Spectra
Upstream Site - Afterburner

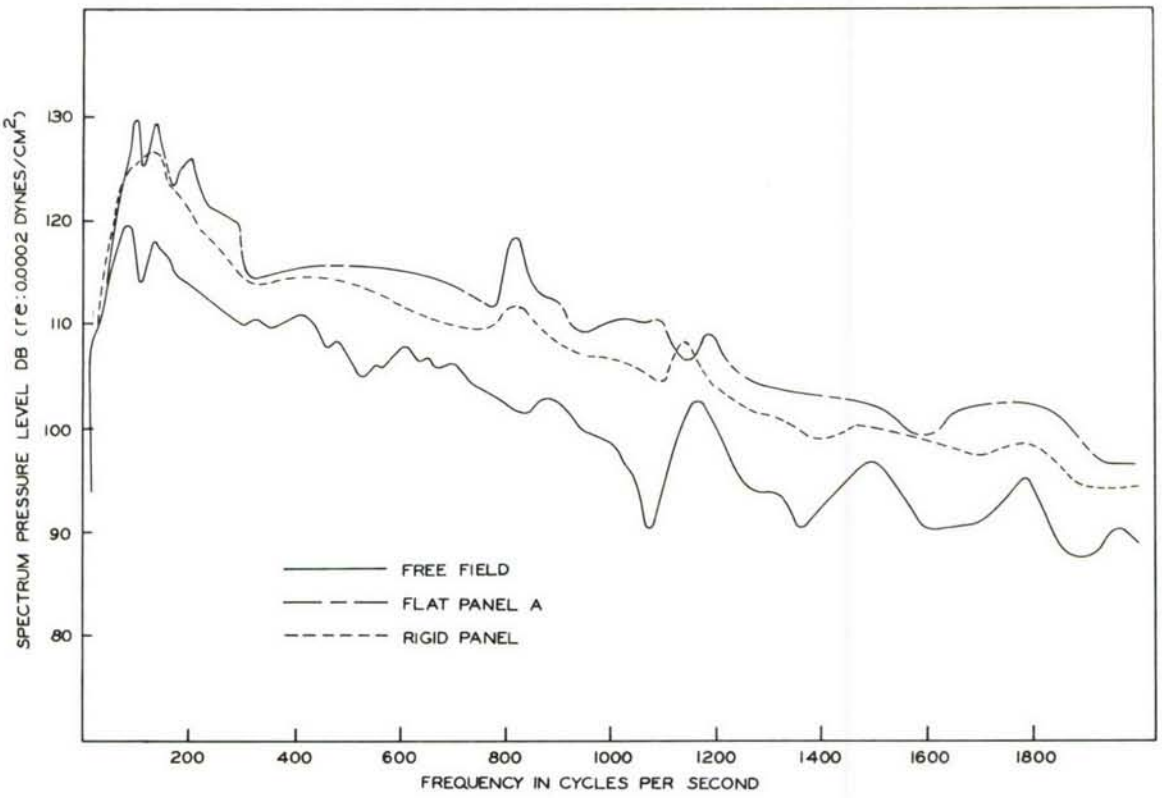

Figure II-42c. Comparison of Sound Pressure Spectra
Downstream Site - Military

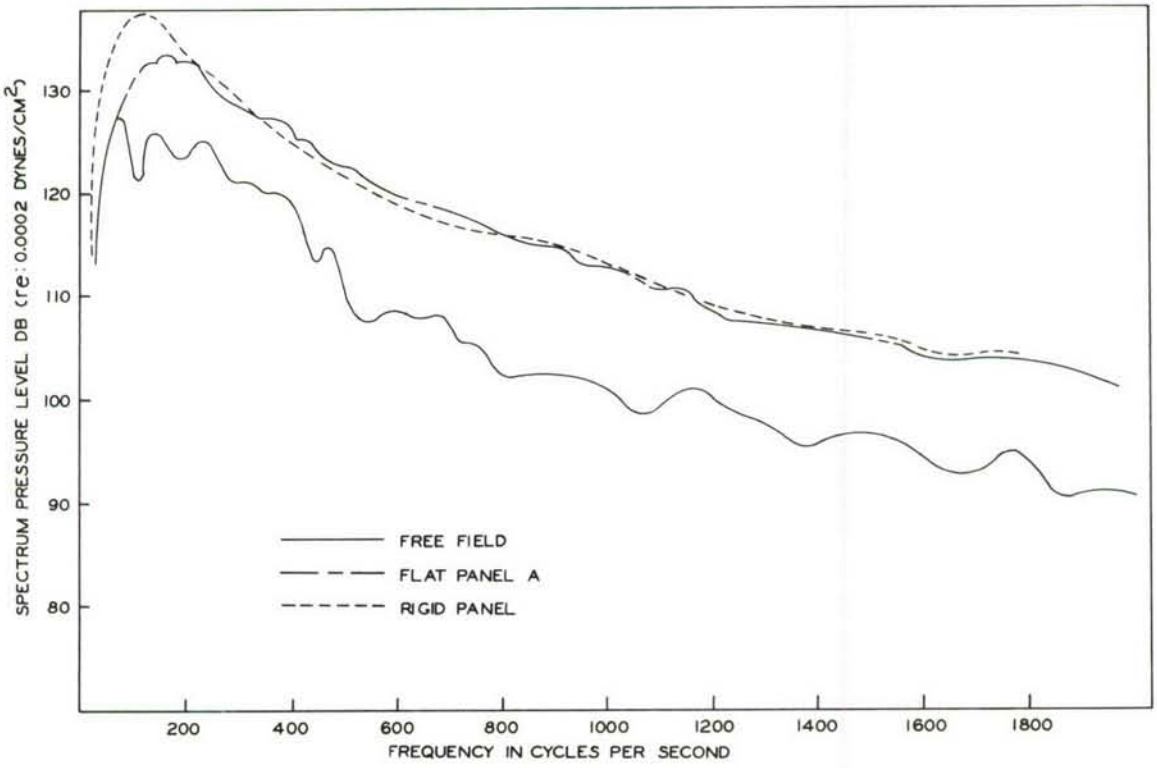

Figure II-42d. Comparison of Sound Pressure Spectra
Downstream Site - Afterburner

c. Probability Distribution of Pressure Amplitude

Probability distributions of pressure amplitudes for free field at the panel, flat panel A, and rigid panel are shown in Figures II-43, II-44 and II-45, pages 75 through 77, respectively. The distributions are for three octave bands and the overall signal for two-engine conditions and two boundary sites. An analysis of these distributions is given in Table II-7, page 42.

3. Miscellaneous Results

Table II-10 gives the range of overall sound pressure levels obtained at the free field monitor microphone during each test series. The range as used here is the difference between the maximum and minimum levels observed.

Maximum observed jet wake probe temperature in degrees F by record number, engine condition and probe position are given in Table II-11.

TABLE II-10

RANGE OF OVERALL SOUND PRESSURE LEVELS AT THE FREE FIELD MONITOR MICROPHONE

Test	Range (Decibels)		
	RPM 100	Military	Afterburner
Free Field Survey	1	3	1
Rigid Panel			
Downstream	-	5	3
Upstream	-	2	2
Flat Panel A Correlation			
Downstream	-	2	0
Upstream	-	2	3
Flat Panel A Response	-	1	0
Free Field at the Panel			
Downstream	-	2	1
Upstream	-	3	2
Curved Panel A			
Downstream	1	-	0
Flat Panel B	3	-	0
Flat Panel D	-	0	0
Flat Panel E	-	0	0
Curved Panel B	-	0	0
Curved Panel D	0	-	0
(Mean Levels of All Tests)	2	4	4

TABLE II-11

JET WAKE PROBE MAXIMUM TEMPERATURES

Record Number	Engine Condition	Position (Feet)	Maximum Temperature in Degrees F.
032559-1003	Military	80,0	93
1004	Afterburner		188
1005	Military	80,5	92
1006	Afterburner		162
1007	Military	80,10	85
1008	Afterburner		125
1009	Military	60,0	110
1010	Afterburner		250
1011	Military	60,5	---
1012	Afterburner		210
032559-2004	Military	60,10	80
2005	Afterburner		110
2006	Military	50,0	120
2007	Afterburner		250
2008	Military	50,5	96
2009	Afterburner		155
2010	Military	40,0	140
2011	Afterburner		300
2012	Military	40,5	80
2013	Afterburner		100

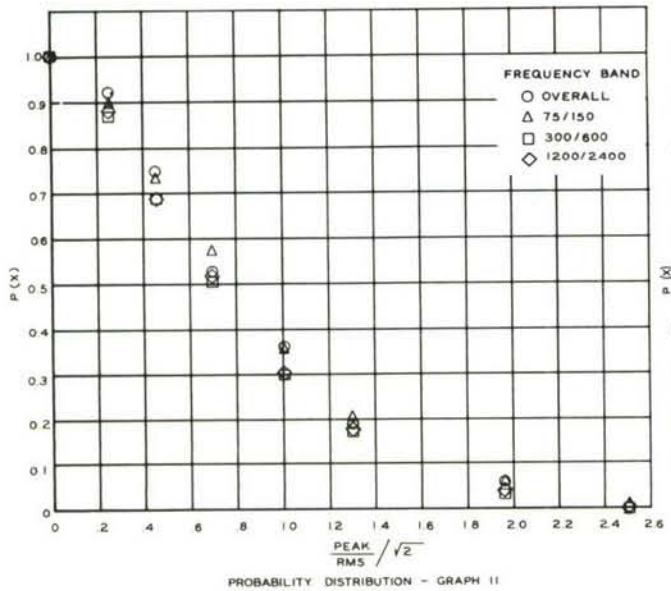

Figure II-43a. Probability Distribution of Pressure Amplitudes - Free Field at the Panel - Military - Upstream Panel Site

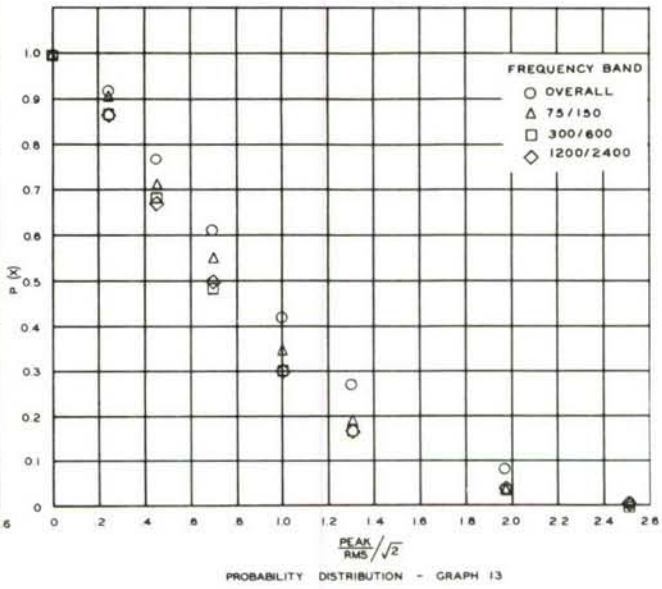

Figure II-43b. Probability Distribution of Pressure Amplitudes - Free Field at the Panel - Military - Downstream Panel Site

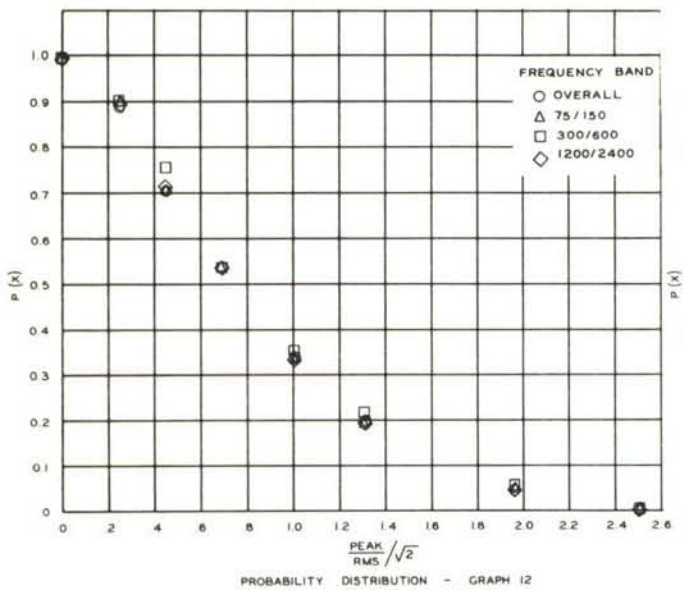

Figure II-43c. Probability Distribution of Pressure Amplitudes - Free Field at the Panel - Afterburner - Upstream Panel Site

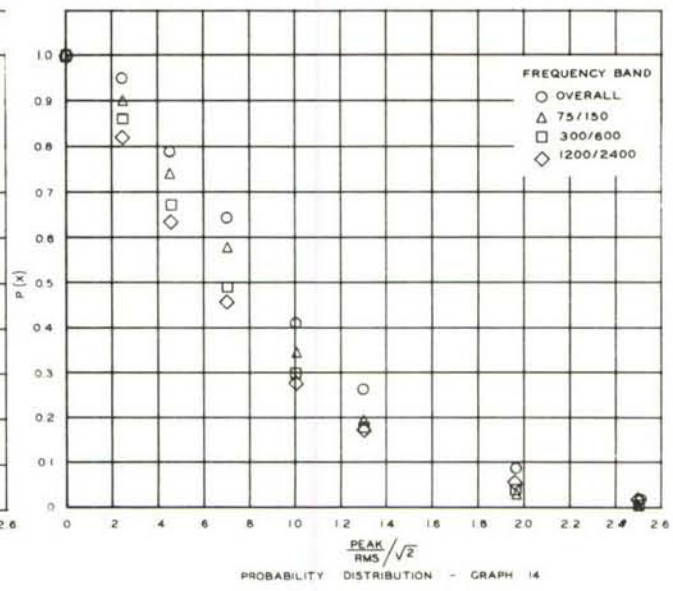

Figure II-43d. Probability Distribution of Pressure Amplitudes - Free Field at the Panel - Afterburner - Downstream Panel Site

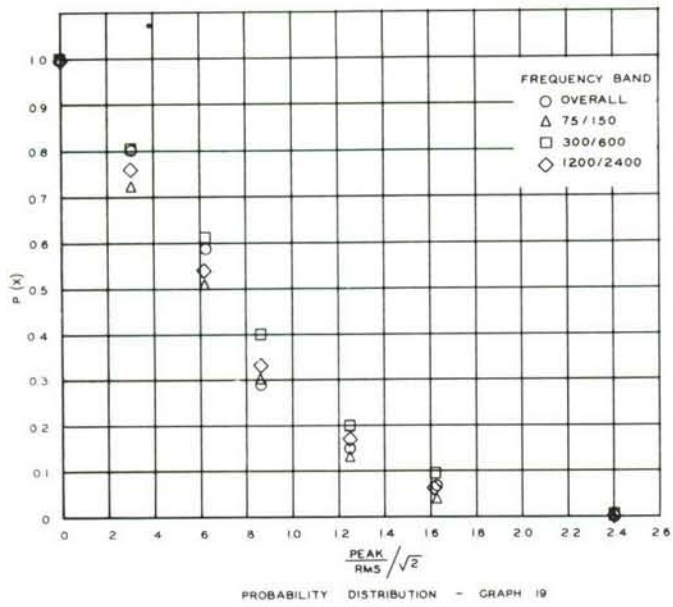

Figure II-44a. Probability Distribution of Pressure Amplitudes - Flat Panel A - Military - Upstream Panel Site

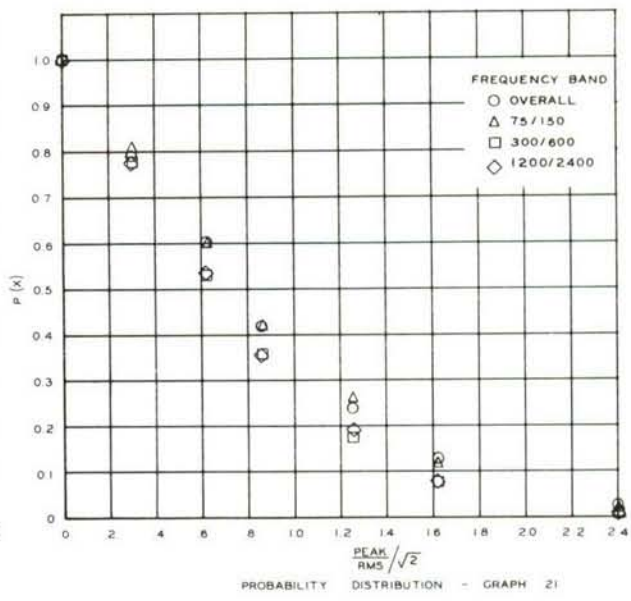

Figure II-44b. Probability Distribution of Pressure Amplitudes - Flat Panel A - Military - Downstream Panel Site

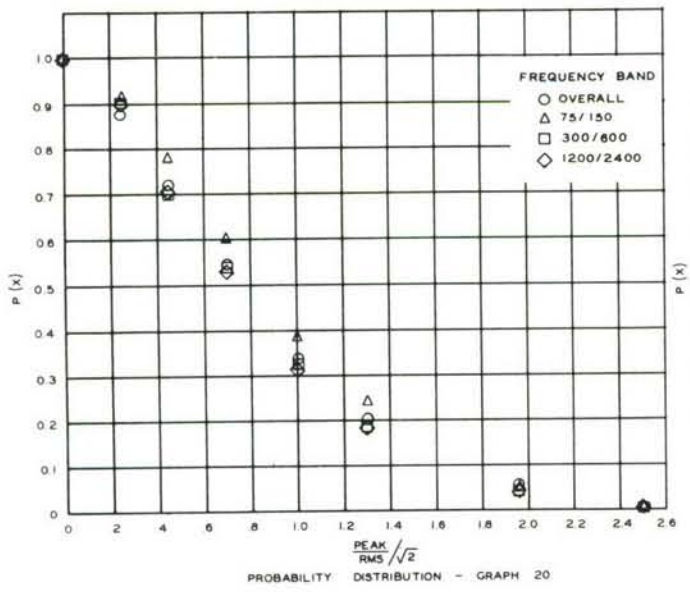

Figure II-44c. Probability Distribution of Pressure Amplitudes - Flat Panel A - Afterburner - Upstream Panel Site

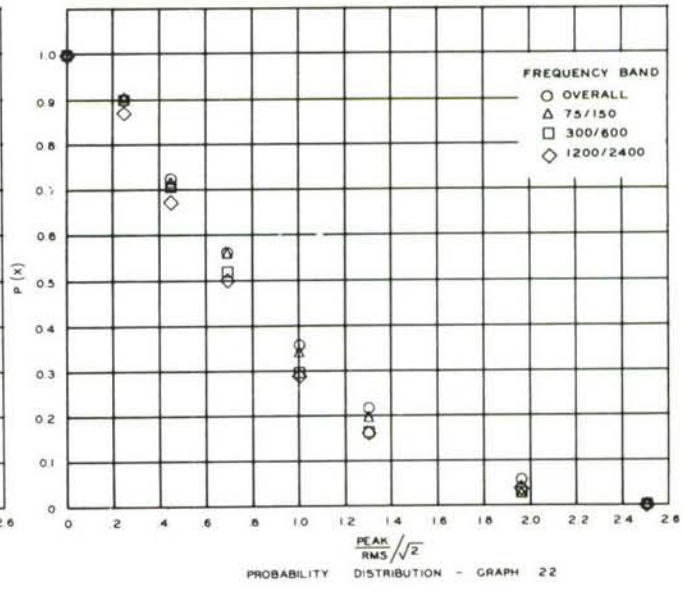

Figure II-44d. Probability Distribution of Pressure Amplitudes - Flat Panel A - Afterburner - Downstream Panel Site

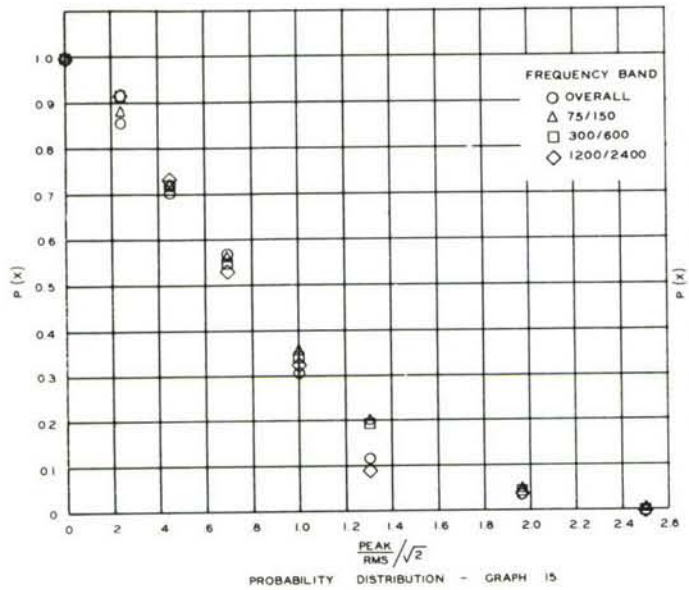

Figure II-45a. Probability Distribution of Pressure Amplitudes - Rigid Panel - Military - Upstream Panel Site

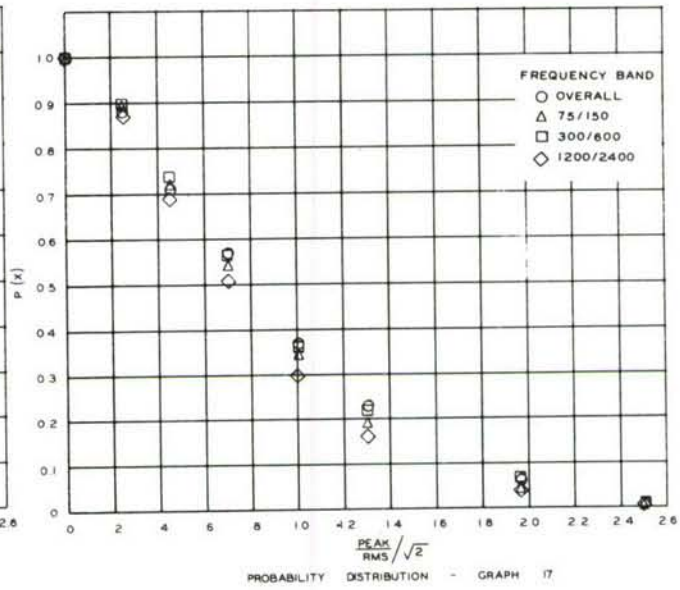

Figure II-45b. Probability Distribution of Pressure Amplitudes - Rigid Panel - Military - Downstream Panel Site

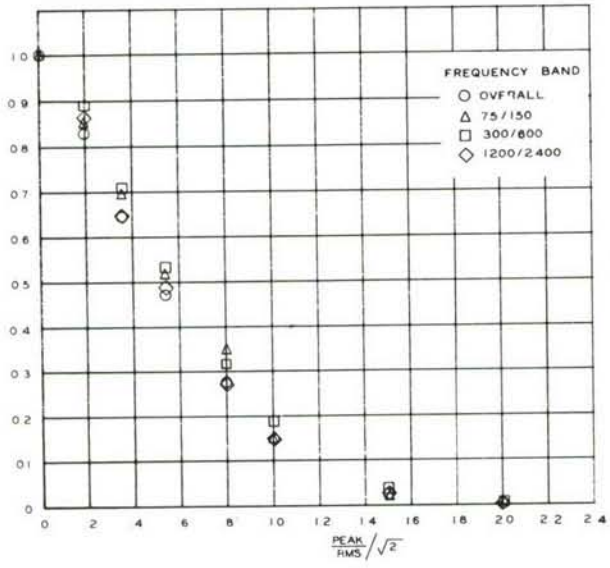

Figure II-45c. Probability Distribution of Pressure Amplitudes - Rigid Panel - Afterburner - Upstream Panel Site

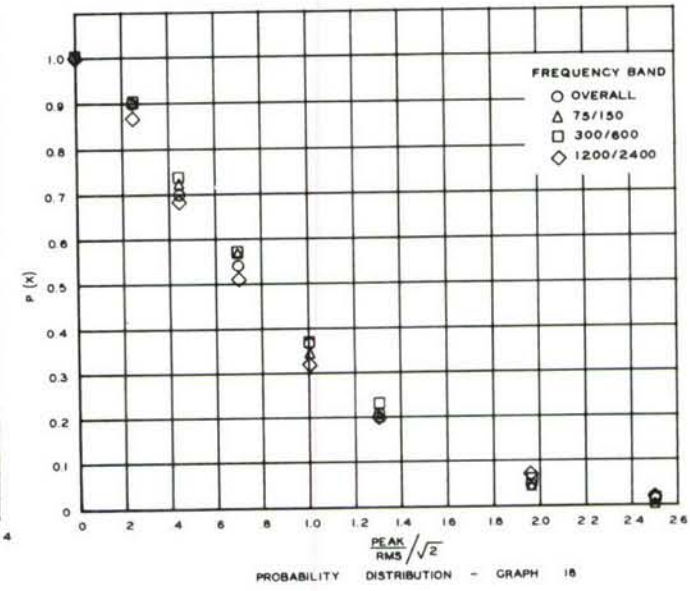

Figure II-45d. Probability Distribution of Pressure Amplitudes - Rigid Panel - Afterburner - Downstream Panel Site

Results of a test to determine the effect of placing the microphones in front of the test panel boundaries are shown in Figure II-46. This figure shows spectra obtained simultaneously with one microphone in the holding frame in front of the rigid panel and another mounted flush with the panel surface. Figure II-47 is a plot of the ratio of mean square pressures of these two microphones as a function of wavelength of sound in air.

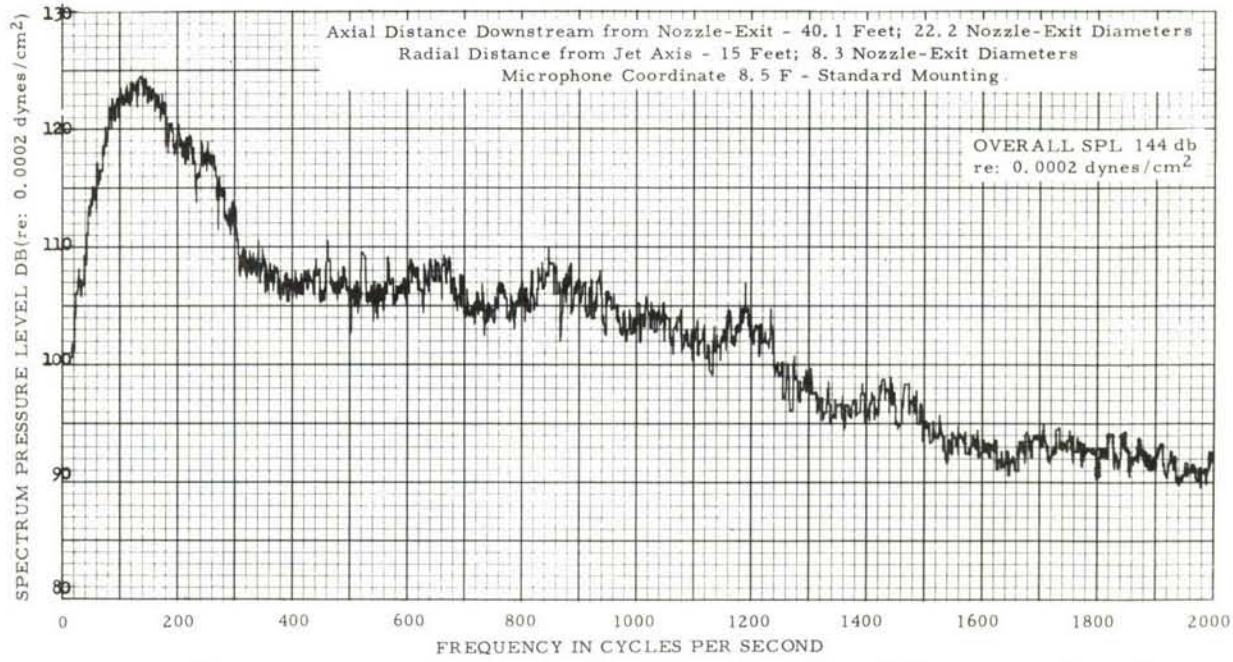

Figure II-46a. Narrow Band Analysis (10 cps) of Sound Pressure Levels - Microphone Shadow - Military

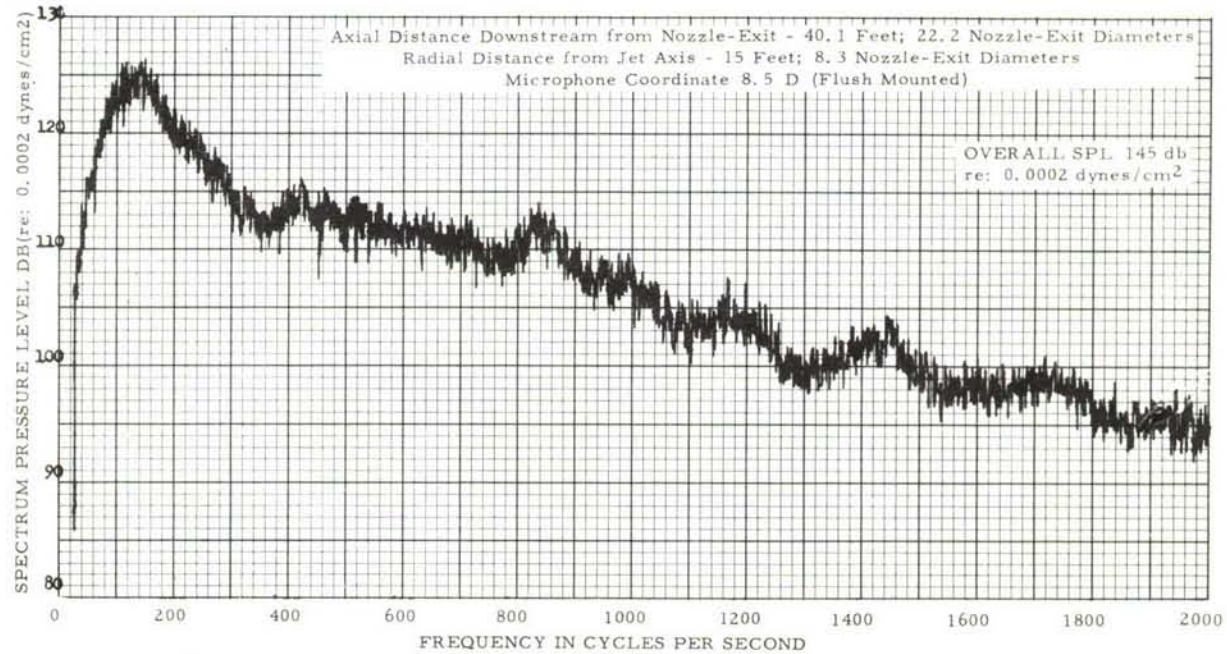

Figure II-46b. Narrow Band Analysis (10 cps) of Sound Pressure Levels - Microphone Shadow - Military

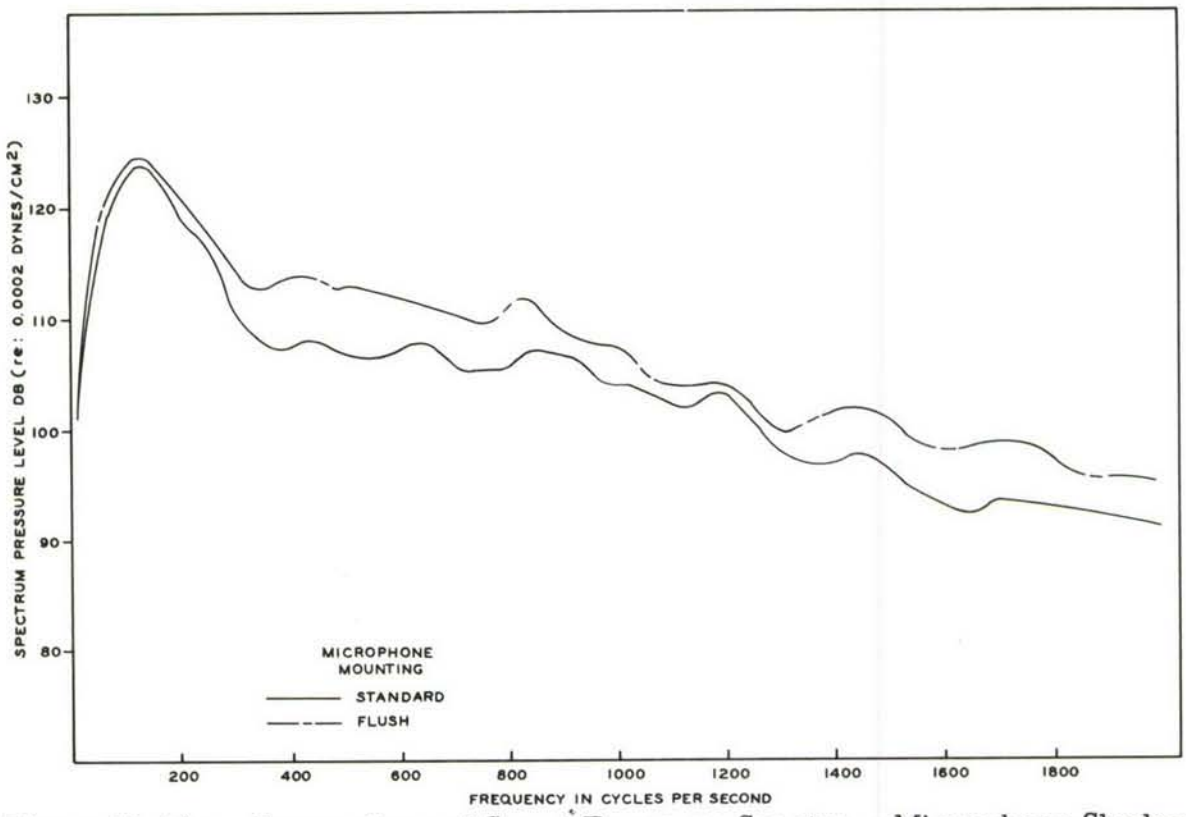

Figure II-46c. Comparison of Sound Pressure Spectra - Microphone Shadow - Military Engine Condition - Downstream Site

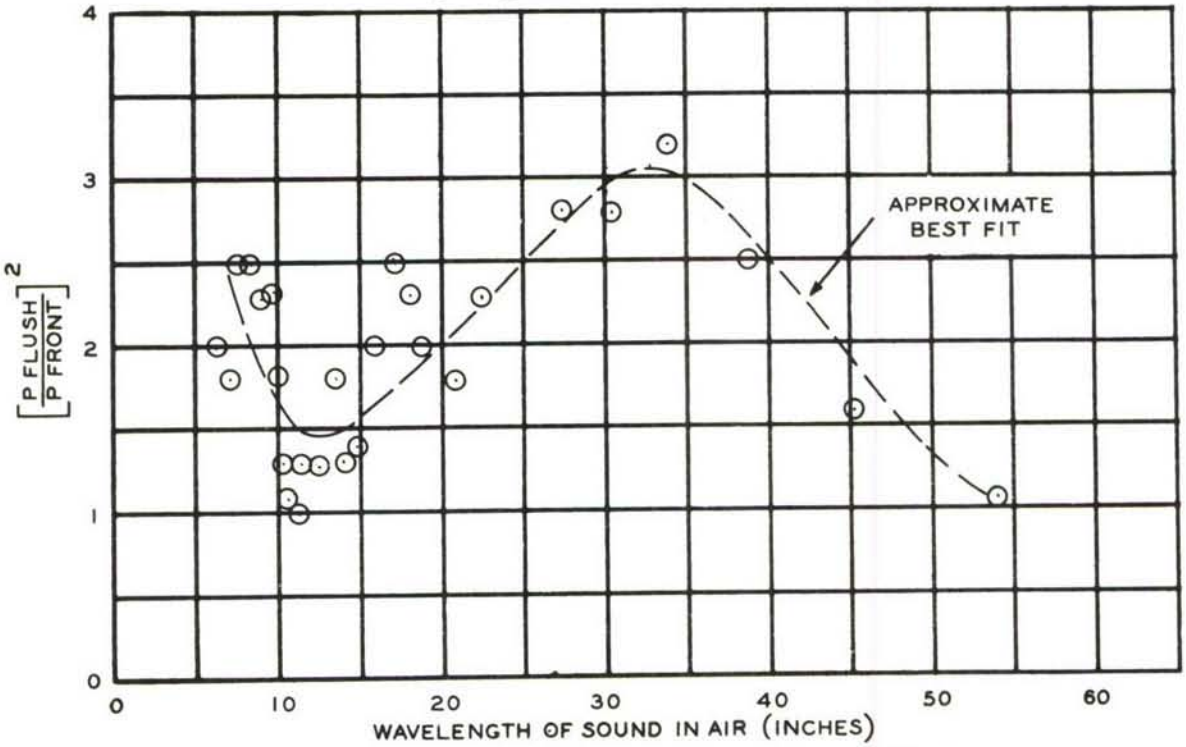

Figure II-47. Ratio of Excess Mean-Square Pressure Measured with a Flush Mounted Microphone

Sound pressure levels measured inside the panel backing chamber for two chamber volumes, along with simultaneous measurements at the exterior surface of flat panel A are shown in Figure II-48, pages 80 through 83, for the afterburner engine condition. These curves have been replotted for comparison in Figure II-49, page 84.

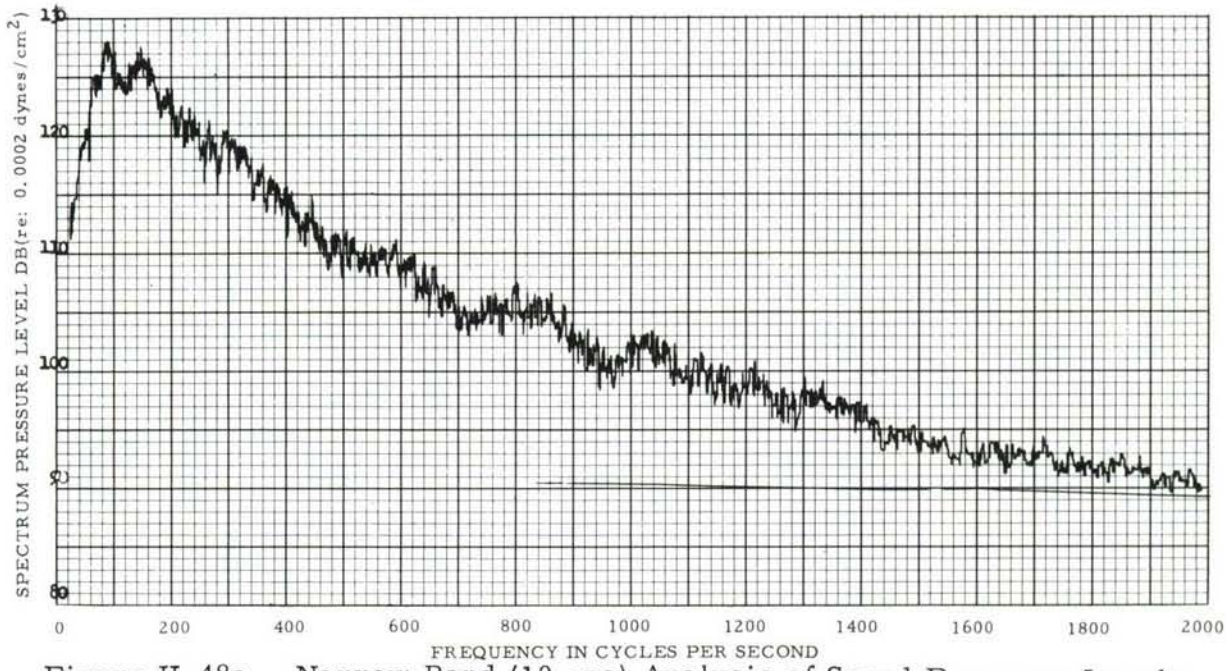

Figure II-48a. Narrow Band (10 cps) Analysis of Sound Pressure Levels - Normal Volume Test - Afterburner - Microphone Coordinate 7D Outside

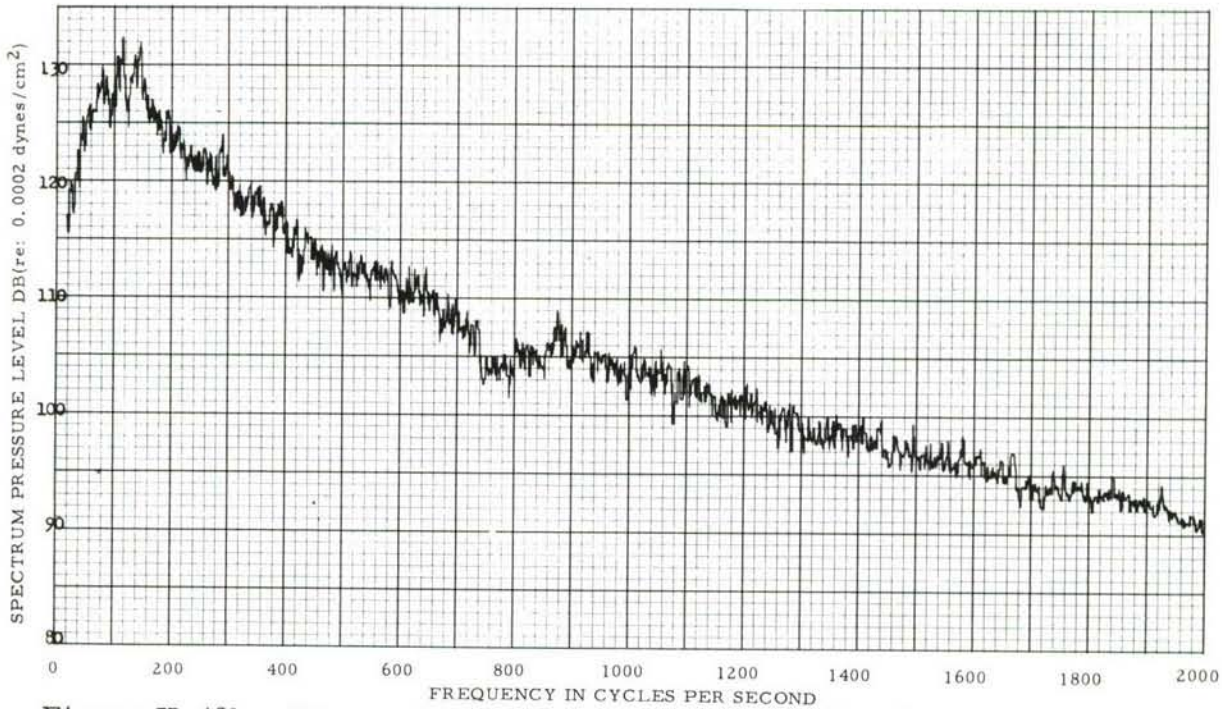

Figure II-48b. Narrow Band (10 cps) Analysis of Sound Pressure Levels - Normal Volume Test - Afterburner - Microphone Coordinate 4D Outside

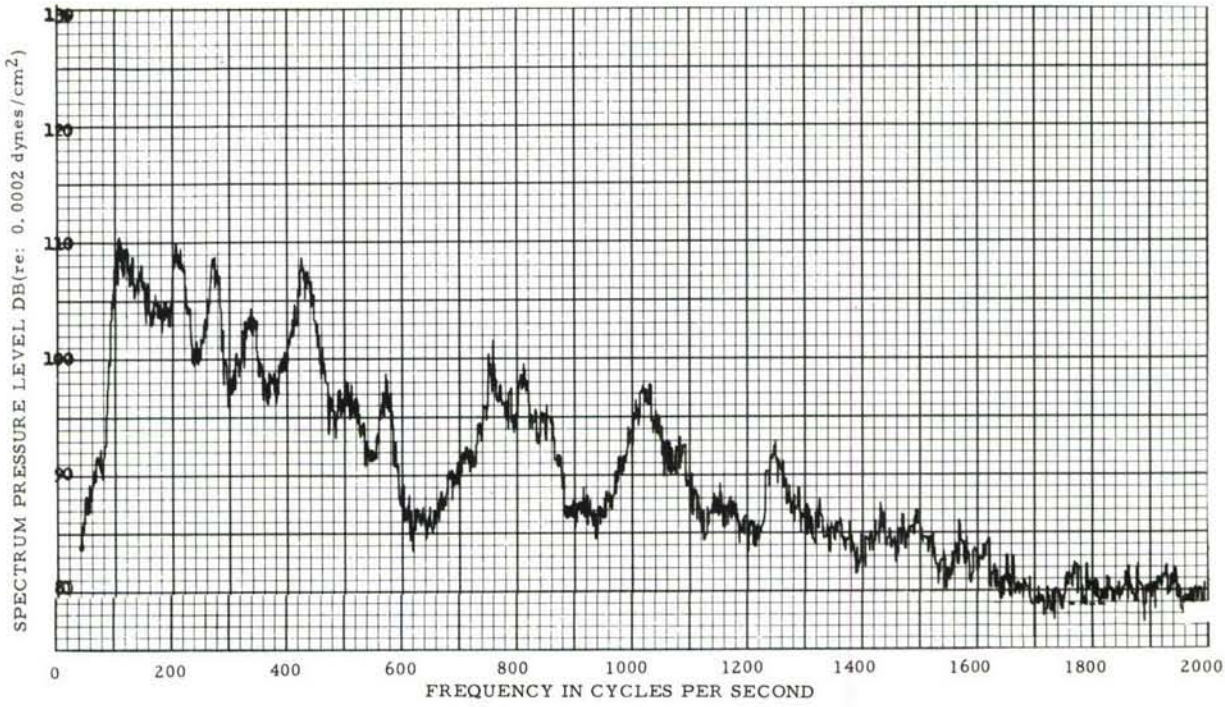

Figure II-48c. Narrow Band (10 cps) Analysis of Sound Pressure Levels - Normal Volume Test - Afterburner - Microphone Coordinate 7D Inside

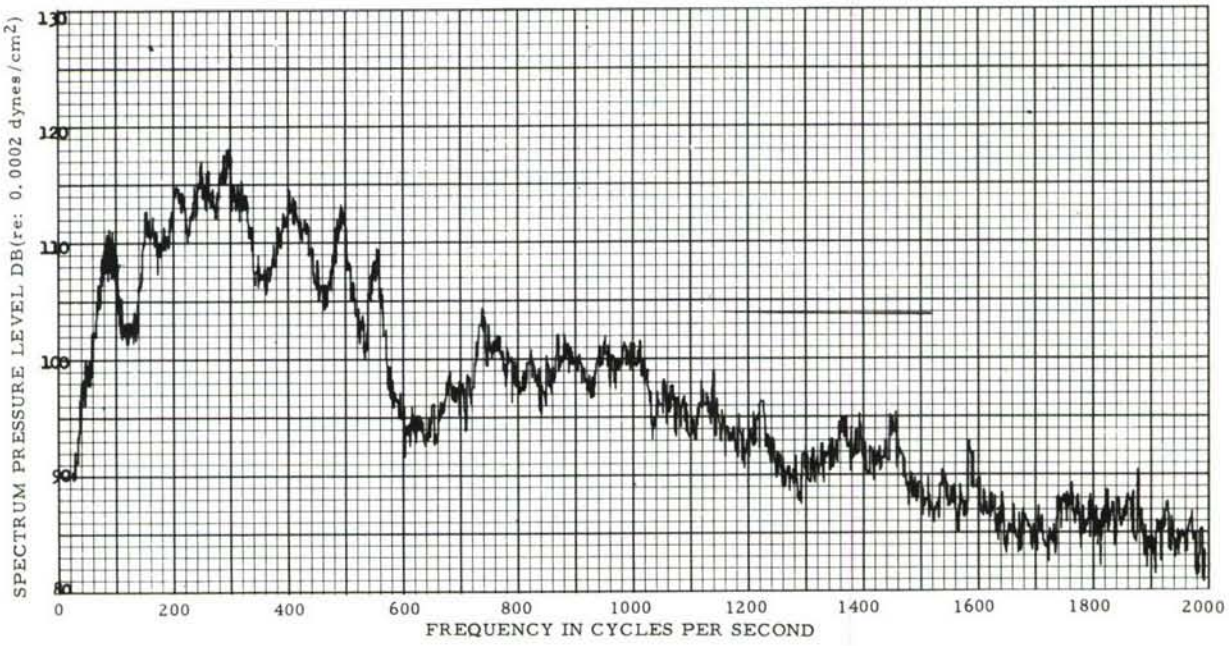

Figure II-48d. Narrow Band (10 cps) Analysis of Sound Pressure Levels - Normal Volume Test - Afterburner - Microphone Coordinate 4D Inside

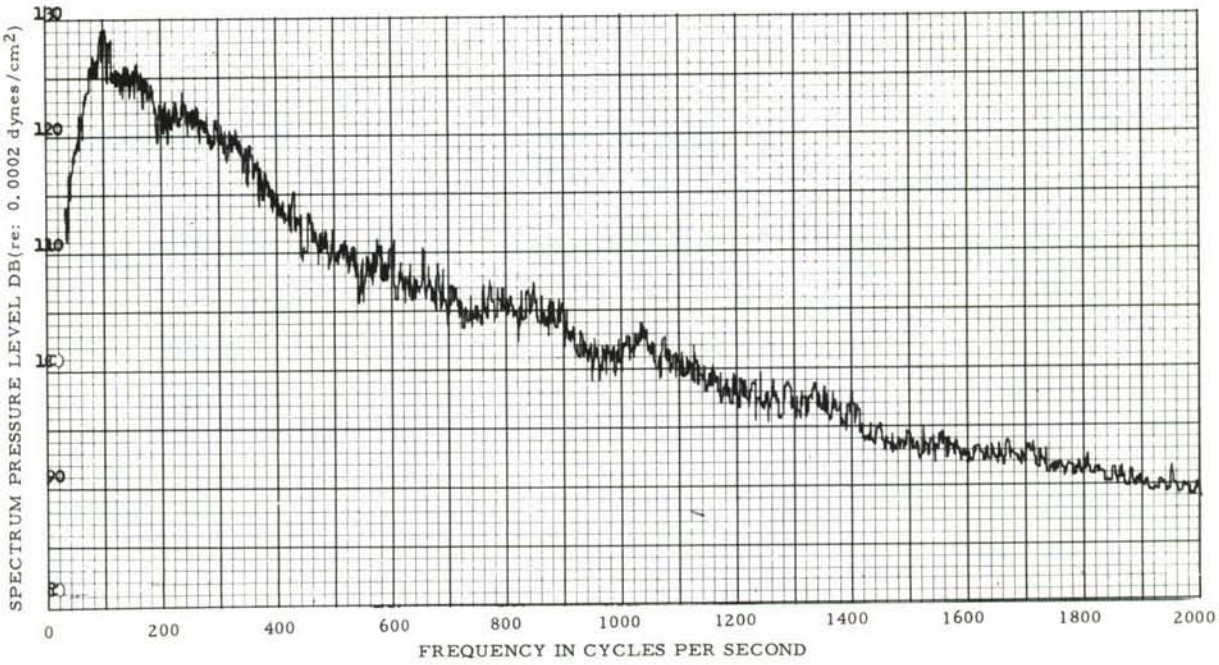

Figure II-48e. Narrow Band (10 cps) Analysis of Sound Pressure Levels - Minimum Volume Test - Afterburner - Microphone Coordinate 7D Outside

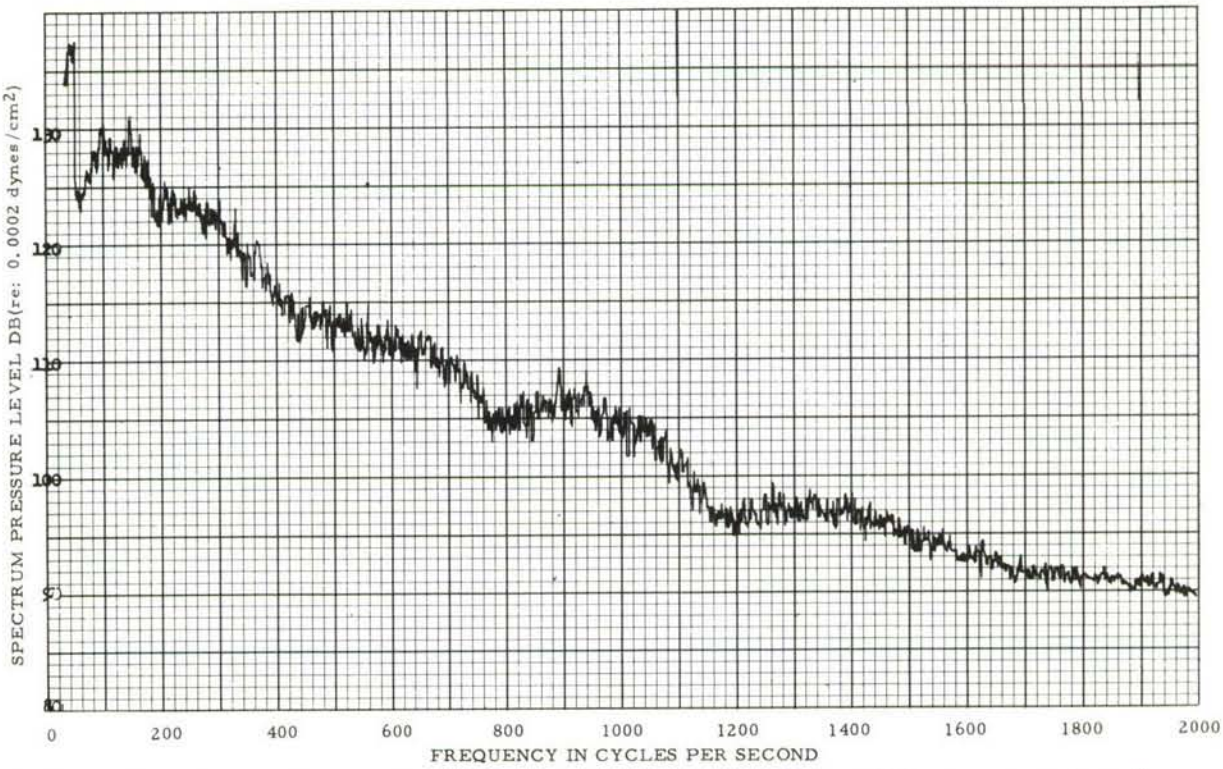

Figure II-48f. Narrow Band (10 cps) Analysis of Sound Pressure Levels - Minimum Volume Test - Afterburner - Microphone Coordinate 4D Outside

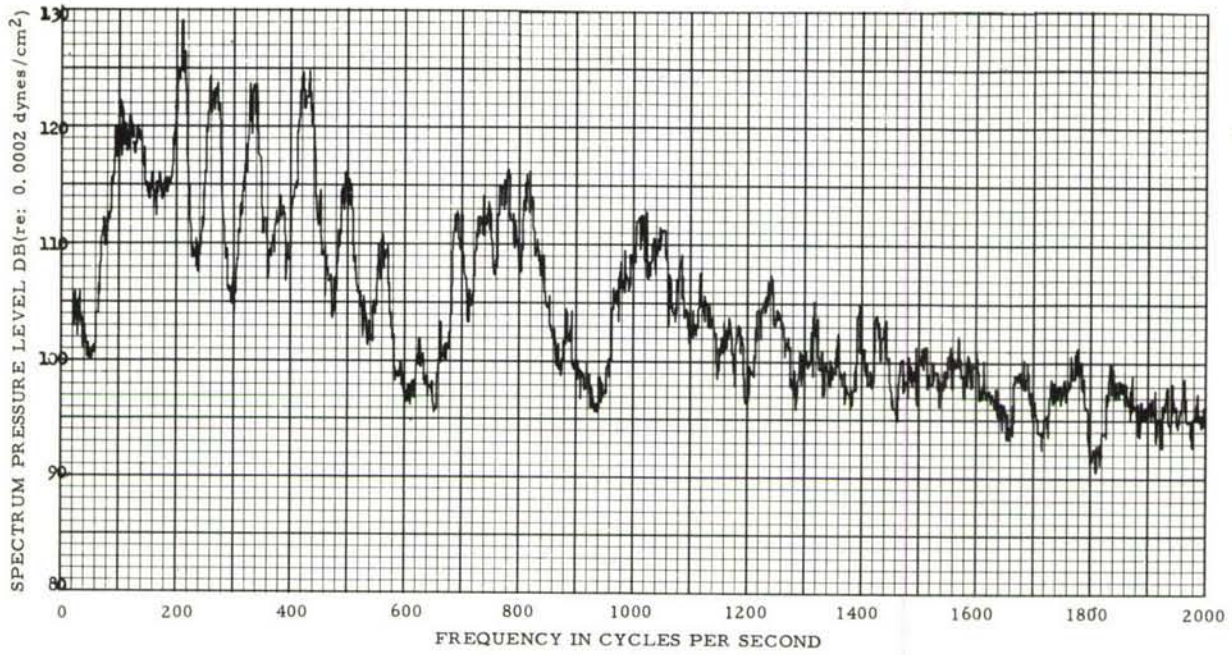

Figure II-48g. Narrow Band (10 cps) Analysis of Sound Pressure Levels - Minimum Volume Test - Afterburner - Microphone Coordinate 7D Inside

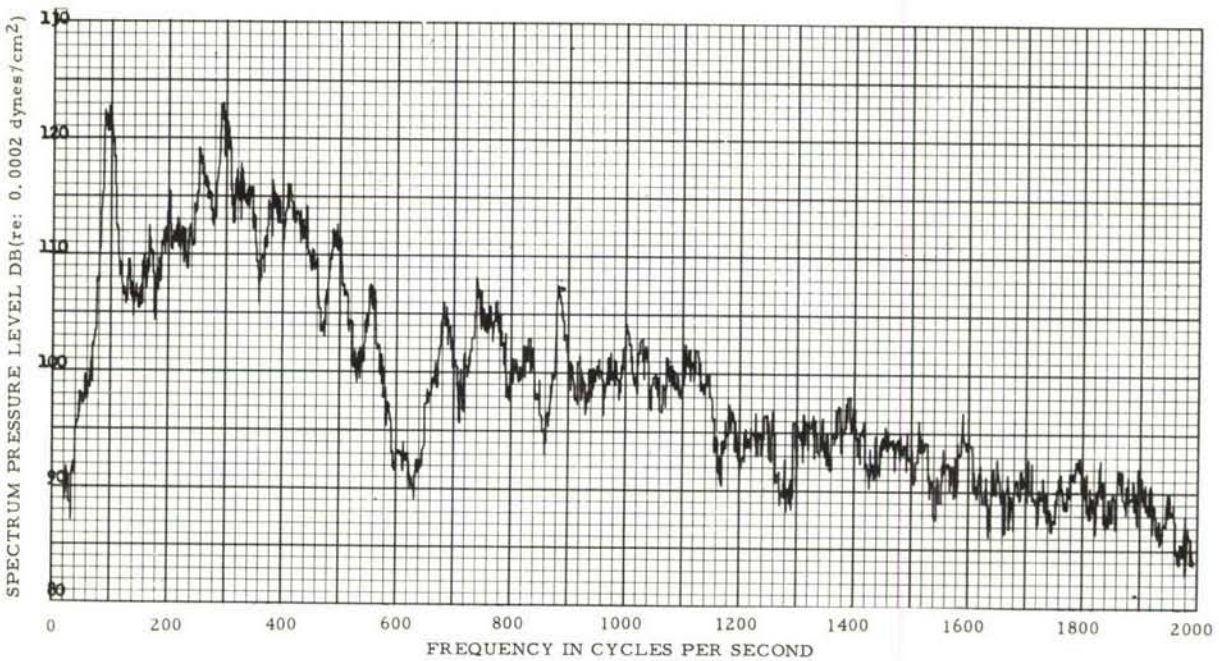

Figure II-48h. Narrow Band (10 cps) Analysis of Sound Pressure Levels - Minimum Volume Test - Afterburner - Microphone Coordinate 4D Inside

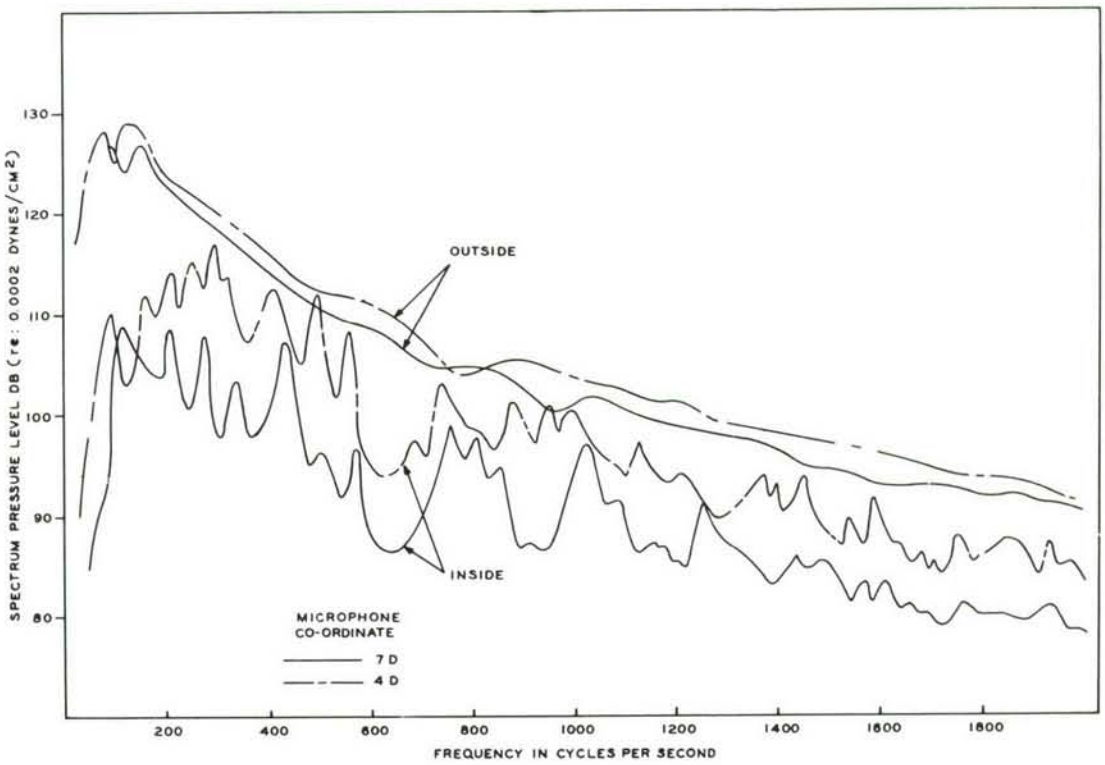

Figure II-49a. Comparison of Sound Pressure Spectra - 2 Volume Test
Normal Volume - Afterburner - Downstream Site

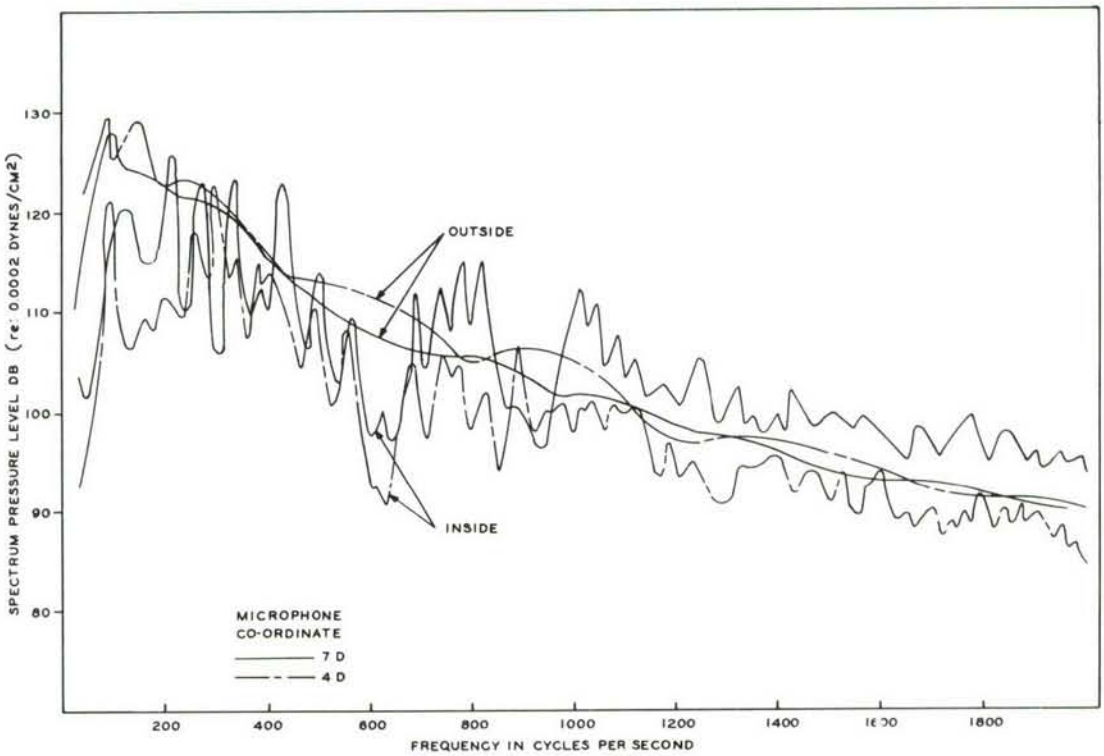

Figure II-49b. Comparison of Sound Pressure Spectra - 2 Volume Test
Minimum Volume - Afterburner - Downstream Site

E. Accuracy of the Data

Accuracy considerations have been discussed in Section II-C above for the data processing systems. However, several other possible sources of error remain and these are the subject of this section of the report.

1. Microphones (Altec Lansing)

Sources of error for microphones include atmospheric effects, load circuitry and calibration.

To eliminate as many of these sources of error as possible, a daily routine was established to insure adequate maintenance of the field test equipment including all microphones and recording equipment. This routine consisted of a system calibration check using an acoustic calibrator (Altec Lansing Type 12185) providing a known acoustic input to the microphone. Overall system calibration was then determined by measuring the input signal to the tape recorder. In addition, the test signal waveform was monitored with an oscilloscope to detect excessive noise or distortion.

The microphones were fitted with windscreens and heavy duty pre-amplifier cases to minimize wind and microphonic tube noise. Field tests of the microphones indicate an overall wind noise improvement of 10 to 15 db with the windscreens. Tests with and without the heavy duty microphone bases showed an overall improvement of 10 db. Measurement of the output of capped and uncapped microphones at overall sound pressure levels of 150 db (re: 0.0002 dynes/cm^2) showed the signal to be at least 30 db above the internal noise level of the microphone systems when using the heavy duty pre-amplifier cases and windscreens.

Microphones were calibrated for three conditions: free field grazing incidence, free field normal incidence, and pressure coupler. Free field calibrations were performed in an anechoic room. A W.E. 640AA microphone was employed as the reference standard. The results were averaged to provide a single calibration factor.

2. Microphones (Photocon Research Products)

Laboratory calibration was accomplished with a static pressure calibrator of the precision manometer type and an electro-acoustic plane wave tube capable of producing sound pressure levels up to 150 db (re: 0.0002 dynes/cm^2). No facilities are presently available in this laboratory to permit calibration at other than room temperature. However, all available data (Reference 1) indicates good temperature stability with the water cooling system used.

3. Amplifying-Recording-Playback System

As was noted previously, routine acoustic calibration checks were performed on the measuring system including all amplifiers, attenuators, and microphones. Each channel of every reel of magnetic tape was likewise calibrated with a known electrical signal. Known acoustic signals were also recorded on one tape

through the complete measuring system and processed through the data processing computer to obtain a complete system performance check. The complete system calibration check agreed with the known input signals within 1 db.

4. Data Plotting

When manual data plotting consists only of converting numbers into corresponding points on a graph, only very small errors are usually involved. This is the case with the data in this report with the exception of the constant sound pressure level contours. In this case it was necessary to interpolate the results in order to obtain constant level contours at prescribed values. It is estimated that this interpolation probably introduces errors as large as 3 or 4 db in some portions of these curves.

F. Discussion of Results

The purpose of the noise field measurements was to define the acoustic environment of the test structures and not to develop or test a theory of jet noise generation. Therefore, most of the discussion in this section is limited to interpretations based on presently available theory and comparison with the results obtained by previous investigators.

1. The Free Field Survey

Results obtained in the free field survey including constant sound pressure level contours, spectra and probability distribution of amplitude are discussed in this section.

a. Sound Pressure Level Contours

The constant sound pressure level contours of Figures II-20 and II-21 exhibit the now well known form of the near noise field of a turbojet engine exhaust. A comparison of these curves with the work of Howes, Callaghan, Coles and Mull (Reference 2) shows some differences.

First, the present results include constant sound pressure level contours for the exhaust interior. The combined interior-exterior constant sound pressure level contours exhibit apparent continuity near the measurement boundary. No serious attempt has been made to explain this form of the contours in the exhaust interior since at present no detailed theory is available. However, as suggested in Reference 8, the contours in the wake appear to be the result of an inward radiating source along the exhaust boundary. For both engine conditions the sound pressure levels along the axis approach a decrease per double distance of 6 db beyond 60 feet downstream of the nozzle-exit.

Second, the overall contours for the sound field exterior to the exhaust differ in that the present overall levels are lower in magnitude by about 5 db. An average third power velocity relationship would account for a difference of 2 db.

The remaining difference is probably due to the fact that the levels reported in Reference 2 are quasi-peak values and not true RMS as given here. Some small additional difference would also be due to the present relatively limited overall frequency bandwidth.

It should also be observed that the contours presented in Reference 2 are apparently 1/3 octave band levels while those given here are for octave bands of frequency reduced to spectrum levels.

b. Free Field Spectra

Several features of the spectra in Figures II-22 through II-27 are worthy of notice. The spectra for positions along the centerline of the exhaust for both engine conditions show a slight decrease in high frequency content and decreasing overall sound level with distance from the nozzle-exit as would be expected. Nearly all of the sound energy appears to be concentrated in the frequency range below 200 cps. In this respect the spectra are similar to the spectral density of turbulence data of Reference 3 taken along the jet centerline at distances greater than 16 nozzle-exit diameters.

Spectra for microphone locations outside the exhaust are typical for the near noise field of a turbojet, i. e., increased high frequency sound levels near the mixing region compared to locations further downstream. An unusual feature is the discrete frequency component near 850 cps with some indication of its harmonic. This phenomenon may be explained by assuming that in some cases the jet was slightly supersonic. The data reported in Reference 4 for an unheated supersonic jet indicates that the relation between the wave length (λ) of the emitted sound and the nozzle diameter (d) is approximately

$$\lambda \approx 1.3\, d$$

Using average values from Table II-2, page 8, for exhaust gas temperature and nozzle diameter for the military operating condition, the average local speed of sound in the jet is

$$C = C_0\sqrt{1 + \frac{T}{273}} \approx 1120\sqrt{1 + \frac{565}{273}} = 1960\ \frac{FT.}{SEC.}$$

$$f = \frac{C}{\lambda} = \frac{C}{1.3d} = \frac{1960}{(1.3)(1.81)}$$

$$f \approx 835\ cps$$

This value is very close to the observed frequency. Therefore it seems plausible to assume that during some engine runs, supersonic conditions did occur. It is interesting that very little or no sound of unusual magnitude was observed near this frequency for the afterburner condition. This is not as expected since the calculated nozzle pressure ratios appear to be similar for both conditions.

2. Probability Distribution of Amplitude

Probability distribution of peak amplitudes for a Gaussian random process should follow a Rayleigh distribution function (References 5 and 6):

$$P(R>R_0) = e^{-R_0^2/2\sigma^2}$$

where $P(R>R_0)$ = probability that the envelope of peak values (R) of the random variable will exceed some specified peak value R_0

e = base of the system of natural logarithms

σ^2 = variance (mean-square) value of the random variable.

In this report

R_0 = peak value of the signal

σ = root-mean-square value of the signal

and all probability distributions are plotted in terms of

$$\overline{\sigma} \equiv \frac{R_0}{\sqrt{2}\,\sigma}$$

Hence,

$$e^{-R_0^2/2\sigma^2} = e^{-(PEAK/\sqrt{2}\,r\cdot m\cdot s)^2} = e^{-(\overline{\sigma})^2}$$

is the equivalent distribution.

For this distribution, values of R_0 are uniquely associated with corresponding values of the probability P and $\overline{\sigma}$, thus:

R_0	P	$\overline{\sigma}$
	0.607	.707
2	0.135	1.414
3	0.012	2.121

The distribution summary of Table II-7, page 42, is in terms of the above values of R_0 and the corresponding average observed values of $\overline{\sigma}$. For example, under the column labeled ($\overline{\sigma}$) are given the average observed values of ($R_0/\sqrt{2}\,\sigma$) corresponding to the probability 0.607 for $R_0 = \sigma$. The theoretical value from the above table for $R_0 = \sigma$ is 0.707. Average values have been tabulated since the range of individual results by frequency bands is small in nearly all cases.

In addition, Table II-7 shows the ratios

$$\frac{2\overline{\sigma}}{\sigma} \text{ and } \frac{3\overline{\sigma}}{\sigma}$$

which in the theoretical case should have numerical values of 2 and 3, respectively.

A comparison of the variation of the mean value for each set of data in the distribution summary about the theoretical distribution shows that the means of the observed data are skewed slightly positive, i. e., the mean of each set of data is greater than 0.707. Assuming a normal distribution of these means, the theoretical mean is less than one standard deviation from the observed grand mean. Thus, the theoretical mean does not appear significantly different from the experimental grand mean within the accuracy of the data. Within groups the data scatter for both $\overline{\sigma}$ and $\overline{2\sigma}$ is less than one standard deviation from the calculated group means.

Two anomalous conditions are observed when examining the data individually by groups. First, the mean value of $\overline{\sigma}$ for the jet wake data is greater than 3 standard deviations from the theoretical mean. Second, the standard deviation is zero (all results equal) for the data at the free field panel site, although an obvious difference exists from the theoretical mean.

Now for $\overline{2\sigma}$, the data scatter by groups becomes greater than for $\overline{\sigma}$. These data are also positively skewed. Thus the mean of the rigid panel data is the only mean within 3 standard deviations of the theoretical mean while the grand mean for all data is 1.7 standard deviations from the theoretical. These facts tend to indicate reduced accuracy by groups at the higher peak to root-mean-square ratios. Scatter of individual data within groups remains essentially the same as for $\overline{\sigma}$. Therefore, at small values of the observed distributions the data (with the exception of the jet wake) do not differ significantly from a Rayleigh distribution. At large values of $\overline{\sigma}$ (greater than 2) there is a significant departure from theory, but, since the departure is accompanied by relatively large data scatter, it is not possible to determine if this is a real effect.

3. Bounded Field Survey

Noise data obtained in detail at the two panel boundary sites including spectra and space-phase correlation of sound pressure are discussed in this section.

a. Space-Phase Correlation of Sound Pressure

As expected, the general form of the correlations is similar for all conditions and in most respects is much like the correlations reported in Reference 2.

The effect produced by correlating sound pressures along one horizontal line across the panel with a reference sound pressure displaced in a vertical direction is more or less predictable; that is, the correlation for the sound pressure directly below the reference is the vertical correlation at that panel position. In those cases where the vertical correlation (Survey Line C - Zero Separation) is near unity, the correlation is changing slowly in that direction as is observed for most of the downstream data. Small changes in the vertical correlation would tend to imply little difference in horizontal correlation between the two survey lines. This general effect is borne out in comparing the data for distance to first

zero crossing which shows a high degree of similarity by survey lines for almost all conditions.

Comparison of the zero crossing data by panel location shows greater zero-distances at the upstream site. Since the noise sources are probably nearer the upstream site, this effect would also be expected if a simple plane wave source is assumed near the jet mixing region; that is, the slant distance (and consequently fractional wavelength) changes more rapidly with distance (parallel to the jet) from the assumed source.

In all cases, maximum negative correlation is observed to be greatest at the downstream site. This fact would indicate that at the downstream site the sound pressures appear to emanate from a localized source while upstream the source appears to be a spatially distributed system of generators with little correlation.

No significant correlation difference was observed by boundary condition.

An apparent correlation anomaly was observed at about 400 cps where the zero crossing distance is greater than would be expected from the general trend by frequency. In all cases this anomalous increase is greater for the military than afterburner engine condition. This phenomenon appears to be an artifact caused by computation errors approaching the small correlation difference in this frequency range and accentuated in the upstream cases by the small slope of those curves near the zero correlation axis.

b. Sound Pressure Spectra

At the upstream site, maximum average sound pressure levels by frequency were found to occur around the 1/3 octave band center frequencies of 200, 250 and 320 cps. Downstream, maximum levels were found to occur generally at lower frequencies; in the 1/3 octave bands between the center frequencies 80 and 100 cps for the military condition and between 50 and 320 cps for the afterburner.

Average overall sound pressure level increase with the afterburner compared to the military condition was 7 db at the downstream site and 6 db upstream. At the upstream site the afterburner produces a nearly uniform spectrum increase over the frequency range examined, while downstream little increase was observed in the upper half of the spectrum with a nearly uniform increase in the lower half.

In the frequency range for the 1/3 octave bands between 40 and 125 cps, average sound levels at the downstream site are as much as 18 db higher than for corresponding frequencies at the upstream site for both engine conditions. Between 125 and 1000 cps the average levels tend toward similar values at both sites.

4. Miscellany

Tests were performed to evaluate possible effect of placing the microphones in front of the panel boundaries and the effect of panel boundary chamber termination.

Below 250 cps no significant difference was observed between sound levels measured with a microphone mounted flush in the surface of the rigid panel and a microphone installed in the holding jig in front of this panel. Between 250 and 2000 cps sound levels for the flush mounted microphone appear to be from 0 to 4 db greater depending on frequency. The calibration of these two microphones show differences of less than 1 db within the frequency range of interest. Both pieces of data were obtained with essentially similar and largely identical recording and data processing equipment. The difference in observed level, therefore, appears to be a real phenomenon, which, by virtue of the sound-in-air wavelengths involved, seems to be a panel and holding jig diffraction effect. For precise calculations above 250 cps, this effect would require further investigation.

Sound pressures measured at two locations within the panel backing chamber for two sound terminating conditions show an average sound level increase of 5 to 10 db when the chamber volume and absorption are minimized. In general, the reduced chamber volume and absorption tends to produce a significant increase in the ratio of peak to minimum sound levels at those frequencies that appear to correspond to panel resonances.

G. Conclusions

1. The near noise field characteristics of the turbojet engine used for the present test series are similar to those determined by previous experimenters. An interesting feature of the noise spectra of the test engine was observed, namely the appearance of discrete frequency "screech" at a nominal frequency of 850 cps.

2. Constant sound pressure level contours within the exhaust suggest an inward radiating source along the jet boundary. This conclusion appears to be in general agreement with the ideas advanced in Reference 8.

3. Probability distribution of amplitude of sound pressures for all test conditions and frequency bands investigated were not greatly different from each other or the theoretical Rayleigh distribution.

4. Space-phase correlations of sound pressures were found to be of expected forms for the noise field locations examined and essentially the same as had been reported by other investigators.

5. Space-phase correlations of sound pressures along a horizontal displaced line are similar to the correlations for a non-displaced line for conditions where the vertical correlation is near unity, and significantly different when the vertical correlation is appreciably less than unity.

6. There appears to be a real difference between the sound pressures measured at the surface and slightly forward of the surface of the rigid panel over portions of the spectrum investigated.

SECTION III

THEORETICAL PANEL RESPONSE

A. Introduction

In this section the methods used for the theoretical determination of panel response in the jet noise field are presented. Comparisons of theoretical results with both laboratory and field tests are shown.

The basis for the theoretical response determination is the assumption that the panel dynamic characteristics may be defined in terms of a number of lightly damped and hence sensibly uncoupled natural modes of the panel. These modes are determined both analytically and by laboratory resonance tests. They are used in conjunction with measured pressure characteristics in the jet noise field to determine the acceleration response of the panel.

The analytical investigation has been confined to the flat, unstiffened 6- x 20-inch panel and the flat panel A.

B. Theoretical Panel Modes and Comparison with Laboratory Resonance Tests

1. 6- x 20-inch Panel

The natural mode shapes and frequencies are determined by the method of Reference 13, for both clamped and simply supported edges, for the modes having zero, two, four, and six node lines in the short direction.

The natural frequency is given by Reference 12 as:

$$F_o = \frac{\lambda h \pi}{a^2} \left[\frac{E_g}{48 \rho (1-\sigma^2)} \right]^{1/2}$$

where λ = frequency factor, and is given by Reference 12 as a function of nodal pattern and panel edge condition.

The frequencies calculated by this method are compared with laboratory test results in Figure III-1, and the theoretical and test mode shapes are compared in Figure III-2.

It may be seen from Figure III-1 that the variation of natural frequency with nodal pattern as shown in the laboratory tests implies an edge condition approaching simple support, and from Figure III-2 that the mode shapes depart rather markedly from the theoretical case in which the nodal lines break up the panel into approximately equal areas.

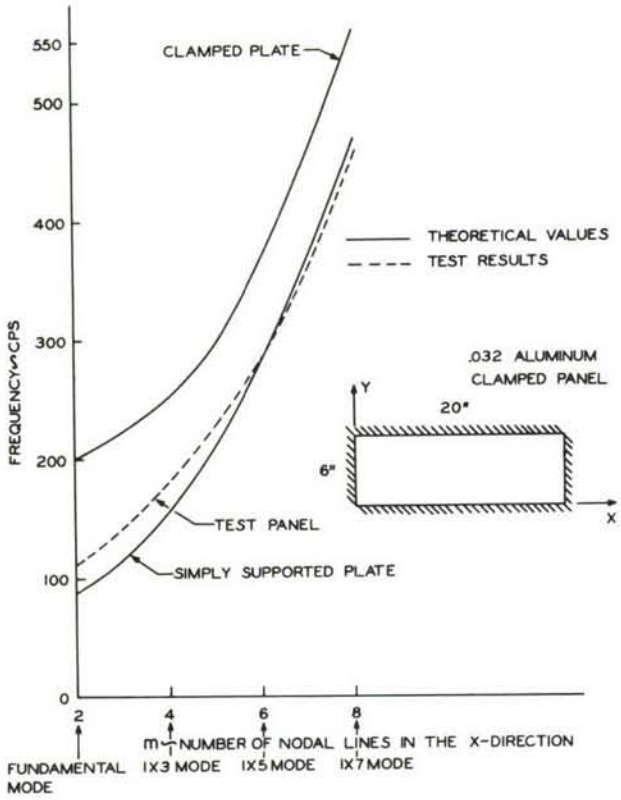

Figure III-1. 6" x 20" Panel Natural Frequency - Comparison of Theoretical and Test Results

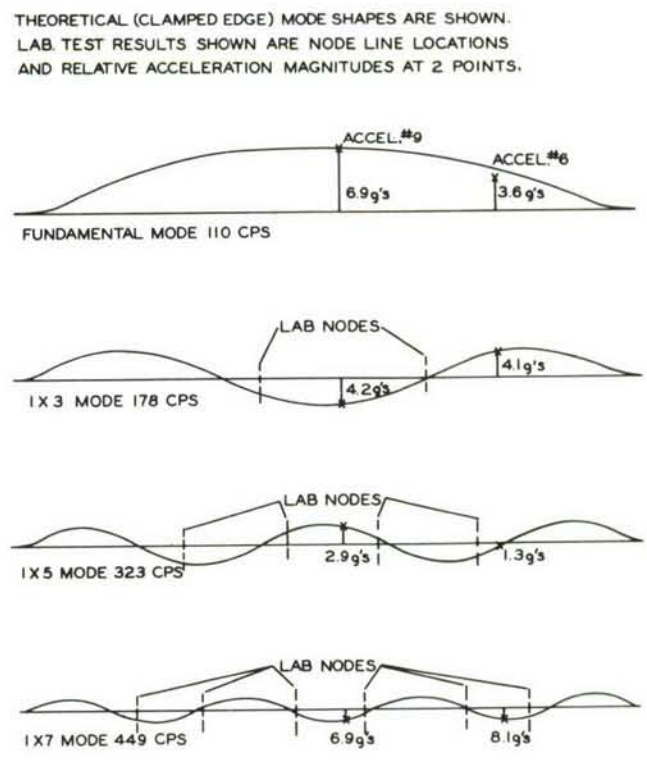

Figure III-2. 6" x 20" Panel Mode Shapes - Comparison of Theoretical and Lab Test Results

2. Flat Panel A

A Rayleigh type method of analysis is used for the prediction of mode shapes and frequencies of this multi-panel structure.

The generalized coordinates used in the analysis are the displacements at the center of individual panels, at the midpoint of the stiffening members, and at the intersection points of the stiffening members. These coordinates are shown in Figure III-3.

The displacement in each of these coordinates is written in terms of the inertia loading and the structural characteristics of the panel, using simple beam and plate theory. The resulting homogeneous equations are solved for the natural frequencies and mode shapes by means of a digital computer.

The procedure used in setting up the equations is illustrated in Figure III-4 where the various steps involved in determining the deflection at the center of a panel are shown. The resulting matrix of equations is shown in Table III-1, together with the solutions in terms of mode frequency and mode shape normalized on the coordinate "z."

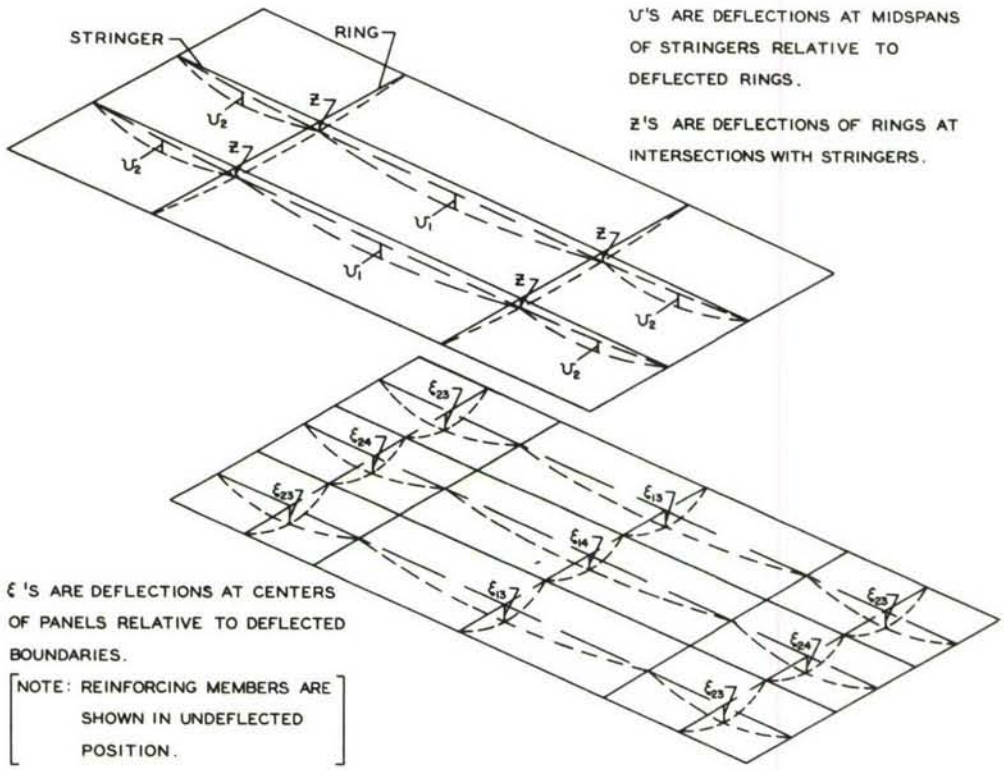

Figure III-3. Coordinates for Panel A Theoretical Mode Shape Determination

TABLE III-1

PANEL "A" THEORETICAL MODE DETERMINATION

MODE	1	2	3	4	5	6	7
ROOT	309.821	295.048	191.758	188.967	14.071	3.464	0.387
f, CPS	90.5	92.7	115.0	115.8	424	855	2560
ξ_{13}	54.0	-682	-0.925	-0.885	-2.04	0.903	0.548
ξ_{14}	88.1	815	-1.828	-1.79	-4.07	1.825	1.10
ξ_{23}	0.2	0.228	142.6	-87.4	-0.258	-0.935	1.610
ξ_{24}	0.4	0.460	79.7	306	-0.529	-1.88	3.210
U_1	2.77	2.76	-0.645	-0.643	1.895	-2.56	-2.01
U_2	-0.41	-0.413	0.639	0.638	-0.234	0.834	-3.13
Z	1.00	1.00	1.00	1.00	1.00	1.00	1.00

$$\begin{bmatrix} \xi_{13} \\ \xi_{14} \\ \xi_{23} \\ \xi_{24} \\ U_1 \\ U_2 \\ Z \end{bmatrix} = 10^{-6}\omega^2 \begin{bmatrix} 296.132 & 0 & 0 & 0 & 188.524 & 0 & 218.117 \\ 0 & 293.262 & 0 & 0 & 373.393 & 0 & 426.749 \\ 0 & 0 & 190.696 & 0 & 0 & 121.401 & 73.874 \\ 0 & 0 & 0 & 187.986 & 0 & 239.351 & 147.743 \\ 5.493 & 5.493 & -0.537 & -0.537 & 18.632 & -1.998 & 23.985 \\ -0.826 & -0.826 & 0.537 & 0.537 & -2.814 & 1.905 & -2.133 \\ 1.951 & 1.951 & 0.831 & 0.831 & 6.530 & 2.746 & 14.903 \end{bmatrix} \times \begin{bmatrix} \xi_{13} \\ \xi_{14} \\ \xi_{23} \\ \xi_{24} \\ U_1 \\ U_2 \\ Z \end{bmatrix}$$

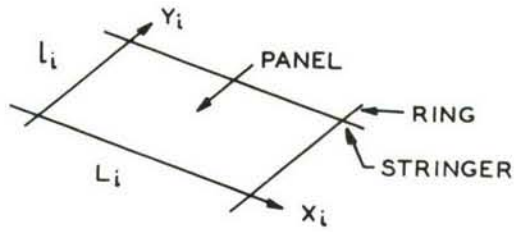

DEFLECTIONS OF STRUCTURAL ELEMENTS

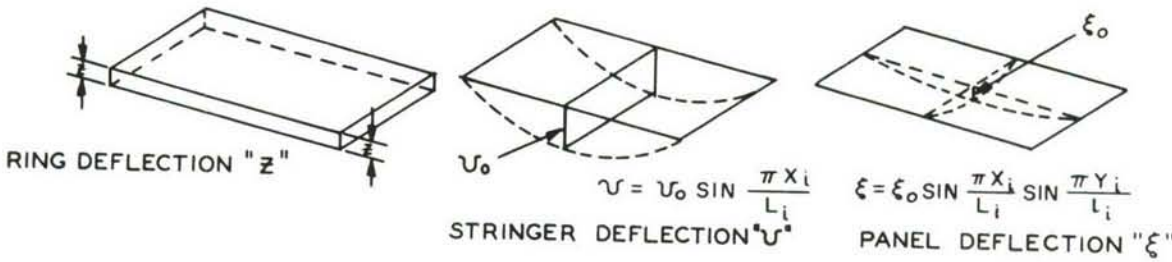

LOADS ON PANEL

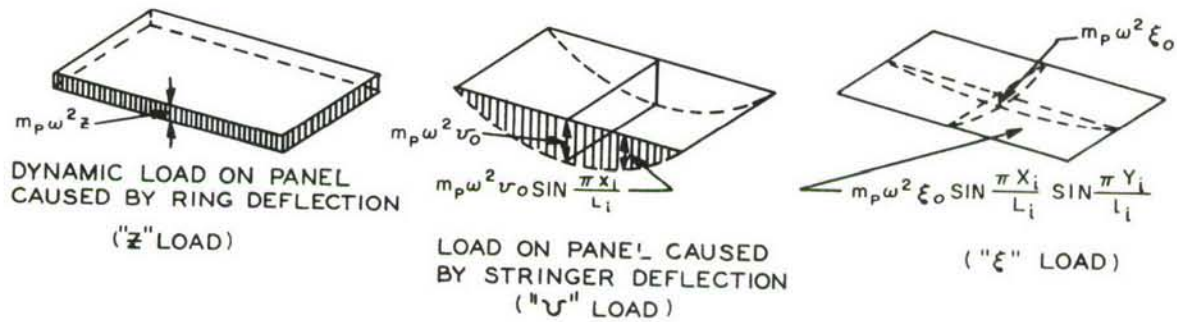

PANEL DEFLECTIONS

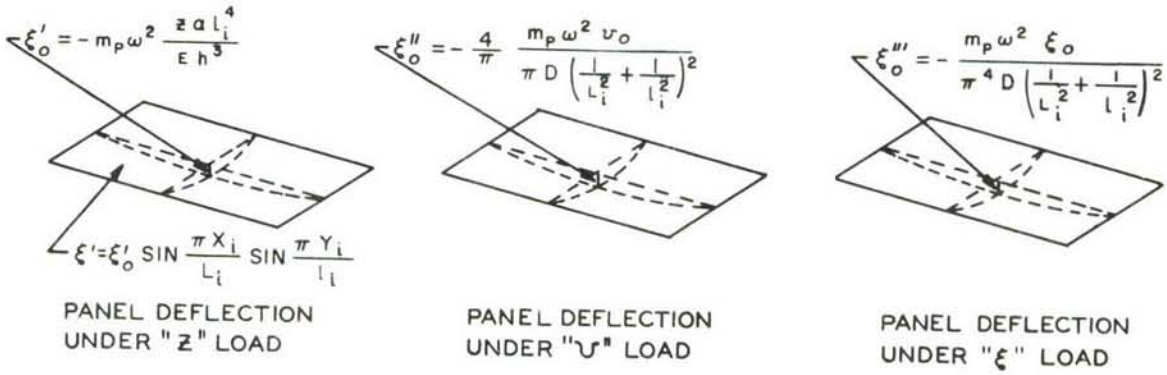

Figure III-4. Panel A Mode Determination

The first three natural modes obtained by this procedure are shown in Figure III-5, together with corresponding modes determined by laboratory resonance tests.

Figures III-5a. - III-5c.

Panel A Natural Frequencies and Mode Shape - Comparison of Theoretical and Lab Test Results

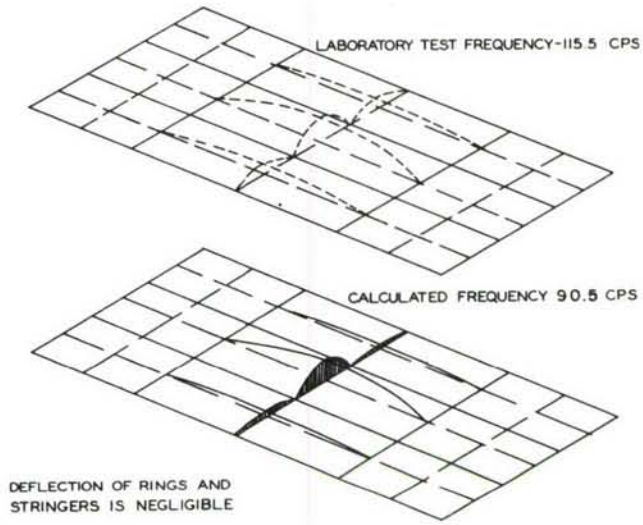

Figure III-5a.

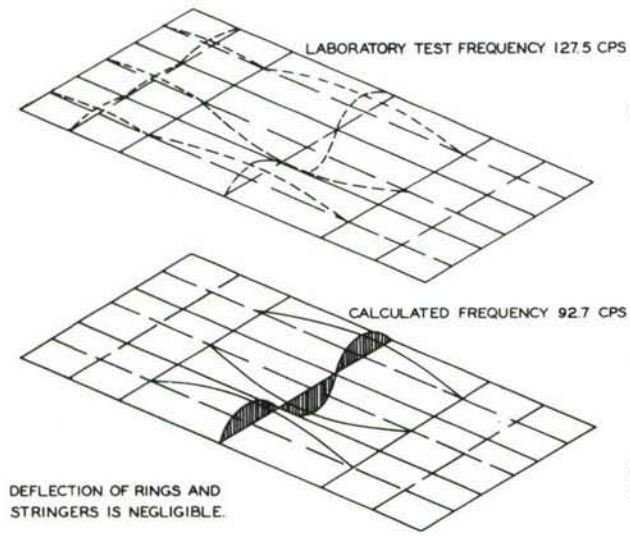

Figure III-5b.

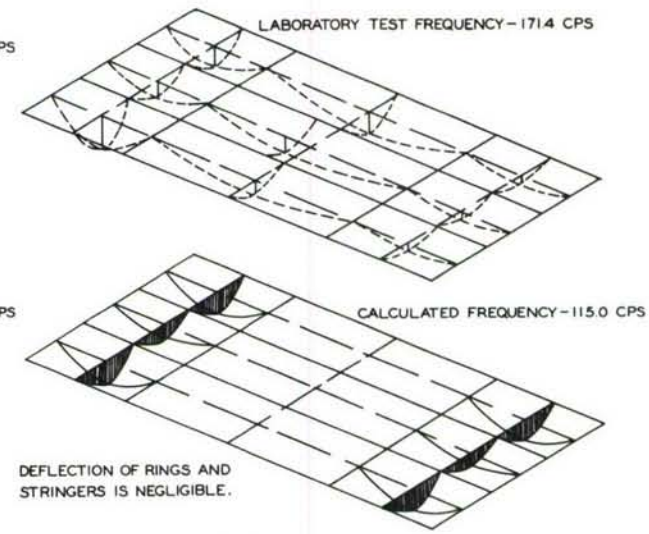

Figure III-5c.

Comparison of theoretical and laboratory test modes indicates the following:

a. The mode shapes for the fundamental and second modes are predicted reasonably well, but the predicted frequencies are 20% to 30% lower than determined by test.

b. Agreement on both mode shape and frequency is poor for the third mode, the comparison shown being valid only inasmuch as predicted higher modes have frequencies greater than 400 cps and higher test modes show node lines within individual panels, a mode shape not admissible with the coordinates used in the theoretical analysis. (See Figures IV-21 and IV-22, pages 127 and 128.)

C. Panel Damping from Laboratory Resonance Tests

Since knowledge of panel damping is essential to prediction of the panel response in the jet noise field, damping is estimated on the basis of resonances obtained during the laboratory loudspeaker tests.

1. 6- x 20-inch Panel

The damping ratios are calculated from the response curve, Figure IV-20, page 126.

The expression used is

$$\delta = \frac{\Delta f}{2 f_o}$$

where:

δ = damping ratio;

Δf = bandwidth measured at 0.7 of height of response curve for a given mode (cps);

f_o = the corresponding resonant frequency.

The results are shown in Table III-2.

TABLE III-2

DAMPING RATIOS - 6" X 20" PANEL

Mode	Fundamental	1 x 3	1 x 5	1 x 7
cps	110	178	323	449
cps	6	5	9	33
	.0273	.014	.014	.0368

2. Flat Panel A

The relative damping in a mode is determined from

$$\delta = \frac{P \sum a_i \Delta A_i}{\sum a_i^2 \Delta m} \times \frac{1}{2 \xi_o \omega_o^2}$$

where the pressure is assumed to be uniform over the surface of the panel. (Here the term $P \sum a_i \Delta A_i$ represents the generalized force in the mode, $\omega_o^2 \sum a_i^2 \Delta m$ the generalized stiffness.)

The mode shapes (a_i's) are given in Table III-4. The data pertinent to the calculation of δ are obtained from laboratory test results and are shown in Table III-3 with calculated values of δ.

TABLE III-3

DAMPING RATIOS - PANEL "A"

Mode cps	Generalized Mass lbs/sec^2/ft	Damping δ Ratio	ft^2	ft/sec^2
115.5	17.9 x 10^{-3}	.0204	1.358	173.
127.5	33.2 x 10^{-3}	.0222	1.026	95.2
181.4	16.8 x 10^{-3}	.0640	1.04	271.
185.0	10.7 x 10^{-3}	.0332	.644	441.
210.6	41.0 x 10^{-3}	.0187	.164	315.

TABLE III-4

PANEL "A" DATA

FOR FIELD RESPONSE CALCULATIONS

VALUES OF "a_i" FOR 115.5 CPS MODE

.00	.06	.10	.15	.19	.19	.15	.10	.06	.00	.06	.11
.22	.55	1.00	1.00	.55	.22	.11	.06	.06	.11	.22	.55
1.00	1.00	.55	.22	.11	.06	.00	.06	.10	.15	.19	.19
.15	.10	.06	.00								

VALUES OF "a_i" FOR 127.5 CPS MODE

-0.11	-0.22	-0.30	-0.82	-1.33	-1.37	-0.82	-0.30	-0.52	-0.26	-0.15	-0.19
0.07	0.70	1.00	0.96	0.37	-0.11	-0.19	-0.11	-0.11	-0.15	0.04	0.52
0.67	0.63	0.15	-0.11	-0.15	-0.04	-0.07	-0.11	-0.19	-0.82	-1.26	-1.30
.82	-0.22	-0.19	-0.15								

VALUES OF "a_i" FOR 181.4 CPS MODE

-.29	-.52	-.24	-.33	-.14	0.43	0.57	0.48	1.00	0.48	0.19	0.19
0.14	0.33	0.38	0.00	-.33	0.05	0.62	0.29	0.19	0.14	0.19	0.43
0.52	0.19	-.14	0.05	0.48	0.14	-.49	-.71	0.00	0.14	0.38	0.90
.86	0.19	0.48	0.05								

VALUES OF "a_i" FOR 185 CPS MODE

0.61	0.56	0.08	0.06	0.19	0.11	0.00	0.06	0.38	0.28	-.50	-.50
-.06	0.17	0.33	-.03	0.22	0.08	0.33	0.14	-.50	-.47	-.06	0.17
0.33	-.02	-.22	0.08	0.33	0.14	0.78	1.00	0.11	0.00	0.00	0.11
.11	0.06	0.36	0.25								

VALUES OF "a_i" FOR 210 CPS MODE

-.17	-.44	0.22	1.00	0.89	0.95	1.35	0.39	0.67	0.50	-.44	-.50
-.44	-.89	0.78	0.67	-.17	0.00	0.44	0.33	-.56	-.83	-.39	-1.05
1.00	0.55	-.61	0.00	0.28	0.39	-.78	-1.05	0.39	0.94	0.56	0.00
.44	0.11	0.28	0.17								

VALUES OF P_i^* (PSF) FOR 125 CPS BAND - AFTERBURNER CONDITION

5.85	6.55	6.76	6.46	7.21	6.58	6.31	6.50	6.57	6.76	6.60	7.25
6.92	6.21	6.90	5.20	5.80	6.47	8.93	7.04	6.60	7.25	6.92	6.21
6.90	5.20	5.80	6.47	8.93	7.04	5.85	6.55	6.76	6.46	7.21	6.58
6.31	6.50	6.57	6.76								

VALUES OF P_i^* (PSF) FOR 125 CPS BAND - MILITARY CONDITION

3.06	2.70	2.66	2.56	2.68	2.71	2.63	3.07	3.14	3.16	2.50	2.78
2.66	2.39	2.63	2.49	2.46	3.05	3.20	3.19	2.50	2.78	2.66	2.39
2.63	2.49	2.46	3.05	3.20	3.19	3.06	2.70	2.66	2.56	2.68	2.71
2.63	3.07	3.14	3.16								

VALUES OF P_i^* (PSF) FOR 200 CPS BAND - AFTERBURNER CONDITION

6.22	6.91	6.54	5.86	6.54	6.62	6.59	5.68	5.47	5.64	7.38	7.67
7.05	6.42	6.88	6.41	7.02	6.38	8.21	6.21	7.38	7.67	7.05	6.42
6.88	6.41	7.02	6.38	8.21	6.21	6.22	6.91	6.54	5.86	6.54	6.62
6.59	5.68	5.47	5.64								

VALUES OF P_i^* (PSF) FOR 200 CPS BAND - MILITARY CONDITION

2.54	2.69	2.44	2.14	2.36	2.30	2.44	2.21	2.19	2.18	3.00	3.03
2.69	2.34	2.55	2.61	2.87	2.43	2.42	2.32	3.00	3.03	2.69	2.34
2.55	2.61	2.82	2.43	2.42	2.32	2.54	2.69	2.44	2.14	2.36	2.30

VALUES OF ΔM_i - SLUGS PER ΔA_i

1.990E-3 1.990E-3 4.100E-3 1.990E-3 1.990E-3 1.990E-3 1.990E-3 4.100E-3 1.990E-3

1.990E-3 3.085E-3 3.085E-3 5.195E-3 3.085E-3 3.085E-3 3.085E-3 3.085E-3 5.195E-3

3.085E-3 3.085E-3 3.085E-3 3.085E-3 5.195E-3 3.085E-3 3.085E-3 3.085E-3 3.085E-3

5.195E-3 3.085E-3 3.085E-3 1.990E-3 1.990E-3 4.100E-3 1.990E-3 1.990E-3 1.990E-3

1.990E-3 4.100E-3 1.990E-3 1.990E-3

D. Theoretical Panel Response in Jet Noise Field

1. Outline of Theory

Panel response to the random pressures in the jet noise field is computed in terms of the response in each of the natural modes of the system, such modes representing a set of uncoupled single-degree-of-freedom, lightly damped systems.

If we divide the panel up into a number of small areas, and consider random pressures $P_i(\omega)$ acting on these areas, then the response of the panel in the mode may be considered as the response of a dynamic system to a set of simultaneous random disturbances.

In general, we may write (see Equation 9.43 of Reference 5):

$$\phi_y(\omega) = \sum_i \sum_j \phi_{ij}(\omega)\, T_i(\omega)\, T_j^*(\omega) \tag{1}$$

where $\phi_y(\omega)$ is the power spectral density of the response of the system,

$\phi_{ij}(\omega)$ is the cross-spectrum of the excitation at points "i" and "j,"

$T_i(\omega)$ is the frequency-response function relating excitation at point "i" to the response,

$T_j^*(\omega)$ is the complex conjugate of the frequency response function relating excitation at point "j" to the response.

In the present application of modal displacement response of the panel, let

$$\phi_{ij}(\omega) = (\phi_{Rij} + j\phi_{Iij})$$

and

$$T_i(\omega) = \frac{\Delta A_i\, a_i}{M_e\, \omega_o^2}(m + jn)$$

(from a generalized force per unit pressure $\Delta A_i a_i$, generalized stiffness $M_e \omega_o^2$, natural frequency ω_o, and dynamic factor $(m + jn)$.

Similarly,

$$T_i^*(\omega) = \frac{\Delta A_j\, a_j}{M_e\, \omega_o^2}(m - jn)$$

Then, substituting in Equation (1) the power spectral density of displacement in the mode will be given by:

$$\phi_\xi(\omega) = \frac{1}{M_e \omega_o^2} \sum_i \sum_j (\phi_{Rij} + j\phi_{Iij}) \Delta A_i \Delta A_j a_i \cdot a_j (m^2 + n^2) \tag{2}$$

Noting that ϕ_{ij} is the complex conjugate of ϕ_{ji}

i. e., $\phi_{ji} = \phi_{Rij} - j\phi_{Iij}$

then the terms $j\phi_{Iij}$ will disappear as a result of the summation.

Also, in terms of the measured pressure correlation,

$$\phi_{Rij} = C_{ij}(\phi_i\ \phi_j)^{1/2}$$

and with a dynamic magnification factor = γ^2 we may write

$$\gamma^2 = (m^2 + n^2)$$

Finally, then, the power spectral density of displacement in the mode may be written

$$\phi_\xi(\omega) = \frac{\gamma^2}{M_e \omega_o^2} \sum_i \sum_j C_{ij} (\phi_i^{1/2} a_i \Delta A_i)(\phi_j^{1/2} a_j \Delta A_j) \tag{3}$$

On the basis of the relatively small damping in the modes (see Section III-C), each mode is considered as a lightly damped single-degree-of-freedom system, and the mean square value of the response in the mode is derived from Equation (9) of Reference 11, where, for the present application,

$$\phi_{\ddot{\xi}}(\omega) = \frac{f(\omega)}{|Z(\omega)|^2}\,; \quad \omega_0 = 2\pi f_0$$

and

$$\beta = 2\delta\omega_0 = 4\pi\delta f_0\,; \quad f(\omega) = \frac{1}{2\pi} f(f)$$

Then the mean square displacement in the mode is given by:

$$\overline{\xi^2} = \frac{1}{64\pi^3\delta_o f_o^3 M_e^2}\left[\sum_i\sum_j(\phi_i^{1/2} a_i\Delta A_i)(\phi_j^{1/2} a_j\Delta A_j) C_{ij}\right] \tag{4}$$

and, since this power spectrum will be over a narrow band centered on $f = f_0$, the mean square acceleration due to response in the mode is approximately

$$\overline{\ddot{\xi}_o^2} = \frac{\pi f_o}{M_e^2 4\delta_o}\left[\sum_i\sum_j(\phi_i^{1/2} a_i\Delta A_i)(\phi_j^{1/2} a_j\Delta A_j) C_{ij}\right] \tag{5}$$

From Equation (3), with $\phi_i^{1/2} = \phi_j^{1/2}$ (i.e., the pressure field is homogeneous), we may obtain an expression for the frequency-response function relating the power spectral density of pressure to the power spectral density of acceleration response

$$|T(f)|^2 = \left(\frac{f}{f_o}\right)^4 \times \frac{1}{M_e^2} \times \frac{\sum_i\sum_j(a_i\Delta A_i)(a_j\Delta A_j) C_{ij}}{[1-(f/f_o)^2]^2 + 4\delta^2(f/f_o)^2} \tag{6}$$

With the further assumption that response in a number of different modes is uncorrelated, the mean square response due to response in a number of modes is

$$\overline{\xi^2} = \sum_n \overline{\xi_n^2} \tag{7}$$

We may also define, for convenience, the power spectral density of generalized force

$$\phi_F = \sum_i\sum_j C_{ij}(\phi_i^{1/2} a_i\Delta A_i)(\phi_j^{1/2} a_j\Delta A_j) \tag{8}$$

which is consistent with the expression for the power spectral density of the response given by Equation (3).

2. Response Calculations for 6" x 20" Panel

The power spectral density of generalized force, as defined by Equation (8) of Section III-D-1, is determined using the pressure data (Figures IV-27 and IV-34) of Section IV, and the mode shape data (Figure IV-20) of Section IV from the laboratory resonance data.

The mean square displacement and acceleration in the mode is then determined by use of Equation (4) and (5) of Section III-D-1, using the damping

determined from the laboratory resonance tests, and presented in Table III-2, page 98.

The power spectral density of generalized force at the mode frequency and the resulting mean square displacement and acceleration response in the modes are tabulated in Table III-5.

TABLE III-5

RESPONSE OF 6" X 20" PANEL

Mode	Freq.*	PSD of Generalized Force-lb^2/cps		Mean Square Displacement in Mode - ft^2		Mean Square Acceleration in Mode - g^2	
		Military	Afterburner	Military	Afterburner	Military	Afterburner
Fundamental	125	10.7×10^{-3}	42.5×10^{-3}	11.38×10^{-6}	44.8×10^{-6}	4,160	16,400
1 x 3	177	3.74×10^{-3}	23.8×10^{-3}	0.96×10^{-6}	6.12×10^{-6}	1,415	9,050
1 x 5	260	1.33×10^{-3}	22.4×10^{-3}	0.066×10^{-6}	1.11×10^{-6}	449	7,540
1 x 7	397	2.77×10^{-3}	2.64×10^{-3}	0.0212×10^{-6}	0.02×10^{-6}	788	750

*Note that the frequencies used here are those of the observed resonances in the field; discrepancies between these and the laboratory resonances are noted in Section III-B-1.

In addition to the determination of mean square responses, the frequency-response function of Equation (6) of Section III-D-1 is computed, and is used in conjunction with the pressure power spectral density data of Section IV to define continuous power spectra of accelerations over a frequency range centered on the mode frequency.

The power spectra so derived are then averaged over 10-cps bandwidths, thus simulating the effect of the approximately rectangular 10-cps filter used in presenting the test results of Figures IV-28 and IV-35, pages 133 and 137, respectively.

The resulting "10-cps" spectra are compared with test results in Figures III-6a and b and III-7a and b; in Figure III-6a and b the mode frequencies are those of the laboratory tests, while in Figure III-7a and b the field resonances have been assumed to define the mode frequencies.

3. Response Calculation for Flat Panel A

The procedure used is similar to that outlined in Section III-D-2 for the 6- x 20-inch panel; the mode shape data are obtained from the laboratory test data of Section IV and the damping in the modes from Table III-3, page 99.

The power spectral density of generalized force, and the resulting mean square displacement and acceleration response in the mode are tabulated in Table III-6.

As in Section III-D-2, the frequency-response function defined by Equation (7) of Section III-D-1 is computed, and used to obtain "10-cps" spectra. Such spectra are compared with test results in Figure III-8 where the mode frequencies are assumed to be defined by the field resonances.

TABLE III-6

RESPONSE OF PANEL "A"

Mode	Freq.*	PSD of Generalized Force-lb²/cps		Mean Square Displacement (in.²)		Mean Square Acceleration in Mode - g²	
		Military	Afterburner	Military	Afterburner	Military	Afterburner
1st	115.5	10.3	60.40	23.6×10^{-4}	139×10^{-4}	4,420	25,900
2nd	127.5	8.06	49.00	3.61×10^{-4}	11.1×10^{-4}	998	6,020
				$\Sigma 27.21 \times 10^{-4}$	150.1×10^{-4}	5,418	31,920
3rd	181.5	2.70	19.75	45.0×10^{-6}	330×10^{-6}	520	3,780
4th	185.5	0.93	7.15	70.5×10^{-6}	548×10^{-6}	860	6,600
5th	210.6	4.10	30.20	26.0×10^{-6}	190×10^{-6}	520	3,810
				$\Sigma 141.5 \times 10^{-6}$	$1,068 \times 10^{-6}$	1,900	14,190

*Note, as for 6" x 20" panel, that discrepancies between laboratory and field resonant frequencies occur; the frequencies used here being those of the laboratory resonances.

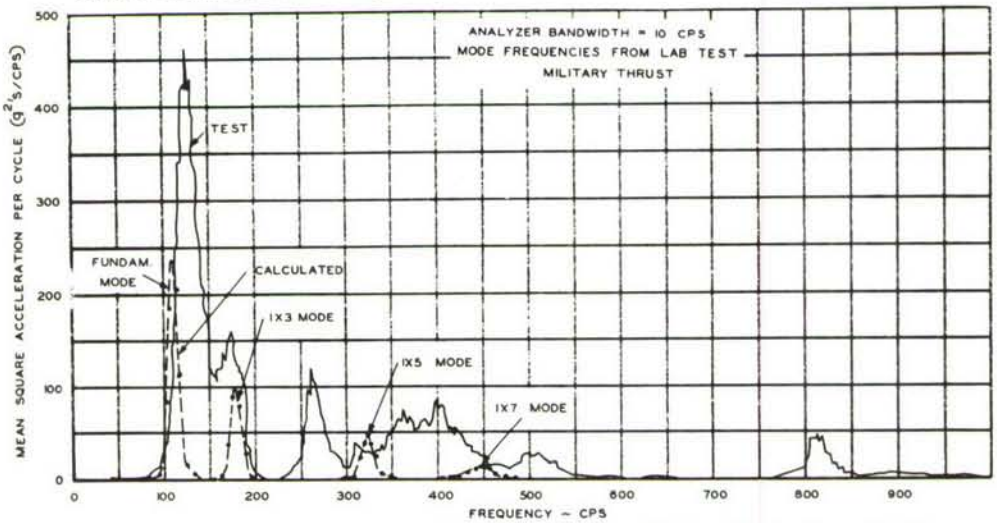

Figure III-6a. 6" x 20" Panel, Comparison of Predicted and Measured Acceleration Spectrum in Jet Noise Field (at Panel Center)

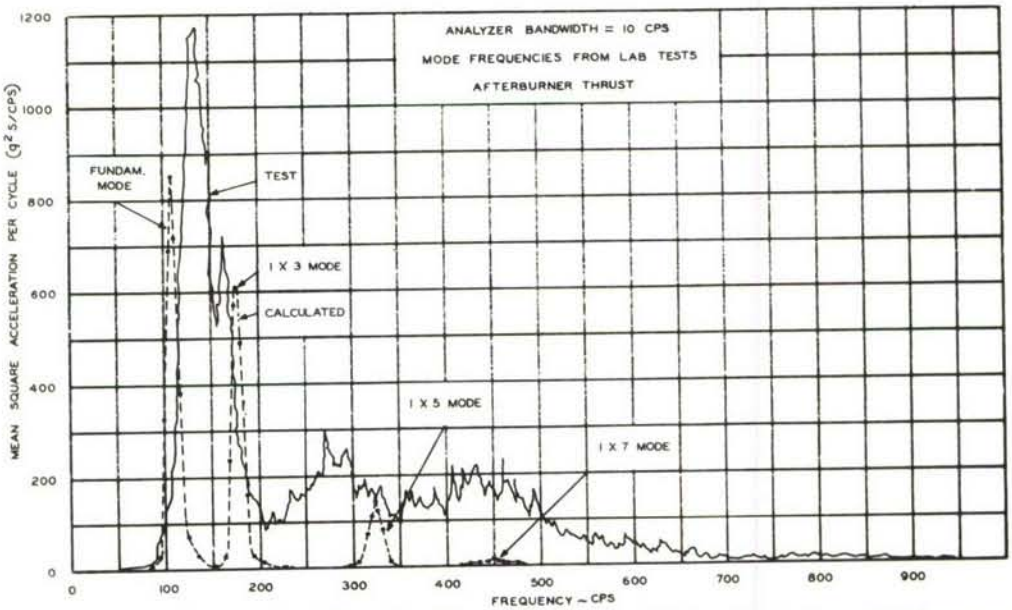

Figure III-6b. 6" x 20" Panel, Comparison of Predicted and Measured Acceleration Spectrum in Jet Noise Field (at Panel Center)

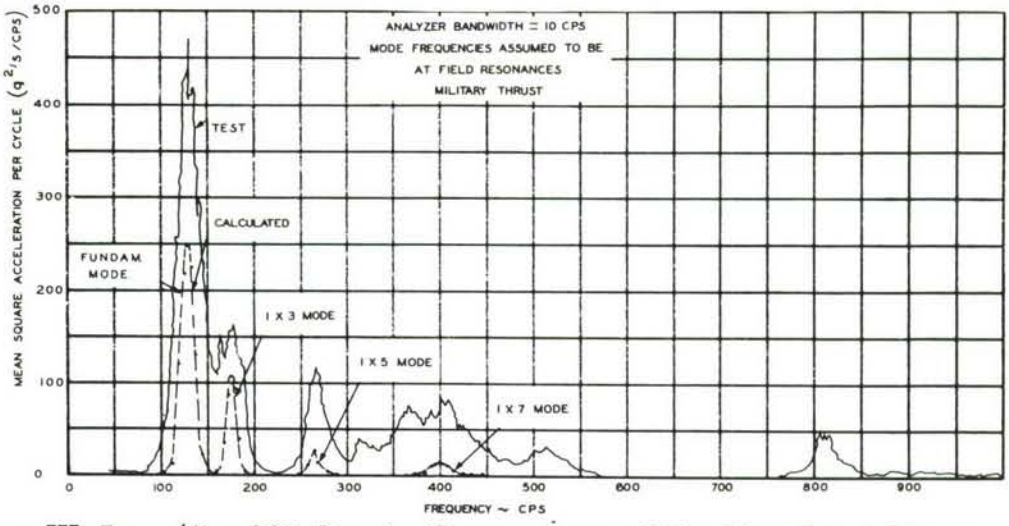

Figure III-7a. 6" x 20" Panel, Comparison of Predicted and Measured Acceleration Spectrum in Jet Noise Field (at Panel Center)

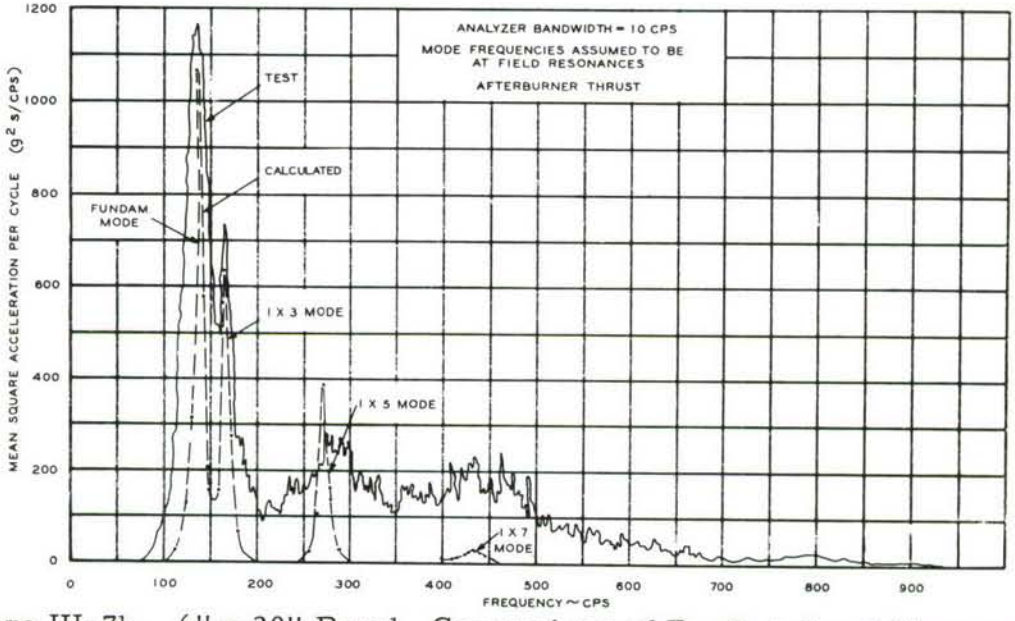

Figure III-7b. 6" x 20" Panel, Comparison of Predicted and Measured Acceleration Spectrum in Jet Noise Field (at Panel Center)

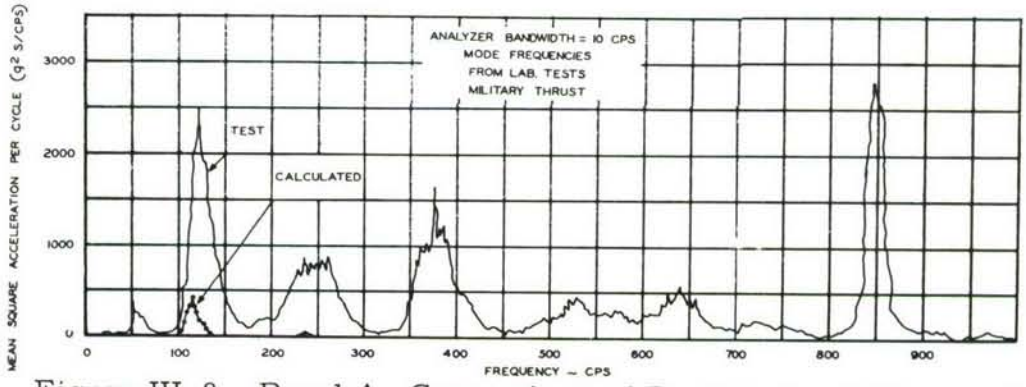

Figure III-8. Panel A, Comparison of Predicted and Measured Acceleration Spectrum in Jet Noise Field (at Panel Center)

E. Correlation of Accelerations and Bending Strains

For the 6- x 20-inch panel, field measurements were made of acceleration and bending strains at the center of the panel. (See Figures IV-35 and IV-38, pages 137 and 138.)

From Reference (13) (Timoshenko's "Theory of Plates and Shells"), the deflection at the center of a uniformly loaded rectangular plate may be written:

$$\xi_o = \alpha \frac{q\, a^4}{E\, h^3}$$

and the bending stress at the center may be written

$$f_B = \beta\, q\, a^2 \frac{6}{h^2}$$

where α and β are functions of panel aspect ratio and edge conditions. The ratio between bending stress and central deflection will not be sensitive to changes of load distribution, so that, for the predominantly inertial loading occurring at resonance in the fundamental modes, we may write:

$$\left.\frac{f_B}{\xi_o}\right|_{RES.} = \left.\frac{f_B}{\xi_o}\right|_{\substack{UNIF.\\PRESS}} = \frac{\beta}{\alpha} \times \frac{6Eh}{a^2}$$

And the ratio of the power spectral densities of stress and acceleration may then be written

$$\frac{\phi_{STRESS}}{\phi_{ACCEL.}} = \left[\frac{\beta}{\alpha} \times \frac{6Eh}{a^2} \times \frac{386}{(2\pi f)^2}\right]^2 \frac{(PSI)^2}{g^2}$$

With $E = 10^7\ psi$; $h = .032\ in$; $a = 6\ in$

and values of β and α from Reference (13), the ratio of power spectral densities is determined to be:

$$\frac{\phi_{STRESS}}{\phi_{ACCEL.}} = \frac{.213 \times 10^{12}}{f^4}$$ for a plate with simply supported edges,

or

$$= \frac{.60 \times 10^{12}}{f^4}$$ for a plate with clamped edges.

For the Frequency range 100 to 150 cps, covering the fundamental mode resonance, the values of $\phi_{STRESS}/\phi_{ACCEL}$ are computed as above, and are compared with the value based on measured stress and acceleration in Figure III-9.

It may be seen that, in the vicinity of mode resonance (120 to 130 cps), the test results are in reasonable agreement with theory for a simply supported plate.

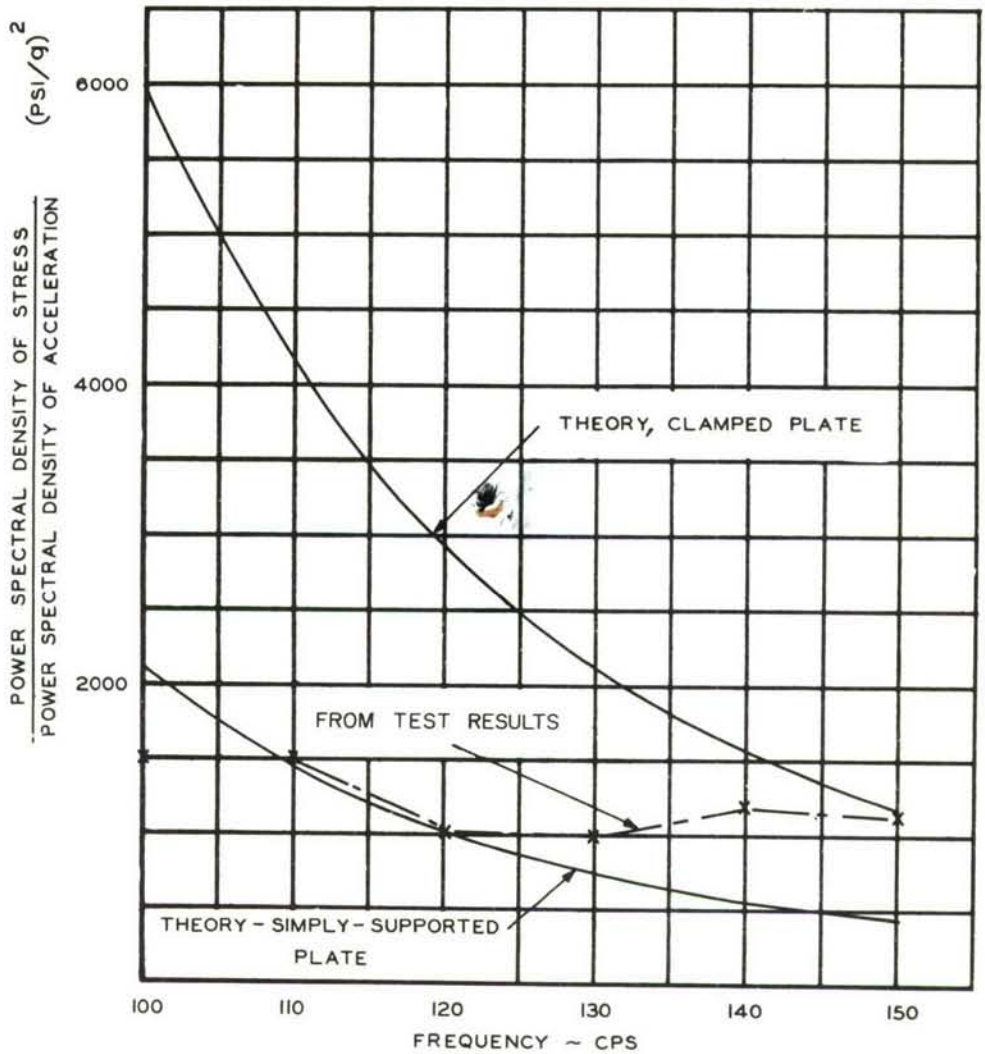

Figure III-9. Relation between Acceleration and Bending Stress at Center of Panel - in Fundamental Mode - 6" x 20" Panel Military Thrust Condition

F. Discussion

1. Panel Natural Modes

a. 6- x 20-inch Panel

It would appear that difficulty in assessing the degree of edge fixity is at least partly responsible for the differences in natural frequency between predictions and test results. Thus, for the 6- x 20-inch panel, the supposedly "clamped edge" panel has natural frequencies approximating the theoretical "simply supported edge" condition.

Reasonable agreement appears to be obtained between the theoretical mode shapes and the node line locations and relative acceleration magnitudes determined experimentally (See Figure III-2).

b. Flat Panel A

The prediction of natural frequencies for panel A which are lower than determined experimentally, by 20% to 30%, may be considered to be due in some measure to the assumption of simply supported panel edge conditions; in practice the continuity of panels across supporting members, and some rotational restraint at these members, may render a "clamped edge" condition more appropriate.

The inability to define precisely the effective stiffness of reinforcing members attached to the panel surface, and the effect of discontinuities present in such members, may also give rise to differences between predicted and test modes.

The agreement between theoretical and test mode shapes appears to be good for the first two modes (see Figure III-5a and b, page 97) but qualitative differences are apparent in the third mode (Figure III-5c, page 97). As indicated in Section III-B-2, a number of laboratory test modes exists in higher frequencies in which node lines appear within the individual panel boundaries. The generalized coordinates used in theoretical mode determination (see Figure III-3, page 95) do not permit such modes, but, clearly, could be extended to do so.

Such extension of the method of mode determination, and inclusion of the effects of edge fixity, would be expected to give improved agreement with test results. However, it should be noted (see Figure IV-22, page 128) that the laboratory test results show a lack of symmetry in some cases, a result possibly indicative of marked sensitivity to slightly different boundary conditions resulting from the use of "J" section stiffening members asymmetrically disposed. Any inclusion of such effects in a theoretical mode prediction would require a very much more detailed analysis of the panel edge support than has been carried out; it would probably be preferable in such analysis to utilize the Lagrange rather than Rayleigh method.

2. Panel Response in Jet Noise Field

The two most noteworthy features of the panel response in the jet noise field are:

(1) the apparent shift of mode frequency from the value determined by laboratory tests;

(2) the marked difference between the levels of predicted and measured acceleration response.

a. Mode Frequency Shift

Such a frequency shift is most clearly exhibited in the 6- x 20-inch panel results; for example, see Figures III-6a and b, page 103. Similar frequency variations have been noted in the laboratory test (see Section IV) and are

ascribed to varying temperature environment and differential expansion of panel and edge members. A similar phenomenon may be responsible for frequency shifts between laboratory and field results.

b. Comparison of Predicted and Test Acceleration Response

The differences shown in Figures III-7a and b and III-8, page 104, are of such a magnitude that a review of the procedures used in predicting response and examination of possible shortcomings of these procedures is appropriate.

The concept of response in each of a number of sensibly uncoupled, lightly damped natural modes would appear to be validated by examination of the power spectra of applied pressure and acceleration response in the field (see Figures IV-27 and IV-28, for example). It may be seen that, with a relatively flat input spectrum, the acceleration spectrum has the sharp peaks characteristic of resonant response of a lightly damped system.

It appears unlikely that differences in panel damping appropriate to laboratory and field tests would result in the differences noted. The damping determined from laboratory tests (see Section III-C) might be expected to be lower rather than higher than in field tests, as a result of the absorbent backing used in the field (see Figure IV-8, page 119), thereby resulting in field response lower than predicted.

The characteristics of the acceleration response spectra compared with the predicted spectra suggest a somewhat larger damping and very much larger flexibility than derived from laboratory tests. This large flexibility is, of course, at variance with the fair agreement in resonant frequency between laboratory and field results.

It is of interest, in this connection, to compare static stiffnesses measured in static laboratory tests, static stiffnesses derived from fundamental mode characteristics, and the dynamic response as measured in the field tests. Such comparisons are made below for panel A.

From the static pressure test results presented in Figure IV-13, page 122, static stiffness in terms of uniform pressure and deflection at center panel

$$= 830 \text{ lbs/ft}^2\text{/in}$$

From the fundamental mode characteristics defined in Section III-C-2, the generalized stiffness

$$= M_e\omega_o^2 = 17.9 \times 10^{-3} (2\pi \times 115.5)^2 = 9,470 \text{ lb. sec.}^2\text{/ft.}$$

$$= 790 \text{ lb. sec.}^2\text{/in.}$$

With a static stiffness (as above) = k lb. sec.^{2}/in., a damping factor δ, a power spectral density of pressure $= \phi_p$, then at resonance, power spectral density of acceleration $= \phi_a$

$$= \phi_p (4\pi^2 f_o^2 / 2\delta K \times 386)^2 \quad g^2/cps$$

with

$f_o = 115.5$ cps; $\delta = .03$ (See Section III-B)

$K \approx 800$ (from above)

then

$$\frac{\phi_a}{\phi_p} = 800 \, (g^2/\overline{PSF}^2)$$

By comparison of the pressure spectrum of Figure IV-48, page 144, with the computed and measured accelerations of Figure III-8, page 104, it may be seen that, at resonance, use of the computed response gives

$$\frac{\phi_a}{\phi_p} \approx \frac{410}{.45} = 910 \, (g^2/\overline{PSF}^2)$$

whereas the measured response gives

$$\frac{\phi_a}{\phi_p} \approx \frac{2,400}{.45} = 5,340 (g^2/\overline{PSF}^2)$$

It may thus be seen that the computed results are consistent with the static test results and with the fundamental mode characteristics, for a damping of about 3%, whereas the measured resonant peak would require a damping of about 1 to 2% for compatibility with static characteristics, which damping is not compatible with the breadth of the measured resonance.

SECTION IV

RESPONSE MEASUREMENTS

A. Introduction and Objectives

1. Introduction

This section covers the experimental work conducted to describe the response characteristics of the structural elements selected for study. All data obtained in this phase were used to supply some fundamental parameter related to the analysis and prediction of structural responses. To be more specific, that portion of the experimental work conducted in the laboratory involved both static and discrete frequency panel loading conditions. The results of such tests consisted of spring rate characteristics, response frequencies and mode shapes, and structural damping. All such data were used as inputs for the analytical work. The remaining portion of the experimental data was primarily concerned with the measurement of panel response to jet noise excitation. Such information was then used as the basis for the evaluation of predicted response.

The experimental work of the response section of this study has been limited to use of specimens falling in the general classification of "typical structures." As such, they represented several types of lightweight exterior surface panels of modern airframe design. Each specimen contained representative characteristics of asymmetry, non-uniform boundary conditions for the complete panel, as well as the elements within the panel, normal variations in workmanship, and a normally complex distribution of mass and stiffness. These varied characteristics constitute a major departure from the use of the idealized panel. This, however, fulfills one of the basic objectives of the study, i.e., the prediction of the response characteristics of complex structures. It is intended that this approach would bridge the gap between the analysis of an idealized structure and a full-scale vehicle structure. In an attempt to carry this objective one step further, one panel configuration was built in two sizes, one of which contained three times the area of the smaller panel.

In the design of the test panels no attempt was made to obtain optimum strength of stiffness-to-weight ratios since no real basis for such optimization existed. Following the same reasoning, the construction details are considered typical and no further attempt was made to eliminate or reduce the local stress concentrators. However, one objective in the selection of the various configurations was to obtain a wide range of stiffness and strength characteristics. Some additional variation was also obtained by incorporating a nominal amount of curvature in three of the panel specimens.

2. Objectives

The objectives of the experimental phase of the structural response study were as follows:

(a) to measure under laboratory conditions of discrete frequency sonic excitation, the significant mode shapes, resonant frequencies, and the response amplitudes of the various panel specimens;

(b) to measure the response characteristics of the various structural configurations under several defined conditions of jet noise excitation;

(c) to compare and evaluate the response characteristics of the several panel configurations excited by the various loading conditions.

B. Test Speciments and Equipment

1. Description of Test Panels

The bulk of the data was obtained with panels whose nominal size was forty by sixty inches. Three different configurations, both flat and curved (60-inch radius) were constructed in this size. One of the above configurations was constructed as flat panels with nominal dimensions of forty by sixty inches. All panels retain the identical substructure rib spacing of twenty inches. A summary description of all panels is shown in Table IV-1. The detailed description of each panel type is shown by the drawings reproduced in Figures IV-1 through IV-4, pages 112 through 115.

TABLE IV-1

IDENTIFICATION OF TEST PANELS

Panel Identification	Inches	Inches	Longitudinal Stiffener Spacing Inches	Skin Thickness Inches	Description of Configuration
A (Flat)	20 x 40	20	6	.040	Skin and Stringer - Fig. 4-2
A (Curved)	20 x 40	20	6	.040	Skin and Stringer - Fig. 4-2
B (Flat)	20 x 40	20	-	.012	Honeycomb Sandwich - Fig. 4-3
B (Curved)	20 x 40	20	-	.012	Honeycomb Sandwich - Fig. 4-3
D (Flat)	20 x 40	20	.9		Corrugated Inner Skin - Fig. 4-4
D (Curved)	20 x 40	20	.9	.012	Corrugated Inner Skin - Fig. 4-4
E (Flat)	40 x 60	20	6	.012	Skin and Stringer - Fig. 4-5
6 x 20	6 x 20	None	None	.040	Plain Sheet
C Flat/Curved			--Not Used--		

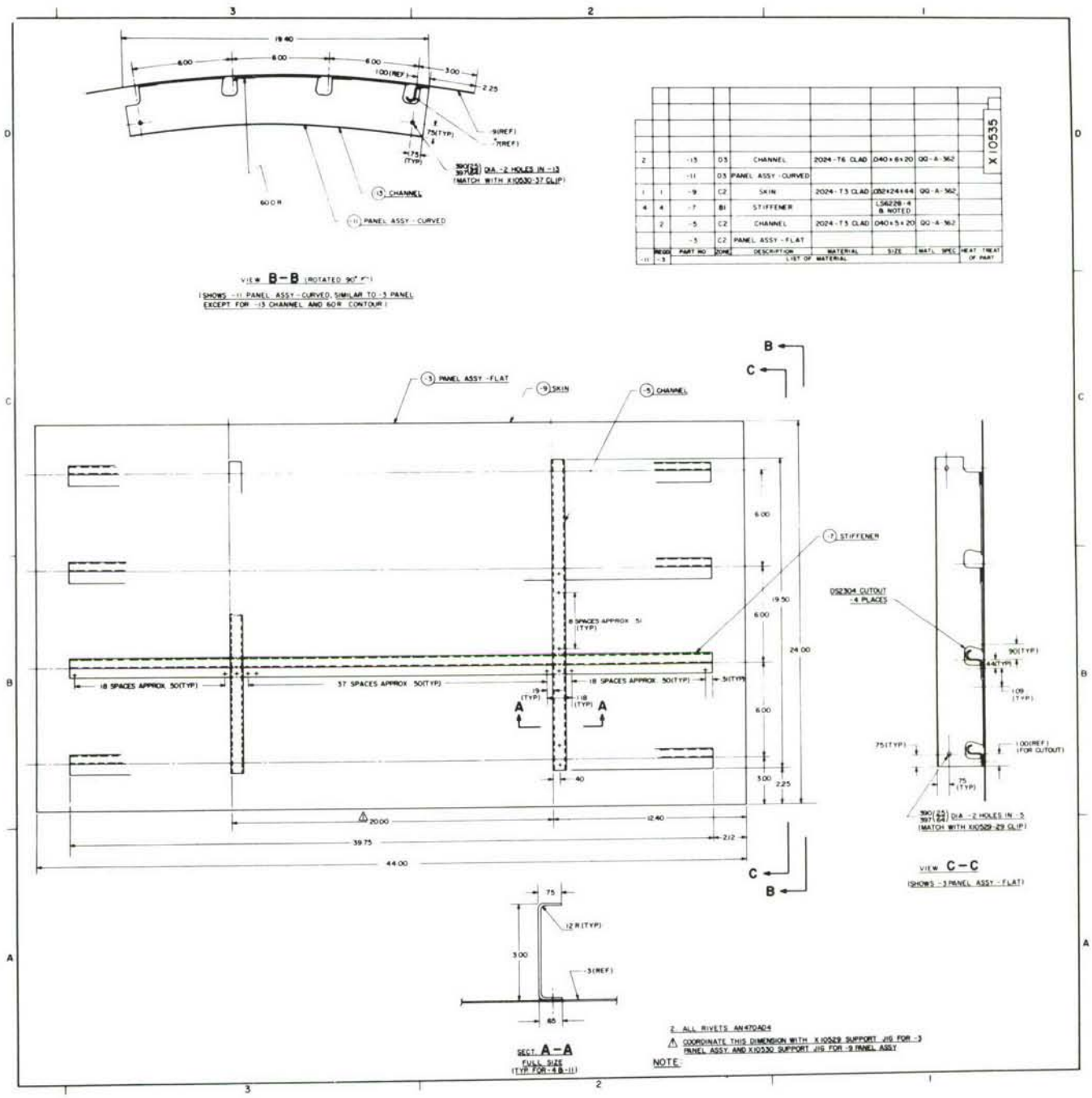

Figure IV-1. Panel A

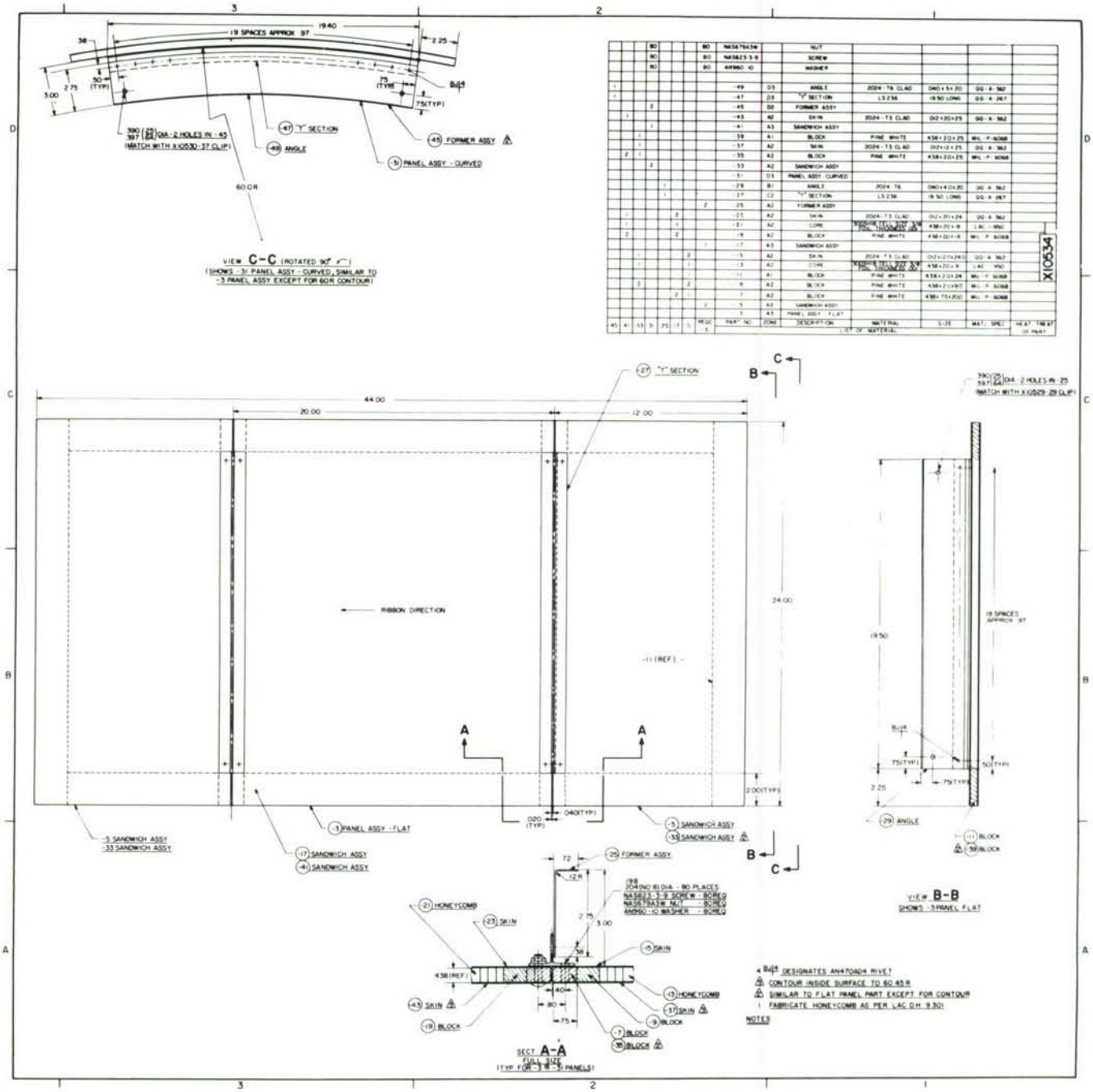

Figure IV-2. Panel B

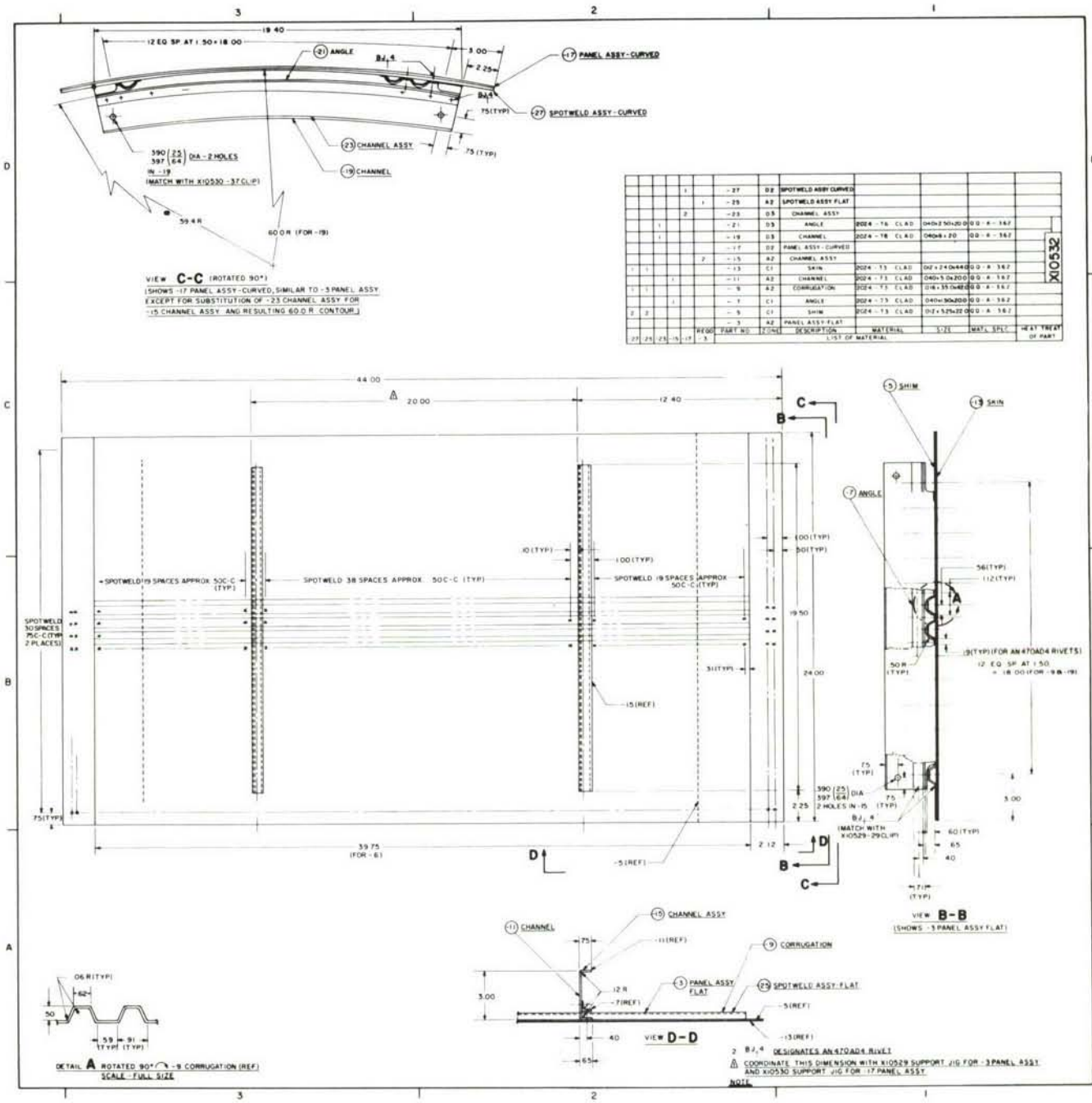

Figure IV-3. Panel D

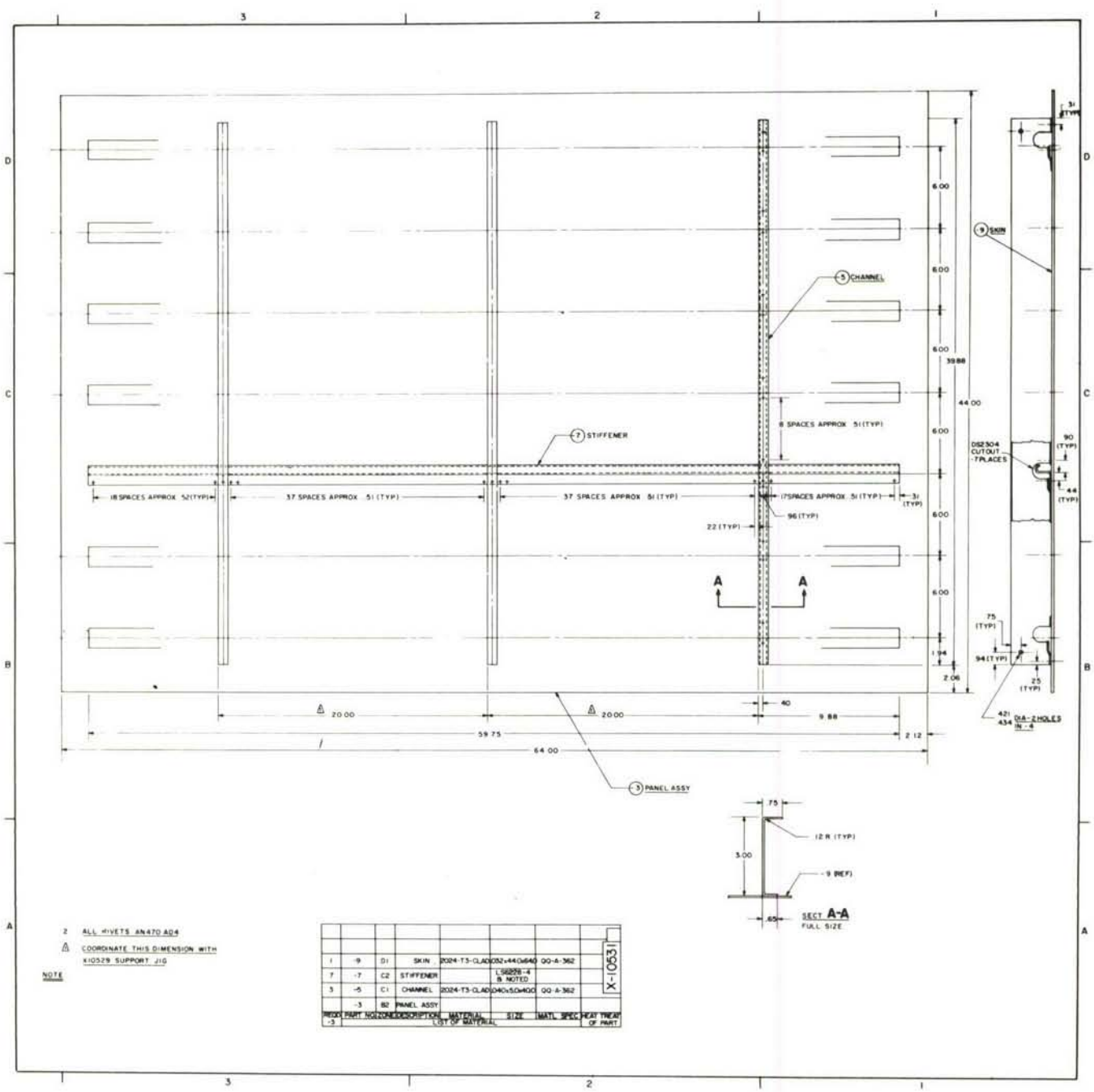

2 ALL RIVETS AN470 AD4

△ COORDINATE THIS DIMENSION WITH K10529 SUPPORT JIG

NOTE

ITEM	PART NO.	ZONE	DESCRIPTION	MATERIAL SIZE	MATL SPEC	HEAT TREAT OF PART
	-3		LIST OF MATERIAL			
1	-9	D1	SKIN	2024-T3-CLAD.052×44.0×64.0	QQ-A-362	
7	-7	C2	STIFFENER	L 56258-4 AS NOTED		
5	-5	C1	CHANNEL	2024-T3-CLAD.040×5.0×40.0	QQ-A-362	
	-3	B2	PANEL ASSY			

X-1053

Figure IV-4. Panel E

In addition to the test panels described above, one simple instrumented panel was made for the purpose of checking experimental and analytical procedures. This panel consisted of an .032-inch thick aluminum sheet measuring 6 x 20 inches between clamped boundaries. This size was selected to correspond to skin panel sizes of Type "A" configuration. A photograph of the mounted panel is shown in Figure IV-5. This assembly was used in both the laboratory and the field phases of the experimental program.

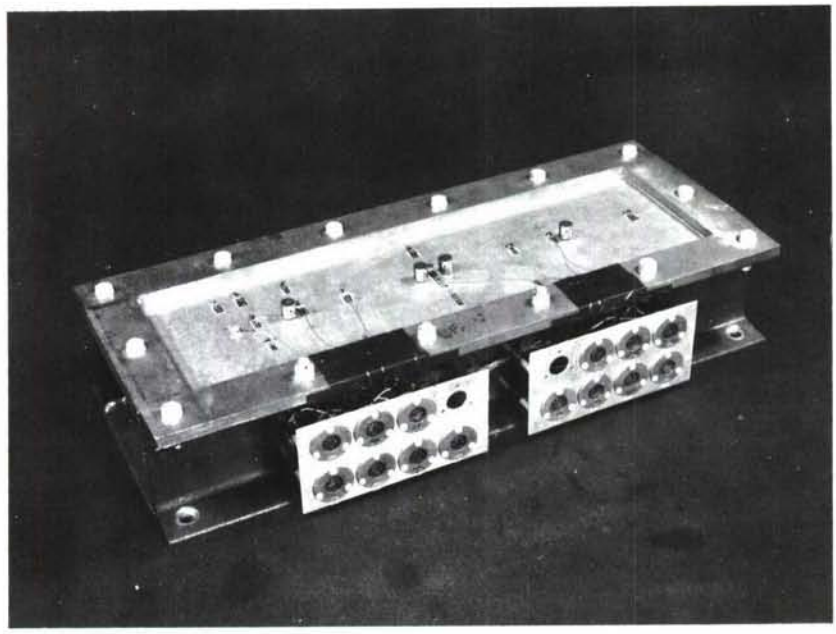

Figure IV-5. 6" x 20" Test Panel

2. Jigs and Fixtures

a. Field Tests

During the measurements of structural response, bounded field pressure and correlation and free field correlations under jet noise excitation, a special jig was used to serve as the boundary and support for the test panels. The face of this jig is sixty-four inches long and forty-four inches high. The horizontal centerline of this area was at the same elevation as the longitudinal axis of the test engine. The details of this jig (Dwg. X-10529), which was used for all of the flat panels, are shown in Figure IV-6. The similar jig for mounting curved panels (Dwg. X-10530) is shown in Figure IV-7. The rear of the above panel support jigs was closed by means of the glass fiber packed attenuation chamber (X-10527) shown in Figure IV-8.

All panels were mounted in the above support jigs by clamping both the periphery of the surface skin and the rib ends. These panels were reclamped periodically to allow the test panel to partially relieve itself of strains induced by differential thermal expansion of the aluminum specimen and the steel jig.

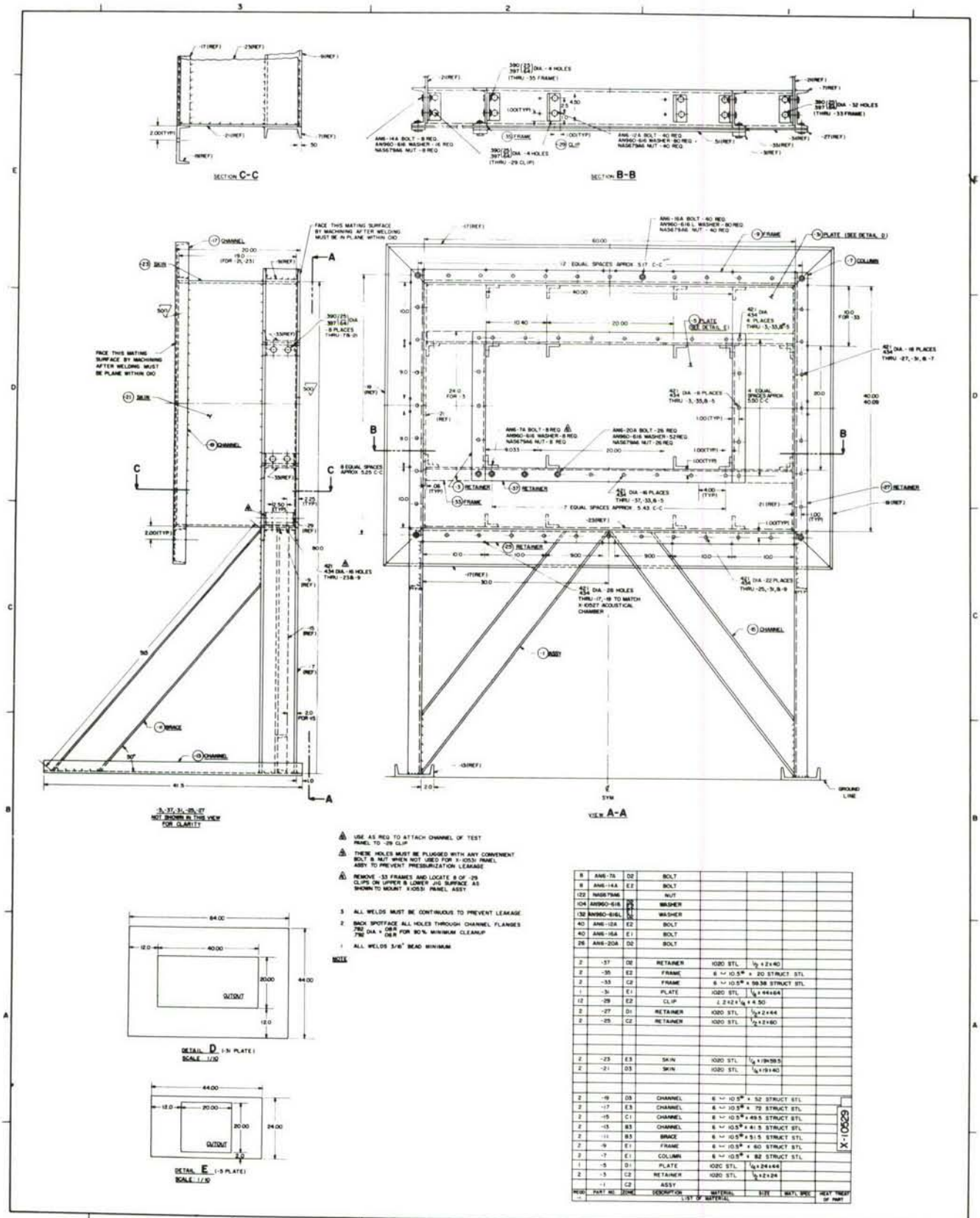

Figure IV-6. Flat Panel, Support Jig

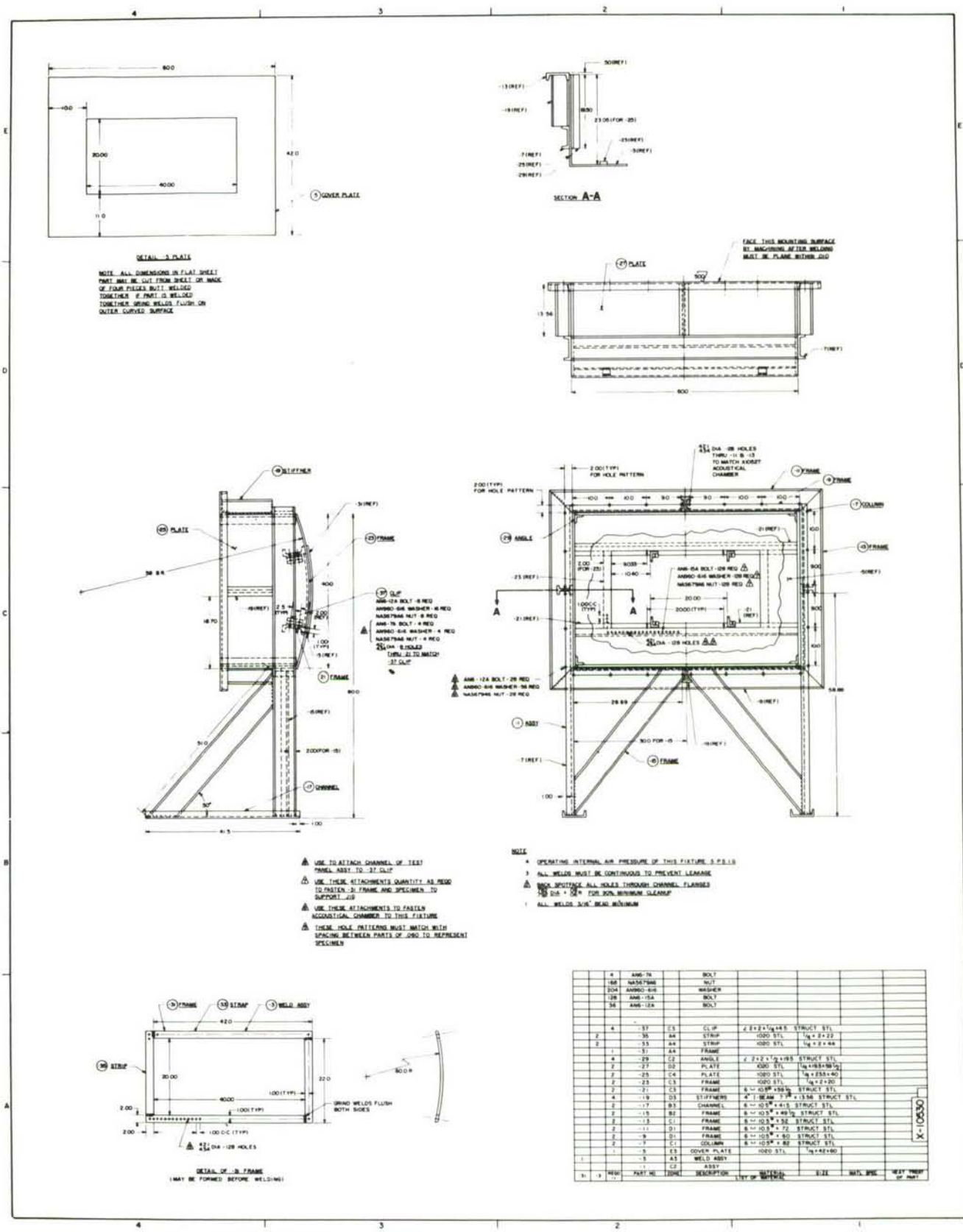

Figure IV-7. Support Jig, Curved Panel

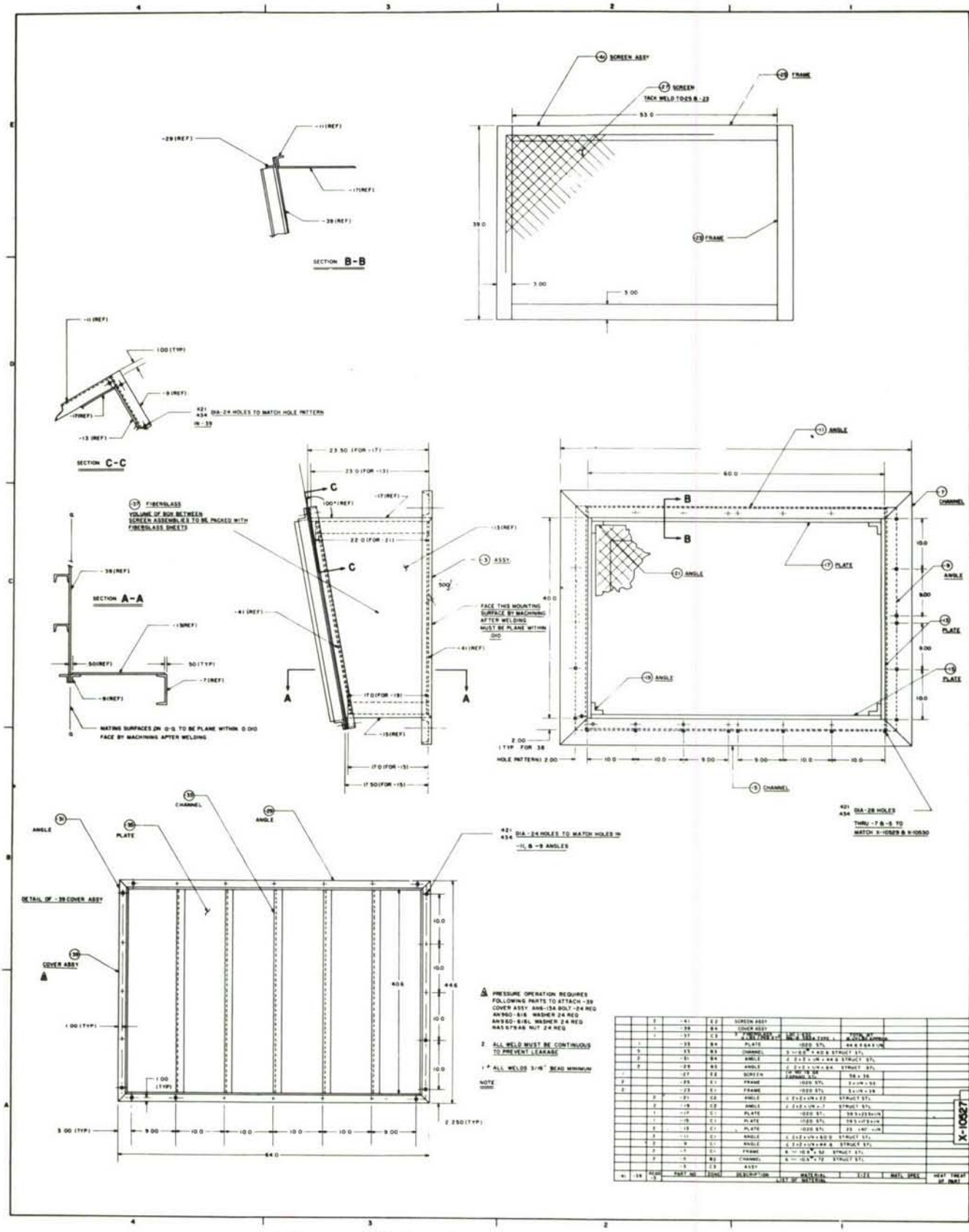

Figure IV-8. Acoustical Chamber

The noise field was generated by means of a YJ-79-3 jet engine which was bailed from government stores specifically for use in this program. This engine and its installation in the test stand are shown in Figure IV-9.

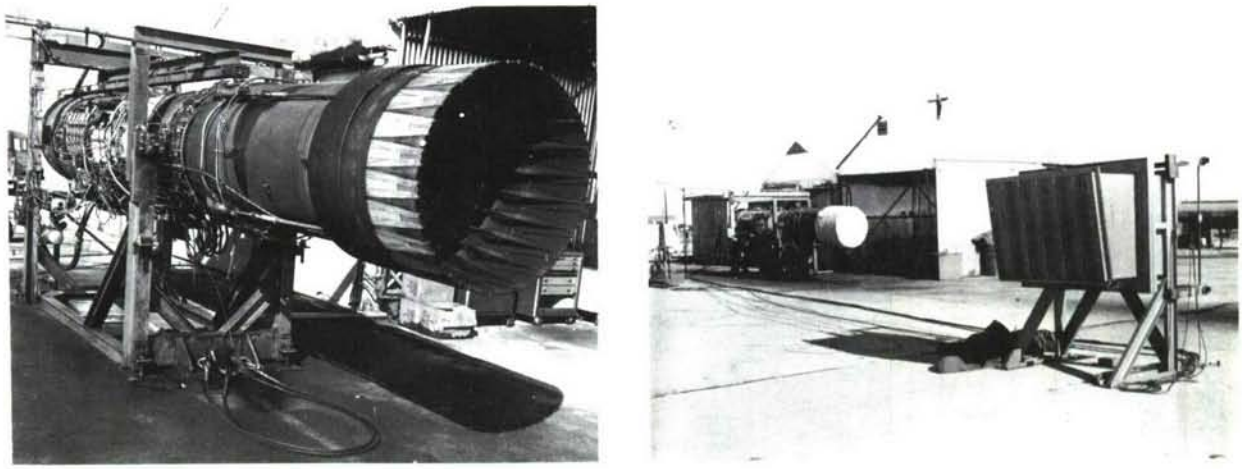

Figure IV-9. Engine Stand Setup

b. Laboratory Tests

During the laboratory measurements the 20- x 40-inch panels were mounted in a steel frame which duplicated the attachment of the field tests. Provisions were made to close the back of this frame for the application of static pressure. A photograph of this installation as used in the test is shown in Figure IV-10.

Figure IV-10. Test Setup for Dynamic Response and Mode Survey under Discrete Frequencies - Panel A

Also shown in the above referenced figure are the two speakers which were used to drive the test panels. This arrangement produced a plain sinusoidal pressure wave striking the test panel with grazing incidence. These two speakers were similarly used with the test panel measuring 40 x 60 inches. During the latter tests, the panels were clamped in an adjustable frame made from aluminum extrusions.

C. Test Procedures and Results

1. Laboratory Test Procedures and Results

The tests and procedures of the laboratory phase of the program served to define basic response characteristics of the test panels. Such characteristics include: (a) the strain and deflection distribution vs. static pressure loading, (b) the definition of mode shapes under discrete frequency excitations, and (c) the corresponding measurements of bending and tensile strain, normal acceleration, and normal velocity. Both the data and the procedures employed are described below.

a. Static Pressure Test (6- x 20-inch Panel)

The test panel was mounted in its clamped edge frame. A pressure chamber was provided behind the panel by covering the back of the mounting frame with a steel plate. Positive internal air pressure was then applied to the panel in increments from zero to ten inches of water. Normal deflections plus bending and tension strains were measured at the center of the panel. These data are presented in Figure IV-11.

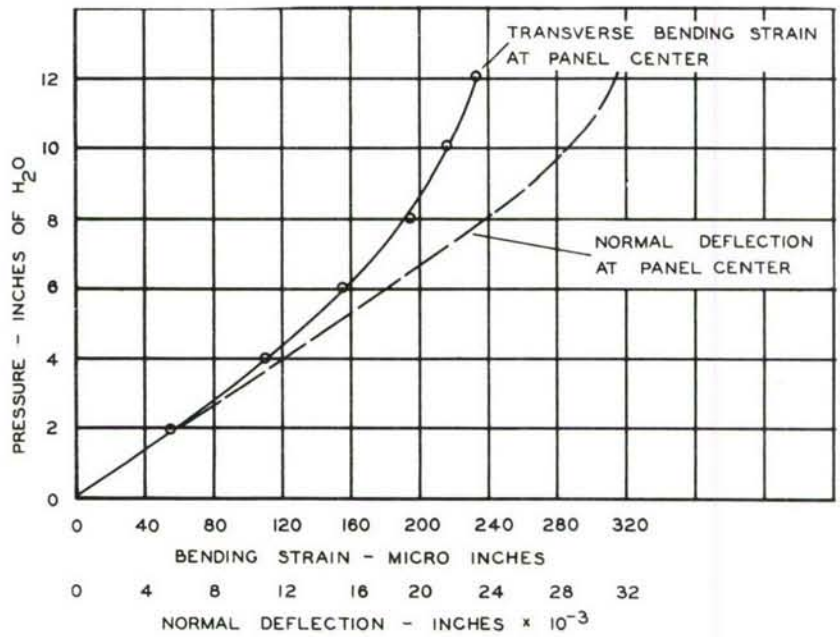

Figure IV-11. Static Pressure Test - 6" x 20" x .032 Panel

b. Static Pressure Test (Panel A)

The same procedures were followed here as in the static test of the 6- by 20-inch test panel. Figure IV-12 shows the setup. Measured strain, deflection of the panel surface and location of measurement are shown in Figures IV-13 through IV-18, pages 122 through 125.

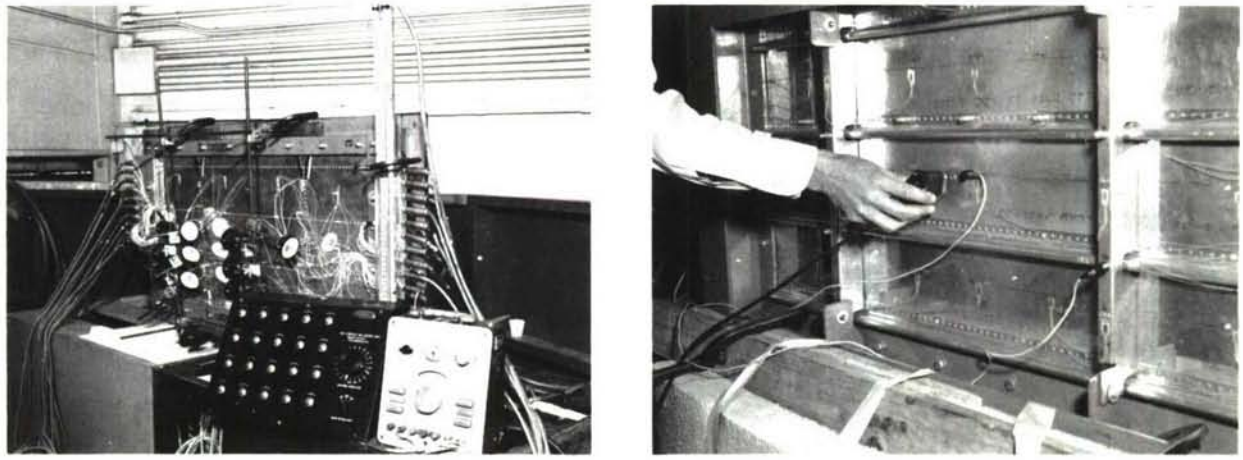

(a) (b)

Figure IV-12. Panel A: (a) Static Strain and Deflection Measurement, (b) Velocity Contour Survey under Discrete Frequencies

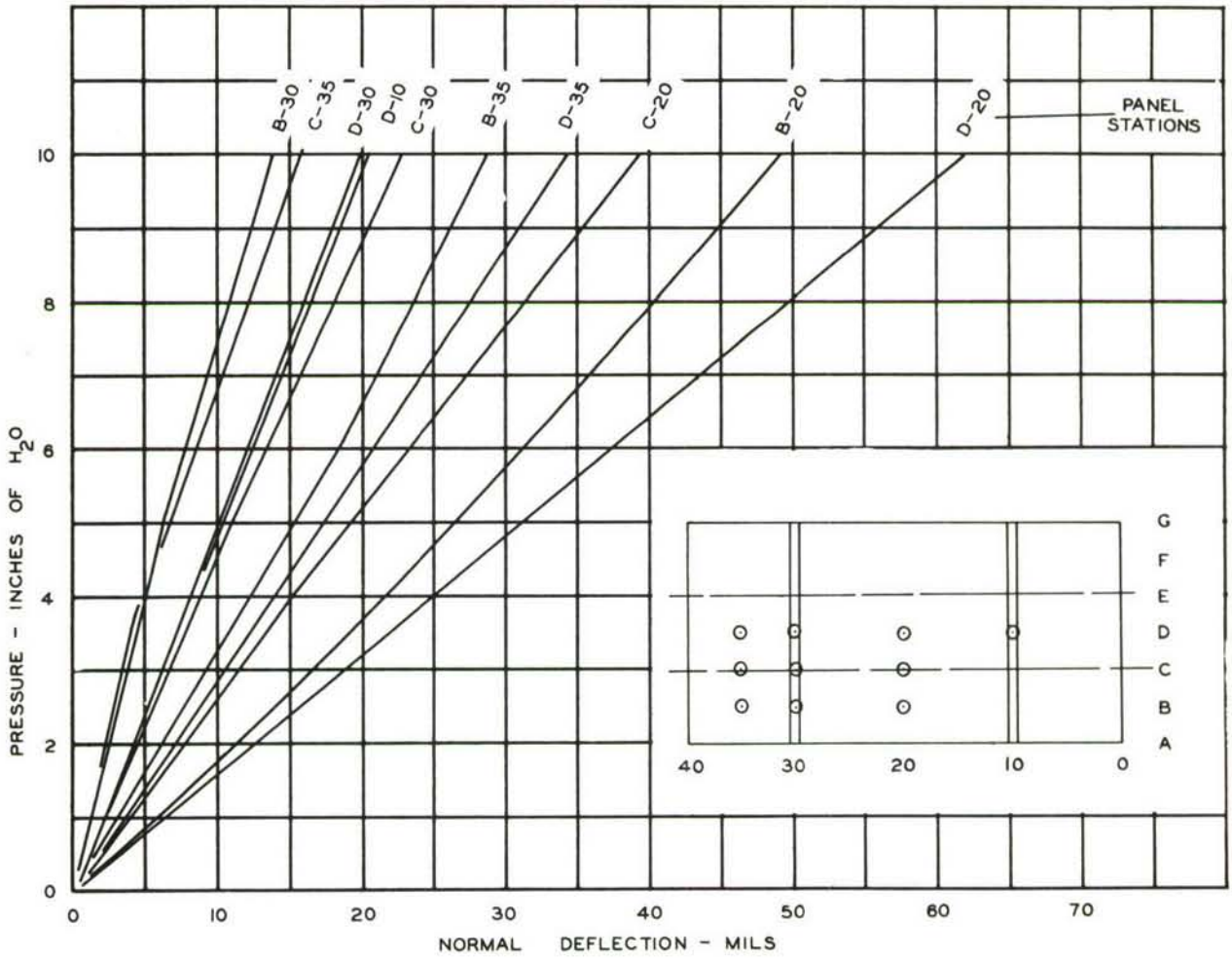

Figure IV-13. Static Deflection - Panel A

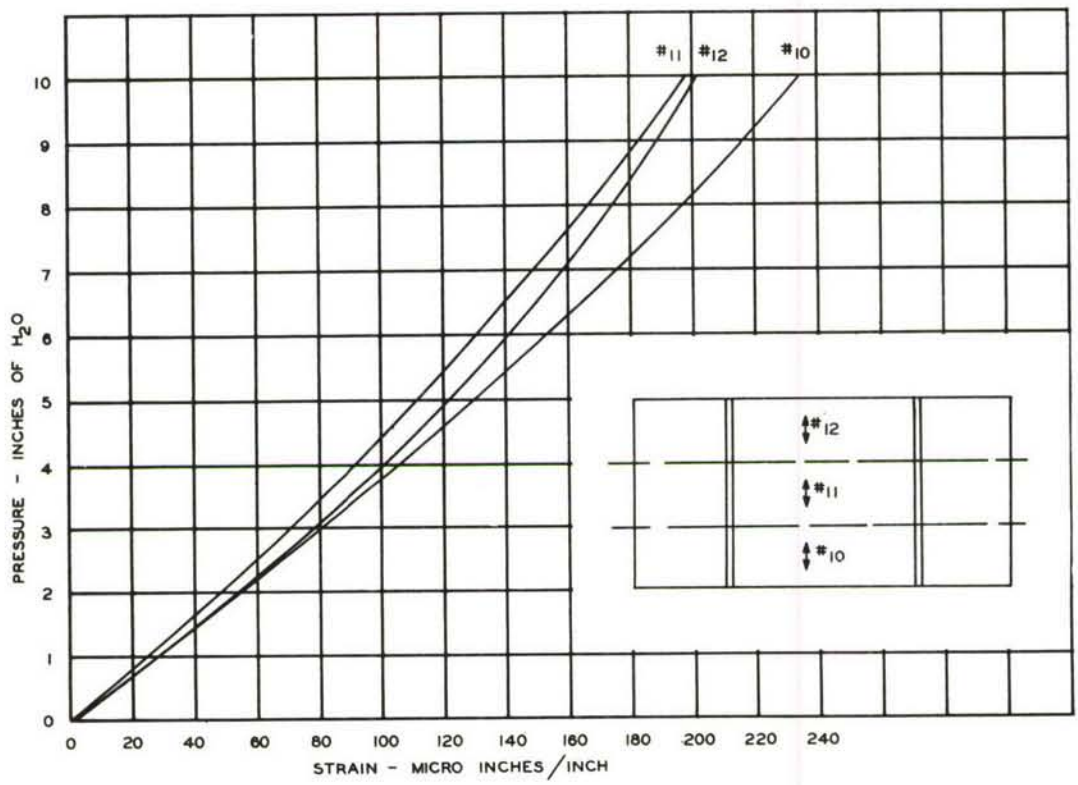

Figure IV-14. Static Bending Strain - Panel A

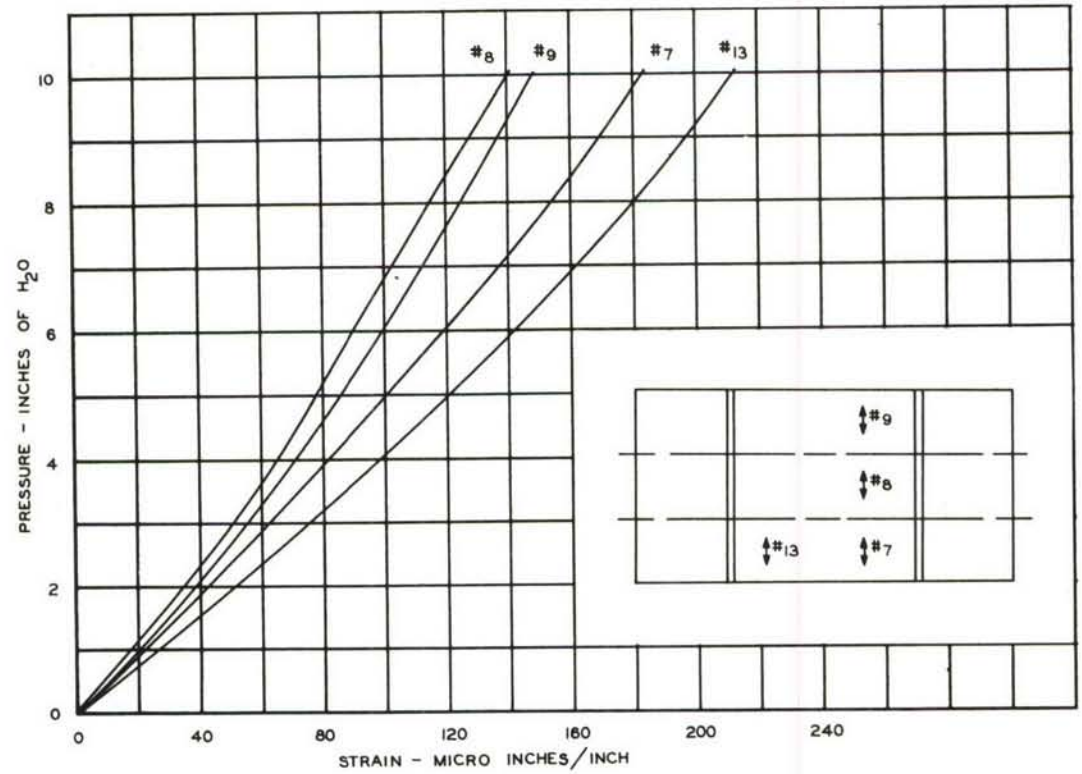

Figure IV-15. Static Bending Strain - Panel A

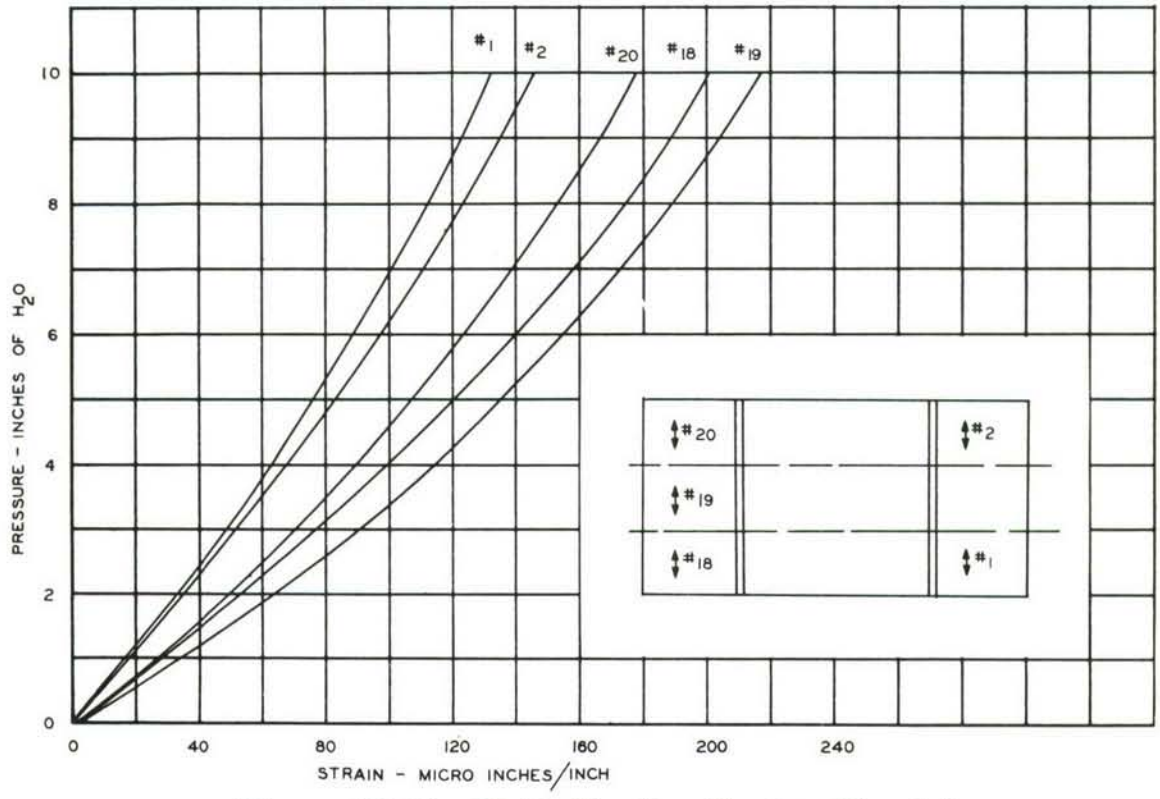

Figure IV-16. Static Bending Strain - Panel A

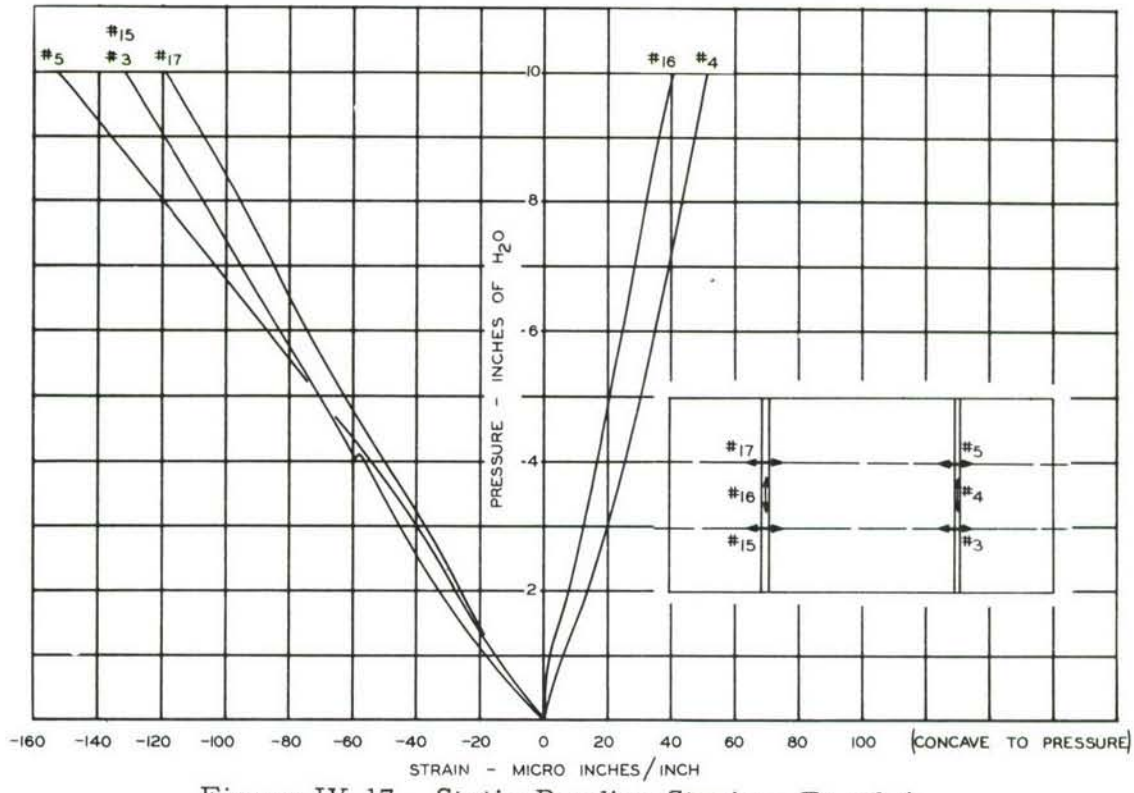

Figure IV-17. Static Bending Strain - Panel A

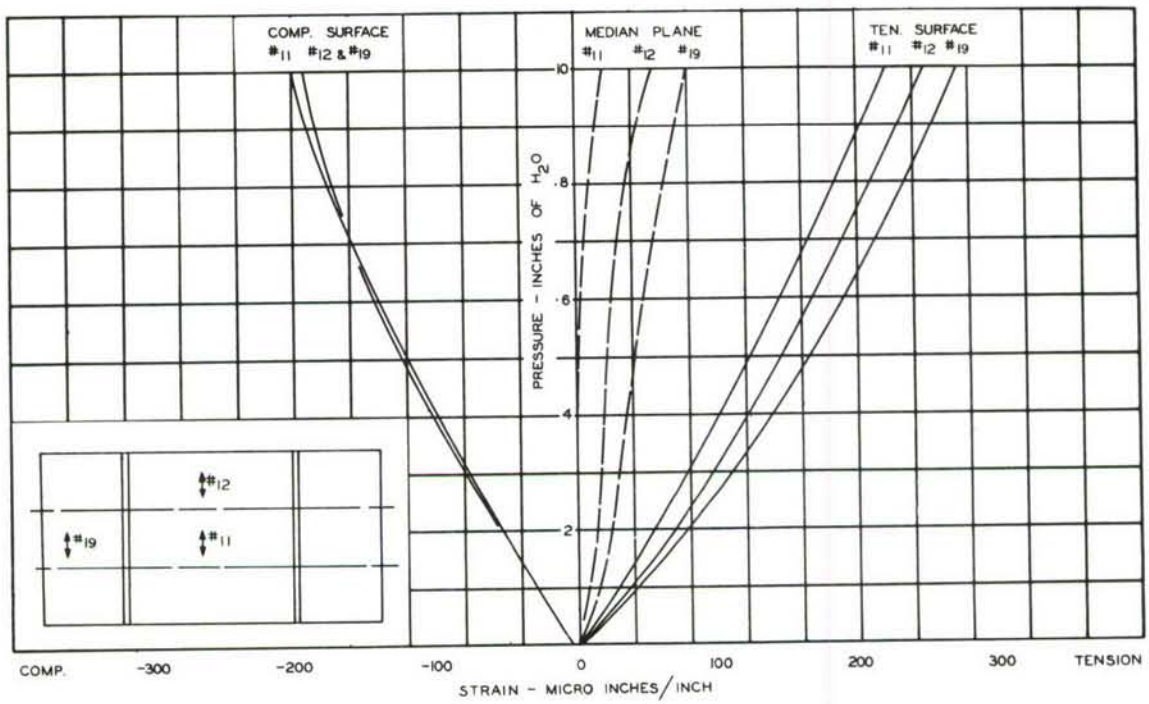

Figure IV-18. Strain Distribution - Panel A - Static

c. Dynamic Test (6- x 20-inch Panel)

This simple clamped edge panel was speaker-excited by discrete frequency plain pressure waves of normal incidence. Under these conditions measurements were made to determine the mode shape and response characteristics. Instrumentation consisted of strain gages, accelerometers, variable reluctance type noncontracting displacement pickup and free particles on the panel for definition of nodal lines.

The significant modes and the response in these modes are shown in Figures IV-19 and IV-20.

During the program some variations in the resonant frequency of the individual modes were obtained. These variations were found to be directly related to the differential thermal expansion of the steel clamping frame and the aluminum panel. Where it was not possible to entirely eliminate these effects during periods of rapid temperature variation, the measured frequencies were corrected to agree with those obtained for the condition without static in-plane edge loading. Corresponding values of response level are shown as measured.

d. Dynamic Test (Panel A)

The procedures used with 6- x 20-inch panel were applied here with two notable exceptions: (1) The panel was so oriented that the approximately plain sound pressure waves impinged with grazing incidence. (2) A hand-held velocity pickup was used as the primary tool in determining mode shape.

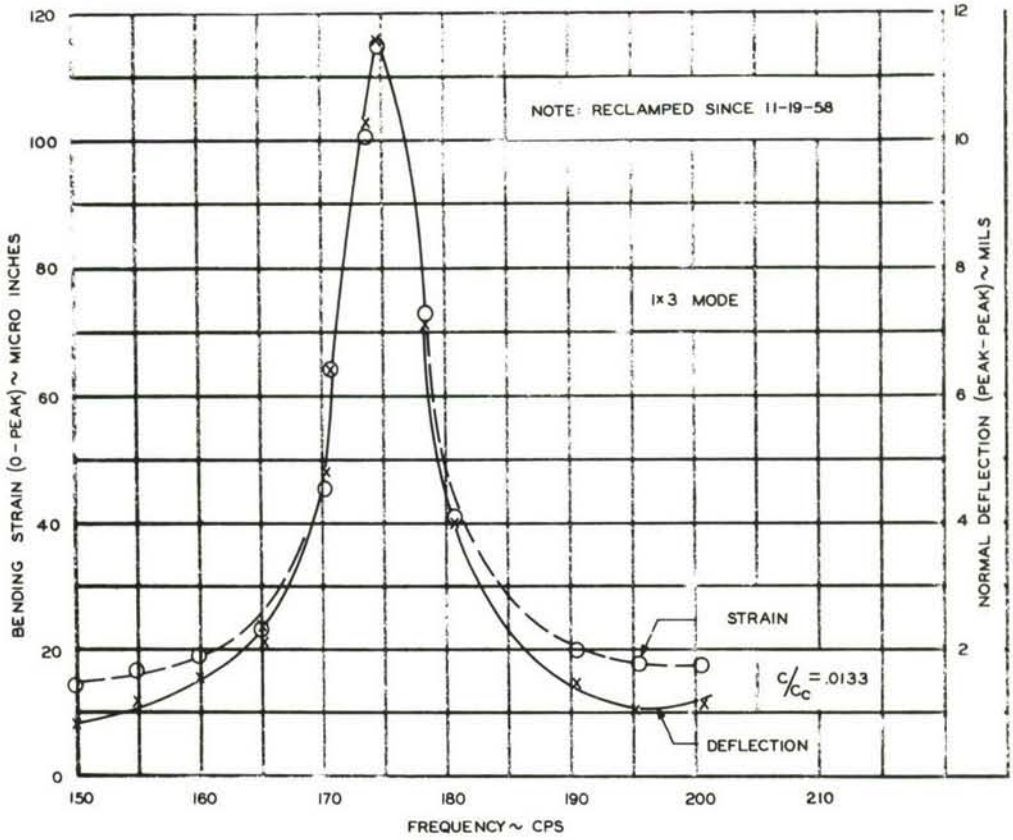

Figure IV-19. Dynamic Response - 6" x 20" x .032 Alum Test Panel

MODE	FREQ. *	DEFLECTION IN.X10^{-3} rms	BENDING STRAIN MICRO IN./IN. rms	
	CPS	STA. 10.5*	STA. 15.0*	STA. 10.0*
1X1	105	6.7	131	178
1X3	181	1.7	47	52
1X5	298	0.3	21	22
1X7	417	0.5	54	69

* TEMPERATURE VARIATION AFFECTS CLAMPED PANEL RESONANT FREQ.

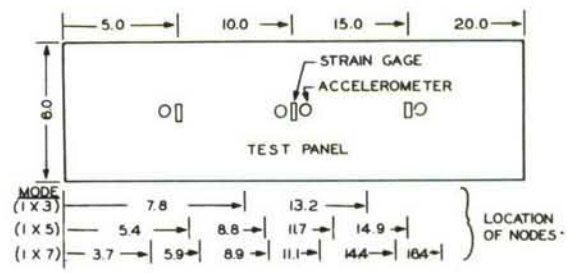

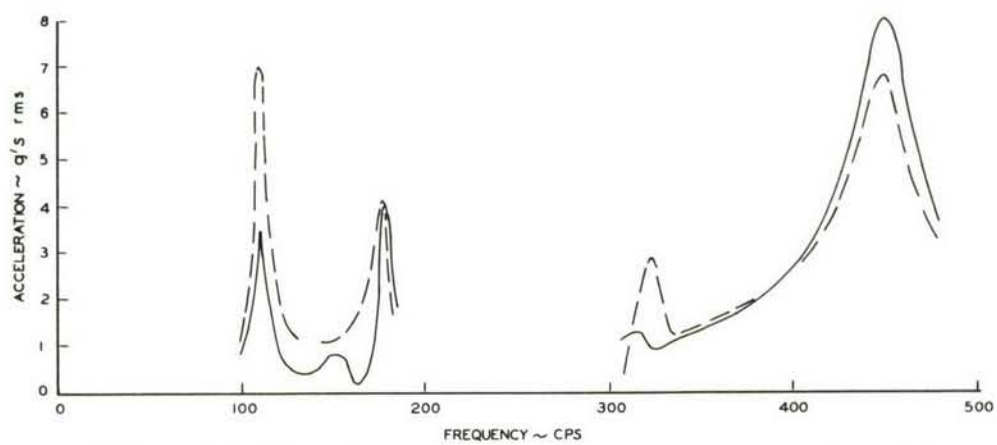

Figure IV-20. Frequency Response - 6" x 20" Panel

A sweep of the frequency range from 40 to 2000 cps showed that, with the exception of the fundamental near 117 cps, all of the significant modes were confined primarily to the response of the three 6- x 20-inch skin bays within the specimen (i. e., substructure elements coincide with nodal lines). These modes were generally characterized by the presence of an odd number of antinodes in the responding bay. While similar modal patterns appeared in each of these three skin bays, the resonant frequencies were usually somewhat different.

The differences in the experimental determination of the exact resonant frequency of a mode lay in the variations in specimen preload. Effects of preloading were observed as a result of the technique of adjusting the edge clamping and also because of the in-plane edge loading induced by the difference in thermal expansion of jig and specimen. The use of such reclamping techniques greatly reduced but did not entirely eliminate the variations of mode shapes and resonant frequencies. However, these variations are considered to be sufficiently small and should produce no noticeable effect on the results obtained from the analytical work of Section III (for the fundamental and other low frequency modes).

With the above factors in mind, the discrete frequency excited response data are self-explanatory. These data are shown in Figures IV-21 through IV-23 and Table IV-2.

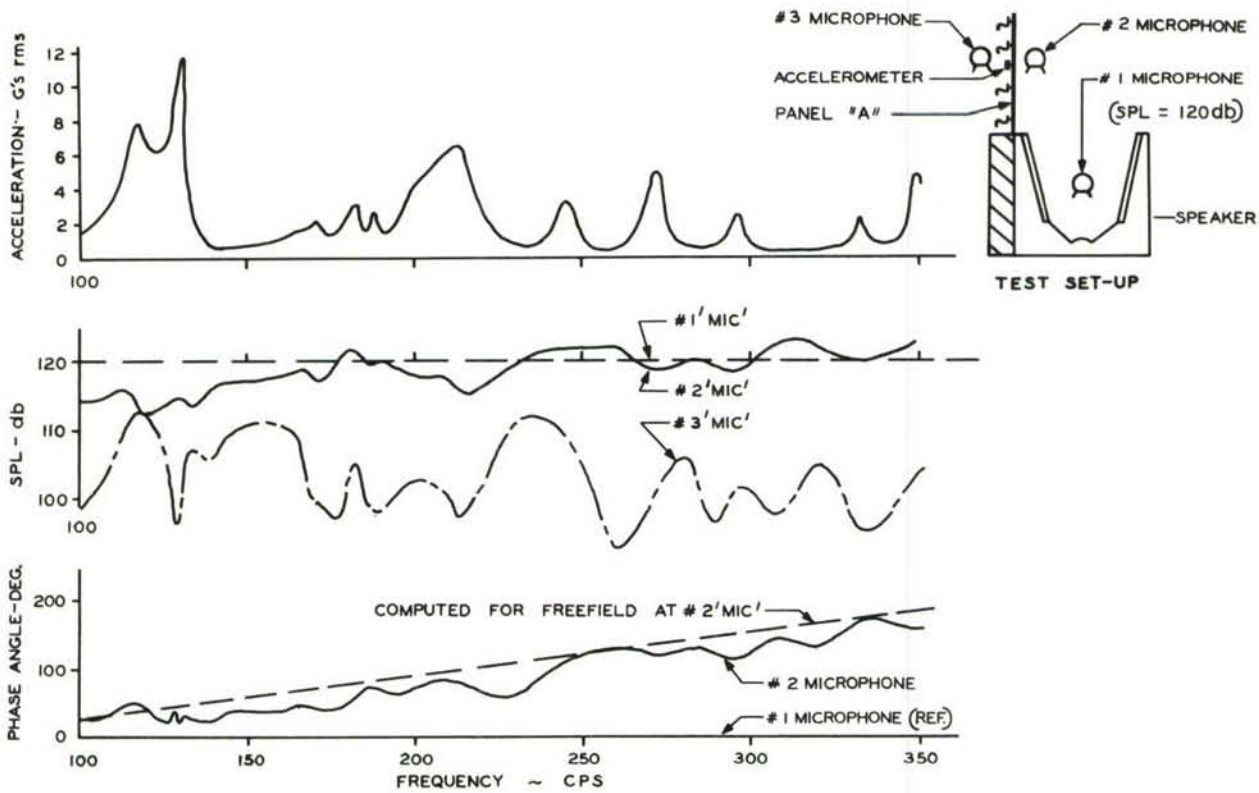

Figure IV-21. Characteristics of Discrete Frequency Excitation and Response of Panel A

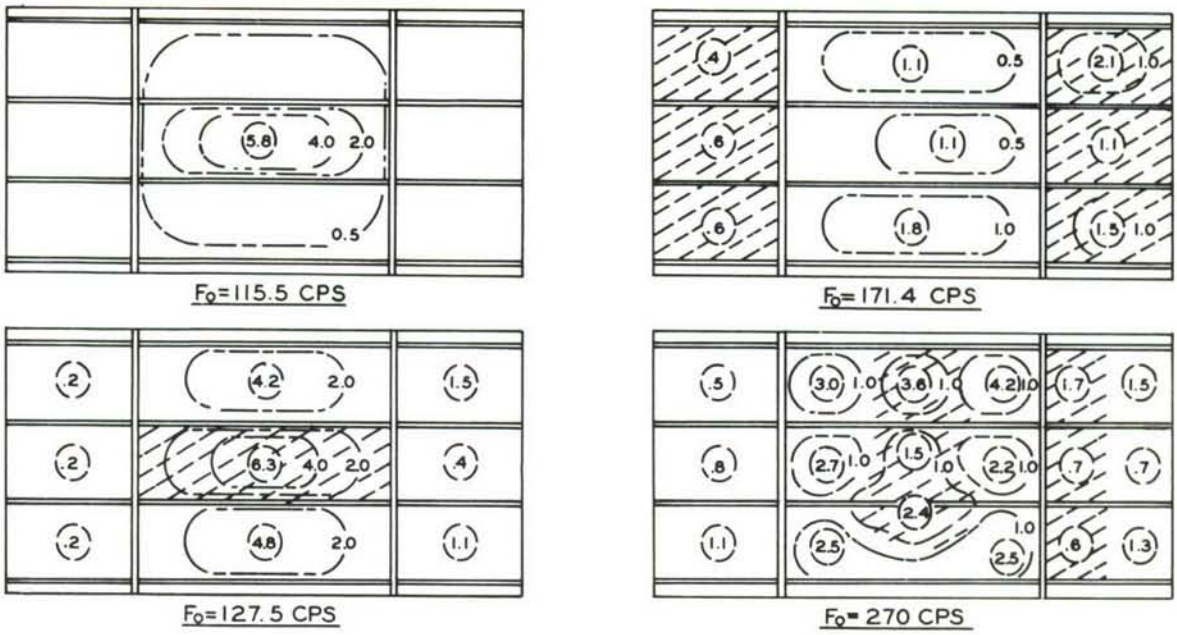

Figure IV-22a. Discrete Frequency Mode Shapes - Panel A

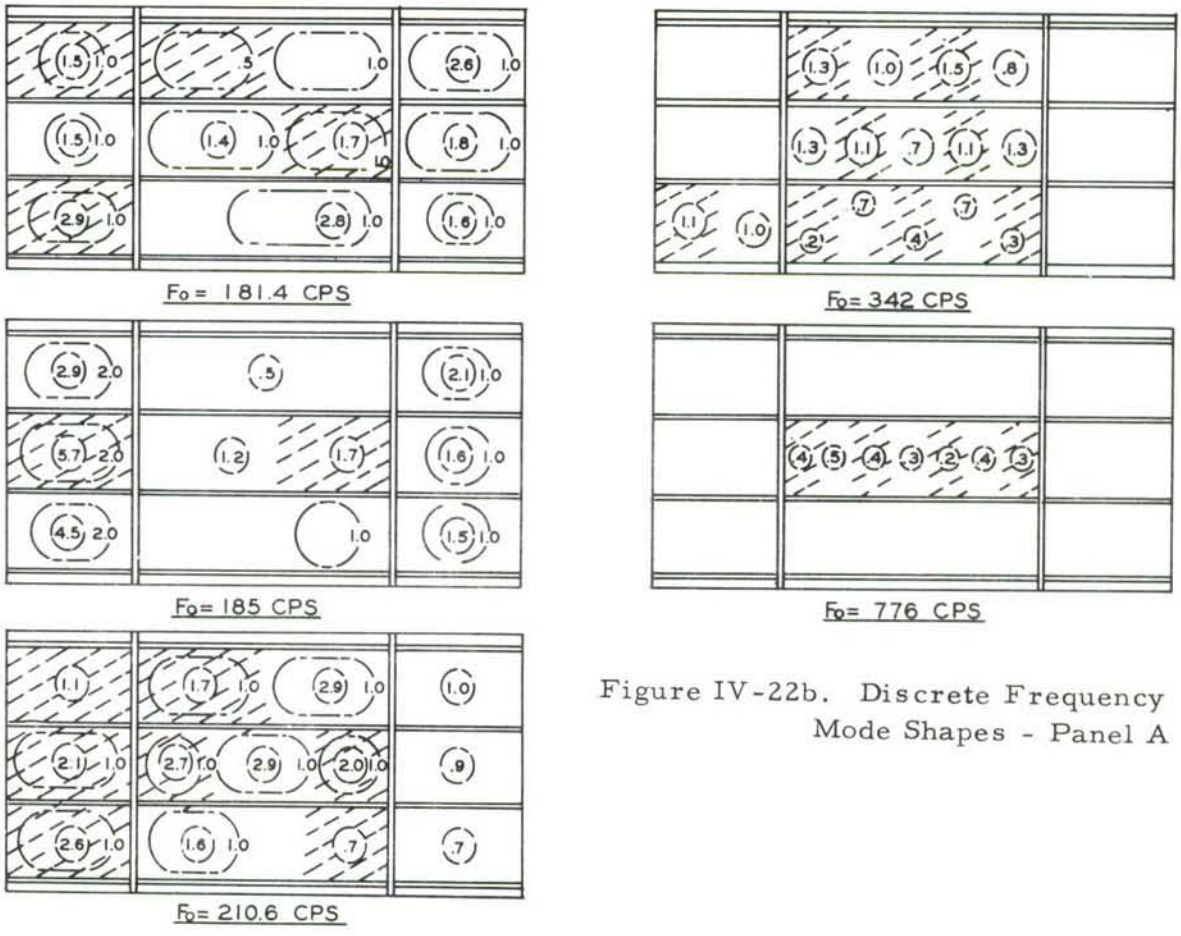

Figure IV-22b. Discrete Frequency Mode Shapes - Panel A

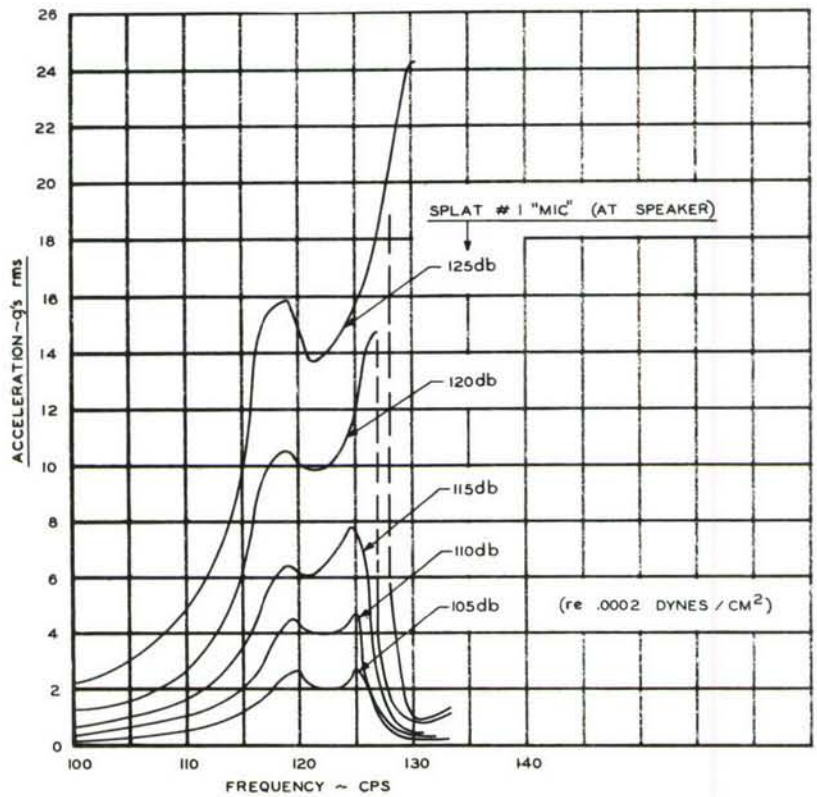

Figure IV-23. Discrete Frequency Response at Center of Panel A

TABLE IV-2

DISCRETE FREQUENCY STRAIN RESPONSE - PANEL "A"

Frequency - CPS		117	127	170	180	208	270	336	773
SPL at speaker - db		120	120	120	120	120	120	120	120
SPL at panel center - db		116	118	116	121	117	117	123	117
Velocity at panel center - inches/sec. rms		6.3	5.3	2.6		4.2	1.7	0.8	0.6
Acceleration at station D-20 - G's rms		11.6	9.5	6.8		10.5	5.8	3.9	9.5
Acceleration at station E-10 - G's rms		1.8	1.0	0.3	1.5	0.9	0.4	1.2	1.0
Bending strain - Inches/inch x 10^{-L} rms	-Sta. D-30	2.3	2.3	7.9	2.8	3.0	3.5	2.3	1.9
" "	-Sta. F-25	6.0	34.5	14.3	22.8	13.0	24.6	4.6	2.3
" "	-Sta. D-25	28.1	17.6	2.8	15.8	19.3	22.9	4.6	3.9
" "	-Sta. F-20	10.2	52.8	21.1	10.5	5.6	4.4	2.5	2.5
" "	-Sta. D-20	67.0	58.0	25.0		31.0	3.8	5.4	5.3
" "	-Sta. D-5	24.6	19.4	10.5	14.0	3.2	5.8	3.0	2.6

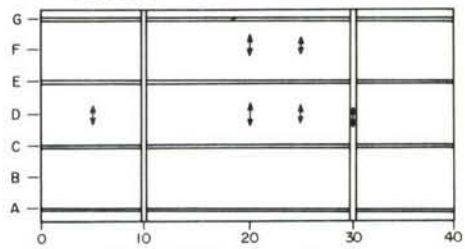

Panel "A" Coordinate System

e. Dynamic Test (Panel E)

Procedures followed with this panel were identical to those used with the Panel A specimens. In these tests, however, the use of the aluminum supporting frame largely eliminated the problem of obtaining reproducible data. Several other basic differences were noted in the response characteristics of this larger and necessarily more complex panel. First, because of the number of almost identical elements, the individual normal modes were more obscured by cross coupling. Second, the effects of pressure correlation, varying as a function of frequency and the distance from the driving speakers, had a more evident effect on the response of panel elements. It should also be noted that the sound pressure levels at the panel varied considerably as a function of distance from the speakers. Because of these complicating factors and the very large number of mode shapes, the data tends to be qualitative. It defines only the more typical modes and resonant frequencies.

Characteristic frequency response and mode shapes are shown in Figures IV-24 through IV-26. Typical relationship among strain, velocity, acceleration and sound pressure level is shown in Table IV-3.

TABLE IV-3

DISCRETE FREQUENCY STRAIN RESPONSE - PANEL "E"

Frequency CPS	SPL db	Velocity in./sec. rms	Vel. x W g's rms	Bending Strain μin./in. rms	Tension Strain μin./in. rms	Acceleration g's rms
113	105	1.48	2.7	7.0*	≤.7*	3.0
113	110	2.75	5.1	12.8	≤.7	5.9
113	115	4.13	7.6	20.5	≤.7	8.6
128	105	.42	.9	1.3	≤.7	.9
128	110	.83	1.7	2.4	≤.7	1.5
128	115	1.64	3.4	4.5	≤.7	2.6
167	105	1.96	5.3	5.9	≤.7	3.7
167	110	3.18	8.6	10.5	1.1	8.3
260	105	.51	2.1	1.9	≤.7	1.9
260	110	1.04	4.4	3.4	1.0	3.3
260	115	1.48	6.5	5.3	1.3	5.7
266	105	.25	1.1	1.9	≤.7	2.0
266	110	.43	1.9	3.5	1.0	4.0
266	115	1.02	4.4	5.6	1.3	6.6
390	105	.21	1.3	2.2	≤.7	1.7
390	110	.54	3.4	4.1	≤.7	3.0
588	105	.25	2.4	1.0	≤.7	2.7
588	110	.48	4.6	1.4	≤.7	3.2
813	105	.14	1.9	1.0	≤.7	1.8
813	110	.23	3.1	1.7	≤.7	3.0

*Noise level = .7μ in./in. rms

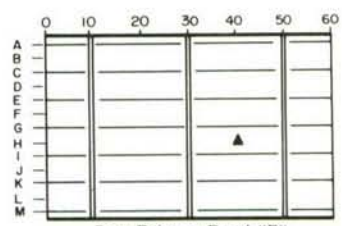

Data Point on Panel "E"

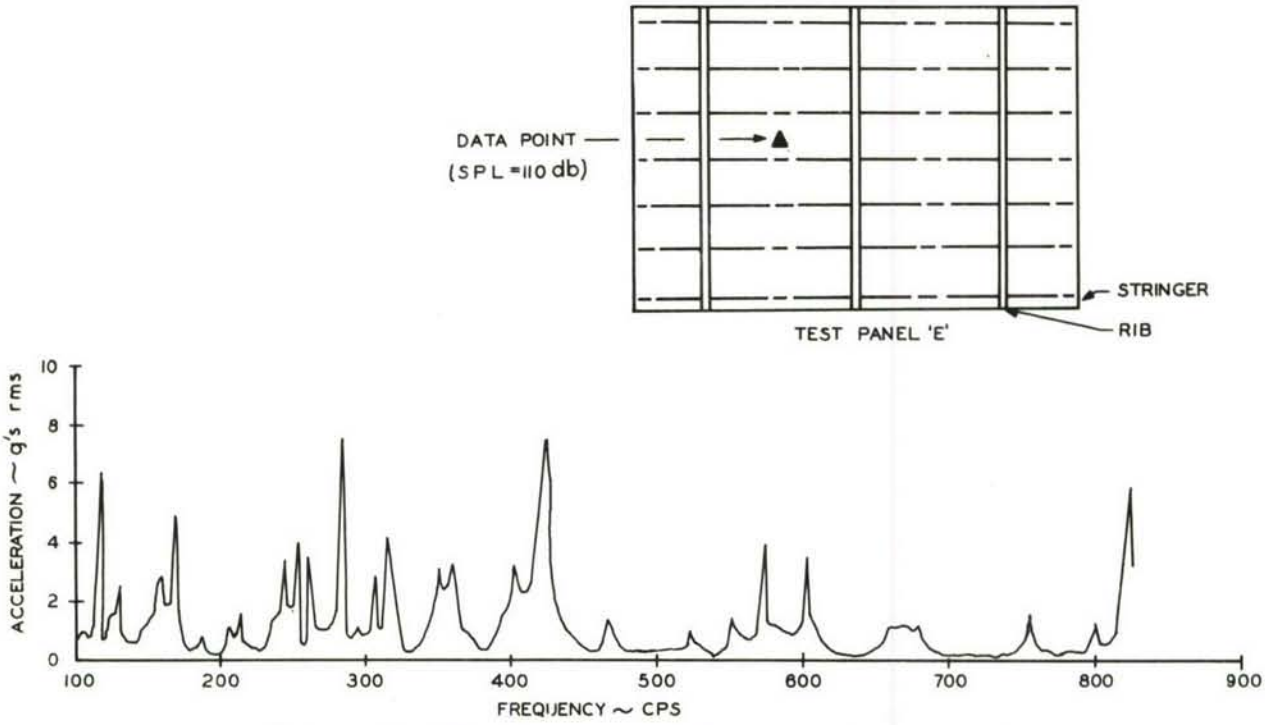

Figure IV-24. Frequency Response of Panel E

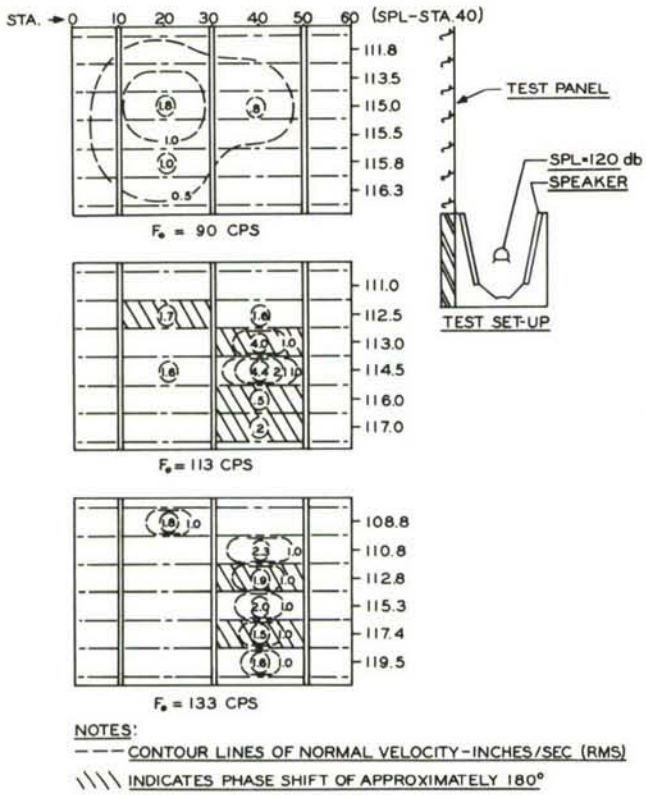

Figure IV-25a.

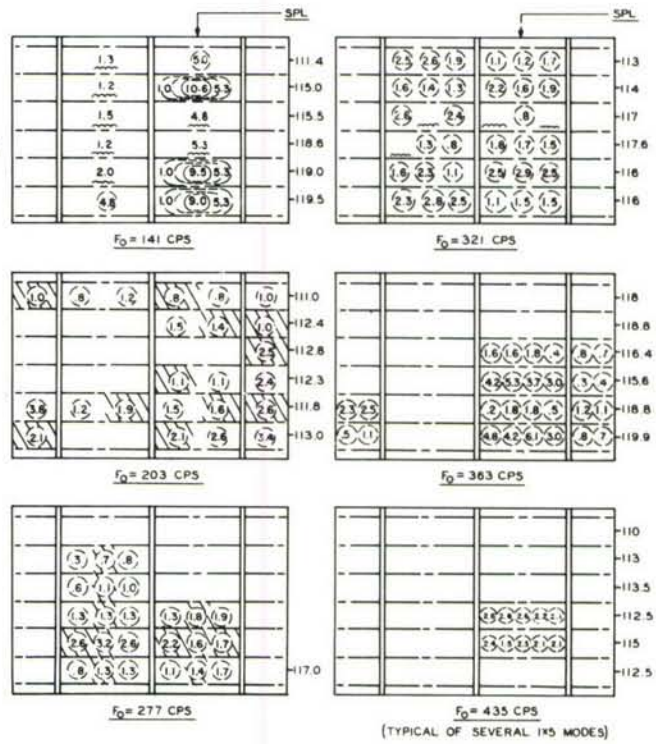

Figure IV-25b.

Figures IV-25a. - IV-25b. Discrete Frequency Mode Shapes for Panel E

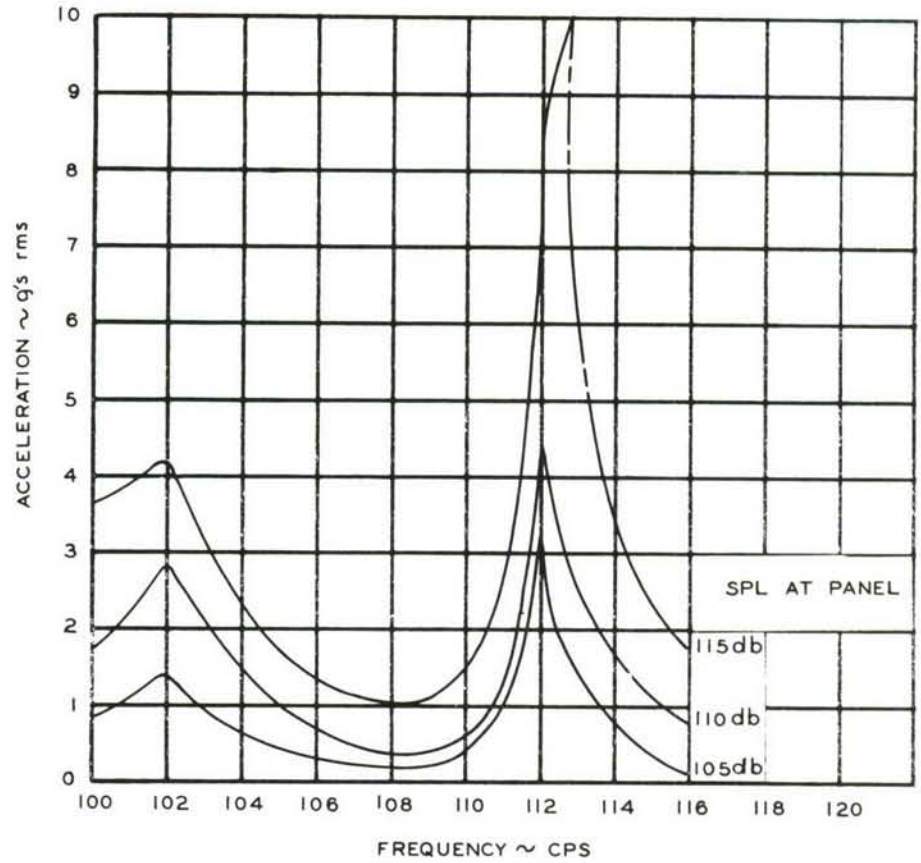

Figure IV-26. Panel E Response - Discrete Frequency Excitation - Sta. F-20

2. Jet Noise Field Test Procedures and Results

a. General Test Procedure

The individual test panels were mounted in the face of the attenuation chamber on the support jig. This assembly was then located in one of the two positions in the previously surveyed noise field. A sketch of this area is shown in Figure II-4, page 6. In both locations the panel faced the jet wake and was parallel to its axis. The coordinates of all positions in the noise field were located up and down stream from the engine exhaust nozzle and laterally from the longitudinal axis of the engine. Thus, the field coordinates to the center of the test panel to the "upstream" position were 14.2 feet downstream by 10 feet laterally. The "downstream" position was located 40.1 feet downstream by 15 feet laterally.

The pressure distribution and correlation across the face of a typical panel in both field positions and for two engine conditions were obtained prior to the response measurements. In addition, during the response measurements, sound pressure data were obtained at one station in the free field and one station at the test panel. These data and the measuring and data reduction techniques of recording and reducing the response data were identical to those used with the acoustical data.

b. Procedures and Results

(1) 6- x 20-inch Test Panel

Strain and acceleration records were recorded to define the response at three different locations on the panel and for both military and afterburner engine

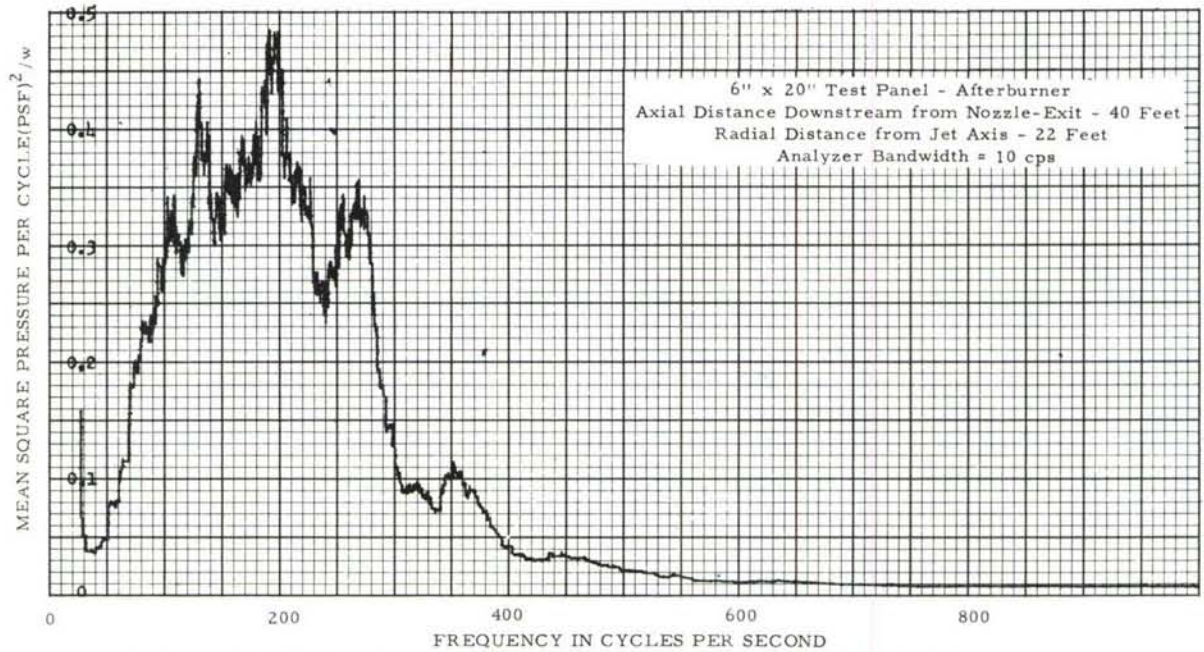

Figure IV-27. Power Spectral Density Analysis of Pressure - 6" x 20" Test Panel - Afterburner

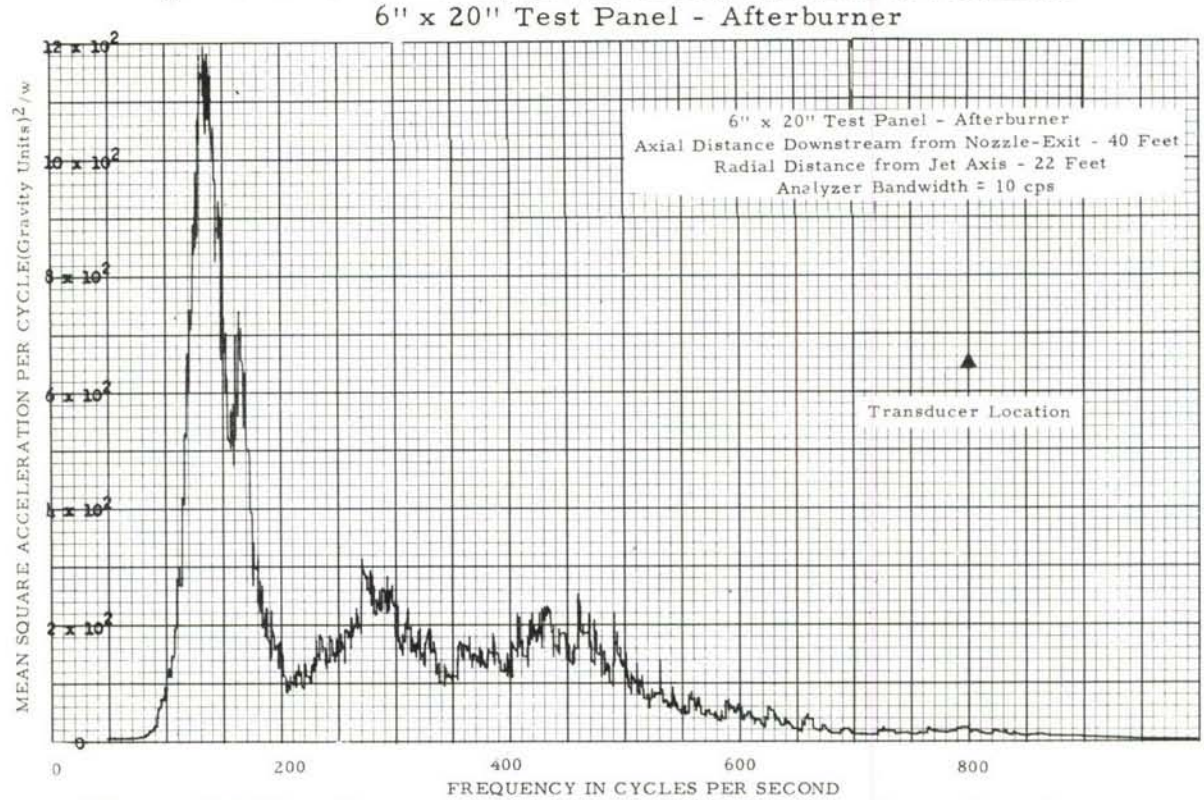

Figure IV-28. Power Spectral Density Analysis of Acceleration - 6" x 20" Test Panel - Afterburner

conditions. These data were then plotted directly from the recorded tapes as power spectral density curves. The resulting curves are shown in Figures IV-27 through IV-40, pages 133 through 139.

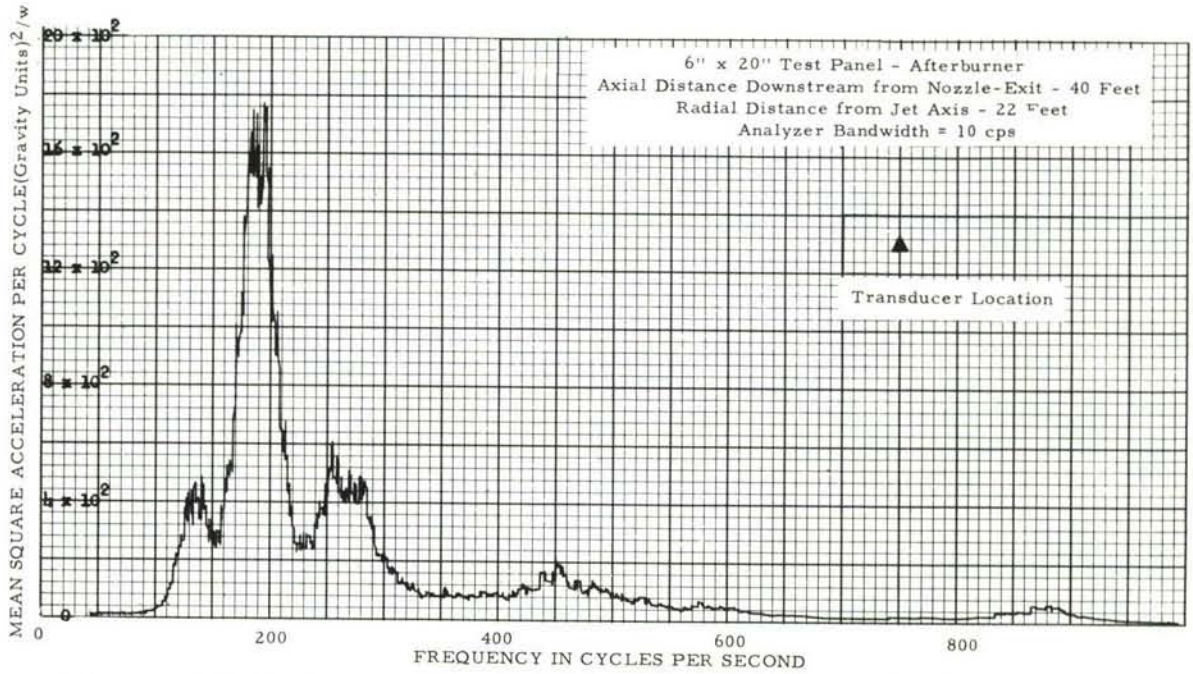

Figure IV-29. Power Spectral Density Analysis of Acceleration - 6" x 20" Test Panel - Afterburner

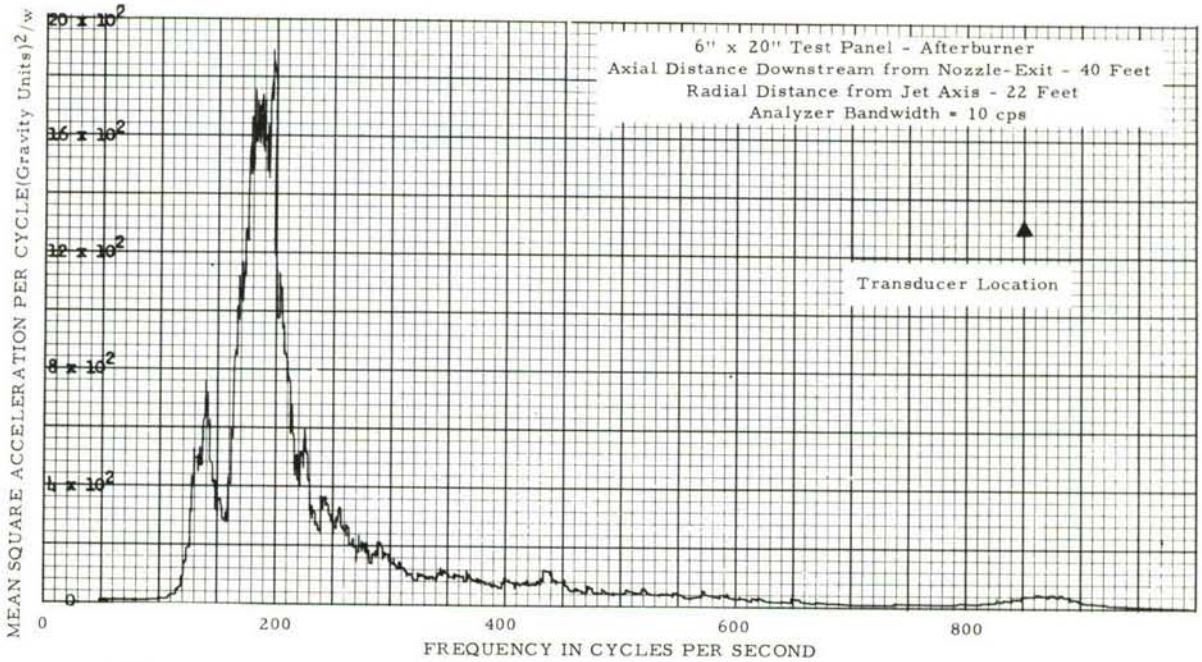

Figure IV-30. Power Spectral Density Analysis of Acceleration - 6" x 20" Test Panel - Afterburner

For this series of tests only, two variations in the test procedure were required. The first variation was the substitution of a production series of J-79 model engines. The second variation was the relocation of the test panel within the noise field (20 feet from the jet axis). The latter change developed as a result

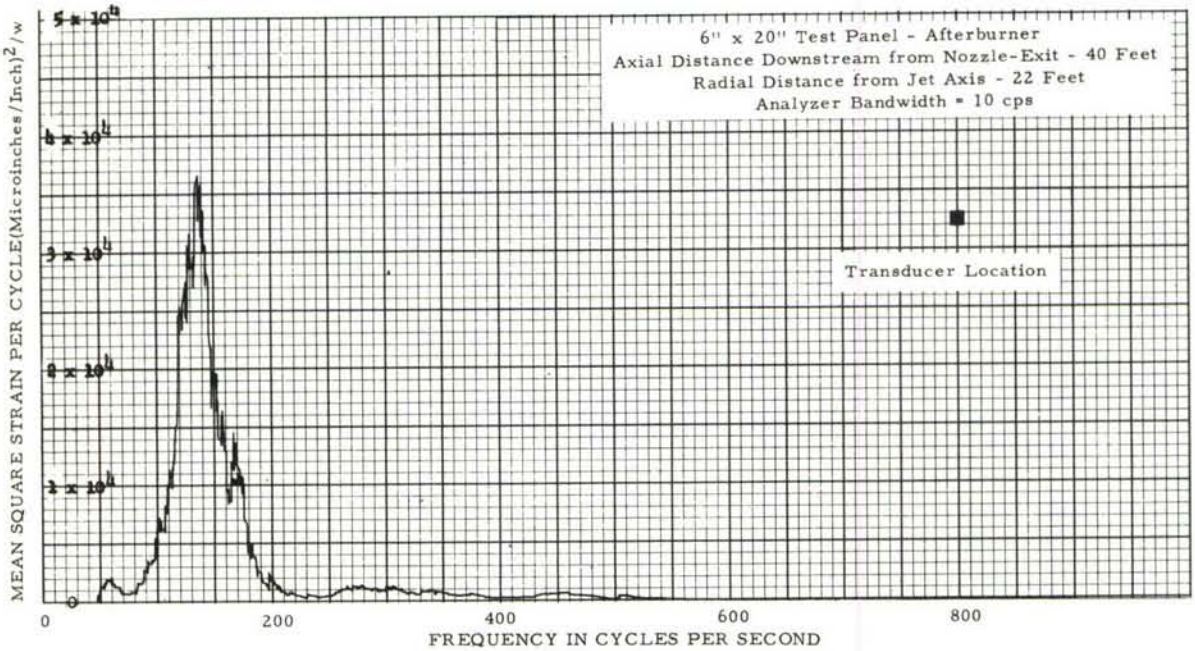

Figure IV-31. Power Spectral Density Analysis of Bending Strain - 6" x 20" Test Panel - Afterburner

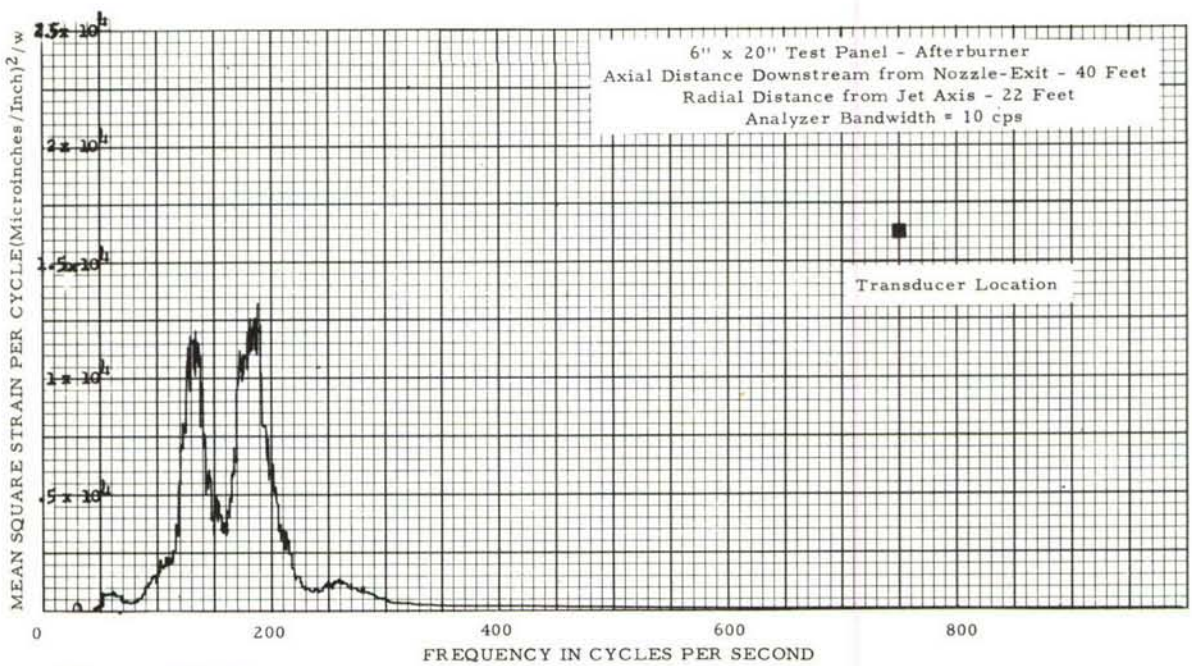

Figure IV-32. Power Spectral Density Analysis of Bending Strain - 6" x 20" Test Panel - Afterburner

of cross wind conditions which caused the hot, low-velocity exhaust gasses associated with the engine starting and idle operation to flow through the area of the normal downstream test site. This change accounts for considerable variation between the noise characteristics at this panel and all subsequent panels tested.

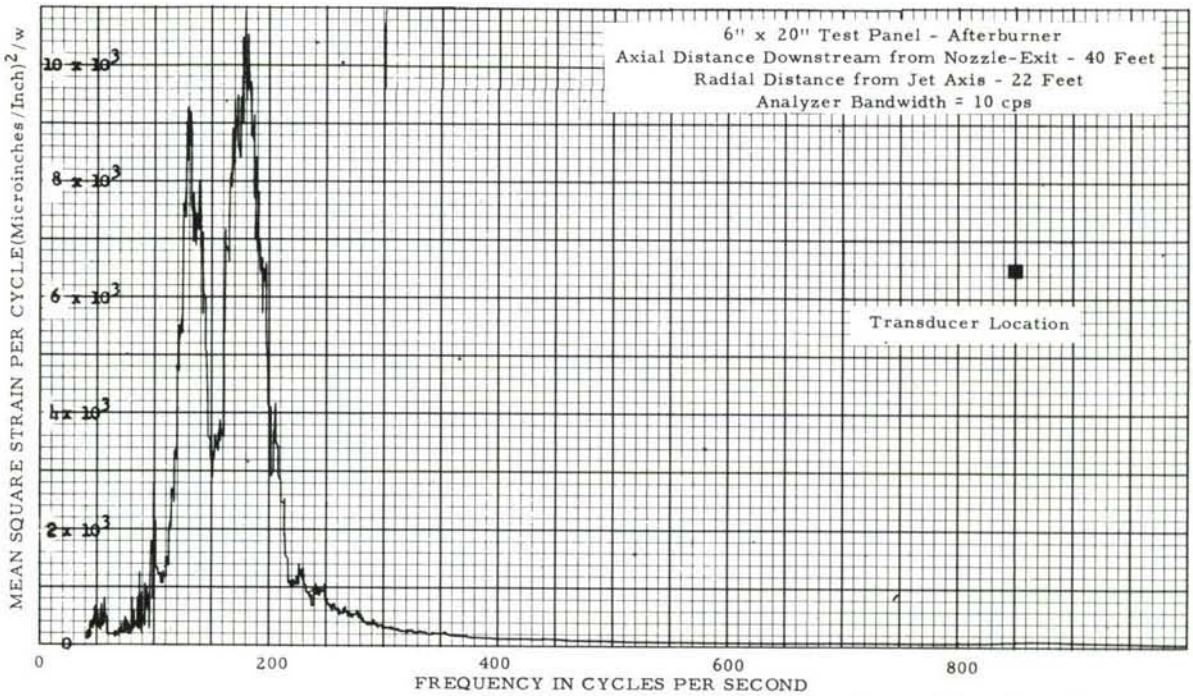

Figure IV-33. Power Spectral Density Analysis of Bending Strain - 6" x 20" Test Panel - Afterburner

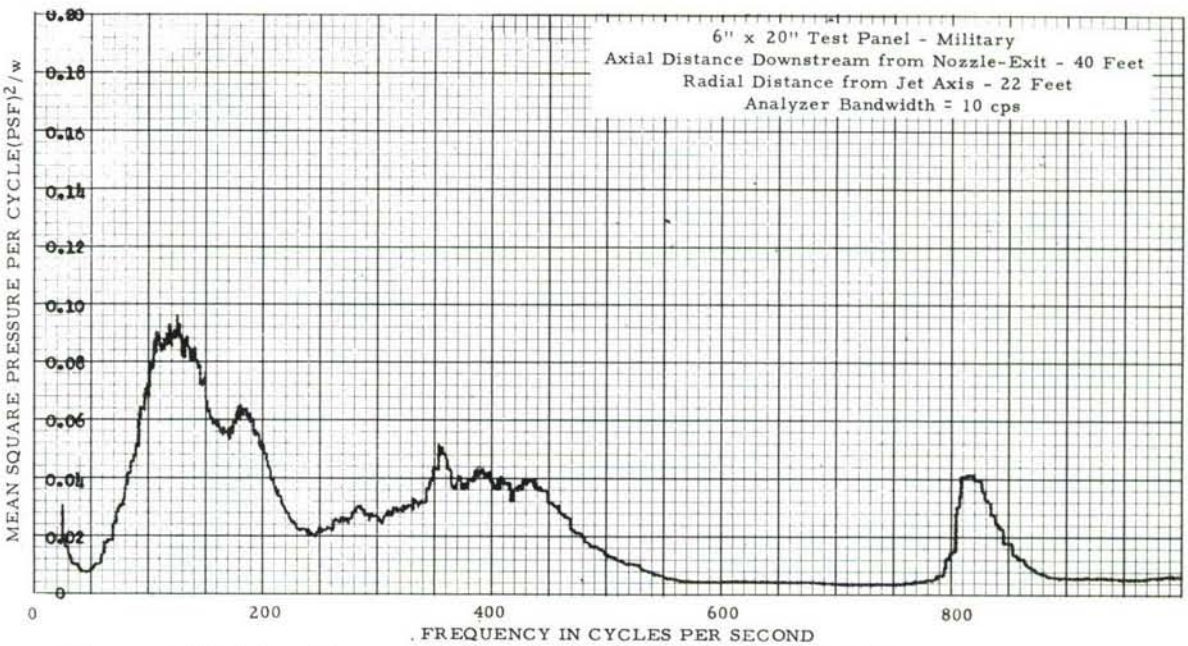

Figure IV-34. Power Spectral Density Analysis of Pressure - 6" x 20" Test Panel - Military

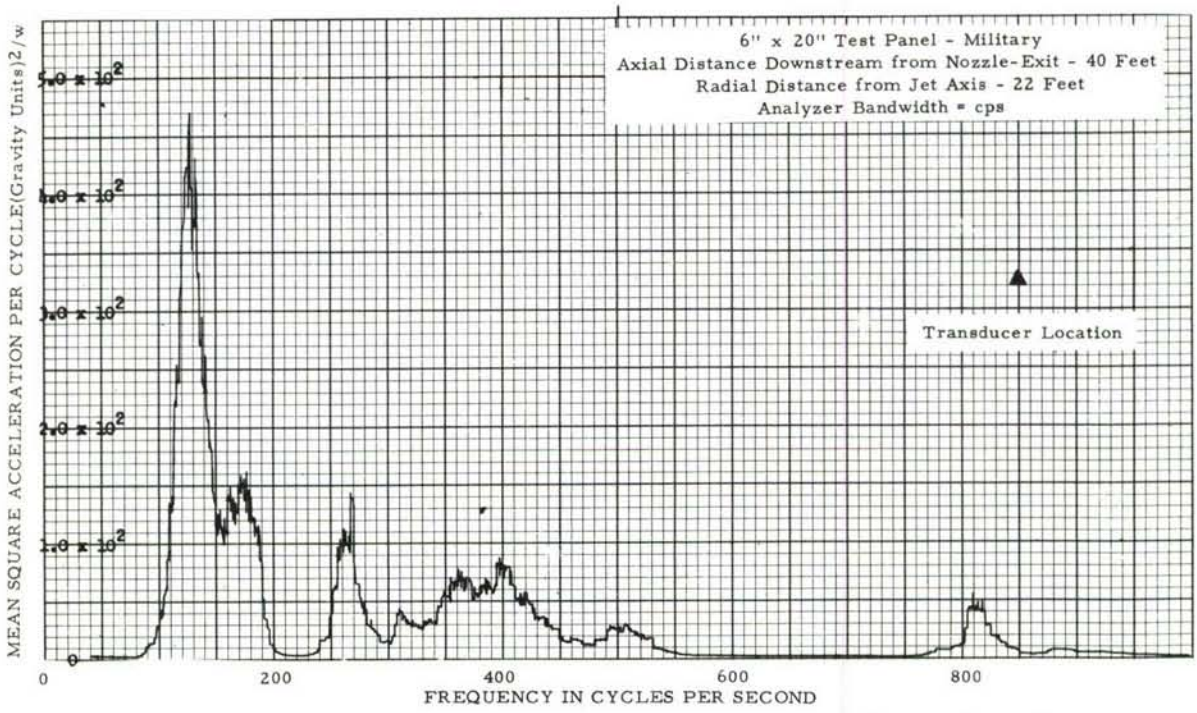

Figure IV-35. Power Spectral Density Analysis of Acceleration - 6" x 20" Test Panel - Military

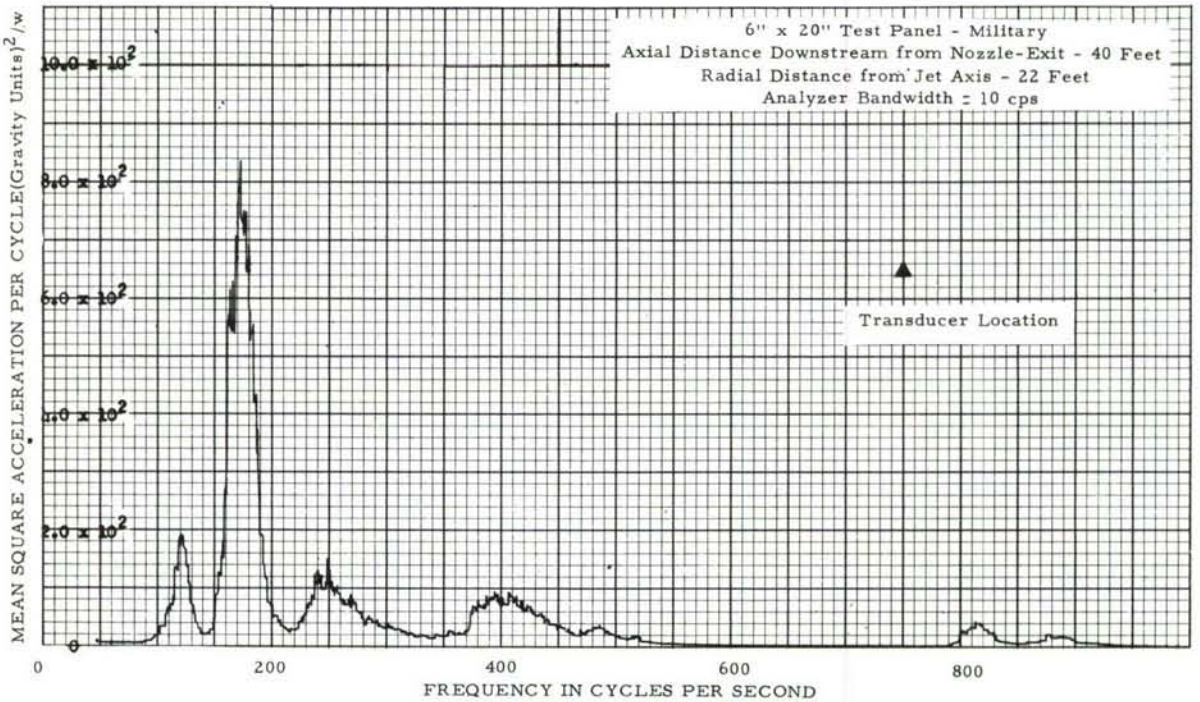

Figure IV-36. Power Spectral Density Analysis of Acceleration - 6" x 20" Test Panel - Military

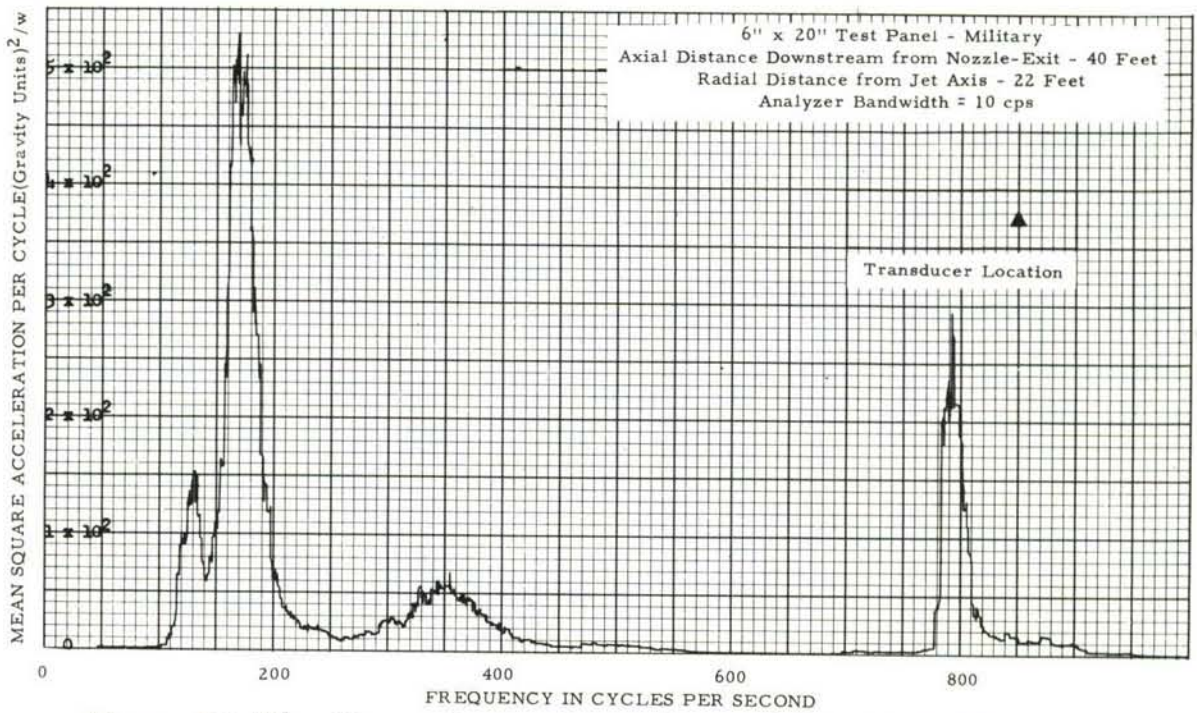

Figure IV-37. Power Spectral Density Analysis of Acceleration - 6" x 20" Test Panel - Military

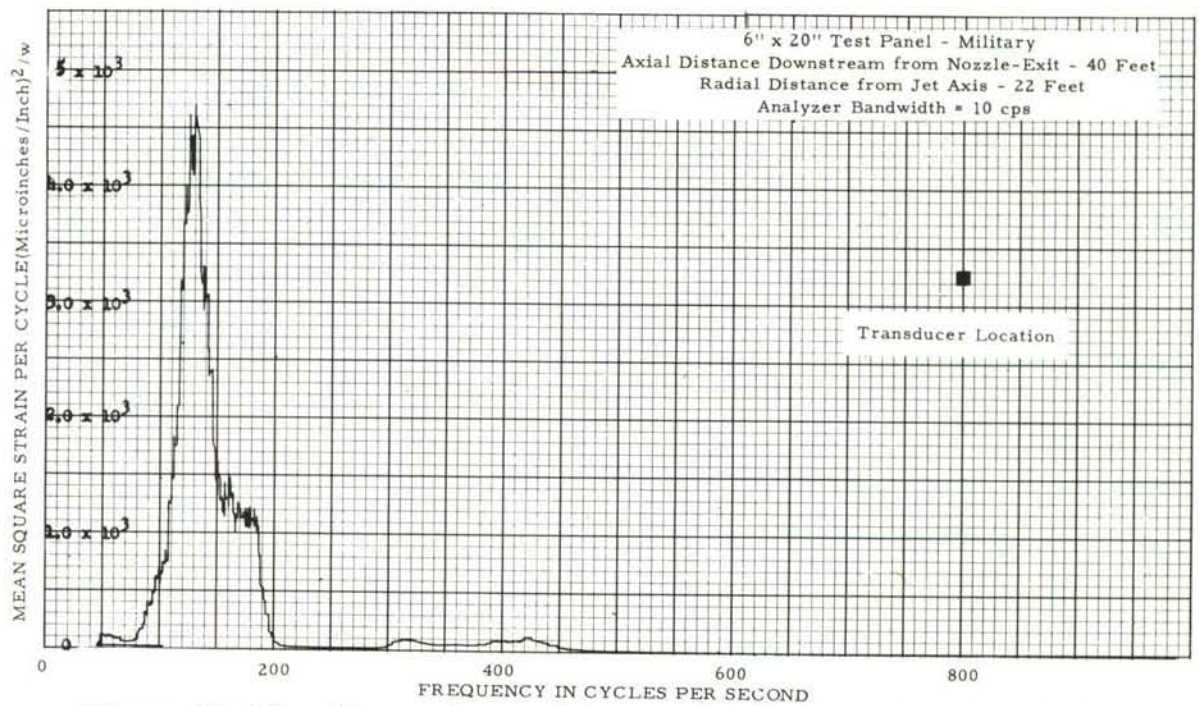

Figure IV-38. Power Spectral Density Analysis of Bending Strain - 6" x 20" Test Panel - Military

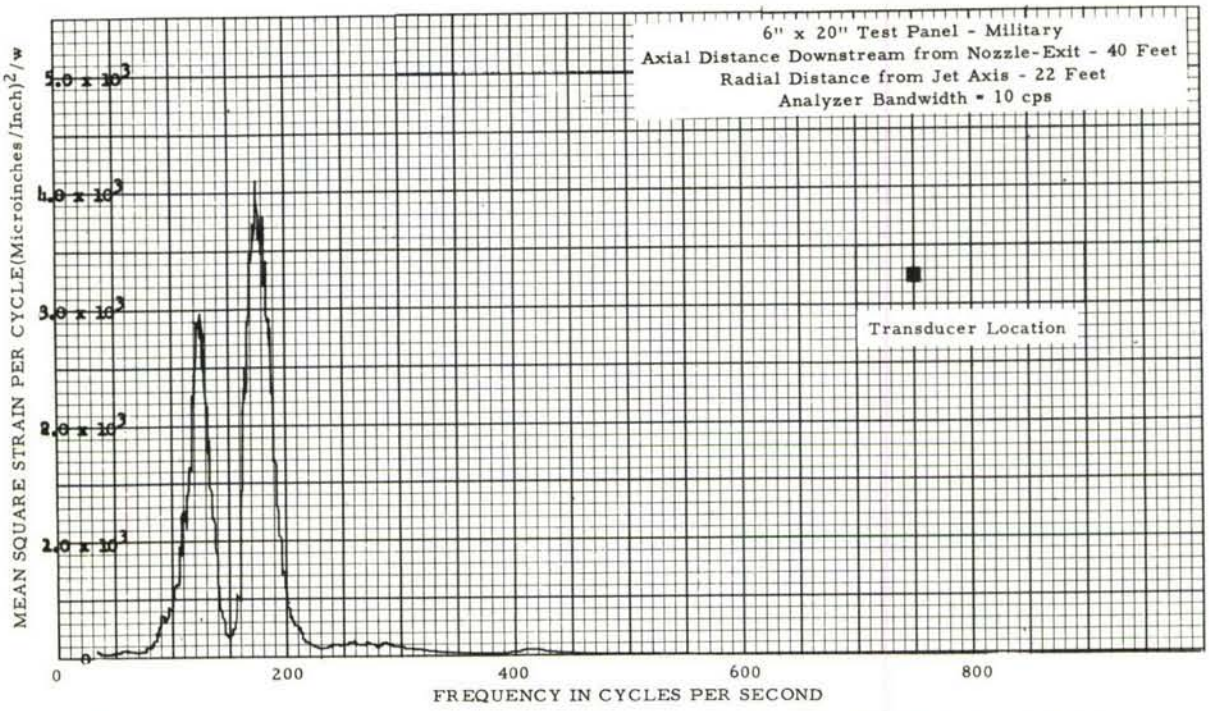

Figure IV-39. Power Spectral Density Analysis of Bending Strain - 6" x 20" Test Panel - Military

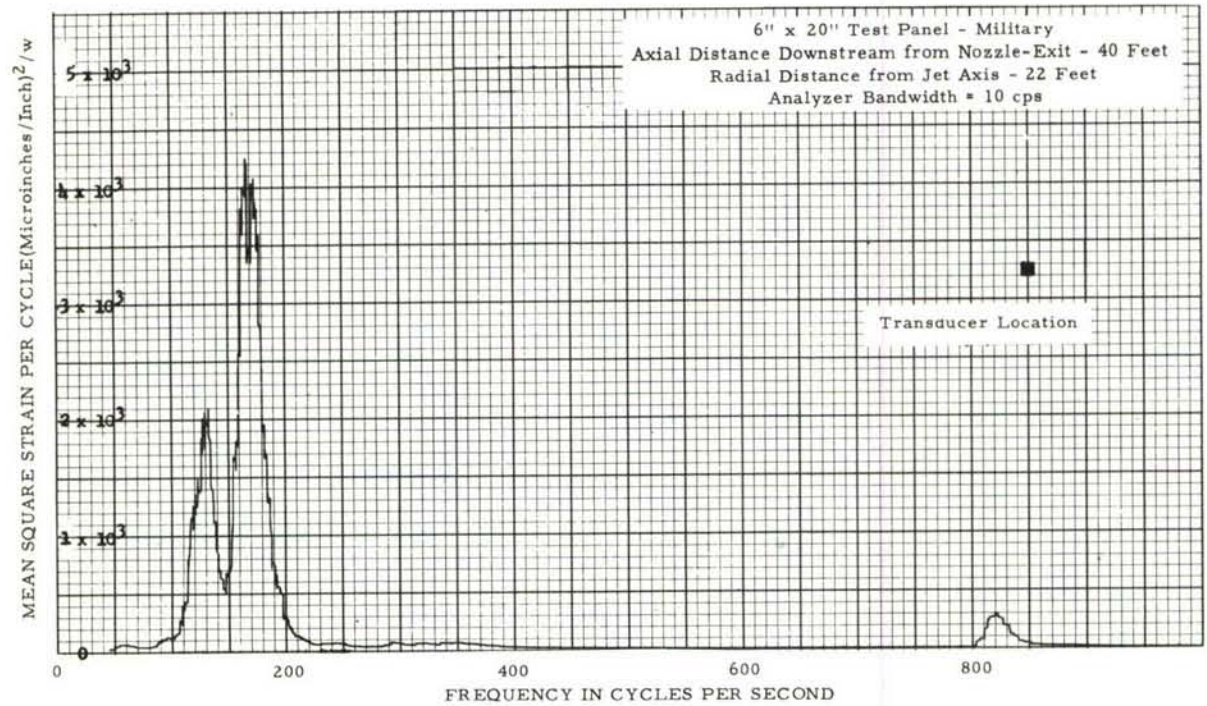

Figure IV-40. Power Spectral Density Analysis of Bending Strain - 6" x 20" Test Panel - Military

(2) Panel A

The largest amount of structural response data was obtained from the flat panels of this configuration. One panel in particular (also used in laboratory tests) was extensively instrumented with strain gages and accelerometers and used throughout the jet noise field response measurements. The panel response was then obtained for both military and afterburner engine conditions and for the one panel location in the noise field. In addition, several typical channels of bending strain, acceleration and pressure were reduced by narrow band techniques and presented as power spectral density curves. These data are shown in Figures IV-41 through IV-55, pages 140 through 147.

Two major difficulties arose with these and all other response data obtained in the jet noise field. The first of these was the mechanical failure of some of the instrumentation attached to the test panel. These failures, occurring primarily in areas of high acceleration, produced intermittent shorts in the instrumentation circuits and they were not detected until the data were reduced after the completion of testing. As a result, it is not possible to obtain direct comparison of all local panel responses for all test conditions. The second difficulty (also noted in the discrete frequency tests) was the shifting of the resonant frequencies of the various modes because of preloads introduced by differential thermal expansion across the panel and between the panel and its supporting jig. Although test procedures were adopted to minimize such effects, an analysis of the test results shows that varying amounts of such frequency shifting occurred.

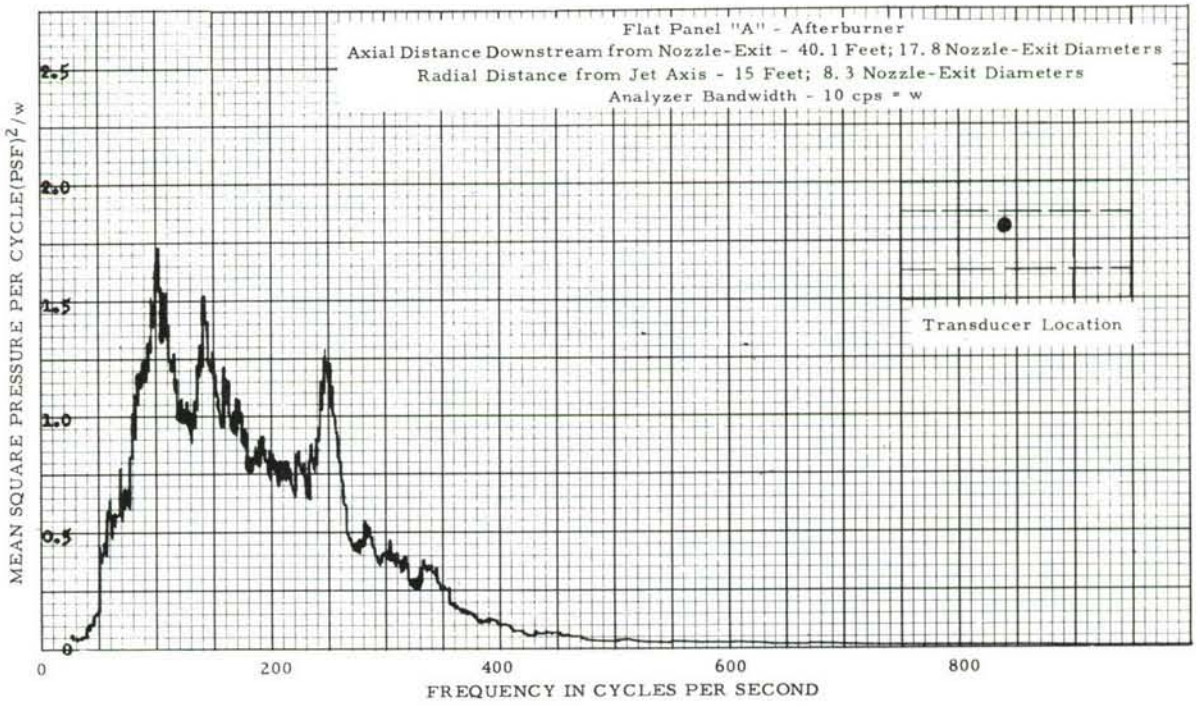

Figure IV-41. Power Spectral Density Analysis of Pressure - Flat Panel A - Afterburner

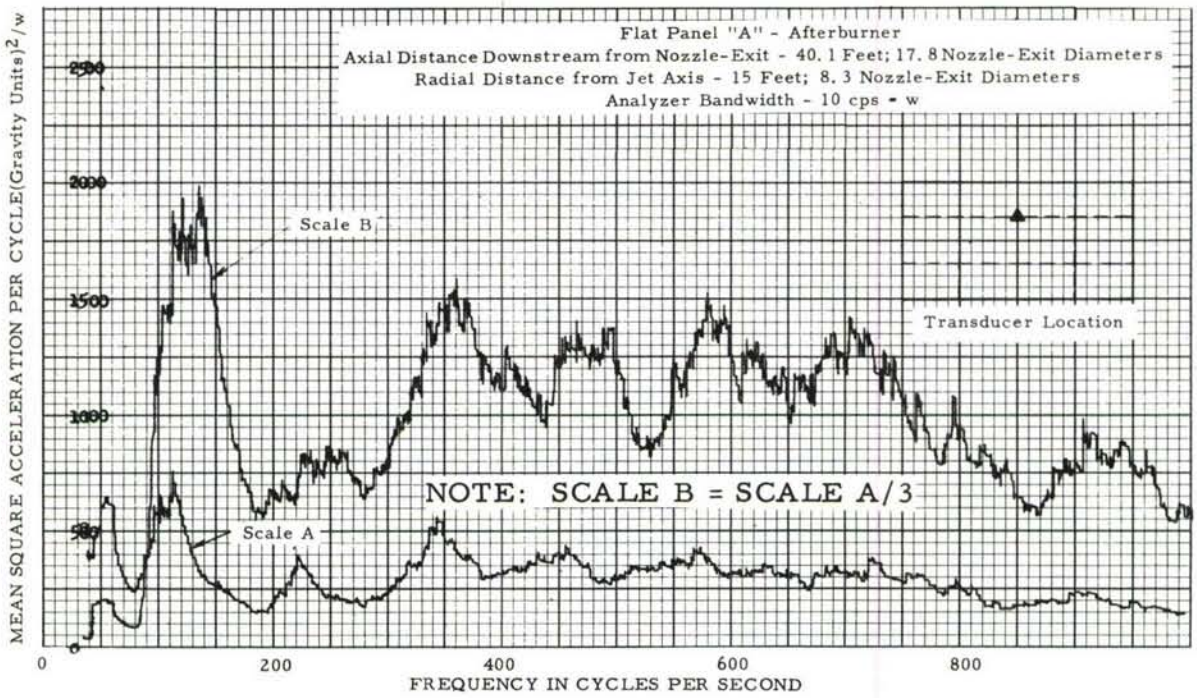

Figure IV-42. Power Spectral Density Analysis of Acceleration - Flat Panel A - Afterburner

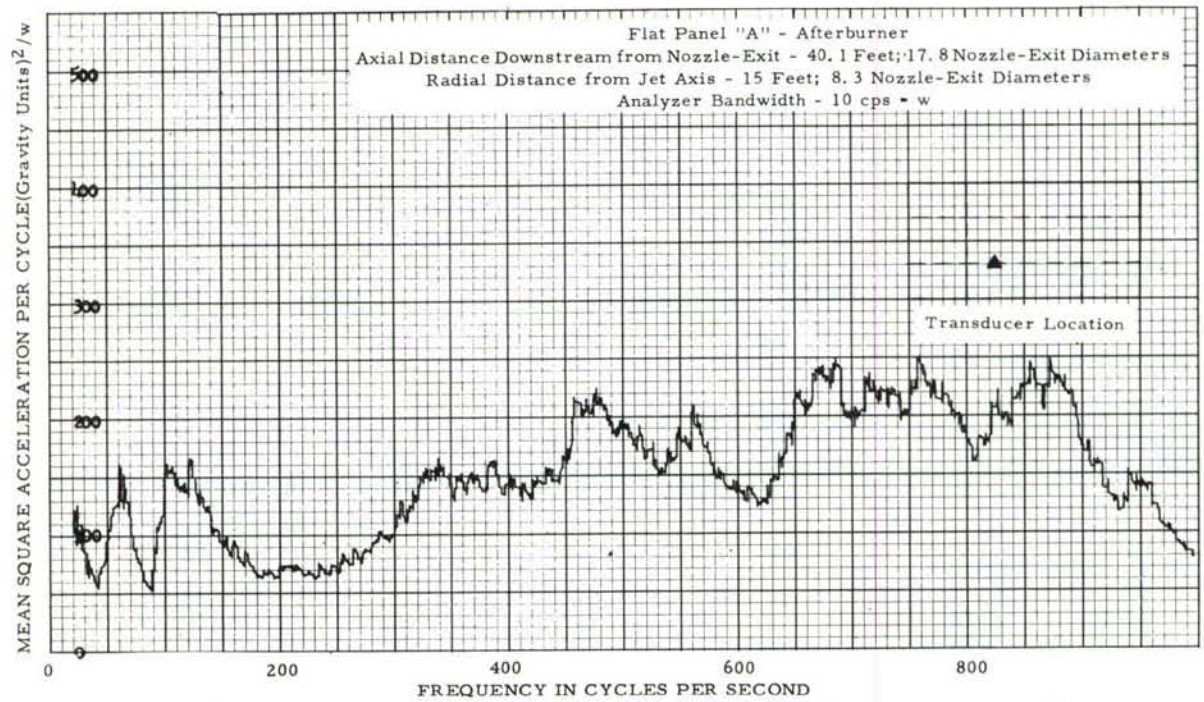

Figure IV-43. Power Spectral Density Analysis of Acceleration - Flat Panel A - Afterburner

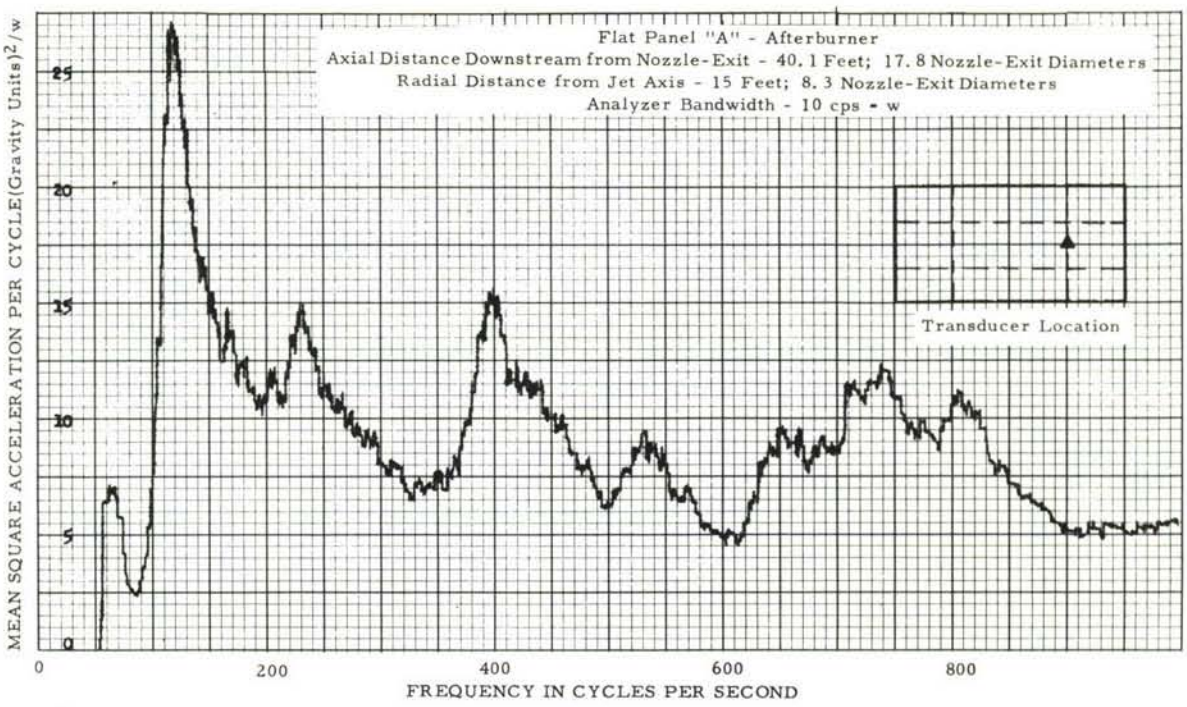

Figure IV-44. Power Spectral Density Analysis of Acceleration - Flat Panel A - Afterburner

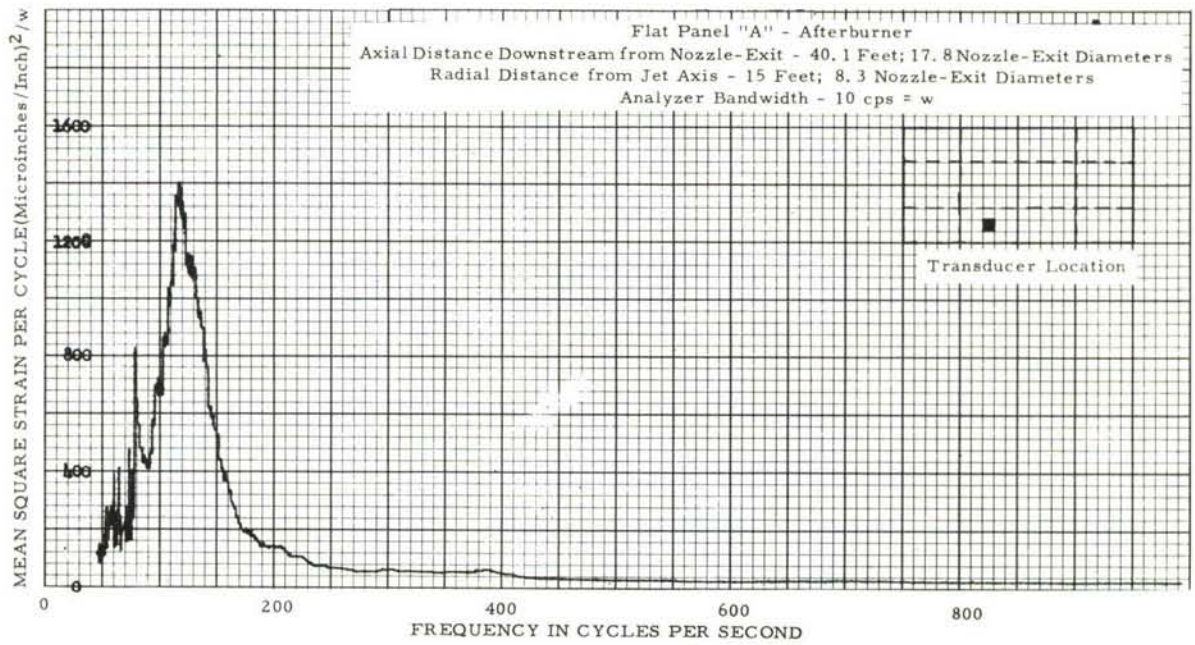

Figure IV-45. Power Spectral Density Analysis of Bending Strain - Flat Panel A - Afterburner

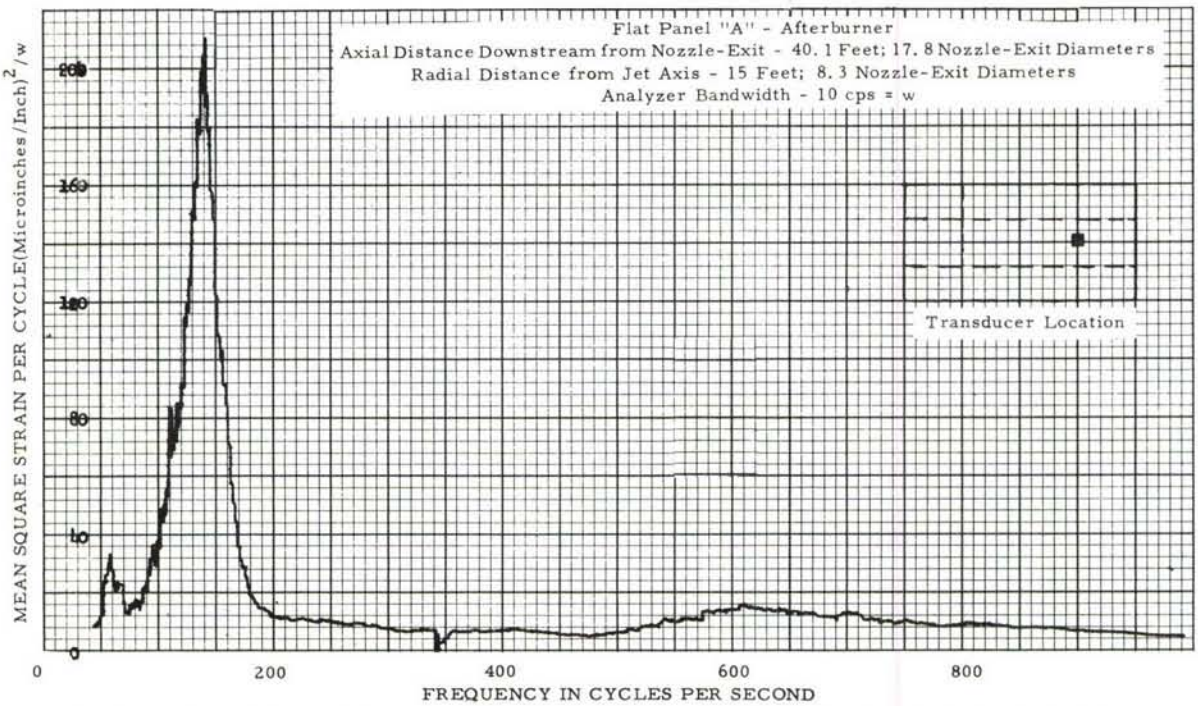

Figure IV-46. Power Spectral Density Analysis of Bending Strain - Flat Panel A - Afterburner

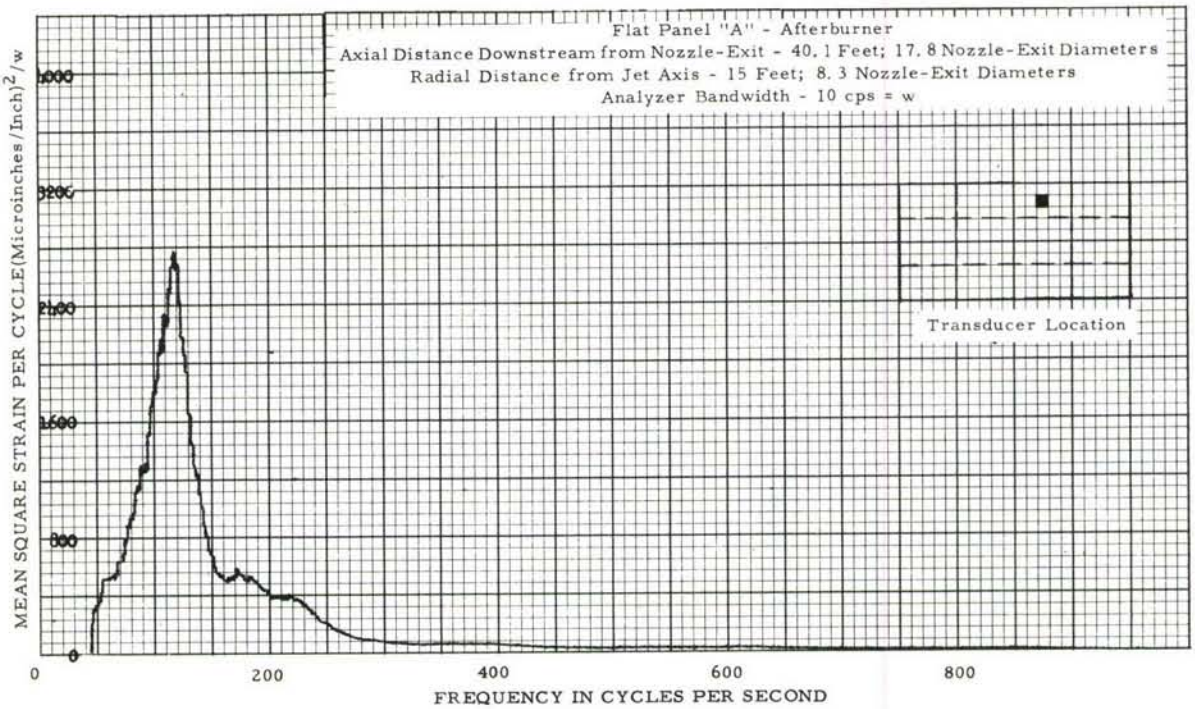

Figure IV-47. Power Spectral Density Analysis of Bending Strain - Flat Panel A - Afterburner

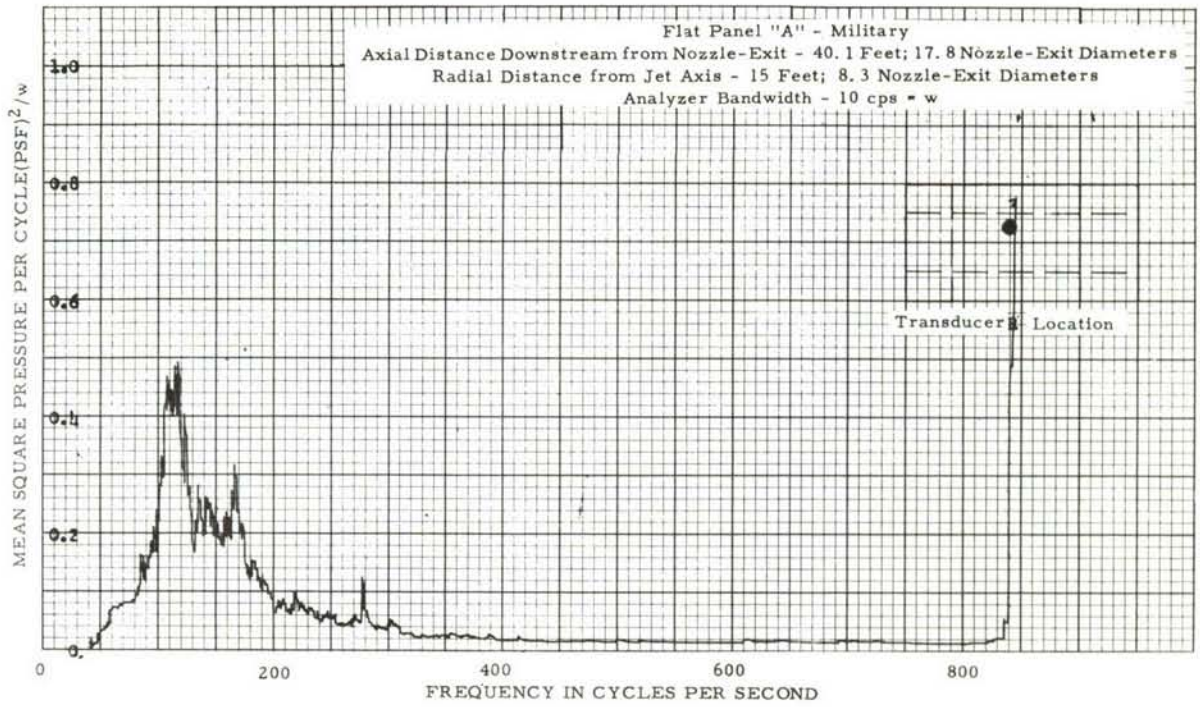

Figure IV-48. Power Spectral Density Analysis of Pressure - Flat Panel A - Military

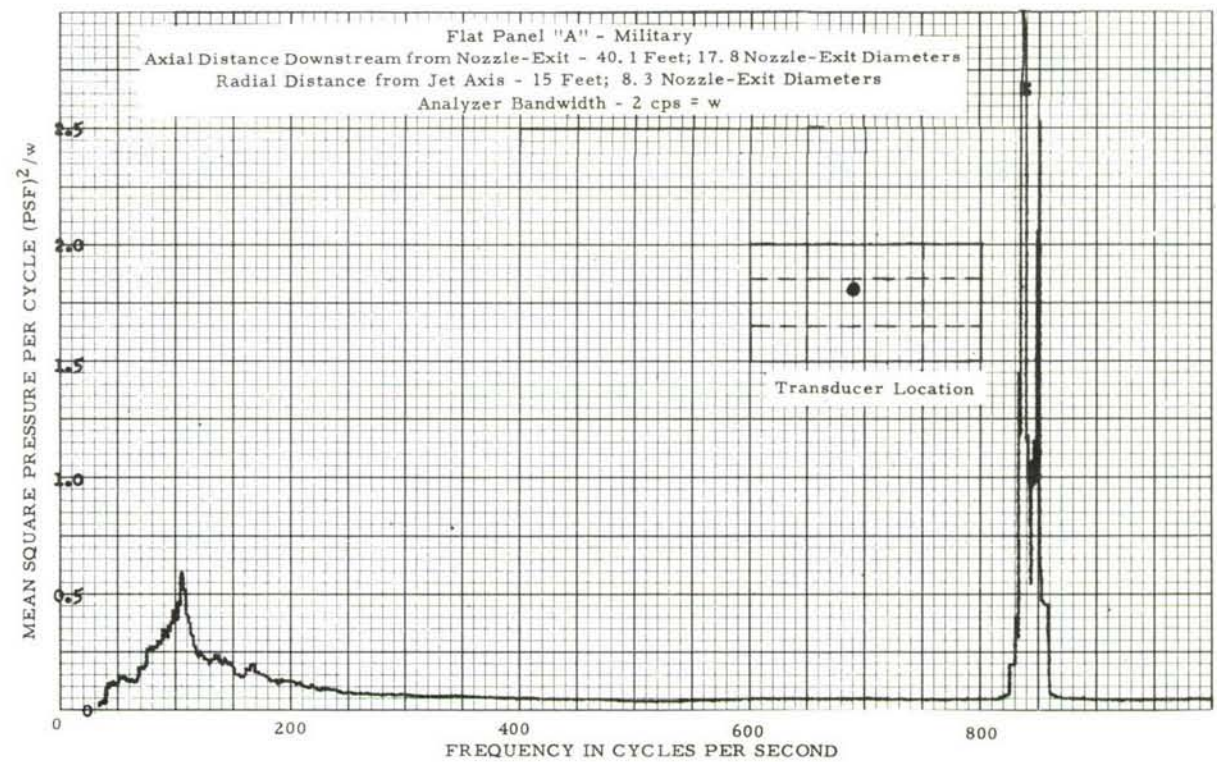

Figure IV-49. Power Spectral Density Analysis of Pressure - Flat Panel A - Military

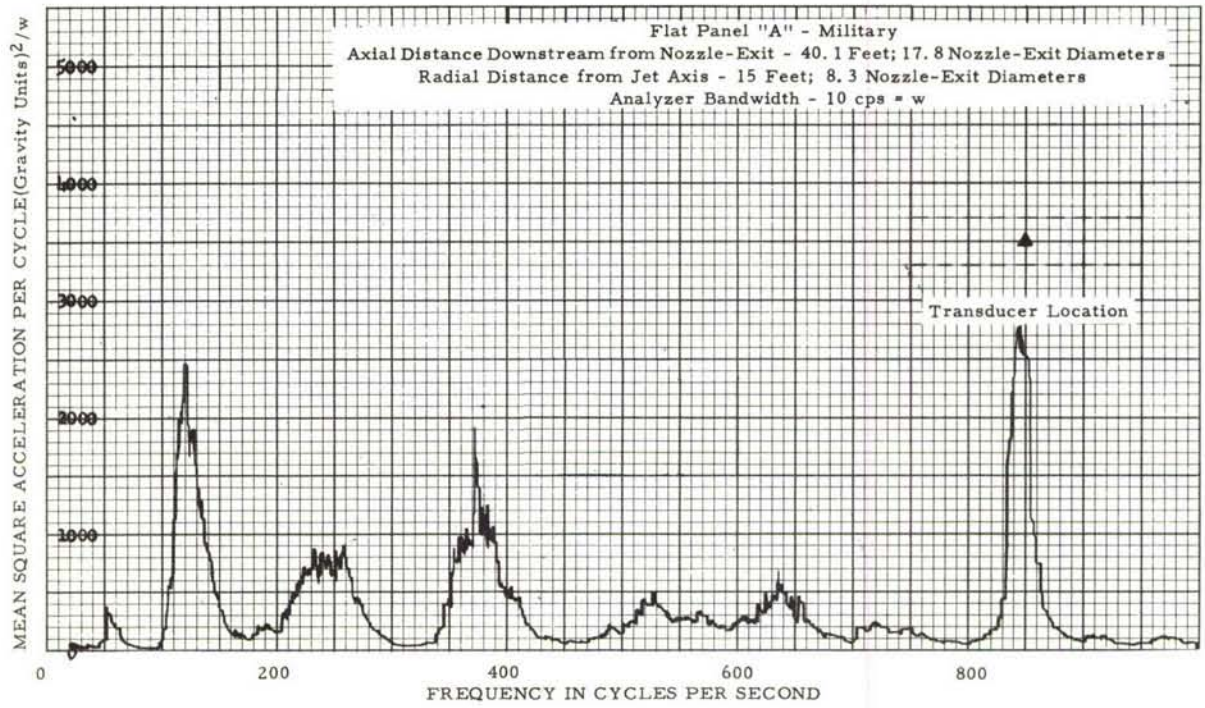

Figure IV-50. Power Spectral Density Analysis of Acceleration - Flat Panel A - Military

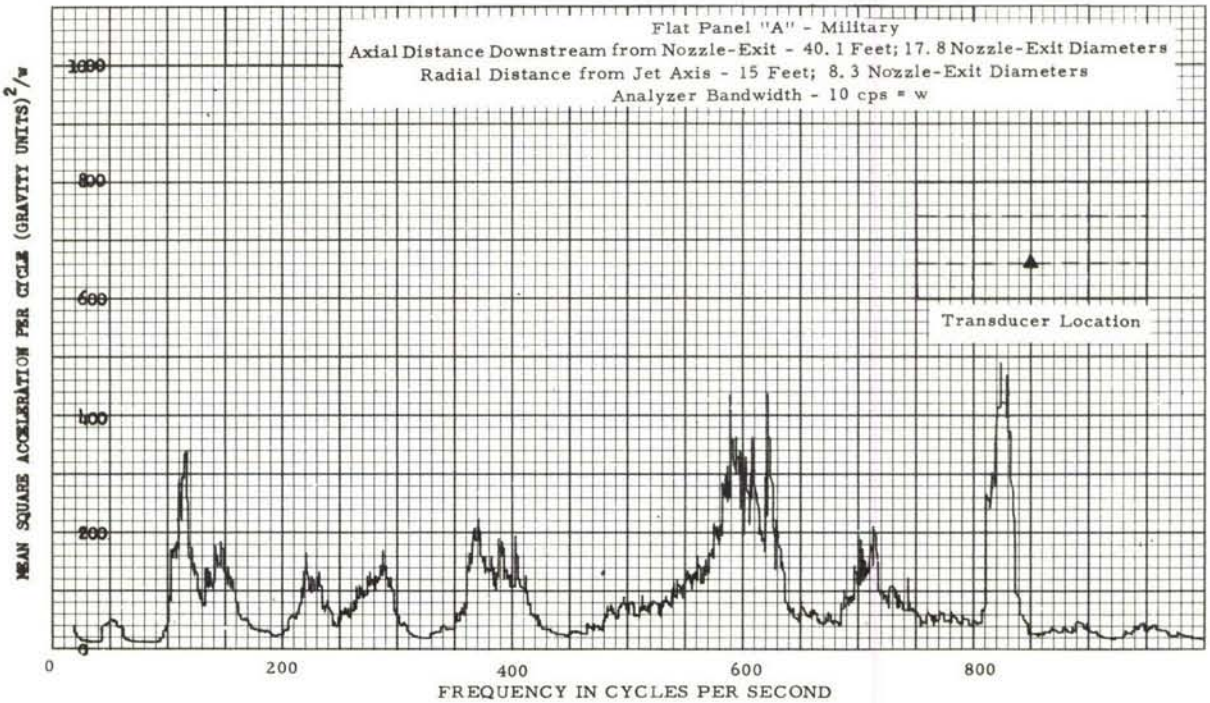

Figure IV-51. Power Spectral Density Analysis of Acceleration - Flat Panel A - Military

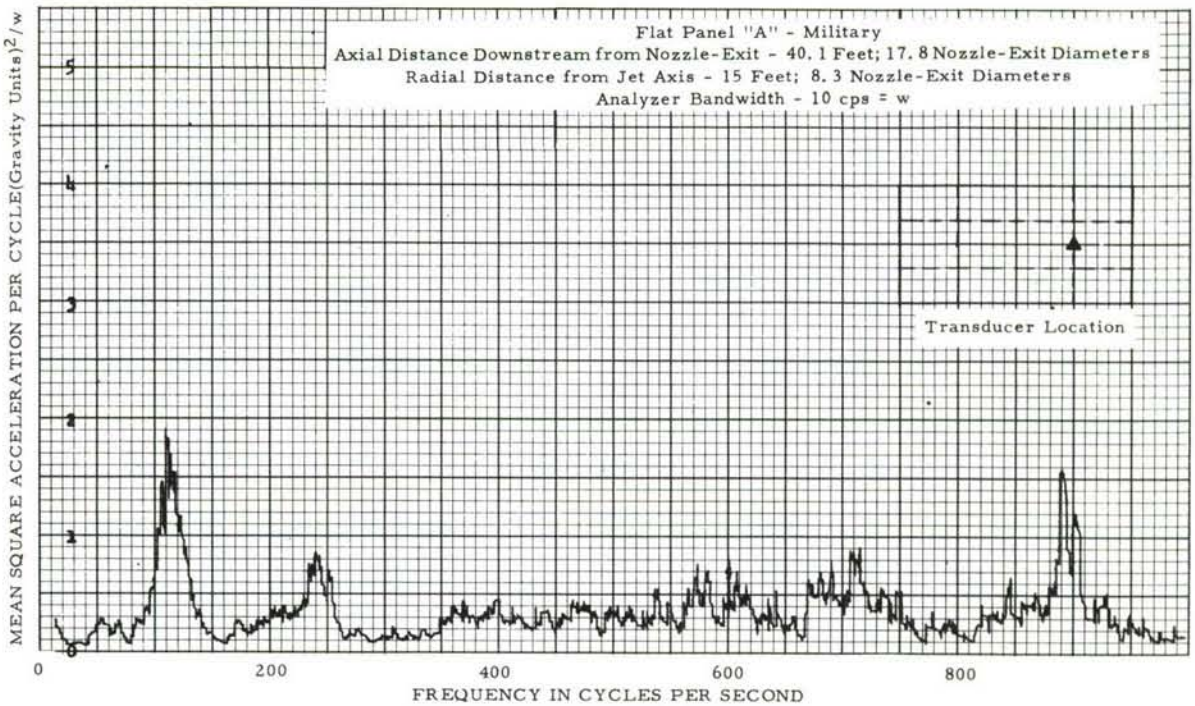

Figure IV-52. Power Spectral Density Analysis of Acceleration - Flat Panel A - Military

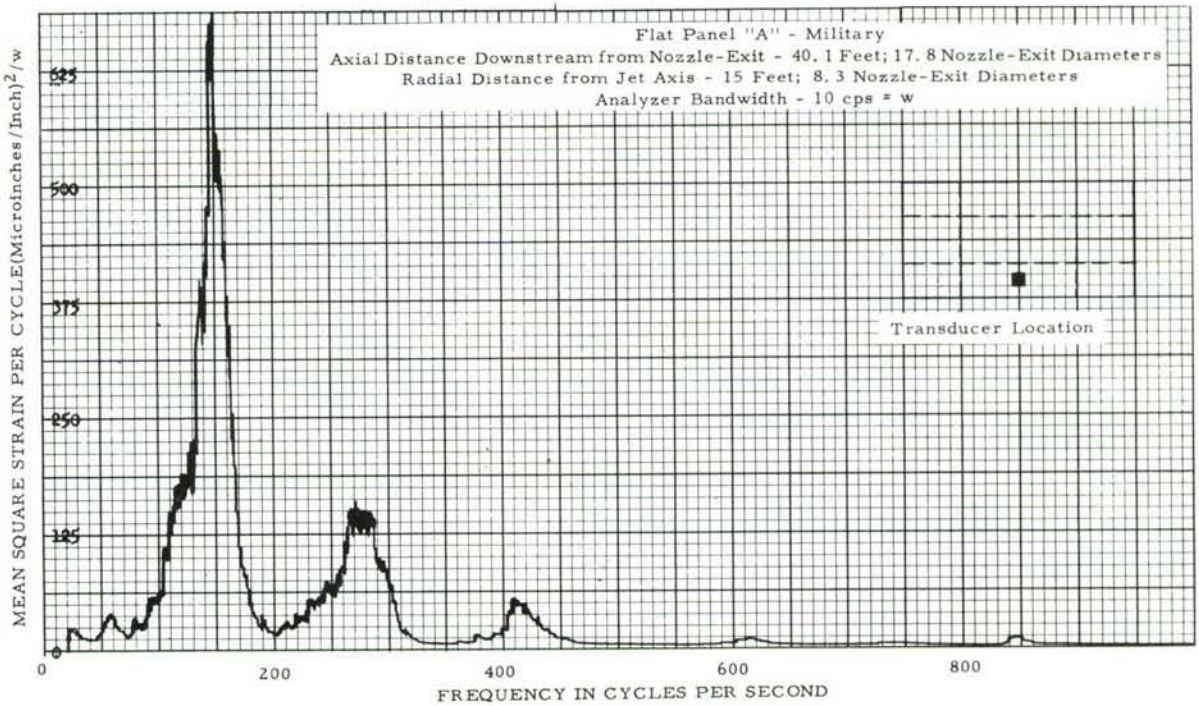

Figure IV-53. Power Spectral Density Analysis of Bending Strain - Flat Panel A - Military

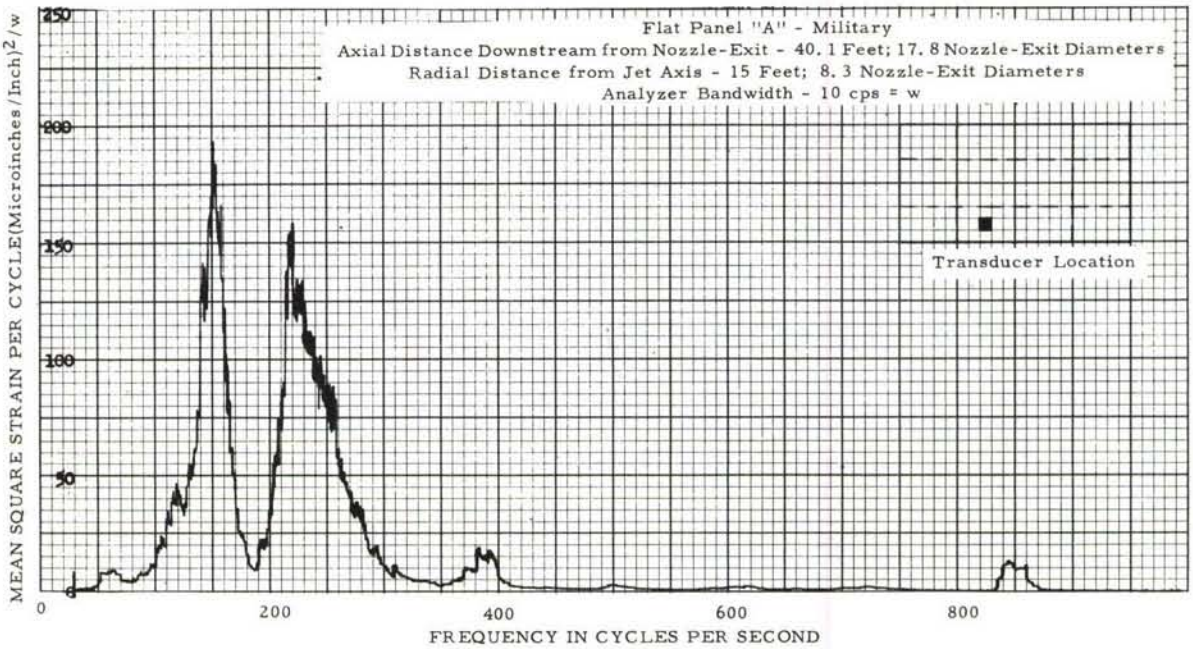

Figure IV-54. Power Spectral Density Analysis of Bending Strain - Flat Panel A - Military

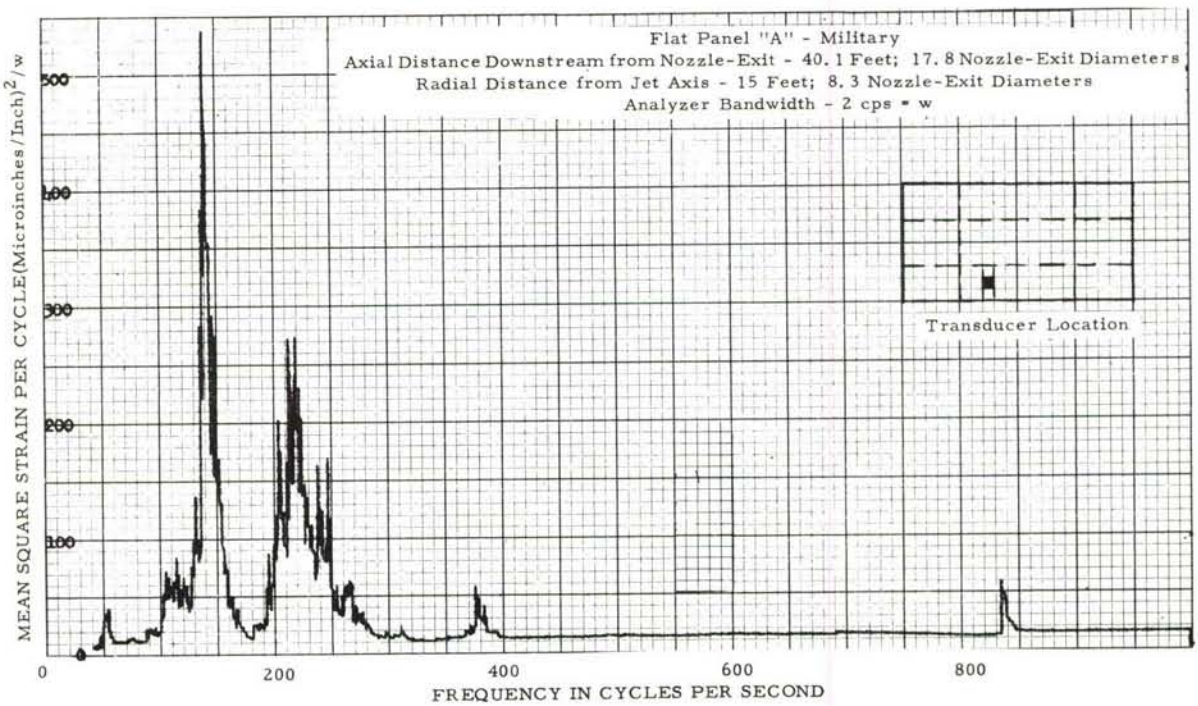

Figure IV-55. Power Spectral Density Analysis of Bending Strain - Flat Panel A - Military

SECTION V

FATIGUE

A. Introduction and Objectives

A total of twelve panel specimens in four general configurations was subjected to the high intensity jet noise environment during the experimental phases of this study. However, the major portion of these tests were conducted as a fundamental part of the structural response study. So the panels involved were placed in the noise field to facilitate the taking of such required measurements. Because it was not considered practical to relocate the fatigue tests to a position of higher intensity within the noise field or economically feasible to operate the engine at high thrust for extended periods, the fatigue failures were limited to lightest of the several configurations tested. Within this limitation the fatigue phase of the program was conducted to obtain the maximum useful data.

The primary objectives of this phase of the program may be defined as follows:

(a) to determine if the experimental data were obtained under stress level conditions which would be of interest in real structures;

(b) to locate the critical area on a particular specimen configuration;

(c) to provide the correlation between the fatigue strength and the predicted and measured response.

B. Procedure

The description of the test panels and mounting details was covered in Section IV. The test position within the noise field was also limited to one of the two locations used in the response measurement phase. Actually, the jet engine time logged during earlier phases of the program constitutes the bulk of the fatigue testing time. Thus the measured noise characteristics and panel response, as covered in Sections II and IV, also describe the conditions under which these tests were conducted.

C. Results

All of the failures were confined to Type A and Type E panels and in these similar configurations the failure initiated at the same structural detail. Such failures first appear in the rib flange at the rivet common to both rib and stringer. While this type of failure occurred in identical areas throughout the panel, the rib ends were particularly vulnerable. When the failures were allowed to propagate at the rib ends, they proceeded out into the rib flange so that skin cracks then developed at the structural discontinuities so formed. Such a typical failure is shown in

photographs of Figure V-1. A log of fatigue testing conditions and time to fail is shown in Table V-1. After the early failure of the A-1 panel, a doubler was added to all subsequent A and E type panels. This doubler which affected the transfer of loads between the substructure and the panel supporting boundary added significantly to the useful testing life of the panels. A photograph of a typical installation of such doublers is shown in Figure V-2. This group of panels was all tested in the same "downstream" site except for the A-2 panel. In this case the higher sound pressure levels at the "upstream" site produced relatively early fatigue failures.

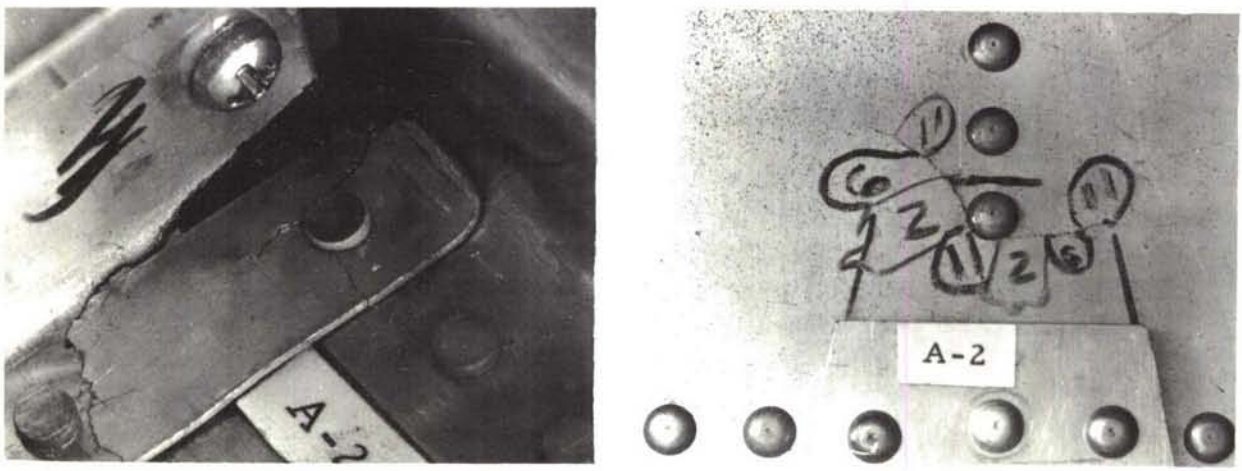

Figure V-1. Fatigue Failures in Panel A

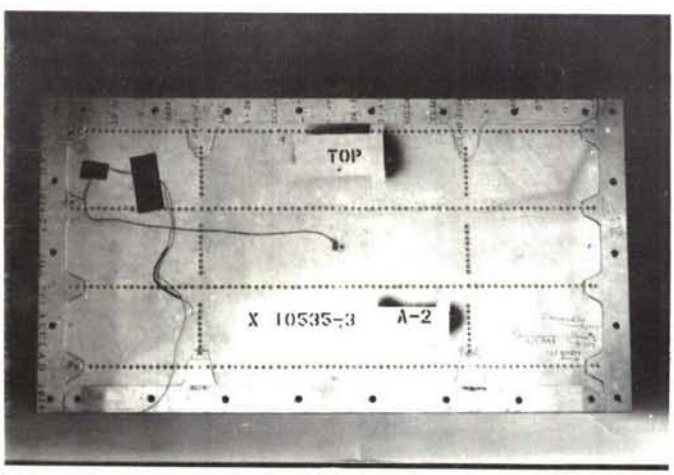

Figure V-2. Doubler Installation - Typical for Type A and Type E Panels

TABLE V-1

LOG OF FATIGUE FAILURES

Panel No.	Type of Failure (1)	Time to Fail Minutes A/B	Time to Fail Minutes Military	Panel Location in Noise Field
A-1	(a)&(b)	10	11	(3)
A-2	(a)&(b)	11	10	(3)
A-3	None	21	21	(4)
A-4	(b)	18	15	(3)
E-1	None	18	15	(3)
E-2	(a)&(b)	(2)	--	(3)

Notes:

(1) Type of Failure (a) crack in rib at cutout
(b) crack in skin at (a)

(2) Six and one-half hours of varying thrust conditions

(3) Located 40.1 feet downstream and 15 feet from jet axis

(4) Located 14.2 feet downstream and 10 feet from jet axis

One other noteworthy variation in the fatigue testing procedure concerns the E-2 panel. Its acoustical loading was produced by a later model production version of the J-79 test engine which was being subjected to performance checkout procedures. Even though the bulk of six and one-half hours of testing time was obtained at less than military thrust (less than two minutes in A/B), the location and character of the fatigue failures were unaltered.

D. Conclusions

The tremendous cost of fatigue testing by means of jet engine generated noise fields has placed stringent limitations on this phase of the test program. Such limitations affected the number of different specimens as well as the number of any one type of specimen that could be tested to failure.

Even so, certain conclusions may be drawn which are related to the basic objectives. Taken in turn, these conclusions may be summarized as follows:

(a) The bulk of the experimental response data was obtained from a specimen configuration which was being driven to sufficiently high levels to produce fatigue failures at its critical detail.

(b) A sufficient number of fatigue failures was obtained in this one configuration to define the location of the critical detail.

(c) The fatigue tests have served to indicate the order of magnitude of fatigue life for the one basic configuration.

SECTION VI

SUMMARY

A. Summary of Conclusions

Generally, the objectives of the program were met. Comprehensive groups of data were obtained which describe the noise environment of a modern turbojet engine, the response of structure within that noise environment, and the basic dynamic parameters of the structure studied. Analytical methods for predicting structural response were developed. Although some significant differences in correlation between calculated and test response were obtained, the basis for the analytical approach is considered sound. Many possibilities for refinement of theory to minimize these differences were beyond the scope of this program.

Specific conclusions can be listed as follows:

1. The free field measurements of the engine noise environment show good correlation with earlier published work. The characteristic lobed isolevel contours were apparent.

2. Data were obtained defining the pressures within the jet wake. A single lobe, extending downstream, was indicated by the isolevel contours.

3. The noise output of the engine, for a given power setting, varied sufficiently to exhibit significant differences between sample averages for the duration of sample used.

4. The noise output from the engine for afterburner and military power settings are different both in level and in spectrum.

5. The prediction of response modes of structures is very difficult for anything but very simple shapes and restraints.

    a. The control and description of boundary restraints are severe limiting factors.

    b. Preload conditions due to thermal loading or external loading significantly affect dynamic characteristics.

    c. More refined determination of structural damping is required.

6. Measured structural amplitudes indicate response amplitudes which should be in the linear region.

7. Early fatigue failure of a typical structure verified the severity of the noise environment for this particular structure.

B. Recommendations

Several of the conclusions suggest areas well worth further study. These and others might be noted as follows:

1. Panel Pressures "Close to" and "On" Rigid Boundary

The results of Section II of the report indicate differences between sound pressures on the rigid plate and adjacent field. Above about 250 cps, the pressures on the plate are up to 4 db higher than those in the field. Since such field measurements are used to define the pressures exciting the structure, it is clearly of importance to understand the nature and magnitude of any effect of this sort. In addition, the ability of existing experimental techniques to measure pressures near a boundary is subject to question. Differences between actual panel pressures and those measured at microphones are not known. The transition distance, if any, between microphone pressures and actual panel pressures is unknown. Possible effects of these differences on spatial correlations are also unknown. Further investigation is therefore recommended.

2. Analytical Determination of Modes

A number of limitations of the analytical method of mode determination is evidenced by the study (see Section III). To overcome such limitations, it is recommended that further development of analytical methods of mode determination be undertaken. Such development should ensure the capability to determine modes having node lines within panel boundaries and to cater for a more detailed description of panel boundary conditions and edge member rotational restraints. Preload effects should also be studied.

3. Curved Panel Response Predictions

It is recommended that further work be done to determine analytically the jet noise field response of the curved panel since it is typical of fuselage construction and that, as a basis for such prediction, additional laboratory resonance tests be carried out to define natural mode data. Curved panels exhibit non-linear characteristics but their dynamic characteristics are less sensitive to thermal induced stress.

4. Possible Cross Correlations

Complete data on spatial correlations of pressure are available on magnetic tape for the 1600 possible cross correlations on

each of the panels studied. A minimum number was reduced for use in the response prediction calculations. It was assumed that reciprocity held. A sufficient quantity of data should be reduced and analyzed to verify this assumption.

5. New Questions

In the spectral analysis of the data the assumption as to the "stationary" character of the noise raises some questions. What are the effects of different sampling times on the statistical properties of the jet engine noise? What are the effects of observation bandwidth, the shape of the band and sweep rate on the results? The available data should be studied further in an attempt to answer these questions.

REFERENCES

1. Kamperman, G. W., "Measurement of Hi-Intensity Noise," Noise Control, September 1958.

2. Howes, Walton L., Edmund E. Callaghan, Willard D. Coles, and Harold R. Mull, Near Noise Field of a Jet-Engine Exhaust, NACA Report 1338.

3. Laurence, James C., Intensity, Scale and Spectra of Turbulence in Mixing Region of Free Subsonic Jet, NACA Report 1292.

4. Lassiter, L. W., and H. H. Hubbard, The Near Noise Field of Static Jets and Some Model Studies of Devices for Noise Reduction, NACA Technical Report 1261.

5. Davenport, W. B., Jr., and W. L. Root, Random Signals and Noise, McGraw-Hill Book Co., Inc., New York, N. Y., 1958.

6. Bendat, J. S., Principles and Application of Random Noise Theory, John Wiley & Sons, Inc., New York, N. Y., 1958.

7. Beranek, L. L., Acoustics, McGraw-Hill Book Co., Inc., New York, N. Y., 1954.

8. Mollo-Christensen, Erik, Jet Noise Generation and Suppression, MIT Fluid Dynamics Research Group, Report No. 59-5, May 1959.

9. Phase I Interim Report on Study of the Characteristics of Modern Engine Noise and the Response Characteristics of Manned Vehicle Structures, Lockheed Report No. 13206, September 1958.

10. Proposal for Study of the Characteristics of Jet Noise and the Response of Aircraft Structures to Jet Noise, Lockheed Report No. 12735, December 1957.

11. Liepmann, H. W., "On the Application of Statistical Concepts to the Buffeting Problem," Journal of the Aeronautical Sciences, December 1952.

12. Warburton, C. B., "The Vibration of Rectangular Plates," Proceedings of the Institute of Mechanical Engineers, Vol 168, No 12, 1954.

13. Timoshenko, S., "Theory of Plates and Shells."